WHOI-98-09

Rotating Hydraulic Control

1997 Summer Study Program

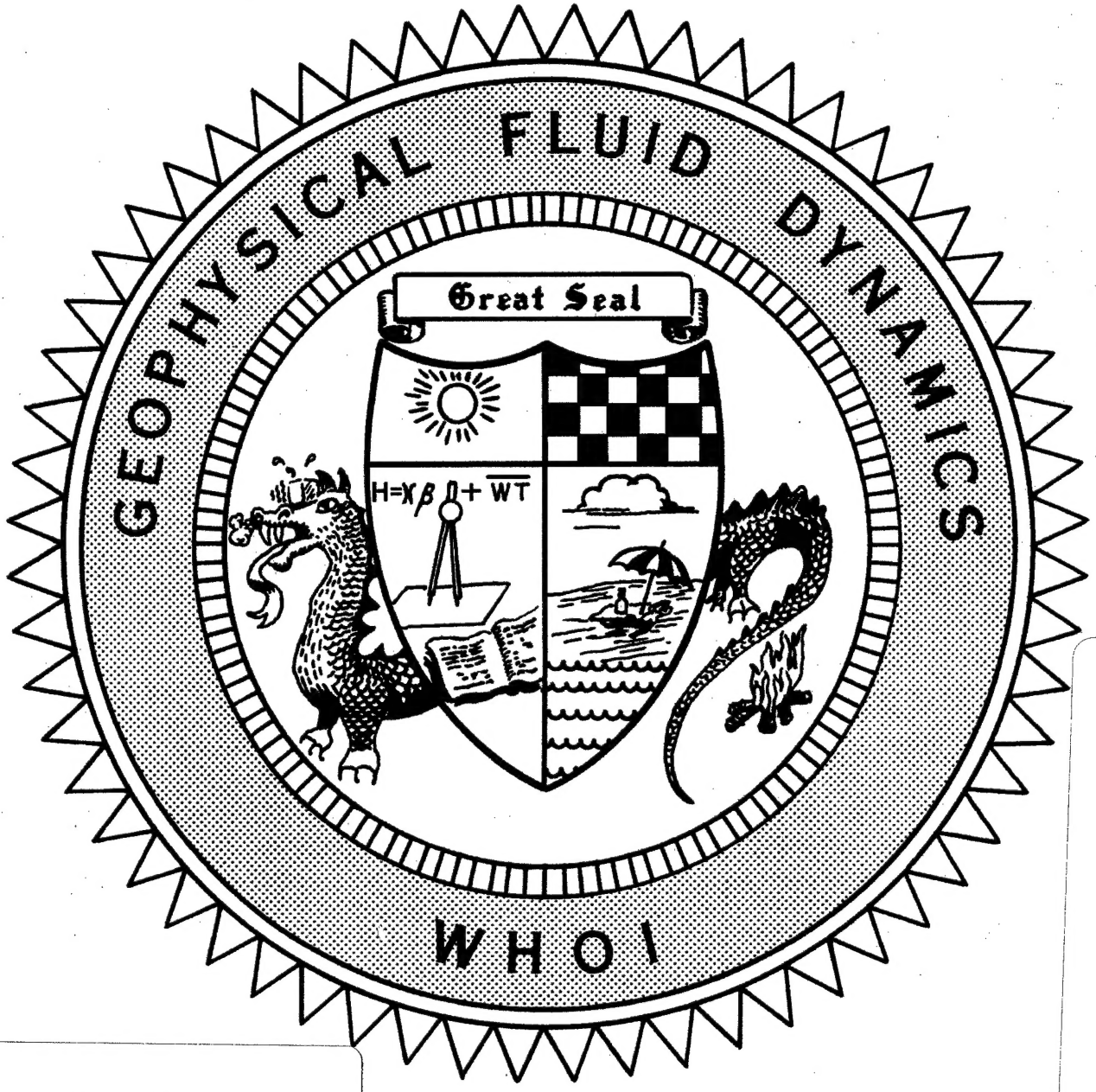

19981209 048

Reproduced From
Best Available Copy

DTIC QUALITY INSPECTED 4

Course Lectures
Fellows Project Reports

WHOI-98-09

Rotating Hydraulic Control

1997 Summer Study Program in Geophysical Fluid Dynamics

by

John A. Whitehead, Director

Woods Hole Oceanographic Institution
Woods Hole, Massachusetts 02543

July 1998

Technical Report

Funding was provided by the National Science Foundation
through Grant No. OCE-9314484 and the Office of Naval Research
through Grant No. ONR-N00014-97-1-0934

Reproduction in whole or in part is permitted for any purpose of the United States Government. This report should be cited as Woods Hole Oceanog. Inst. Tech. Rept., WHOI-98-09.

Approved for public release; distribution unlimited.

Approved for Distribution:

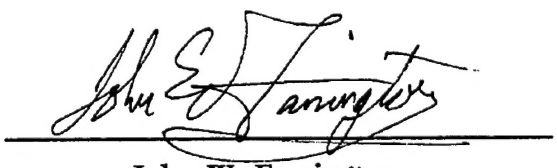

John W. Farrington
Associate Director for Education
and Dean of Graduate Studies

PREFACE

The topic of the thirty ninth year of the program, "Rotating Hydraulic Control", was principally centered about those nonlinear problems in which either a free surface or internal stratification is so modified by flow that it acts to choke off increased flux as the forcing is increased. It is a peculiar form of convection, which shares many constraints with more general buoyancy driven motion but which has its own internal limits. These make the studies both unique and interesting. This years principal lectures were given by Larry Pratt with additional lectures by Doron Nof, Dan Ohlsen, and Peter Killworth, but also with a single Physical Oceanography lecture reviewing applications in the ocean by the director. The program involved the participation of most of the founders of this young field of study and the lecture notes summarize a sizable percentage of the present understanding.

The ten student projects constitute the heart of the summer GFD experience. They describe the development of studies on new, original, and tractable problems by our fellows who are in the midst of their graduate work. We expect that some of the studies will grow to full projects to be published in due course, as has been the case many times in the past. But whatever the results of this summer's experience is for each fellow, be it a fully finished work, new ideas, fearless and honest inquiry, or simply experience working with a staff member in our craft, we wish our fellows well in their future studies and research.

Especial thanks go to a number of people who served to make the program flow smoothly. Lee Ann Campbell ran the office and performed administrative work for the many visits and lectures. Her work in preparation during the "slack" season (completely misnamed) was especially appreciated by this novice director, as was her cheerful support of the fellows and visitors all summer. John Salzig created apparatus and helped with at least four laboratory experiments, plus helped with odd tasks such as retrieving locked keys and repairing old bicycles. Eric Chassignet and Glenn Flierl assembled computer resources and networks to keep everyone hooked up digitally. George Veronis ran the world-class softball team which counted a number of wins in the season.

Thanks go to the National Science Foundation for support for this program under OCE81-44840. Support was also provided by the Office of Naval Research, Processes and Prediction Division, Physical Oceanography Program, under grant N0014-97-1-0934.

Jack Whitehead
Director

Contents

Page

I **PREFACE** i

II **PARTICIPANTS** iv

III **LECTURE SCHEDULE** viii

IV **PRINCIPAL LECTURES**

General Principles
Larry Pratt, Physical Oceanography Department, WHOI

Review of the Hydraulics of Nonrotating Flows and Nonlinear Waves **1**

Review of Semigeostrophic Waves **8**

Steady Theories of Rotating Hydraulics **13**

Steady Theory, continued - Rotating Shocks **22**

Potential Vorticity Wave Hydraulics **40**

~~~~~~~~~~~~

Critical Control of Deep Ocean Sill Flows
Jack Whitehead, Physical Oceanography Department, WHOI **49**

Inter-basin Exchange Through Broad Channel and Gaps
Doron Nof, Florida State University
Part I **59**
Part II **69**

Rotating Channel Exchange: Experiments and Numerics
Dan Ohlsen, Colorado Research Associates **77**

Bounding Rotating Hydraulic Flows **88**
Peter D. Killworth, Southampton Oceanography Center
~~~~~~~~~~~~

V FELLOW'S REPORTS

Eddy Shedding From a Boundary Current Around a Cape Over a Sloping Bottom
Claudia Cenedese 95

The Rotating Hydraulic Jump From an Axisymmetric Jet
Christopher Hills 111

Fluid Intrusion in a Rotating Channel
Allen Kuo 127

Boundary Layer Separation in the Surface Quasi-Geostrophic Equations
Annalisa Bracco 149

Hydraulic Control and Mixing in a Semi-Enclosed Reservoir
Mary-Louise Timmermans 175

An Experimental Investigation of a Coastally-Trapped Surface Density Current
Jeffrey Parsons 191

Derivations of Linear Stability Criteria for Shear Flow Using Barston's Method
Jurgen Theiss 201

Hydraulics of Branching Channels
Keir Colbo 216

Hydraulic Control With Entrainment
Katsumata Katsurou 228

Flow in a Narrow Channel With Rotation and Friction
Jon Xinzhong Chen 242

1997 GFD Participants

The Fellows

Annalisa Bracco	University of Torino, Italy
Claudia Cenedese	University of Cambridge, UK
Jon Xinzhong Chen	Columbia University
Keir Colbo	University of Victoria, Canada
Christopher P. Hills	University of Cambridge, UK
Katsurou Katsumata	University of Tokyo, Japan
Allen C. Kuo	Columbia University
Jeffrey D. Parsons	University of Illinois
Jurgen Theiss	University of Cambridge, UK
Mary-Louise Timmermans	University of Cambridge, UK

Staff and Visitors

James Anderson	Stevens Institute of Technology
Neil Balmforth	Scripps Institution of Oceanography, University of California, San Diego
Konstantin Bezhanov	Moscow Institute of Physics & Technology, Russia
Karin M. Borenas	Göteborg University, Sweden
Alexander Casti	Columbia University
Eric Chassignet	University of Miami
Paul J. Dellar	University of Cambridge, UK
Alexey V. Fedorov	Scripps Institution of Oceanography, University of California, San Diego
Glenn Flierl	Massachusetts Institute of Technology
Rupert Ford	Imperial College, UK
Ross W. Griffiths	Australian National University, Australia
Karl Helfrich	Woods Hole Oceanographic Institution
Louis N. Howard	Florida State University
Ted R. Johnson	University College, UK
Joseph B. Keller	Stanford University
Peter D. Killworth	University of Southampton, UK
Gregory F. Lane-Serff	University of Southampton, UK
Norman R. Lebovitz	University of Chicago
Sonya Legg	Woods Hole Oceanographic Institution
Stefan G. Llewellyn Smith	Scripps Institution of Oceanography, University of California, San Diego
Alex Mahalov	Arizona State University
Willem V.R. Malkus	Massachusetts Institute of Technology
Stephen Meacham	Florida State University
Philip J. Morrison	University of Texas at Austin

David Muraki	New York University
Doron Nof	Florida State University
Anatoly Odulo	Applied Science Associates, Inc.
Daniel R. Ohlsen	Colorado Research Associates
Matheos P. Papadakis	University of Miami
Claudia Pasquero	University of Torino, Italy
Joseph Pedlosky	Woods Hole Oceanographic Institution
Larry J. Pratt	Woods Hole Oceanographic Institution
Antonello Provenzale	University of Torino, Italy
Audrey Rogerson	Woods Hole Oceanographic Institution
Claes G. Rooth	University of Miami
Richard L. Salmon	Scripps Institution of Oceanography, University of California, San Diego
Roger Samelson	Woods Hole Oceanographic Institution
Vitalii Sheremet	Woods Hole Oceanographic Institution
Harper Simmons	Florida State University
David Smeed	University of Southampton, UK
Ronald B. Smith	Yale University
Edward A. Spiegel	Columbia University
James Stephens	University of Reading, UK
Melvin Stern	Florida State University
Louis Tao	Columbia University
Jean-Luc Thiffeault	University of Texas at Austin
George Veronis	Yale University
Jack Whitehead	Woods Hole Oceanographic Institution

1997

Standing (left to right): E Spiegel, L. Campbell, R. Ford, W. Malkus, K. Borenas, V. Sheremet, K. Katsumata, S. Meacham, K. Bezhanov, C. Hills, T. Johnson, J. Pedlosky, C. Rooth, R. Smith, A. Mahalov

Seated on porch (left to right): D. Muraki, L. Tao, J. Theiss, J. Parsons, C. Cenedese, G. Veronis, J. Keller, M. Stern, K. Colbo, A. Bracco, M. Timmermans, J. Chen

Seated on ground (left to right): A. Kuo, N. Balmforth, R. Salmon, S. Legg, J. Whitehead

Not pictured: J. Anderson, A. Casti, E. Chassignet, P. Dellar, A. Fedorov, G. Flierl, R. Griffiths, K. Helfrich, L. Howard, P. Killworth, G. Lane-Serff, N. Lebovitz, S. Llewellyn Smith, P. Morrison, D. Nof, A. Odulo, D. Ohlsen, M. Papadakis, C. Pasquero, L. Pratt, A. Provenzale, A. Rogerson, R. Samelson, H. Simmons, D. Smeed, J. Stephens, J. Thiffeault

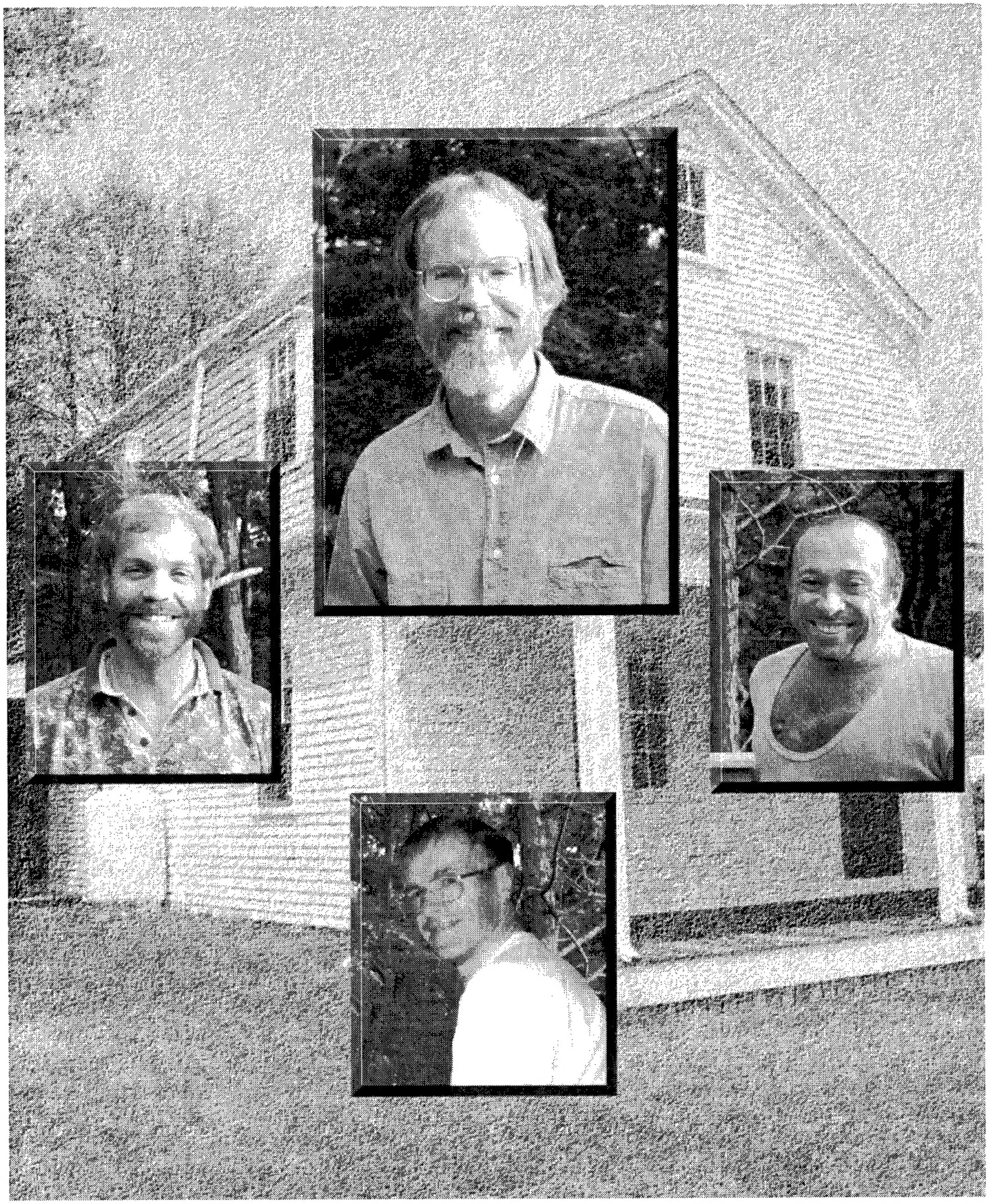

1997 GFD Principal Lecturers

Pictured clockwise from top are 1997 GFD Principal Lecturers Larry Pratt, Doron Nof, Peter Killworth, and Daniel Ohlsen.

GFD 1997 Lecture Schedule

Monday, June 16
10:00 John W. Farrington, Associate Director for Education and Dean of Graduate Studies and Jack Whitehead
Welcome to WHOI and to GFD

10:15 Larry Pratt
Review of the Hydraulics of Nonrotating Flows and Nonlinear Waves

Tuesday, June 17
10:00 Larry Pratt
Review of Simigeostrophic Waves

15:00 Jack Whitehead, Physical Oceanography Department Seminar
Critical Control of Deep Ocean Sill Flows

Wednesday, June 18
10:00 Larry Pratt
Steady Theories of Rotating Hydraulics

14:00 Doron Nof
Inter-basin Exchange Through Broad Channel and Gaps, Part I

Thursday, June 19
10:00 Larry Pratt
Steady Theory, continued - Rotating Shocks

14:00 Doron Nof
Inter-basin Exchange Through Broad Channel and Gaps, Part II

Friday, June 20
10:00 Larry Pratt
Potential Vorticity Wave Hydraulics

14:00 Dan Ohlsen
Rotating Channel Exchange: Experiments and Numerics

Monday, June 23
10:00 Peter D. Killworth
Bounding Rotating Hydraulic Flows

Tuesday, June 24
10:00 Norman R. Lebovitz
Stability in Conservative Gyroscopic Systems

Wednesday, June 25
10:00 Peter D. Killworth
On the Parameterisation of Baroclinic Eddies

14:00 Stefan G. Llewellyn Smith
Dynamics of Interface Layer in a Stratified and Turbulent Fluid

Thursday, June 26
10:00 Melvin E. Stern
Coastal Flow Controlled by Topographic Waves

14:00 Norman R. Lebovitz
Slow Evolution in Conservative Systems

Friday, June 27
10:00 Ted Johnson
Nonlinear Western Boundary Currents and Separation

Monday, June 30
10:00 Vitalii Sheremet
Multiple Equilibria and Inertial Runaway in Wind-Driven Circulation

Tuesday, July 1
10:00 Louis Tao
Turbulent Magnetic Flux Expulsion

Wednesday, July 2
10:00 Sonya Legg
Turbulent Entrainment in Convection

Thursday, July 3
10:00 Ted Johnson
Scattering of Coastal Waves

Friday, July 4
July 4th Holiday, No Lectures

Monday, July 7
10:00 Alex Mahalov
Asymptotic Nonlinear Baroclinic Wave Dynamics and Adjustment of Pancake Dynamics

Tuesday, July 8
10:00 Alexey Fedorov
Breaking Internal Waves and Hydraulic Jumps in Rotating Fluids at Boundaries in the Ocean and Atmosphere

Wednesday, July 9
10:00 Karin Borenas
Upstream Separation in a Rotating Channel Flow

Thursday, July 10
10:00 Antonello Provenzale
Transport by Barotropic Coherent Vortices

Friday, July 11
10:00 Rick Salmon
Linear Theory of the North Atlantic

Monday, July 14
10:00 George Veronis
Laboratory Model of Ocean Circulation: Observation and Linear Theory - Steady Flow and Instabilities

Tuesday, July 15
10:00 Ron Smith
Stratified Flow Near Topography: Continuous and Layered Models

Wednesday, July 16
10:00 Anatoly Odulo
Two-Layer Exchange Flows Through a Constriction

Thursday, July 17
10:00 Ron Smith
2-D Shallow Water Flow With Jumps, Wakes and Vortices

Friday, July 18
10:00 David Muraki
Balance Flow in the Mid-Lateral Atmosphere

Monday, July 21
10:00 Joseph B. Keller
Flows Over Weirs

Tuesday, July 22
10:00 David Smeed
Observations of the Outflow from the Arabian Gulf

Wednesday, July 23
10:00 Rupert Ford
Nonlinear Ocean Circulation Modelling: Realistic Topography and Finite Element Methods

Thursday, July 24
10:00 David Smeed
Exchange Through the Bab al Mandab and Hydraulic Control in a Three-Layer Fluid

Friday, July 25
10:00 Audrey Rogerson and Roger Samelson
A Transcritical Flow Problem in Coastal Meteorology

Monday, July 28
10:00 Eric Chassignet
On the Emergence of Inertial Gyres in a Two-Layer Quasigeostrophic Model

Tuesday, July 29
10:00 Neil Balmforth
Long-Wave Instability in Shear Flows

Wednesday, July 30
10:00 Joseph Pedlosky
Flow Around Islands and Ridges

Thursday, July 31
10:00 Konstantin Bezhanov and Vitalii Sheremet
3-D Flow of Stratified Fluid Over an Obstacle

Friday, August 1
10:00 Edward Spiegel
Gravitational Instability

Monday, August 4
10:00 Gregory Lane-Serff
Eddy Formation by Overflows on Slopes

Tuesday, August 5
10:00 Ross Griffiths
Two Problems with Turbulent Plumes: Mixed Layers and Horizontal Shear Layers

Wednesday, August 6
10:00 Gregory Lane-Serff
Laboratory Models of Multi-Layer Hydraulics

Thursday, August 7
10:00 Ross Grifffiths
Eddy-Shedding in One- and Two-Layer Flows in the Sliced Cylinder Beta-Plane Model

Friday, August 8
10:00 Willem Malkus
Elliptical Instabilities: Tidal Instability as the Source for Io's Magnetic Signature

Tuesday, August 19
10:00 Fellow's Lecture I: Claudia Cenedese
Eddy Shedding From a Boundary Current Around a Cape Over a Sloping Bottom

11:00 Fellow's Lecture II: Christopher Hills
The Rotating Hydraulic Jump From an Axisymmetric Jet

Wednesday, August 20
10:00 Fellow's Lecture III: Allen Kuo
Fluid Intrusion in a Rotating Channel

11:00 Fellow's Lecture IV: Annalisa Bracco
Boundary Layer Separation in the Surface Quasi-Geostrophic Equations

14:00 Fellow's Lecture V: Mary-Louise Timmermans
Hydraulic Control and Mixing in a Semi-Enclosed Reservoir

15:00 Fellow's lecture VI: Jeffrey Parsons
An Experimental Investigation of a Coastally-Trapped Surface Density Current

Thursday, August 21
10:00 Fellow's Lecture VII: Jurgen Theiss
Derivation of the Richardson Number Stability Criteria Using Barston's Methods

11:00 Fellow's Lecture VIII: Keir Colbo
Hydraulic Control in Branching Channels

14:00 Fellow's Lecture IX: Katsurou Katsumata
Hydraulic Control With Entrainment

15:00 Fellow's Lecture X: Jon Xinzhong Chen
Transport in a Narrow Channel With Friction

Review of hydraulics for non-rotating, 1-D, single-layer flows

Larry Pratt, Lecture 1

Notes by: *Chris Hills & Jeff Parsons*

The purpose of the lectures will be to consider the role of hydraulic control in determining the steady flows produced when fluid flows down a channel over varying topology from an upstream reservoir. Physically this situation may arise from flow over a dam, down a spillway, out of an estuary or along a coastline. The most striking oceanic example, however, is flow over a deep ocean sill: observed in the Denmark Strait or Faroe Bank channel. It is clear that the flow produced will be influenced by the effects of rotation, density gradients and the shape of the channel. The flows to be considered lie midway between nonrotating, hydraulically driven currents (in which the velocity and pressure gradients are aligned) and strongly rotating, geostrophic currents (in which the velocity and pressure gradients are perpendicular). As will be shown, the problem of hydraulic control of this flow is essentially non-linear.

Throughout we will be considering flow down a *gradually* varying channel, taking W, L, D to be width, length and depth scales. In this context we take *gradual* to mean that $D/L \ll 1$ (leading to the hydrostatic approximation) and $W/L \ll 1$ (leading to the semi-geostrophic approximation). Without rotation, several different flow regimes may be observed, depending upon the topography of the channel; *e.g.* for flow over a bump (see Long [1]).

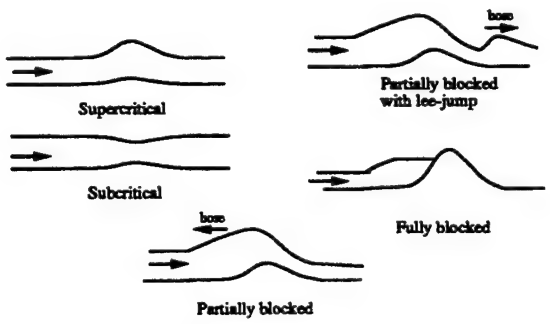

Figure 1.

We shall take axes for the flow as shown in figure 2, with y in the downstream direction, x cross-stream, and z vertically. Then the width of the channel at a downstream position y, is taken to be $w(y)$ and $d(x, y, t)$ to be the depth. The bottom topography is given by $h(x, y)$, and horizontal fluid velocities by u and v as shown.

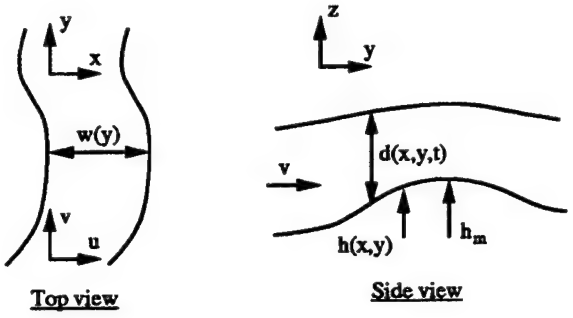

Figure 2.

We first consider, for simplicity, the case of one-dimensional, non-rotating, single-layer flow. In this case,

$$d = d(y,t), \quad h = h(y), \quad v = v(y,t), \quad u = 0. \tag{1.1}$$

For channel flow over a bump (of maximum height, h_m) we use, taking our dimensional assumptions of above, the familiar shallow water equations (SWE),

$$\begin{aligned} \frac{\partial v}{\partial t} + v\frac{\partial v}{\partial y} &= -g\frac{\mathrm{d}h}{\mathrm{d}y} - g\frac{\partial d}{\partial y}, \\ \frac{\partial}{\partial t}(dw) + \frac{\partial}{\partial y}(vdw) &= 0, \end{aligned} \tag{1.2}$$

where (1.2a) expresses conservation of momentum and (1.2b) the conservation of mass with constant density. In the case of constant width and height, equations (1.2) can be expressed in terms of characteristic variables,

$$\frac{\mathrm{d}_\pm}{\mathrm{d}t} R_\pm = 0,$$

where,

$$\begin{aligned} \frac{\mathrm{d}_\pm}{\mathrm{d}t} &= \frac{\partial}{\partial t} + c_\pm \frac{\partial}{\partial y}, \\ R_\pm &= v \pm 2(gd)^{\frac{1}{2}}, \quad c_\pm = v \pm (gd)^{\frac{1}{2}}, \end{aligned} \tag{1.3}$$

so that along the characteristic curves of speed $c_\pm$ the Reimann invariant quantities $R_\pm$ are constant. Consider the problem of a 'simple' wave propogating into quiescent fluid, for which R_- is constant. Take the initial flow to be as shown in figure 3.

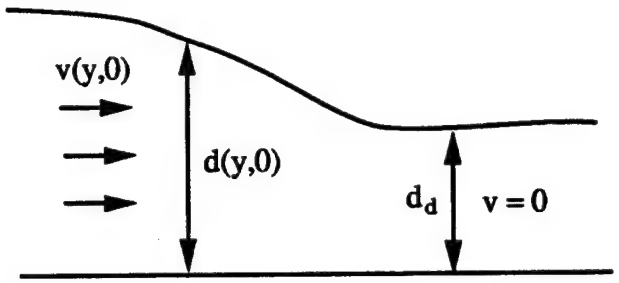

Figure 3.

Then evaluating R_- far downstream (assuming characteristic curves fill the (y,t)-plane) we get

$$v - 2(gd)^{\frac{1}{2}} = -2(gd_d)^{\frac{1}{2}},$$

and therefore,

$$R_+ = v + 2(gd)^{\frac{1}{2}} = 4(gd)^{\frac{1}{2}} - 2(gd_d)^{\frac{1}{2}}. \tag{1.4}$$

Therefore, we see that the depth d is constant along the characterisitc curves $x_+(t)$ determined by $\mathrm{d}x_+/\mathrm{d}t = c_+$, ($R_+, d_d$ are constant) and so is the speed v. This also implies that c_+ is also constant (*i.e.* $c_+ = v + (gd)^{1/2} = 3(gd)^{1/2} - 2(gd_d)^{1/2}$). Along a '+' characterisitc curve d will be constant and thus $c_+ = (gd_0)^{1/2}$ where d_0 is the initial depth. In the figure, large values of d_0 lie to the left of smaller values and thus the large value of d will propagate more rapidly and overtake the smaller values, leading to a shock. This coincides with the intersection of two characteristics (as in figure 4a) and at this point the assumptions of the shallow water equations break down. Alternatively, (see figure 4b), a wave may disperse with time if the characteristic curves diverge – this is rarefaction.

We now introduce a Froude number, F. We define it to be,

$$F = \frac{v}{(gd)^{1/2}}. \tag{1.5}$$

We shall see that through this dimensionless quantity we may characterise the flow as follows:

subcritical	$c_- < 0$	upstream propagation	$F < 1$,
critical	$c_- = 0$	no propagation	$F = 1$,
supercritical	$c_- > 0$	downstream propagation	$F > 1$.

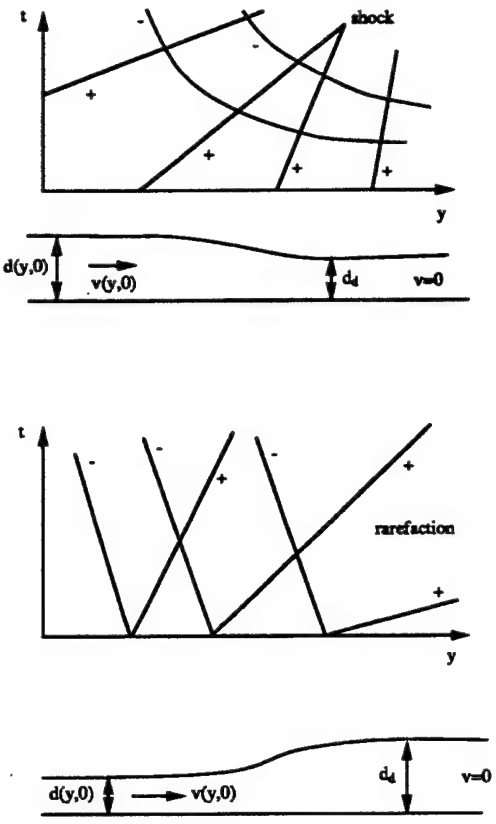

Figure 4.

We now return to the equations for variable width, steady flow,

$$\begin{aligned} v\frac{\mathrm{d}v}{\mathrm{d}y} + g\frac{\mathrm{d}d}{\mathrm{d}y} &= -g\frac{\mathrm{d}h}{\mathrm{d}y}, \\ d\frac{\mathrm{d}v}{\mathrm{d}y} + v\frac{\mathrm{d}d}{\mathrm{d}y} &= -v\frac{d}{w}\frac{\mathrm{d}w}{\mathrm{d}y}. \end{aligned} \tag{1.6}$$

Combining (1.6) we obtain,

$$\frac{\mathrm{d}d}{\mathrm{d}y} = \frac{\frac{\mathrm{d}h}{\mathrm{d}y} - F^2\frac{d}{w}\frac{\mathrm{d}w}{\mathrm{d}y}}{F^2 - 1}, \tag{1.7}$$

so that for critical flow ($F \to 1$) we require

$$\frac{\mathrm{d}h}{\mathrm{d}y} - F^2\frac{d}{w}\frac{\mathrm{d}w}{\mathrm{d}y} = 0. \tag{1.8}$$

Applying equation (1.8) in the two archetypal situations of constant width and constant bottom height we find $\frac{\mathrm{d}h}{\mathrm{d}y} = 0$ and $\frac{\mathrm{d}w}{\mathrm{d}y} = 0$, respectively.

Let us consider further the case of constant width (w = constant). Integrating (1.6) gives,

$$\frac{v^2}{2} + gd + gh = B,$$
$$vd = Q, \tag{1.9}$$

where B is the Bernoulli function, and Q represents the volume flux. A simple rearrangement and non-dimensionalisation by $gD = g^{2/3}Q^{2/3}$ yields,

$$\frac{Q}{2d^2} + gd = B - gh, \qquad \text{or} \qquad \frac{1}{2\hat{d}^2} + \hat{d} = \hat{B} - \hat{h}, \tag{1.10}$$

where a hat indicates dimensionless variables.

A simple extension of these ideas would be to take a $1\frac{1}{2}$ layer system – *i.e.* a single active layer of density ρ_2, overlayed by an inactive layer of density ρ_1 ($< \rho_2$). Our equations would now use modified gravity, $g' = (\rho_2 - \rho_1)g/\rho_2$ instead of g. Further, it is possible to plot, in terms of our non-dimensional parameters, a curve indicating the flow regime (see Figure 5). The part of the curve to the left of the minimum represents supercritical flow, the section to the right subcritical flow and the stationary point the transition that occurs at critical flow. By fixing the topology and varying the 'energy', B, we may obtain the full set of flows shown in figure 1. We can see that if we start on a supercritical branch of the curve and we do not reach the minimum of the curve (*e.g.* if the sill is too low) the flow will remain supercritical [case (a)]. Similarly the flow may also be permanently subcritical as in case (c). The case, (b), where there is a super- to sub-critical or sub- to super-critical jump are called hydraulically controlled and the minimum is reached. It should be noted that the transition from the super- to sub-critical branch is unstable.

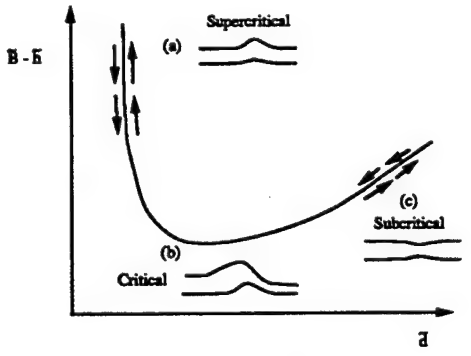

Figure 5.

We shall further investigate the case of a sub to supercritical transition as shown below in Figure 6.

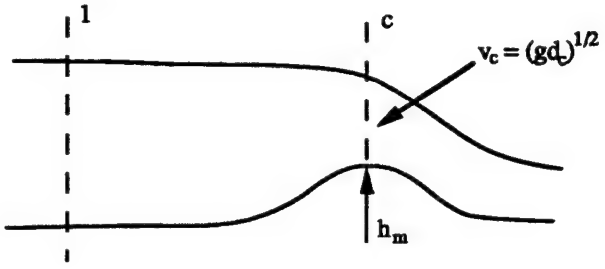

Figure 6.

Then using the fact that B and Q are constants of the flow we have,

$$\begin{aligned} \frac{v_1^2}{2} + gd_1 &= \frac{v_c^2}{2} + gd_c + gh_m, \\ v_1 d_1 &= v_c d_c. \end{aligned} \tag{1.11}$$

Rearranging (1.11) we find,

$$\frac{3}{2} g^{2/3} Q^{2/3} - \frac{Q^2}{2d_1^2} = g(d_1 - h_m). \tag{1.12}$$

If the upstream reservoir is deep, we discard the second term (representing the upstream kinetic energy) as comparatively small to give,

$$Q = \left(\tfrac{2}{3}\right)^{3/2} g^{1/2} \Delta z^{3/2} \qquad \text{where,} \quad \Delta z = d_1 - h_m. \tag{1.13}$$

This is commonly known as a 'weir' formula, and gives a convenient approximation for practical applications – *e.g.* dam construction.

Finally, we note that a unification of the system of equations is to introduce a function $J = J(d(y); w(y), h(y) \ldots B, Q, q)$ so that $J = 0$ (e.g. here $J = (2\hat{d}^2\hat{w}^2)^{-1} + \hat{d} + \hat{h} - \hat{B}$). Then we may find critical curves by considering $\partial J/\partial d = 0$, corresponding to the minimum of figure 5. This condition implies that the dependent flow variable can be altered without changing the topography and that such alteration leads to an acceptable solution. In essence, the flow will support stationary disturbances! Using the chain rule, we can generalise to incorporate the effects of topography, now minimising along the streamwise direction:

$$\frac{\mathrm{d}J}{\mathrm{d}y} = \frac{\partial J}{\partial d}\frac{\mathrm{d}d}{\mathrm{d}y} + \frac{\partial J}{\partial w}\frac{\mathrm{d}w}{\mathrm{d}y} + \frac{\partial J}{\partial h}\frac{\mathrm{d}h}{\mathrm{d}y} + \cdots = 0. \tag{1.14}$$

This is after Gill [2].

References.

(1)LONG, R.R. **1953**, Some aspects of the flow of stratified fluids. I. A Theoretical investigation, *Tellus*, **5**, 42-57

LONG, R.R. **1954**, Some aspects of the flow of stratified fluids. II. Experiments with a two-fluid system, *Tellus*, **6**, 97-115

LONG, R.R. **1954**, Some aspects of the flow of stratified fluids. III. Continuous density gradients, *Tellus*, **7**, 341-357

(2)GILL, A.E. **1977**, The hydraulics of rotating-channel flow, *JFM*, **80**, 641-671

Review of Semigeostrophic Waves

Larry Pratt, Lecture 2

Notes by: *Keir Colbo*

We consider the curve of allowed solutions of hydraulically controlled flow in $B - h$ vs. d space (figure 1); where B is the Bernoulli function, h is the sill height and d is the water depth at the control. We notice that there is a region of $B - h$ parameter space for which there exist no solutions.

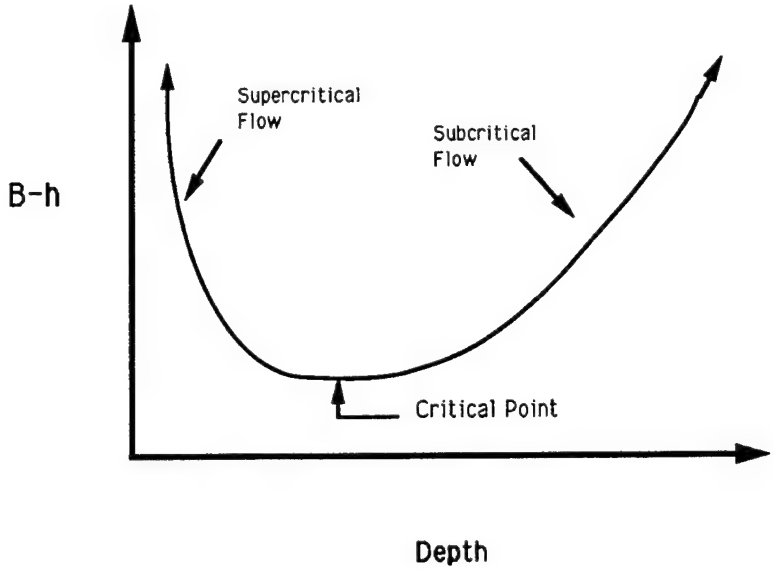

Figure 1: The solution curve for steady flow over an obstacle of height h and upstream Bernoulli potential B.

Since B is determined by upstream conditions and since h is set *a priori*, we might wonder what would happen if such a choice of parameters generated a $B - h$ value where no solution exists. Intuitively, we might suspect that for a given Bernoulli function (energy) B, that for too large a sill the flow would back up and eventually increase the upstream potential energy to the point where the $B - h$ value is on the curve of figure 1. Such a flow corresponds to a critical flow. Also it is important to note that of all the flows which are

on the solution curve, the critical one has the minimum energy. Thus the flow will back up until criticality is reached after which point it will remain in such a state. This is why the study of critical flows is so relevant since they are the naturally occurring minimal energy state.

Consider Long's Experiment of flow over a bump (Long 1953, 1954, 1955). Then the setup is as in figure 2, where the two controlling nondimensional parameters are the Froude Number, $F_0 = \frac{v_0}{\sqrt{gd_0}}$, based on the initial flow, and the ratio of the sill height to the initial depth, $(h_m/d_0) = \delta$.
His analysis of this parameter space showed six regimes (figure 3). The simplest curve to derive is $\overline{EAB}$. We seek flows that correspond to the maximum δ for which the initial flow has sufficient energy to make it over the top of the obstacle, under steady conditions. We employ Bernoulli's equation and conservation of mass, which gives the following equations

$$v_{up}^2/2 + gd_{up} = v_c^2/2 + g(d_c + h_m) \quad (1)$$

$$v_{up}d_{up} = v_c d_c = Q \quad (2)$$

Where d_{up} and v_{up} are the initial upstream depth and velocity and where d_c and v_c are the corresponding values at the critical point. Q is just the volume flux. A simple manipulation of the above produces

$$\frac{3}{2}g^{2/3}Q^{2/3} - \frac{Q^2}{2d_{up}^2} = g(d_{up} - h_m) \quad (3)$$

or

$$\frac{3}{2}F_0^{2/3} - F_0^2/2 - 1 = \delta \quad (4)$$

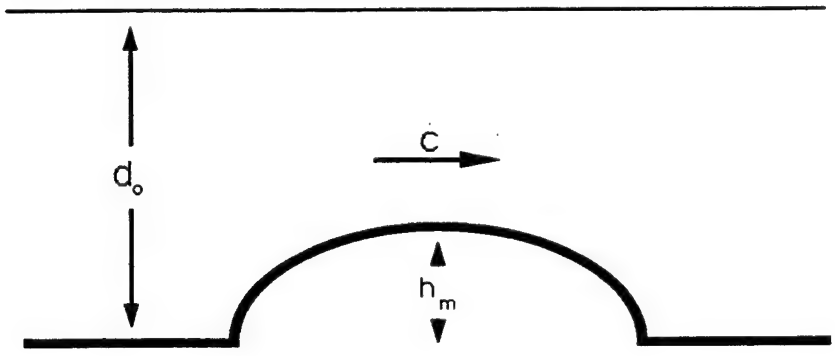

Figure 2: The setup of Long's Experiment

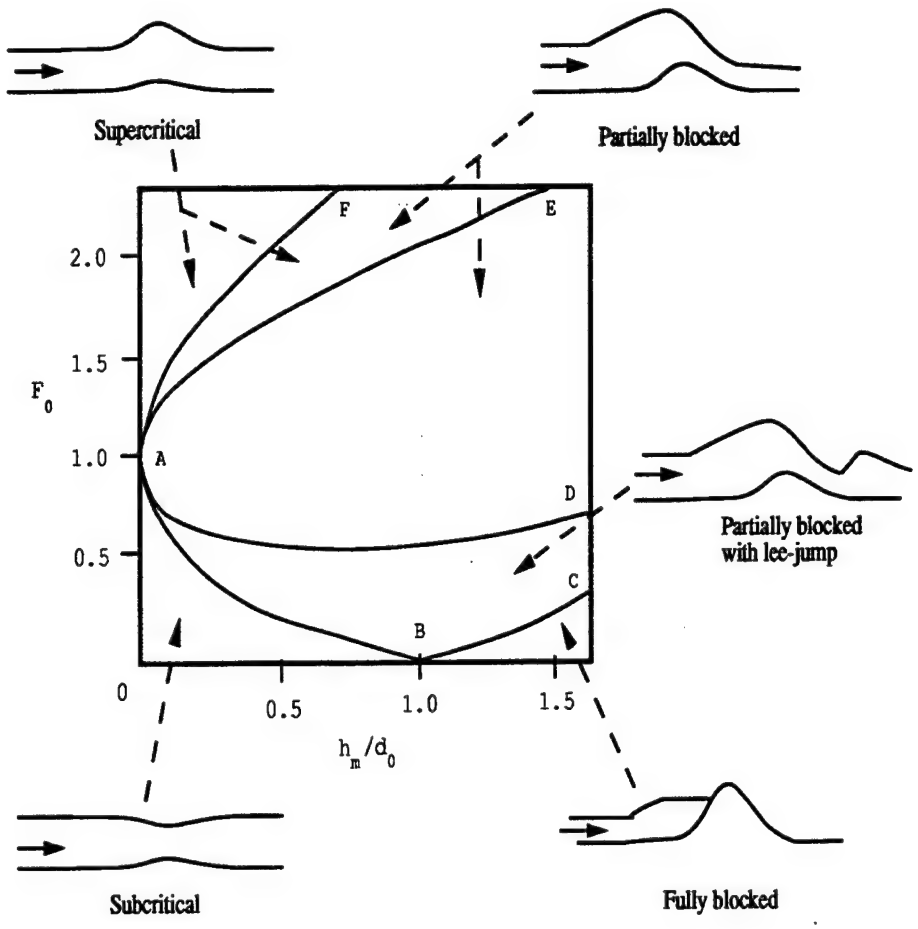

Figure 3: The six regimes in phase space for Long's experiment, along with the type of solution expected in each region.

In order to consider additional systems, we must first consider what equations to apply across a discontinuous hydraulic jump. If we are in a frame of reference centered on the jump and we consider a control volume containing the jump then it is clear that we must have no net flux into the control volume. Thus we have

$$v_{up} d_{up} = v_{down} d_{down} \tag{5}$$

where the subscripts refer to flow properties upstream and downstream of the hydraulic jump. The other shock joining equation is derived by assuming that in the above reference frame there is no external force acting on the jump. Thus the depth integral of the pressure force and the momentum flux must balance on either side of the discontinuity. This leads to the second equation

$$d_{up}v_{up}^2 + gd_{up}^2/2 = d_{down}v_{down}^2 + gd_{down}^2/2 \tag{6}$$

With these we can derive the complete blocking curve, $\overline{BC}$. If we consider a flow which is just blocked, then there will exist an upstream reservoir with depth and velocity of d_{up} and v_{up}. Additionally there will be a bore propagating upstream which will be moving at a speed c. Between the bore and the obstacle the fluid will be at rest and the water depth will be just the sill height, h_m. We have the shock joining equations (5) and (6) above, but written in a stationary frame with a moving shock. These can be written as

$$\begin{aligned}(v_{up} - c)d_{up} &= (v_{down} - c)d_{down} \\ &= (0 - c)h_m \\ &= -ch_m\end{aligned} \tag{7}$$

and

$$\begin{aligned}d_{up}(v_{up} - c)^2 + g/2d_{up}^2 &= d_{down}(v_{down} - c)^2 + g/2d_{down}^2 \\ d_{up}(v_{up} - c)^2 + g/2d_{up}^2 &= h_m c^2 + g/2h_m^2\end{aligned} \tag{8}$$

One can solve this system of equations to form the relationship

$$F_0 = (\delta - 1)(\frac{1+\delta}{2\delta})^{1/2} \tag{9}$$

To derive the $\overline{AF}$ curve, which marks the transition between supercritical and partially blocked flow, we consider a stationary hydraulic jump upstream of the obstacle, with water of depth d_1 and velocity v_1 between the jump and the sill. On top of the sill the flow is critical with parameters d_c and v_c. Unlike the previous simple case, this gives a system of five equations in the five unknowns $(v_1, d_1, v_c, d_c, h_m)$:

$$v_{up}d_{up} = v_1 d_1 \tag{10}$$

$$
\begin{aligned}
d_{up}(v_{up}-c)^2+g/2d_{up}^2 &= d_1v_1^2+g/2d_1^2 && (11)\\
v_1d_1 &= v_cd_c && (12)\\
v_1^2/2+gd_1 &= v_c^2/2+g(d_c+h_m) && (13)\\
v_c^2 &= gd_c && (14)
\end{aligned}
$$

Where the first two equations are the shock joining equations of before, the third equation is conservation of volume (mass), the fourth is conservation of energy downstream of the hydraulic jump and the fifth equation is just the critical condition on the sill. This can be solved to give

$$\delta=\frac{(8F_0^2-1)^{3/2}}{16F_0^2}-\frac{3}{2}F_0^{1/3}-\frac{1}{4} \qquad (15)$$

All the other cases can be similarly solved, although the algebra becomes tedious. Particularly, the transition into the partially blocked with lee jump region which has ten equations in ten unknowns. One thing to notice is that we have not attempted to apply the conservation of energy equation across the hydraulic jump. That is that we have not tried to match Bernoulli functions on either side of a hydraulic jump, but only in regions between them. This is because the jump is dissipative in nature and to consider this further we can calculate this energy loss. The energy flux is QB so that the we have

$$
\begin{aligned}
Q(B_{up}-B_{down}) &= Q(v_{up}^2/2+gd_{up}-v_{down}^2/2-gd_{down})\\
&= Qg(d_{down}-d_{up})^3/4 && (16)
\end{aligned}
$$

From Eq. (16) we note that $d_{down}\geq d_{up}$ or else we are providing an energy source, which is physically unrealistic.

Bibliography

- Long, R.R. **1953**, Some aspects of the flow of stratified fluids. I. A Theoretical investigation. *Tellus*, **5**, 42-57
- Long, R.R. **1954**, Some aspects of the flow of stratified fluids. II. Experiments with a two-fluid system. *Tellus*, **6**, 97-115
- Long, R.R. **1955**, Some aspects of the flow of stratified fluids. III. Continuous density gradients. *Tellus*, **7**, 341-357

Steady Theories of Rotating Hydraulics

Larry Pratt

Notes by: Claudia Cenedese and Mary-Louise Timmermans.

1 Introduction

Deep-water flows may take place through passages or over sills that hydraulically control the flow. These passages are of such lateral extent that rotation plays a major role in the dynamics of the geostrophically balanced flow. Some examples of such large passages include the Denmark Strait, the Faroe Bank Channel and the Vema Channel. The following analysis will concentrate on channels which are slowly varying along their direction. This assumption leads to a semigeostrophic state in which the cross stream momentum balance is geostrophic, while the along stream momentum balance is ageostrophic.

2 Governing Equations

We consider a rotating channel aligned along the y^*-axis with the x^*-axis in the cross channel direction. The superscript asterix denotes dimensional quantities. We let the bottom elevation be $h^*(x^*, y^*)$, which varies on a horizontal scale L^*, W^* is a characteristic width of the channel and the depth of the flow is $d^*(x^*, y^*)$, as in Figure 1. Let D be a scale which typifies the depth (and topographic variations) at the section of interest. We will consider a homogeneous layer of fluid in the channel with velocity components $u(x^*, y^*)$ and $v^*(x^*, y^*)$ along the x^* and y^* directions respectively.

Substitution into (??), (??) and (??) yields the following non-dimensional equations

$$\delta^2 \left(\frac{\partial u}{\partial t} + u\frac{\partial u}{\partial x} + v\frac{\partial u}{\partial y} \right) - v = -\frac{\partial d}{\partial x} - \frac{\partial h}{\partial x} + \delta F^{(x)} \qquad (1)$$

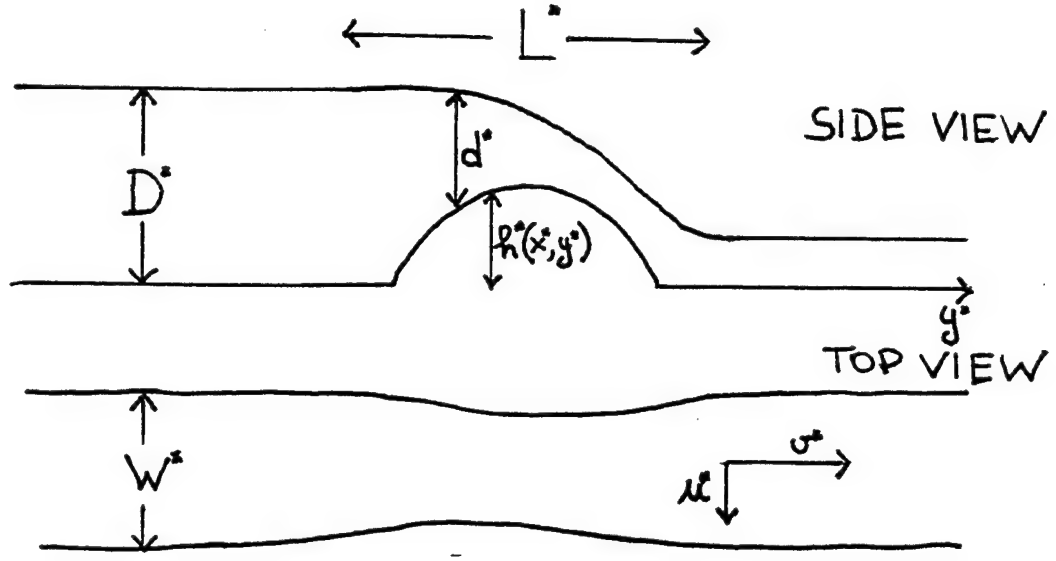

Figure 1: Schematic diagram of channel geometry.

$$\frac{\partial v}{\partial t} + u\frac{\partial v}{\partial x} + v\frac{\partial v}{\partial y} + u = -\frac{\partial d}{\partial y} - \frac{\partial h}{\partial y} + F^{(y)} \tag{2}$$

$$\frac{\partial d}{\partial t} + \frac{\partial d}{\partial x}(ud) + \frac{\partial}{\partial y}(vd) = 0, \tag{3}$$

where $\delta = \frac{\sqrt{gD}}{fL}$. This parameter δ can be thought of as a horizontal aspect ratio of the flow. We make the assumption that the flow varies slowly along its axis, that is $\delta << 1$. This assumption leads to a semigeostrophic flow in which the along stream velocity is geostrophic and the cross channel velocity is ageostrophic.

The potential vorticity is defined by

$$q^* = \frac{f + \frac{\partial v^*}{\partial x^*} - \frac{\partial u^*}{\partial y^*}}{d^*}. \tag{4}$$

We non-dimensionalize q^* by $\frac{f}{D}$ to yield

$$q = \frac{1 + \frac{\partial v}{\partial x} - \delta^2\frac{\partial u}{\partial y}}{d}, \tag{5}$$

which, in the semigeostrophic limit, becomes

$$q = \frac{1 + \frac{\partial v}{\partial x}}{d}. \tag{6}$$

We will consider the special case in which the potential vorticity is uniform. For example, this would be the case for a fluid that starts from rest from a reservoir of uniform depth D_∞ say. This upstream depth $D\infty$ can be thought of as the fluid depth at points where the relative vorticity is zero. Hence, the constant potential vorticity is given by

$$q^* = \frac{f}{D\infty}, \tag{7}$$

or non-dimensionalizing,

$$q = \frac{D}{D_\infty}. \tag{8}$$

An equation for the cross channel depth d may be derived by using equation (6) and the geostrophic relation for v

$$\frac{\partial^2 d}{\partial x^2} - qd = -1 - \frac{\partial^2 h}{\partial x^2}, \tag{9}$$

where we will only consider the case of no variations in the bottom elevation in the x-direction so that $\frac{\partial^2 h}{\partial x^2} = 0$.

In a rectangular channel there are two types of cross channel depth profiles. In the first type, called attached flow, the depth is finite across the channel and the width of the channel is allowed to vary from $x = -w/2$ to $x = w/2$, as in Figure 2(a). In the second case, the flow is separated from the left sidewall and extends a distance w_e across the width of the channel as in Figure 2(b). This flow is called detached. These two types of channel flow must be analyzed separately. Note that these two types of flow are simply artifacts of the rectangular geometry of the channel. For a cross section with continuous variations in $h(x)$, no distinction between the two cases need be made. However, the technical difficulty of the latter outweighs the inconvenience of the former.

2.1 Attached Flow

We may integrate equation (9) (where $q > 0$ and constant) to give profiles of surface elevation d

$$d(x,y,t) = q^{-1} + \hat{d}(y,t)\frac{\sinh(q^{\frac{1}{2}}x)}{\sinh(\frac{1}{2}q^{\frac{1}{2}}w)} + (\bar{d}(y,t) - q^{-1})\frac{\cosh(q^{\frac{1}{2}}x)}{\cosh(\frac{1}{2}q^{\frac{1}{2}}w)}, \tag{10}$$

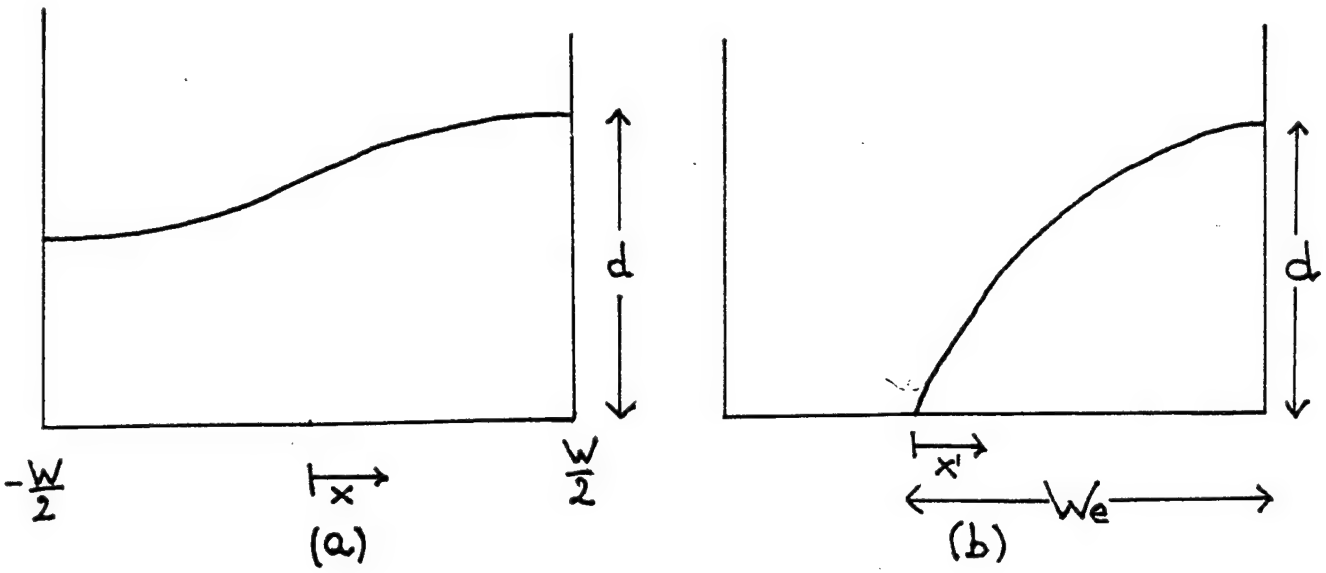

Figure 2: Schematic diagram showing (a) attached and (b) detached flow in a channel

and the velocity v follows from this depth profile by the geostrophic relation

$$v = q^{\frac{1}{2}}\hat{d}(y,t)\frac{\cosh(q^{\frac{1}{2}}x)}{\sinh(\frac{1}{2}q^{\frac{1}{2}}w)} + q^{\frac{1}{2}}(\bar{d}(y,t) - q^{-1})\frac{\sinh(q^{\frac{1}{2}}x)}{\cosh(\frac{1}{2}q^{\frac{1}{2}}w)}, \qquad (11)$$

where an overbar will denote an average of the values at the two walls of the channel and the $\hat{}$ will denote half the difference between its values at the walls. That is,

$$\bar{d} = \frac{1}{2}\left[d(\frac{1}{2}w,y,t) + d(-\frac{1}{2}w,y,t)\right]$$

$$\hat{d} = \frac{1}{2}\left[d(\frac{1}{2}w,y,t) - d(-\frac{1}{2}w,y,t)\right],$$

and

$$\bar{v} = \frac{1}{2}\left[v(\frac{1}{2}w,y,t) + v(-\frac{1}{2}w,y,t)\right] = q^{\frac{1}{2}}T^{-1}\hat{d}$$

$$\hat{v} = \frac{1}{2}\left[v(\frac{1}{2}w,y,t) - v(-\frac{1}{2}w,y,t)\right] = q^{\frac{1}{2}}T(\bar{d} - q^{-1}),$$

where

$$T = \tanh(\frac{1}{2}q^{\frac{1}{2}}w).$$

Let us consider a wide channel in which $\frac{w^*}{L_d} >> 1$, where L_d is the Rossby radius of deformation defined by $\frac{\sqrt{gD_\infty}}{f}$ (Note that this deformation radius applies throughout the flow no matter what the *local* depth is). In this limit, the flow has a boundary layer character where the widths of the wall layers are of the order L_d. Outside the boundary layers, the flow is quiescent and the along channel boundary condition is given by

$$u^* = v^* \frac{\partial}{\partial y}\left(\pm\frac{w^*}{2}\right) \qquad [x = \pm w/2]. \tag{12}$$

Now, we substitute relations (10) and (11) and the non dimensional version of the boundary condition (12) into the along channel momentum equation (2) and evaluate it along each of the channel walls. Subtracting the resulting equations yields

$$2q^{-\frac{1}{2}}\frac{\partial}{\partial t}(T\bar{d}) + \frac{\partial Q}{\partial y} = 0, \tag{13}$$

and adding the resulting equations gives

$$q^{\frac{1}{2}}\frac{\partial}{\partial t}(T^{-1}\hat{d}) + \frac{\partial \bar{B}}{\partial y} = 0, \tag{14}$$

where $\bar{B}$ is the average of the Bernoulli constant on either wall given by

$$\bar{B} = \frac{1}{2}\left[B(w/2,y,t) + B(-w/2,y,t)\right] = \frac{1}{2}q\left[T^{-2}\hat{d}^2 + T^2(\bar{d} - q^{-1})^2\right] + \bar{d} + h, \tag{15}$$

and Q is the rate of the flow. From the geostrophic relation, Q can be expressed as

$$Q = 2\bar{d}\hat{d}. \tag{16}$$

Some of the time-dependent properties of (13) and (14) are revealed through a reformulation in terms of characteristic equations. In the wide channel limit ($w^*/L_d >> 1$) the resulting characteristic speeds are given by

$$c_+^* = v^*(w^*/2, y^*, t^*) + \sqrt{gD_\infty} = \left(\frac{g}{D_\infty}\right)^{\frac{1}{2}} d^*_{\text{rightwall}}, \tag{17}$$

and

$$c_-^* = v^*(-w^*/2, y^*, t^*) - \sqrt{gD_\infty} = -\left(\frac{g}{D_\infty}\right)^{\frac{1}{2}} d^*_{\text{leftwall}}. \tag{18}$$

We may interpret $c_\pm$ as the speeds of the nonlinear Kelvin waves on the right and left walls. Unlike linear Kelvin waves, these have a non-zero u. Note that $c_\pm$ depend on the depth at the wall, so that signals with larger d^*_{wall} move faster. This means that any perturbation that increases d^*_{wall} will lead to a nonlinear steepening of the wave.

In the narrow channel limit, $q^{\frac{1}{2}}w = \frac{w^*}{L_d} << 1$. Thus, in this limit, the potential vorticity equation (4) becomes

$$\frac{1}{f}\frac{\partial v^*}{\partial x^*} + 1 = 0, \tag{19}$$

which, upon integration, in dimensionless form, yields

$$v = \bar{v} - x, \tag{20}$$

and

$$d = \bar{d}(y,t) + \bar{v}(y,t)x - \frac{x^2 - (w/2)^2}{2}. \tag{21}$$

Following a similar procedure as for the wide channel limit, we can derive the characteristic speeds

$$c_\pm = \bar{v} \pm \sqrt{\bar{d}}. \tag{22}$$

These are the speeds of rotationally modified long gravity waves.

2.2 Detached Flow

In the case of detached flow, the depth on the left wall is zero and we use the free edge of the flow as a left hand boundary (now $\bar{d} = \hat{d}$). In the wide channel limit ($w_e >> L_d$) the left wall Kelvin wave that is observed in the case of attached flow is replaced by a frontal wave. This frontal wave is characterized by large cross channel velocities, whereas the corresponding velocity in a Kelvin wave is zero. On the right wall, a Kelvin wave propagates as in the attached case. For the analysis of detached flow, it is convenient to change dependent variables. We will let x' be the across channel coordinate, where the position of $x' = 0$ corresponds to the position of the left free boundary of the flow, as illustrated in Figure 2(b).

In the narrow channel limit, equation (19) can be applied to yield the velocity

$$v = v_e - x', \tag{23}$$

and depth profile

$$d = x'\left(v_e - \frac{1}{2}x'\right), \tag{24}$$

where v_e is the along channel velocity at the free edge. Hence the depth profile is a parabola which can translate with respect to the right wall of the channel as w_e varies. Again, using the method of characteristics, the characteristic speeds for waves that can propagate in this flow are found to be [3]

$$c_\pm = \frac{v_e - w_e}{1 \mp [v_e/(2v_e - w_e)]^{\frac{1}{2}}}. \tag{25}$$

Figure 3 is a plot of v_e vs. w_e illustrating the different regimes of the flow. The Riemann invariants $R_\pm$ are computed by numerical integration. When the depth profile is as in Figure 3(a) and the flow is separated on both sides, $v_e = w_e/2$ and consequently $c_+ = c_- = 0$. Figure 3(b) illustrates subcritical flow in which $c_+ > 0$ and $c_- < 0$ and waves travel both upstream and downstream. For critical flow as depicted in Figure 3(c), $v_e = w_e$ and $c_- = 0$ and $c_+ > 0$ and waves propagate only downstream. Finally, Figure 3(d) shows the supercritical situation in which both c_+ and c_- are positive and waves propagate downstream. The wave propagating at speed c_- is the limiting case of the frontal wave noted above. It can steepen or rarefy corresponding to small (or large) w_e catching up with, or diverging from, large w_e. For example, one could set up a steepening or rarefying simple wave by setting R_+ constant in the initial conditions and then noting the changes in c_- as one moves along a curve of constant R_+. In Figure 3, moving from C to D along the $R_+ =$ constant curve, the values of c_- increase as w_e decreases, leading to a rarefying wave. A steepening wave is observed moving from E to F along $R_+ =$ constant because c_- increases as w_e decreases.

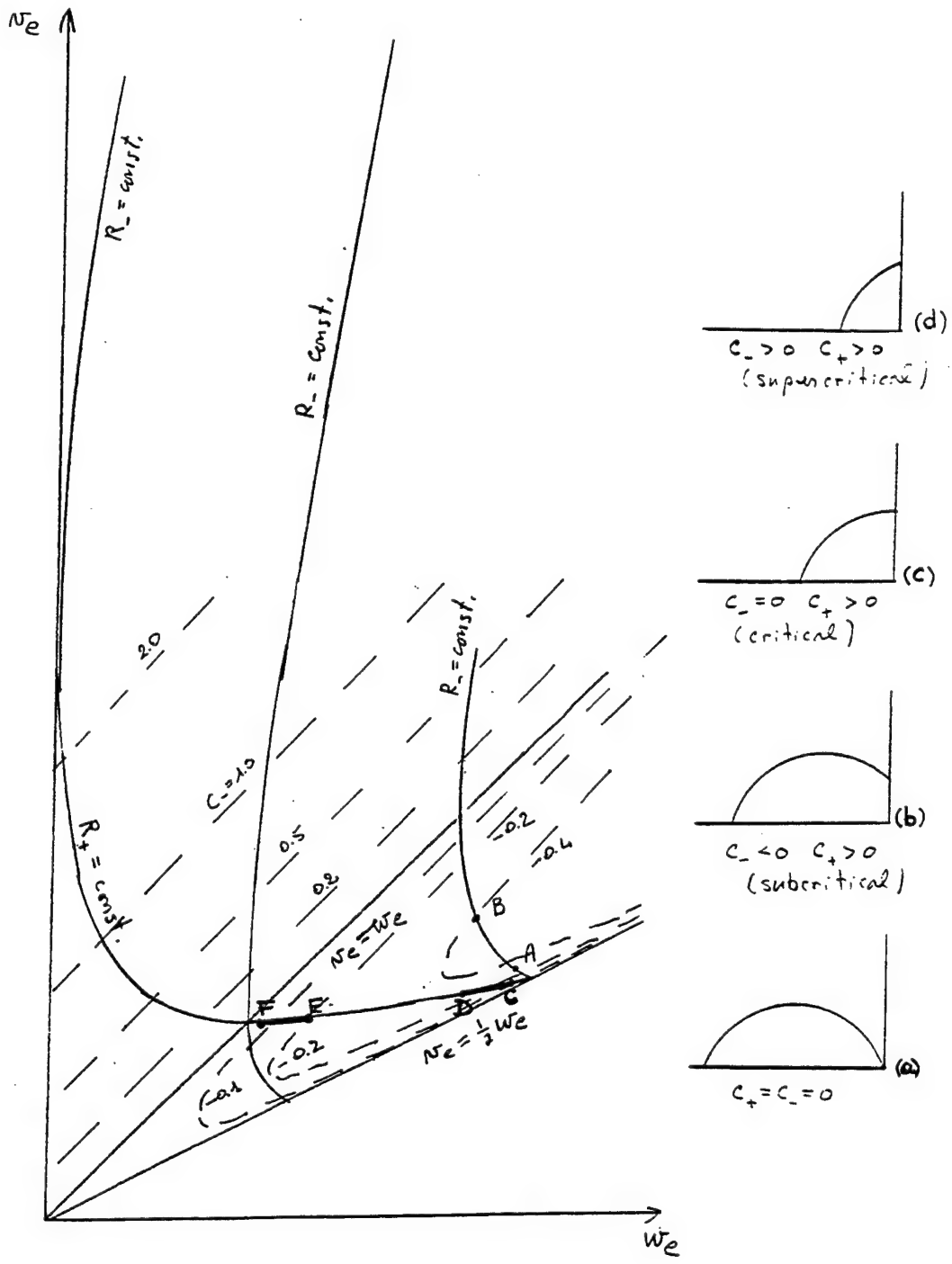

Figure 3: Regime diagram for detached flow.

References

[1] GILL, A.E. 1977 The hydraulics of rotating channel flow. *J. Fluid Mech.* **80** 641-671.

[2] PRATT, L.J. 1983 On inertial flow over topography. Part I: Semi-geostrophic adjustment to an obstacle. *J. Fluid Mech.* **131** 195-218.

[3] STERN, M.E. 1980 Geostrophic fronts, bores, breaking and blocking waves. *J. Fluid Mech.* **99** 687-703.

Rotating Hydraulic Control: Lecture Four
Principal Lecturer: Larry J. Pratt
Notes by: A. C. Kuo

1 Overview

In the previous lecture, time-dependent rotating hydraulic processes were examined. More specifically, we discussed how wave propagation leads to the establishment of a steady state. Today's lecture focuses on the steady state.

The outline of the lecture is as follows. We first deal with flows in the potential vorticity $q \to 0$ limit and determine the cross-channel depth and velocity dependence. We show that two qualitatively different profiles are possible (attached and separated). Using Gill's (1977) theory, we then determine critical flow conditions as well as the fluxes Q at criticality for the above two cases.

When q is nonzero but constant, the cross-channel profiles and critical conditions are again found. The average depth along the channel is examined graphically as functions of the width and topography of the channel. Finally, upstream reservoir depths are determined as a function of the sill height h_c and a measure of the transport when the flow is hydraulically controlled.

Note that all the variables used here are nondimensional unless otherwise specified. The nondimensionalization was given previously.

2 Steady Cross-Channel Profiles, $q \to 0$

A single differential equation governing the x-dependence (cross-channel) of the depth d was derived in the previous lecture from the potential vorticity equation and the assumption that the along stream velocity v was geostrophically balanced. That equations was:

$$d_{xx} - qd = -1 \tag{1}$$

where $q = D/D_\infty$ and D is a generic depth scale. In the limit $D/D_\infty \to 0$, the general solution to the above equation is simply:

$$d = x^2 + C_1(y)x + C_2(y) \tag{2}$$

We can write the integration constants in terms of the depth d at the two side walls $x = \pm w/2$ (the y-axis is placed halfway between the channel walls that are a width w apart):

$$C_1 = (d(x = w/2, y) - d(x = -w/2, y))/w \quad (3)$$

$$C_2 = \frac{1}{2}(d(x = w/2, y) + d(x = -w/2, y)) + \frac{1}{2}(w/2)^2 \quad (4)$$

The full solution will be known after we solve for $d(x = w/2, y)$ and $d(x = -w/2, y)$. But it is much more useful to solve for a measure of the average depth along the channel. Hence, the change of variables introduced yesterday for the average depth $\bar{d}$ and the difference in depth $\hat{d}$ across the channel. In that case:

$$C_1 = 2\hat{d}/w \quad (5)$$

$$C_2 = \bar{d} + \frac{1}{2}(w/2)^2 \quad (6)$$

so that

$$d = \bar{d} + \frac{2\hat{d}}{w}x - \frac{x^2 - (w/2)^2}{2} \quad (7)$$

So now, the along-channel structure will be determined once we find $\bar{d}$ and $\hat{d}$. Before we do so, we may obtain the downstream velocity v using the geostrophic relation $v = d_x$. This gives:

$$v = \frac{2\hat{d}}{w} - x \quad (8)$$

Note that we can similarly define the average downstream velocity and difference in velocity which was done in the previous lecture. Using the above equation, this implies:

$$\bar{v} = \frac{2\hat{d}}{w} \quad (9)$$

$$\hat{v} = -\frac{w}{2} \quad (10)$$

so that:

$$v = \bar{v} - x \quad (11)$$

Below is a schematic of the cross-sectional profile. Note that the flow is "attached" ($d(x = -w/2, y) > 0$).

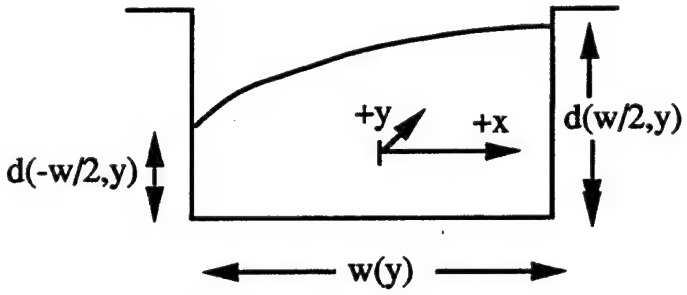

Now that we have gone through all the trouble of introducing the new variables, you'll be happy to know that we can't always use them. A little intuition (or better yet, hindsight) will convince you that large enough downstream velocities can produce a Coriolis force such that the required pressure gradient needed to balance it causes a separation of the flow from the left (looking downstream) channel wall. (This is easily seen from the equation $d_x = v$ for geostrophy). In this case, the two variables we introduced previously give no information, for $\bar{d} = \hat{d}$. We must choose two new (useful) variables to describe the flow- the width of the depth field after separation w_e, and the velocity at the separation point, v_e.

Schematically, the cross-sectional profile looks something like this:

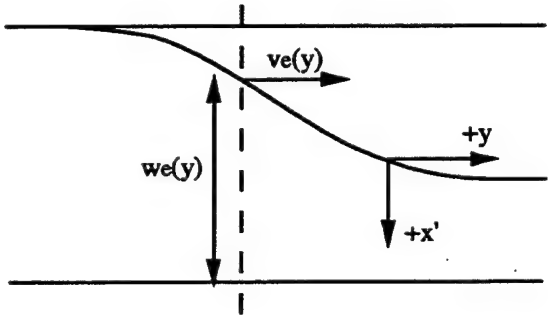

plan view

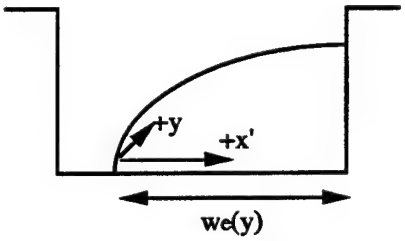

cross-sectional slice

For the case of separation, it is not difficult to show:

$$d = (v_e - x'/2)x' \tag{12}$$

$$v = v_e - x' \tag{13}$$

$x' = 0$ corresponds to the left edge of the fluid rather than the center of the channel, hence the primes which denote a new coordinate system.

Notice that had the channel been, say, parabolic rather than rectangular in cross-section, we would not have had to go through the trouble of introducing these two, new integration constants (Gill pointed this out in his 1977 paper). However, the inconvenience of dealing with the two cases separately is minor compared to the technical difficulty in dealing with continuously-varying topography.

2.1 Critical Flows:Necessary Conditions and Resulting Relations

In this subsection, we will derive the two equations involving the two integration constants $\tilde{d}$ and $\hat{d}$ for the case of attached flows and the two equations for w_e and v_e for the case of separated flows. We could use those two equations to determine the along-channel structure of the flows, but that will be done in the next section for the more general case of constant q (not necessarily small) flows. In this section, we will use the derived equations to determine critical flow conditions using the formalism developed by Gill (1977). Critical conditions can be defined as those conditions required such that the Froude number F (suitably defined) can equal unity. If such is the case in a flow, then the long wave speed up the channel will be arrested at the location of $F = 1$. We will show that at the point of critical flow, the geometrical parameters will influence the upstream depth and velocity fields so that one may also term critical flows "hydraulically controlled" flows.

2.2 Case 1: Attached Flow

The first equation governing the along-channel structure parameters is simply a statement of mass conservation. The total (nondimensional) flow rate Q is:

$$Q = \int_{-w/2}^{w/2} v(x,y)d(x,y)\,\mathrm{d}x$$

$$
\begin{aligned}
&= \int_{-w/2}^{w/2} d_x d(x,y)\,\mathrm{d}x \qquad \text{(by geostrophy)} \\
&= \int_{-w/2}^{w/2} \frac{1}{2}(d^2(x,y)_x\,\mathrm{d}x \\
&= \frac{1}{2}(d^2(w/2,y) - d^2(-w/2,y)) \\
&= \frac{1}{2}(d(w/2,y) + d(-w/2,y))(d(w/2,y) - d(-w/2,y)) \\
&= 2\bar{d}\hat{d}
\end{aligned}
$$

Incidentally, when $q = 0$, we can use the fact that $\bar{v} = 2\hat{d}/w$ (Eq. (9)) to eliminate $\hat{d}$ in favor of $\bar{v}$ to obtain:

$$Q = w\bar{v}\bar{d} \tag{14}$$

In other words, the flow rate is simply the width of the channel times the average velocity times the average depth.

Now the second equation for $\bar{d}$ and $\hat{d}$ is derived in the Appendix and is just a Bernoulli equation. We simplify it here by noting that for semigeostrophic flow, $u << v$.

$$v^2/2 + h + d = B(\psi) \tag{15}$$

We assume that B is known from upstream conditions. Notice that B is only a function of ψ.

Evaluating B at $x = \pm w/2$ (along the streamlines hugging the two channel walls) yields an "average" Bernoulli function written in terms of our unknown variables $\bar{d}$ and $\hat{d}$ (remembering that we assume the topography h has no x-dependence) :

$$
\begin{aligned}
\bar{B} &\equiv \frac{1}{2}(B(x = w/2, y) + B(x = -w/2, y)) \\
&= \frac{1}{2}\left(\frac{v^2(w/2,y)}{2} + \frac{v^2(-w/2,y)}{2} + 2h + d(w/2,y) + d(w/2,y)\right) \\
&= \frac{1}{2}\left(\frac{(\bar{v} - w/2)^2}{2} + \frac{(\bar{v} + w/2)^2}{2} + 2h + 2\bar{d}\right) \\
&= \frac{1}{2}\left(\bar{v}^2 + w^2/4 + 2h + 2\bar{d}\right) \\
&= \frac{\bar{v}^2}{2} + w^2/8 + h + \bar{d}
\end{aligned}
$$

$$= \frac{2\hat{d}^2}{w^2} + w^2/8 + h + \bar{d}$$

In summary, the two required equations for $\bar{d}$ and $\hat{d}$ governing along-channel structure for the case of attached flow are:

$$Q = 2\bar{d}\hat{d} \tag{16}$$

$$\bar{B} = \frac{2\hat{d}^2}{w^2} + w^2/8 + \bar{d} + h \tag{17}$$

Now that we have the two equations, let us first inquire into the conditions for critical flow. Gill (1977) introduced a general theory for "hydraulics type problems." Using the "J" function which implicitly defines an unknown flow variable (in our case either $\bar{d}$ or $\hat{d}$) in terms of geometrical parameters (like the width w and topography h) and upstream conditions (like Q and $\bar{B}$) , he stated that the condition for criticality is :

$$\frac{\partial J}{\partial \bar{d}} = 0 \tag{18}$$

The J function in this case may be obtained by choosing the unknown flow variable to be $\bar{d}$. We can trivially eliminate $\hat{d}$ from Eq. (17) using Eq. (16) to obtain:

$$J(\bar{d}; w, h; Q, \bar{B}) = \frac{Q^2}{2\bar{d}^2 w} + w^2/8 + \bar{d} + h - \bar{B} \tag{19}$$

Using Gill's condition (18) we may obtain a relationship between the flow rate Q and the average fluid depth $\bar{d}$ at the spatial location of critical flow:

$$Q = \bar{d}^{3/2} w \tag{20}$$

One may wonder what the average velocity is at this point and how it is related to $\bar{d}$:

$$\bar{v} = \frac{Q}{w\bar{d}} \qquad \text{by (14)} \tag{21}$$

$$= \frac{(\bar{d}^{3/2} w)}{w\bar{d}} \qquad \text{by (20)} \tag{22}$$

$$= \bar{d}^{1/2} \tag{23}$$

If we defined some sort of x-averaged Froude number $F = \bar{v}/\sqrt{\bar{d}}$, then the above result just implies the average Froude number is equal to unity at criticality. But for general (not necessarily small) q, the Froude number will be defined differently (see Gill 1977) and critical flow would imply that *that* Froude number is unity.

Now the above relations (20) and (23) hold *if* the flow is critical. We can find certain necessary (but not sufficient) conditions for the flow to be critical by differentiating Eq. (19) with respect to y:

$$\frac{\mathrm{d}}{\mathrm{d}\bar{y}} J(\bar{d}; w, h; Q, \bar{B}) = 0 \tag{24}$$

From (18) and (19),this implies:

$$(\frac{w}{4} - \frac{Q^2}{\bar{d}^2 w^3})\frac{dw}{dy} + \frac{dh}{dy} = 0 \tag{25}$$

One might interpret the above equations as follows. If the flow is in a constant width channel, then critical flow can only take place at a maxima of the topography (it can be shown that the minimum does not imply criticality). Likewise, for constant topography, it can be shown that critical flow occurs at a contraction in the channel. The other possibility for constant topography, $(\frac{w}{4} - \frac{Q^2}{\bar{d}^2 w^3}) = 0$, occurs when $d = 0$ at both edges of the flow (no net flux). For neither constant topography or constant width, the two derivatives of w and h in general vanish at different places. Gill (1977) stated that in this case, critical flow must "presumably lie at some point in between."

Finally, it is useful to find a relation relating the sill height h_m and the upstream conditions Q and $\bar{B}$. (Remember, this can be done *if* somewhere along the channel, the flow is critical.) In that case, we take the Bernoulli equation (17) which holds everywhere along the channel and apply the relationship (20) which we know holds true at the critical flow point:

$$\bar{B} = \frac{Q^2}{2\bar{d}^2 w} + w^2/8 + \bar{d} + h_m \tag{26}$$

$$= \frac{Q^2}{2((Q/w)^{2/3})^2 w} + w^2/8 + (Q/w)^{2/3} + h_m \tag{27}$$

$$= \frac{3}{2}(Q/w)^{2/3} + w^2/8 + h_m \tag{28}$$

The above equation shows that when a flow is critical, varying the sill height h_m implies changes in the upstream conditions given by Q and $\bar{B}$. Hence our use of the term "hydraulic control" when the flow somewhere along the channel is critical.

A more useful formula than the one above may be made by assuming the upstream reservoir is relatively deep and quiescent, so that the main contribution to $\bar{B}$ is potential. In this case, assuming the upstream reservoir depth is $D_\infty = D^*_\infty/D$, then $\bar{B} = D_\infty$. Defining $\Delta z \equiv D_\infty - h_m$ (see schematic below):

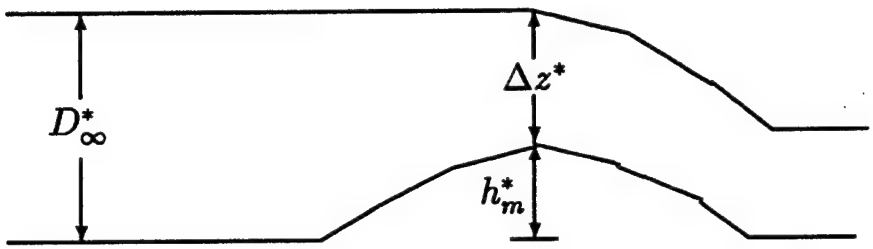

we can solve (28) for Q. Dimensionally (hence the asterisks) , it is given by:

$$Q^* = (\frac{2}{3})^{3/2} w^* g^{1/2} (\Delta z^* - \frac{w^{*2} f^2}{8g}) \tag{29}$$

The dimensional form allows us to see the effects of rotation on the flux Q for flows which are hydraulically controlled- the effect is to *decrease* the flow rate for constant Δz^*. In the limit of $f \to 0$, the formula for the flow rate reduces to a formula well known in the (nonrotating) hydraulics community.

2.3 Critical Conditions, Case 2: Separated Flow

The derivation of the two governing equations for v_e and w_e which determine the along-channel structure is straightforward and follow also from mass and energy conservation, as in Case 1.

Mass conservation implies:

$$\begin{aligned} Q &= \int_0^{w_e} d(x', y) v(x', y)\, dx' \\ &= \int_0^{w_e} ((v_e - x'/2)x')(v_e - x')dx' \text{using 12 and 13} \\ &= (v_e{}^2 x^2/2 - v_e x^3/2 + x^4/8)|_0^{w_e} \\ &= \frac{1}{2} w_e{}^2 (v_e - \frac{1}{2} w_e)^2 \end{aligned}$$

The averaged Bernoulli/energy equation in this case of separated flow is :

$$\begin{aligned}
\bar{B} &= \frac{1}{2}(B(x'=0,y)+B(x'=w_e,y)) \\
&= \frac{1}{2}\left(\frac{v(0,y)^2}{2}+\frac{v(w_e,y)^2}{2}+2h+d(0,y)+d(w_e,y)\right) \\
&= \frac{1}{2}\left(\frac{v_e^2}{2}+\frac{(v_e-w_e)^2}{2}+2h+(v_e-\frac{w_e}{2})w_e\right) \\
&= \frac{1}{2}\left(\frac{v_e^2}{2}+\frac{v_e^2-2v_ew_e+w_e^2}{2}+2h+d_e+v_ew_e-\frac{w_e^2}{2}\right) \\
&= \frac{v_e^2}{2}+h
\end{aligned}$$

Reiterating, the two governing equations for the along-channel structure for the case of separated flow are:

$$Q = \frac{1}{2}{w_e}^2(v_e-\frac{1}{2}w_e)^2 \tag{30}$$

$$\bar{B} = \frac{{v_e}^2}{2}+h \tag{31}$$

It should be noted from the above two equations that once $\bar{B}$ and Q are specified, only changes in the topography h can change the along-channel flow. Separated flows will maintain constant width for constant topography.

With the two equations, we can attempt once again to use the Gill formalism to determine critical flow relations. It turns out the Gill formalism may not be as general as once supposed- blindly taking the Eq. (31) as the J function with v_e as the unknown flow variable and taking the derivative of J with respect to v_e leads to the conclusion that $v_e = 0$ at the point of critical control. This is incorrect (why ?). The reason for the failure may be linked to the fact that one of the flow variables, v_e has no dependence/knowledge of the upstream flow rate Q- the two equations are not really coupled. The correct approach is to eliminate v_e from Eq. (30) by using Eq. (31).

$$J = -Q+\frac{1}{2}{w_e}^2(v_e(\bar{B},h)-\frac{1}{2}w_e)^2$$

Taking the derivative with respect to w_e and setting it equal to zero yields the critical flow condition:

$$\frac{\partial J}{\partial d} = -\frac{1}{2}{w_e}^2(v_e(\bar{B},h)-\frac{1}{2}w_e)+w_e(v_e(\bar{B},h)-\frac{1}{2}w_e)^2 \tag{32}$$

$$= \quad 0 \tag{33}$$

$$\Rightarrow \quad v_e = w_e \tag{34}$$

As in the previous case, we can determine the flow rate in terms of the difference in height between the sill depth and the upstream reservoir depth D_∞ when the flow is hydraulically controlled somewhere along the channel. So analogous to Eq. (29), we have (evaluating Eq. (31) at the location of the critical flow):

$$\begin{aligned} \bar{B} - h_m &= \Delta z \\ &= \frac{{v_e}^2}{2} \\ &= \sqrt{2Q} \qquad \text{by Eq.(30) and Eq.(34)} \end{aligned} \tag{35}$$

Dimensionally, this is implies:

$$Q^* = \frac{(\Delta z^*)^2}{2} \tag{36}$$

3 Steady Cross-Channel Profiles, Arbitrary q

In this section, we derive the equations for the two unknowns $\bar{d}$ and $\hat{d}$ to determine the along-channel flow, but for the more general case of constant (not necessarily small), potential vorticity q. In contrast to the previous sections, we derive the equations only for the case of non-separated flows. We once again work in dimensionless variables.

The mass conservation equation is the same as in the $q \to 0$ limit. The Bernoulli/energy equation is derived after solving the cross-channel structure differential equation Eq. (1). The general solution is written in terms of hyperbolic sines and cosines:

$$d = q^{-1} + C_1(y)\sinh(q^{1/2}x) + C_2(y)\cosh(q^{1/2}x) \tag{37}$$

Entirely analogous to the previous $q \to 0$ case, we determine the two integration constants in terms of $\bar{d}$ and $\hat{d}$. The solution, which we simply state, is:

$$d = q^{-1} + \left(\frac{\hat{d}(y)}{\sinh(\frac{1}{2}q^{1/2}w)}\right)\sinh(q^{1/2}x) + \left(\frac{\bar{d(y)} - q^{-1}}{\cosh(\frac{1}{2}q^{1/2}w/2)}\right)\cosh(q^{1/2}x) \tag{38}$$

One differentiation with respect to x of the above equation gives the cross-channel v structure:

$$v = \left(\frac{q^{1/2}\hat{d}(y)}{\sinh(\frac{1}{2}q^{1/2}w)}\right)\cosh(q^{1/2}x) + q^{1/2}\left(\frac{\bar{d(y)} - q^{-1}}{\cosh(\frac{1}{2}q^{1/2}w)}\right)\sinh(q^{1/2}x) \quad (39)$$

Now the x-averaged Bernoulli equation can be formed with the above two solutions. The following two relations will be needed first:

$$\begin{aligned}
\frac{1}{2}v^2(w/2,y) &= \frac{1}{2}\left(\frac{\hat{d}q^{1/2}}{\tanh(\frac{1}{2}q^{1/2}w)} + q^{1/2}(\bar{d}-q^{-1})\tanh(\frac{1}{2}q^{1/2}w/2)\right)^2 \\
&= \frac{1}{2}\left(\frac{\hat{d}q^{1/2}}{T} + q^{1/2}(\bar{d}-q^{-1})T\right)^2 \\
&= \frac{1}{2}\left(\frac{\hat{d^2}q}{T^2} + q(\bar{d}-q^{-1})^2T^2 + 2q\hat{d}(\bar{d}-q^{-1})\right) \qquad (40)
\end{aligned}$$

similarly

$$\frac{1}{2}v^2(-w/2,y) = \frac{1}{2}\left(\frac{\hat{d^2}q}{T^2} + q(\bar{d}-q^{-1})^2T^2 - 2q\hat{d}(\bar{d}-q^{-1})\right) \qquad (41)$$

Note that in the second step we have used the width variable T defined by $T \equiv \tanh(\frac{1}{2}q^{1/2}w)$.

Now, we may form the average Bernoulli equation:

$$\begin{aligned}
\bar{B} &\equiv \frac{1}{2}\left(B(x=w/2,y) + B(x=-w/2,y)\right) \\
&= \frac{1}{2}\left(\frac{v^2(w/2,y)}{2} + \frac{v^2(-w/2,y)}{2} + 2h + (d(w/2,y) + d(w/2,y)\right) \\
&= \frac{1}{2}\left(\frac{\hat{d^2}q}{T^2} + q(\bar{d}-q^{-1})^2T^2 + 2h + 2\bar{d}\right) \qquad \text{by (40) and (41)} \\
&= \frac{1}{2}q\left(\hat{d^2}T^{-2} + (\bar{d}-q^{-1})^2T^2\right) + h + \bar{d}
\end{aligned}$$

So in sum, the two governing equations for along-channel flow for constant q are:

$$Q = 2\bar{d}\hat{d} \qquad (42)$$

$$\bar{B} = \frac{1}{2}q\left(\hat{d^2}T^{-2} + (\bar{d}-q^{-1})^2T^2\right) + h + \bar{d} \qquad (43)$$

It is not hard to show that the above equation for the Bernoulli function will reduce to the expression given in section 2 when the limit $q \to 0$ is taken.

With these two equations, we may form the J function for q constant, non-separated flow. As it stands, there are three upstream quantities to be specified: Q,$\bar{B}$ and q. We could form the J function for the unknown variable $\bar{d}$ quite easily in terms of those three upstream quantities, as in Pratt (1983). But we will show a relationship between the above three variables, based on solving Eq.(60) in the Appendix. In that case, there are only two indpendent parameters, which we will argue to be q and a measure of Q, as opposed to $\bar{B}$.

Gill envisioned the upstream reservoir as wide, but not necessarily deep. In this case, it turns out that $\bar{B}$ is not a very convenient parameter, since the neglect of the kinetic energy term is no longer consistent with an upstream reservoir that is not deep (*i.e.* we cannot take v=0 upstream). Now, for wide upstream reservoirs, by geostrophy, the flow must be contained in sidewall boundary layers of deformation (based on the upstream depth) width scale . Physically, it should be clear that the upstream parameter controlling the physics is not just the total flux Q, but also the ratio of the fluxes in each boundary layer. By making the depth scale a function of Q (specifically $D = (Q^* f/(2g))^{1/2}$, we can arbitrarily set the total flux to be 2, implying stream function values at the walls: $\psi(w/2) = -1$ and $\psi(w/2) = -1$ consistent with $Q = 2$. Then the ratio of the flux will be determined by our introduction of the upstream parameter ψ_i which is the stream function in the center of the channel. The right boundary layer flux (looking down the channel) is thus specified by $1 - \psi_i$ and the left by $1 + \psi_i$. See the schematic below.

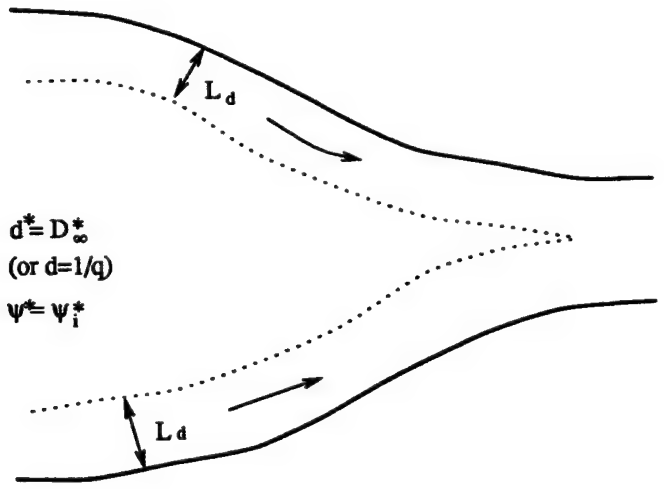

Next, we find the relation between $\bar{B}$, q, and the measure of Q given above, ψ_i. In this way, we eliminate $\bar{B}$ as a parameter. First, integrate Eq. (60):

$$B = q\psi + constant \tag{44}$$

The constant is equal to $q^{-1} - q\psi_i$ and is evaluated given the assumed known upstream conditions of $d = q^{-1}$ (dimensionally $d^* = D_\infty$) on $\psi = \psi_i$. The relation with $\bar{B}$ is:

$$\begin{aligned} \bar{B} &= \frac{1}{2}(B(w/2, y) + B(-w/2, y)) && (45) \\ &= \frac{1}{2}(q(-1+1) + 2q^{-1} - 2q\psi_i) && (46) \\ &= q^{-1} - q\psi_i && (47) \end{aligned}$$

So now we use Eq. (43) as our J function, getting rid of $\hat{d}$ by using Eq. (42) and using the above relation to express $\bar{B}$ in terms of the upstream parameters q and ψ_i. The J function is thus:

$$J(\bar{d}; h(y), T(y); q, \psi_i) = T^2(\bar{d} - q^{-1})^2 + T^{-2}\bar{d}^2 + 2q^{-1}(\bar{d} + h) - 2(q^{-2} - \psi_i) \tag{48}$$

We may use Gill's condition (24) to find a critical flow relation analogous to Eq. (23). It is:

$$\bar{v} = \bar{d}^{1/2}(1 - T^2(1 - q\bar{d}))^{1/2} \tag{49}$$

Though not stated in the lecture, a relation analogous to Eq. (20) seems possible, using the above relation, $Q = 2\bar{d}\hat{d}$, and a relation from the previous lecture: $\bar{v} = q^{1/2}T^{-1}\hat{d}$.

Now that we have the critical flow conditions, let us go back and examine some of the properties of the governing equations. We do this in three diagrams. The first two are based on Eq. (48), and the last on Eq. (48) plus the critical flow condition Eq.(49). In particular, the plots show

- the relation between the width of the channel given by $T \equiv \tanh(\frac{1}{2}q^{1/2}w)$ and the average depth $\bar{d}$ for various values of q. The topography is held constant and $\psi_i = 1$, which implies all the flow comes from the left (looking downstream) boundary layer. This flow configuration is a steady state solution to a dam break problem in a channel (Gill 1976). (labeled figure 1).

- the relation between the bottom topography in the channel h and the average depth $\bar{d}$ for various values of q. The width is held fixed ($T = .63$) and $\psi_i = 1$. For $\bar{d} > 1$, the flow is attached and $\bar{d} < 1$, the flow is separated. Above the dotted lines, the flow is subcritical and below, supercritical. (labeled figure 2).

- the maxima in the sill height and the upstream q value given various values of ψ_i for a flow that is critically controlled. The width is held constant (labeled figure 3).

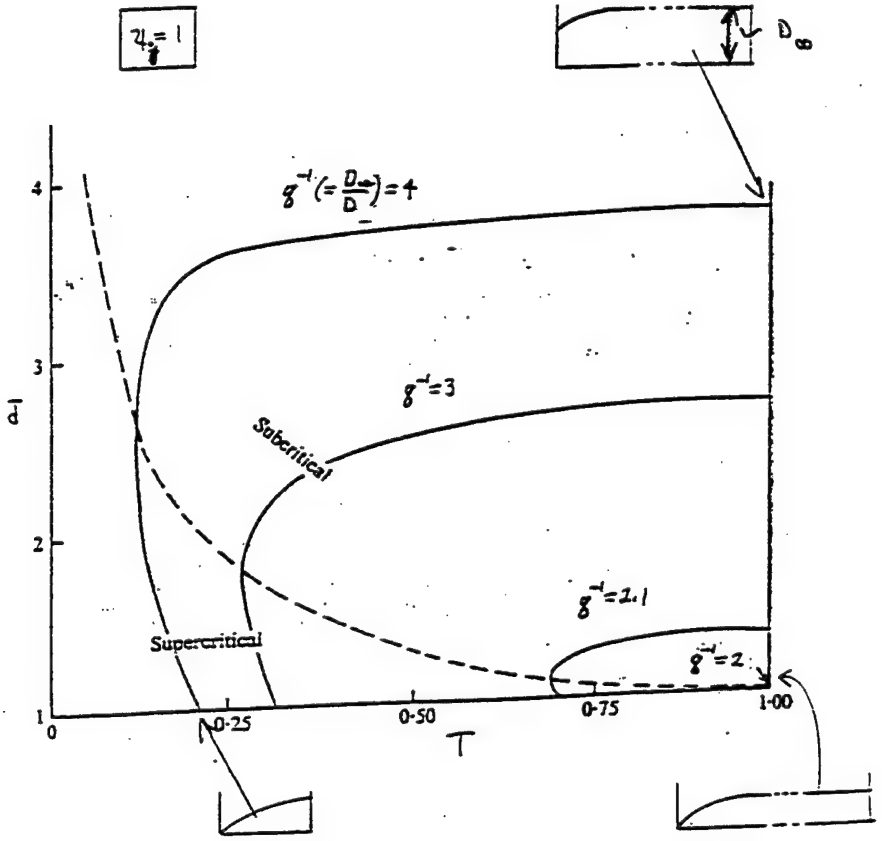

Figure 1

$\eta_I = 1$ $T = .63$
or $\frac{w^*}{L_d} = .75$

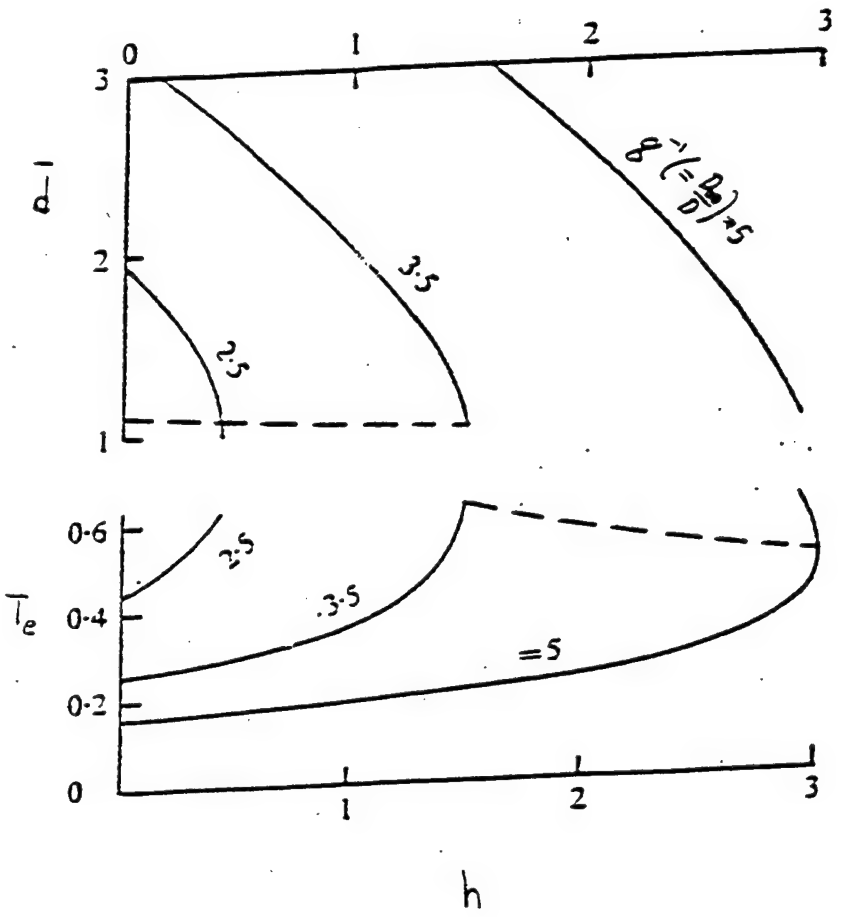

$T_e = \tanh(\frac{1}{2} g w_e)$

Figure 2

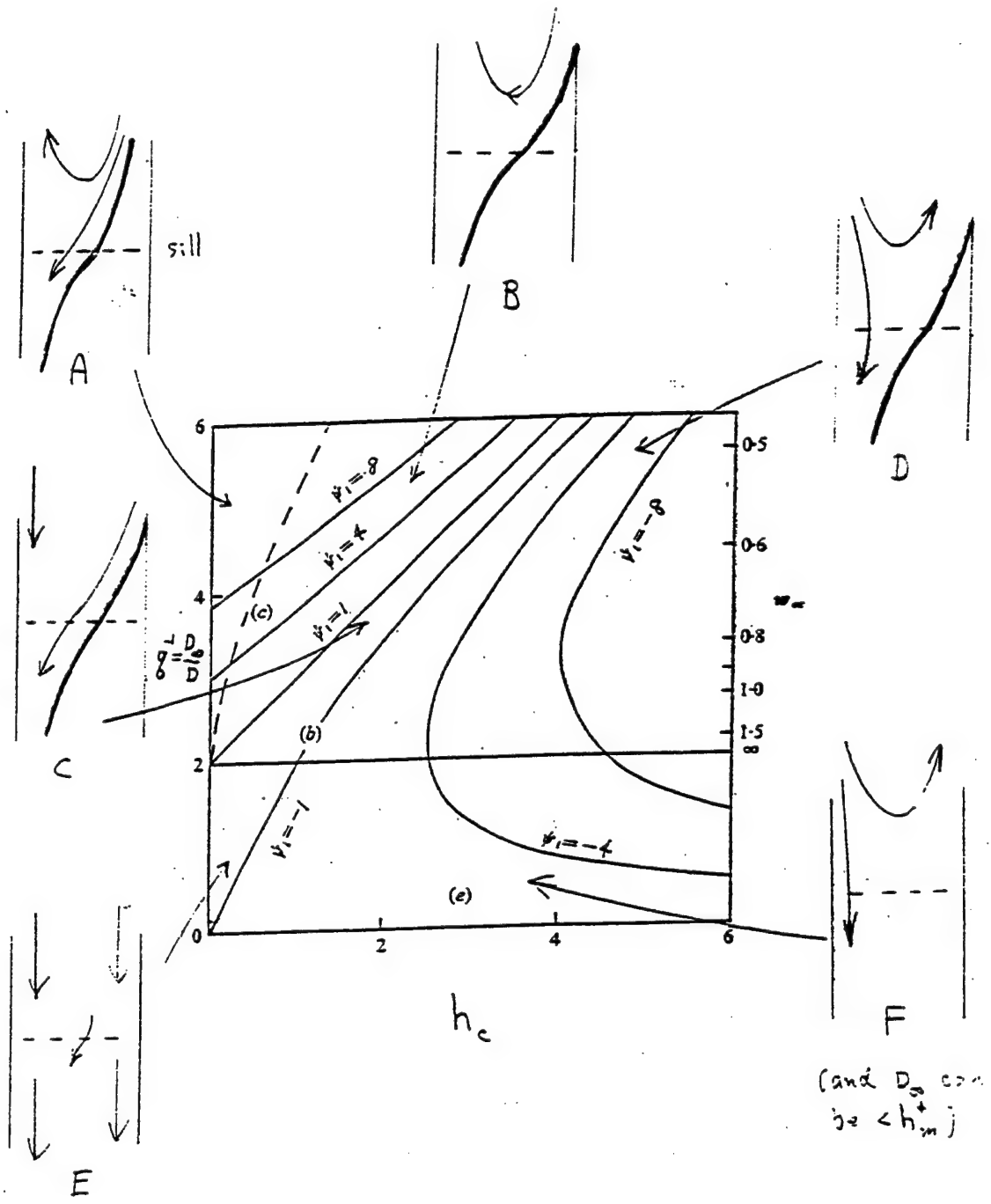
A
still
B
C
D
E
F
(a)
(b)
(c)
(d)
(e)
$\psi_1 = -8$
$\psi_1 = -4$
$\psi_1 = -1$
$\psi_1 = 1$
$\psi_1 = 4$
$\psi_1 = -8$
$\frac{1}{\delta} = \frac{D_\infty}{D}$
h_c
w_∞
0
2
4
6
0·5
0·6
0·8
1·0
1·5
∞

Figure 3

References

Gill, A. E. 1976 Adjustment under gravity in a rotating channel. *J. Fluid Mech.*, 77, 603-621.

Gill, A. E. 1977 The hydraulics of rotating-channel flow. *J. Fluid Mech.*, 80, 641-671.

Pratt, L. J. 1983 On inertial flow over topography. Part 1. Semigeostrophic adjustment to an obstacle. *J. Fluid Mech.*, 131, 195-218.

4 Appendix: Relationship between the Bernoulli function and Potential Vorticity

The steady shallow water momentum equations in dimensional form (hence the asterisks), are:

$$v^* \frac{\partial u^*}{\partial y^*} - fv^* = -g\frac{\partial d^*}{\partial x^*} - g\frac{\partial h^*}{\partial x^*} - u^*\frac{\partial u^*}{\partial x^*} \quad (50)$$

$$u^* \frac{\partial v^*}{\partial x^*} + fu^* = -g\frac{\partial d^*}{\partial y^*} - g\frac{\partial h^*}{\partial y^*} - v^*\frac{\partial v^*}{\partial y^*} \quad (51)$$

Adding $-v^* \frac{\partial v^*}{\partial x^*}$ to both sides of Eq. (50) and $-u^* \frac{\partial u^*}{\partial u^*}$ to both sides of Eq. (50) yields:

$$-v^*(f + \frac{\partial v^*}{\partial x^*} - \frac{\partial u^*}{\partial y^*}) = -\frac{\partial}{\partial x^*}(gd^* + gh^* + \frac{u^{*2} + v^{*2}}{2}) \quad (52)$$

$$u^*(f + \frac{\partial v^*}{\partial x^*} - \frac{\partial u^*}{\partial y^*}) = -\frac{\partial}{\partial y^*}(gd^* + gh^* + \frac{u^{*2} + v^{*2}}{2}) \quad (53)$$

Using the definition of potential vorticity q and defining the Bernoulli function $B^* (\equiv gd^* + gh^* + \frac{u^{*2}+v^{*2}}{2})$ yields:

$$-(v^* d^*)q^* = -\frac{\partial B^*}{\partial x^*} \quad (54)$$

$$(u^* d^*)q^* = -\frac{\partial B^*}{\partial y^*} \quad (55)$$

Because the flow is assumed steady, the continuity equation implies the existence of a stream function defined by:

$$v^* d = \frac{\partial \psi^*}{\partial x^*} \tag{56}$$

$$u^* d = -\frac{\partial \psi^*}{\partial y^*} \tag{57}$$

We can use this in the above Eqs. (54) and (55):

$$q^* \frac{\partial \psi^*}{\partial x^*} = \frac{\partial B^*}{\partial x^*} \tag{58}$$

$$q^* \frac{\partial \psi^*}{\partial y^*} = \frac{\partial B^*}{\partial y^*} \tag{59}$$

or

$$q^* \nabla \psi^* \quad = \quad \nabla B \tag{60}$$

The above equation implies that the Bernoulli function B^* depends only on ψ and also that $q^* = \frac{dB^*}{d\psi^*}$, so that the potential vorticity is constant along streamlines. The specification of B^* upstream immediately implies a given q^* or if q^* is specified upstream, the Bernoulli function is determined up to an integration constant.

George Veronis pointed out that the argument presented here was first due to Fofonoff (JMR 1954).

Lecture 5: Adjustment processes, shock joining theory, Rossby waves

Larry Pratt

NOTES BY Jürgen Theiss

1 Adjustment processes

We consider the establishment of steady flow after an obstacle is introduced into a steady initial flow (Pratt 1983). Experiments to study such adjustment problems were carried out by Long (1954) and Houghton & Kasahara (1968). The initial state is assumed to be a subcritical, geostrophically balanced, steady flow with zero velocity components across the channel and uniform potential vorticity. Once the obstacle is placed into the initial flow an adjustment process takes place. This process as well as the asymptotic state that is reached depends on the height of the obstacle in relation to the critical height. The critical height is the maximum height a steady flow is able to surmount while maintaining the initial flow rate and energy. The adjustment process, triggered by placing an obstacle with less than the critical height into the initial flow, is illustrated in figure 1. The lower frame shows the shape of the obstacle and the upper three frames the adjustment process at three consecutive times. Right after the obstacle is placed into the flow the interface begins to bulge over the obstacle. This bulge then breaks into two isolated Kelvin waves, one moving upstream along the near wall and the other downstream along the far wall. The waves finally move away leaving behind a steady flow with the same flow fields as in the initial state. The Kelvin waves have only temporarily disturbed the flow and thus have not induced any permanent change of the flow away from the obstacle.

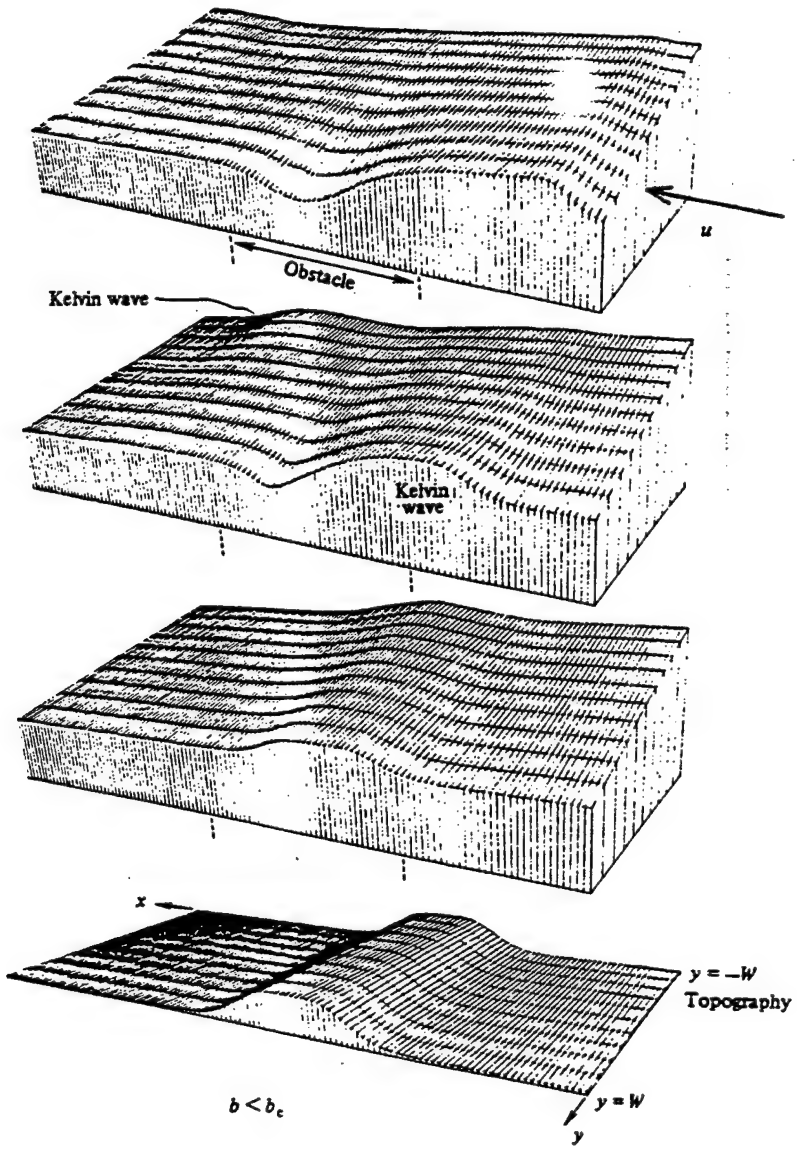

FIGURE 1 Top three frames: Adjustment of an initially subcritical, geostrophically balanced flow after an obstacle is placed into the flow. Bottom frame: Shape of obstacle.

If the height of the obstacle exceeds this critical value then permanent changes are being induced in the flow in order to maintain a steady flow. The corresponding adjustment is shown in figure 2.

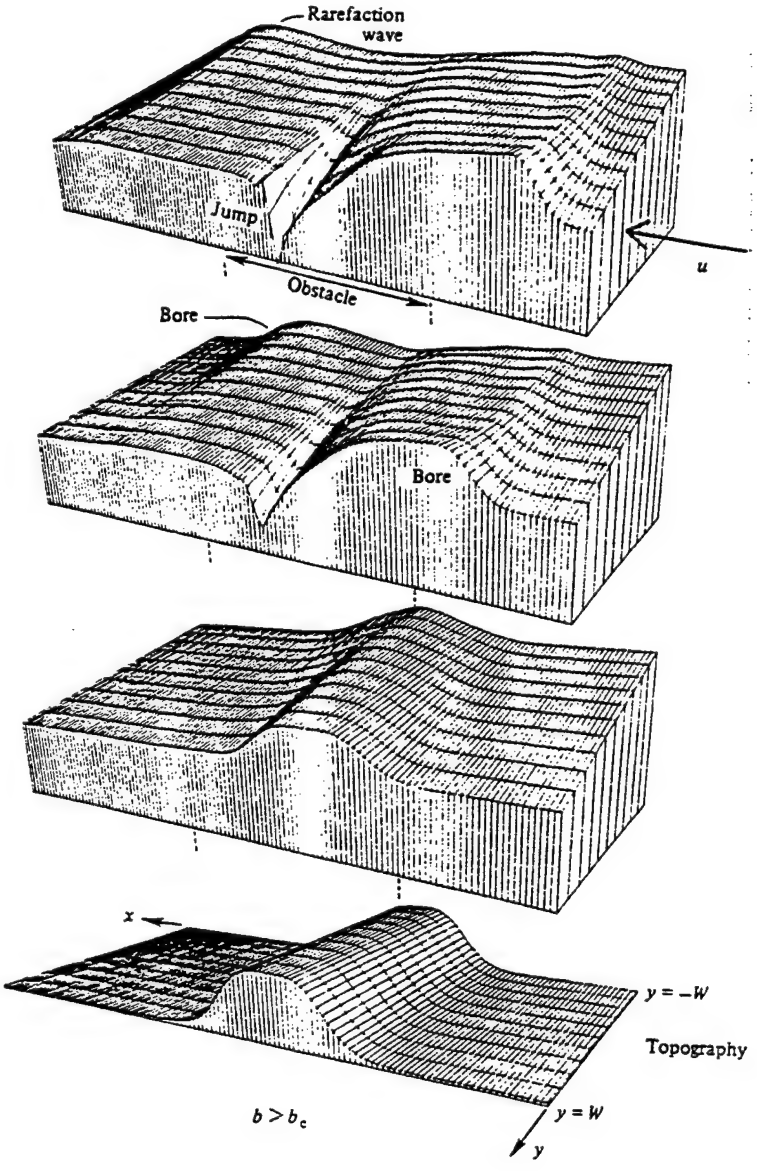

FIGURE 2 Adjustment for an obstacle height greater than the critical value.

Instead of isolated Kelvin waves, the bulge now develops into bores which move along the sidewalls in the same manner as the Kelvin waves. These bores completely move away from the obstacle and nearly steepen to the point of breakage. The bore moving downstream is trailed by a rarefaction wave which is beginning to spread. The adjustment process finally results in a steady flow containing a hydraulic jump in the lee of the sill. This process decreases the flow rate permanently. The resulting flow can therefore be considered to be partially blocked. This permanent change is induced by the upstream moving bore which is itself being triggered by an obstacle whose height exceeds the critical value. Thus the flow is hydraulically controlled.

2 Shock joining theory

In order to calculate the final state of the flow which results from an adjustment process, we need to develop a theory which determines how upstream and downstream states are connected across the bores/shocks (Pratt 1983). Such a theory is called shock joining theory. The interior of the shock is a complicated region which cannot be described by the shallow water approximation. However, within this region as in the rest of the fluid, mass and momentum are conserved. This allows one to connect the upstream and downstream state of the flow by integrating the conservation laws for mass and momentum flux across the discontinuity. Without loss in generality, we introduce a local coordinate system at each point along the shock whereby the axis are normal (n) and tangent (s) to the shock, respectively. The coordinate system is rectangular and fixed in time.

In this new coordinate system, the mass continuity equation takes on the form.

$$\frac{\partial \mathrm{d}}{\partial t} + \frac{\partial}{\partial n}(u^{(n)}\mathrm{d}) + \frac{\partial}{\partial s}(u^{(s)}\mathrm{d}) = 0. \tag{1}$$

To simplify the following calculations, we introduce the notation

$$< a >= a|_{\epsilon} - a|_{-\epsilon} \tag{2}$$

where a is a quantity defined on the domain of the fluid and $-\epsilon < n < \epsilon$ is a short interval containing the discontinuity. Integrating (1) along the n-axis, i.e. across the shock, thus gives

$$\frac{\partial}{\partial t}\int_{-\epsilon}^{\epsilon} \mathrm{d}\, dn + < u^{(n)}\mathrm{d} > + \int_{-\epsilon}^{\epsilon} \frac{\partial}{\partial s}(\mathrm{d}u^{(s)})\, dn = 0. \tag{3}$$

The first term is the rate of change of the area of the cross-section of the shock between the points $-\epsilon$ and ϵ along the n-axis. It can therefore be replaced by $c^{(n)} < \mathrm{d} >$ where $c^{(n)}$ is the velocity component of the shock normal to itself. The third term tends to zero as ϵ tends to zero since the integrand is continuous across the shock. We thus have,

$$c^{(n)} < \mathrm{d} > - < u^{(n)}\mathrm{d} >= 0. \tag{4}$$

Similarly, the depth-integrated shallow water momentum equation are given in the new coordinate system by

$$\frac{\partial(u^{(n)}\mathrm{d})}{\partial t} + \frac{\partial}{\partial n}\left(u^{(n)^2}\mathrm{d} + \frac{1}{2}\mathrm{d}^2\right) + \frac{\partial}{\partial s}\left(u^{(n)}u^{(s)}\mathrm{d}\right) = -\mathrm{d}\frac{\partial h}{\partial n} + \mathrm{d}u^{(s)} \tag{5}$$

$$\frac{\partial(u^{(s)}\mathrm{d})}{\partial t} + \frac{\partial}{\partial n}\left(u^{(n)}u^{(s)}\mathrm{d}\right) + \frac{\partial}{\partial s}\left(u^{(s)^2}\mathrm{d} + \frac{1}{2}\mathrm{d}^2\right) = -\mathrm{d}\frac{\partial h}{\partial s} - \mathrm{d}u^{(n)}. \tag{6}$$

Integrated across the shock and written in the new notation, the momentum equations become

$$c^{(n)} < u^{(n)}\mathrm{d} > - < u^{(n)^2}\mathrm{d} + \frac{1}{2}\mathrm{d}^2 > = 0 \tag{7}$$

$$c^{(n)} < u^{(s)}\mathrm{d} > - < u^{(s)}u^{(n)}\mathrm{d} > = 0 \tag{8}$$

Equation (8) combined with equation (4) gives

$$< u^{(s)} >= 0 \tag{9}$$

using the fact that $< a >= 0$ and $< ab >= 0$ implies $< b >= 0$. The normal velocity component $u^{(n)}$ is discontinuous across the shock, otherwise equation (4) would give $c^{(n)} = u^{(n)}$ which violates equation (7). If furthermore $u^{(s)} \neq 0$, then the velocity vector must also change direction. This implies that the shock must be perpendicular to any solid boundary in which case $u^{(s)} = 0$, otherwise the shock would induce a flow normal to the boundary.

In general, given the upstream velocities $u_u^{(n)}, u_u^{(s)}$ and height h_u, one can determine the downstream velocities $u_d^{(n)}, u_d^{(s)}$ and height h_d using equation (4), (7) and (9). Thus, one is able to connect the upstream and downstream state of the fluid.

In the case the upstream state of the fluid is semigeostrophic, the ratio of v to u approaches zero and the entire shock should be described by a

single velocity. Under these condition it is tempting to describe the shock as a weak solution to the semigeostrophic equations. In such a description the flow would be semigeostrophic at all points not on the shock. However, equations (4),(7) and (9) make no allowance for geostrophy. Given a semigeostrophic upstream state, for example there is no guarantee that the velocity u_d immediately downstream of the shock will be in geostrophic balance with h_d. We therefore submit that the shock is bordered by a region in which the cross channel acceleration $\frac{dv}{dt}$ becomes as large as u and h_y. In this region lateral dispersion becomes important. The width of this dispersive region is of the order of the deformation radius and its role is to adjust the shock to the semigeostrophic flow on either side.

The shock joining theory above requires knowledge of the exact shape of the shock in oder to integrate at each point along the shock the mass and momentum flux across the discontinuity. An alternative approach is to integrate the conservation laws for momentum and energy across the channel upstream and downstream of the shock. For known potential vorticity, the upstream and downstream fluxes are each completely specified by two quantities (such as $\bar{d}$ and $\hat{d}$ in the Gill model). For a given upstream $\bar{d}$ and $\hat{d}$, conservation of width-integrated mass and momentum flux determine the downstream $\bar{d}$ and $\hat{d}$. This approach, however, requires conservation of potential vorticity across the shock which is not guaranteed. In fact, the change of potential vorticity is related to the rate of energy dissipation within the shock. To show that, we use the relation

$$q = \frac{\mathrm{d}B}{\mathrm{d}\Psi} \tag{10}$$

where q is the potential vorticity, B the Bernoulli function and Ψ the streamfunction. Since streamlines are continuous across the shock and using $\Psi_s = u^{(n)}\mathrm{d}$, we have

$$\begin{aligned} < q > &= < \frac{\mathrm{d}B}{\mathrm{d}\Psi} > \\ &= \frac{\mathrm{d} < B >}{\mathrm{d}\Psi} \\ &= \frac{1}{u^{(n)}\mathrm{d}} \frac{\partial}{\partial s} < B > . \end{aligned} \tag{11}$$

Using the standard relation in weak shock theory (Stoker 1958)

$$< B >= \frac{< d^3 >}{d_u d_d} \tag{12}$$

where d_u and d_d are the upstream and downstream depths, respectively, equation (11) becomes

$$< q >= \frac{1}{u^{(n)}\mathrm{d}} \frac{\partial}{\partial s} \frac{< d^3 >}{d_u d_d}. \tag{13}$$

The change in potential vorticity across the jump, which results from the adjustment process shown in figure 2, is displayed in figure 3. Graph A is taken upstream of the bore showing the uniform initial potential vorticity. Graph B is taken between the bore and the jump. The slightly smaller values of potential vorticity are probably within the limits of numerical error. Graph C is taken downstream of the jump which shows a significant increase in potential vorticity.

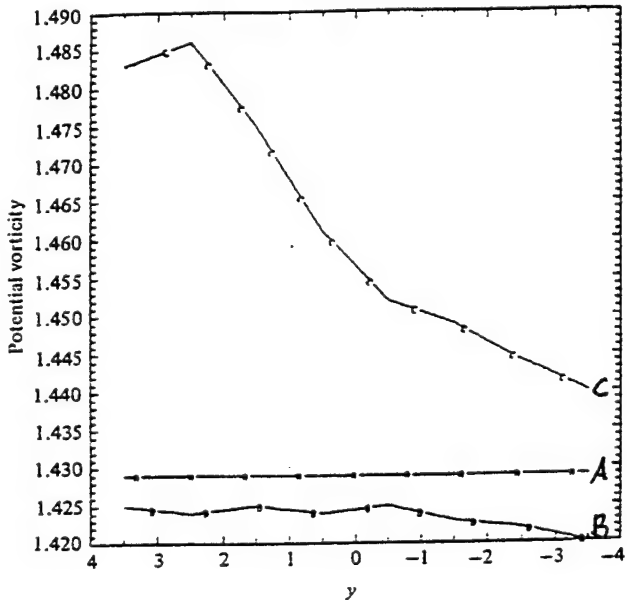

FIGURE 3 Potential vorticity profiles of the flow in figure 2 taken ahead of the upstream-moving bore (A), between this bore and the jump (B) and downstream of the jump (C).

Equation (12) is consistent with these numerical results. Facing downstream, $< h >$ is largest on the left side of the channel which implies

$$\frac{\partial}{\partial s}\left(\frac{< d^3 >}{d_u d_d}\right) > 0. \tag{14}$$

Thus, the change in potential vorticity is positive as shown in figure 3.

3 Rossby waves

Another complication which arises from the nonuniformity of potential vorticity are Rossby waves which can just like gravity waves become stationary in the flow thus adding further critical states to the system (Pratt & Lundberg 1991). This is most easily illustrated by a nonrotating flow in which potential vorticity is given by

$$q = q_0 + \alpha\Psi \tag{15}$$

where q_0 and α are constants.

In the case $\alpha < 0$, the potential vorticity gradient is directed to the left, facing downstream, and Rossby waves propagate upstream. Multiple critically controlled states are now possible and a unique specification of the steady flow no longer exists. The solution curve now has multiple lobes shown in figure 4 each corresponding to a critically controlled flow with respect to a unique wave mode.

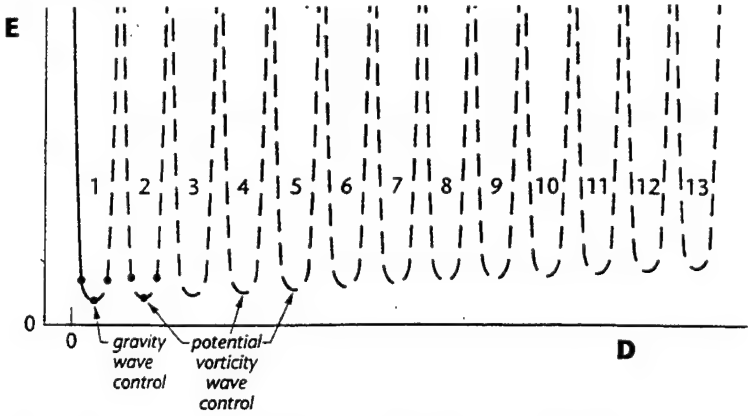

FIGURE 4 Solution curves for the nonrotating, nonuniform potential vorticity flow. D is the fluid depth, E the elevation of the bottom of the channel and volume transport is held fixed.

Pratt & Armi (1987) suggest that the solution controlled by gravity wave mode may be preferred on the basis of stability. However, this nonuniqueness problem requires further investigation using experiments or solutions to an appropriate initial value problem.

Bibliography

HOUGHTON , D.D. & KASAHARA, A. **1968**, Nonlinear shallow fluid flow over an isolated ridge. *Communs Pure Appl. Maths*, **21**, 1-23

LONG, R.R. **1954**, Some aspects of the flow of stratified fluids. II. Experiments with a two-fluid system. *Tellus*, **6**, 97-115

PRATT, L. **1983**, On inertial flow over topography. Part 1. Semigeostrophic adjustment to an obstacle. *J. Fluid Mech.*, **131**, 195-218

PRATT, L. & LUNDBERG P.A. **1991**, Hydraulics of rotating strait and sill flow. *Annu. Rev. Fluid Mech.*, **23**, 81-106

STOKER, J.J. **1958**, *Water waves: the mathematical theory with applications*. Wiley.

Critical Control of Deep Ocean Sill Flows

John Whitehead

NOTES BY Katsurou Katsumata

1 Introduction

The bottom topography of the large ocean basins is characterized by large abyssal plains and sills or gaps connecting between them[1]. Some observations (Fig.1 and Fig.2) indicate the exchange of the deep water over the sill. In this talk, it will be shown that the prediction of the transport across the sill is feasible with a *"back-of-the-envelope"*[2] calculation based on the maximization principle of the geostrophic flow. A methodology of testing the theory against ocean data is presented and the comparison of the prediction and observation is discussed.

2 Theory

Figure 3 shows the configuration under consideration. Take x across the channel and y along the channel. We use a one-and-half layer model where deep and quiescent water of lighter density ρ lies upon the active slightly heavier water of density $\rho + \Delta\rho$.

[1]To name a few sills in the Atlantic Ocean; Denmark Strait, Iceland-Faroe Passage, Faroe Bank Channel, Windward Passage, Anegada-Jungfern Passage, Discovery Gap, Vema Gap, Ceara Abyssal Plain, Vema Channel, Shag Rocks Passage, South Sandwich Island Arc Gap, ...

[2]the size of the envelope is arbitrary, though...(L.Pratt)

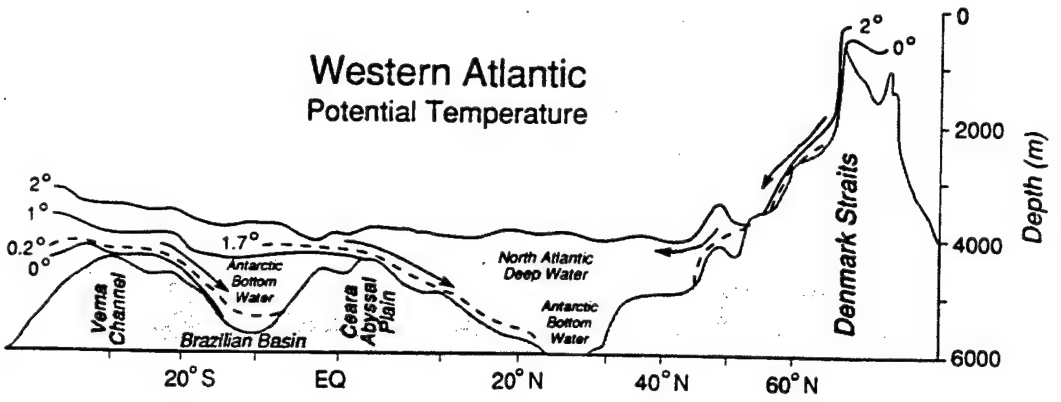

Figure 1 Elevation view of selected isotherms in the western North Atlantic, with three sill flows shown as arrows. The bathymetry between 20 and 40° South has been redrawn to show more accurately the depth of the deepest portion of the ocean.

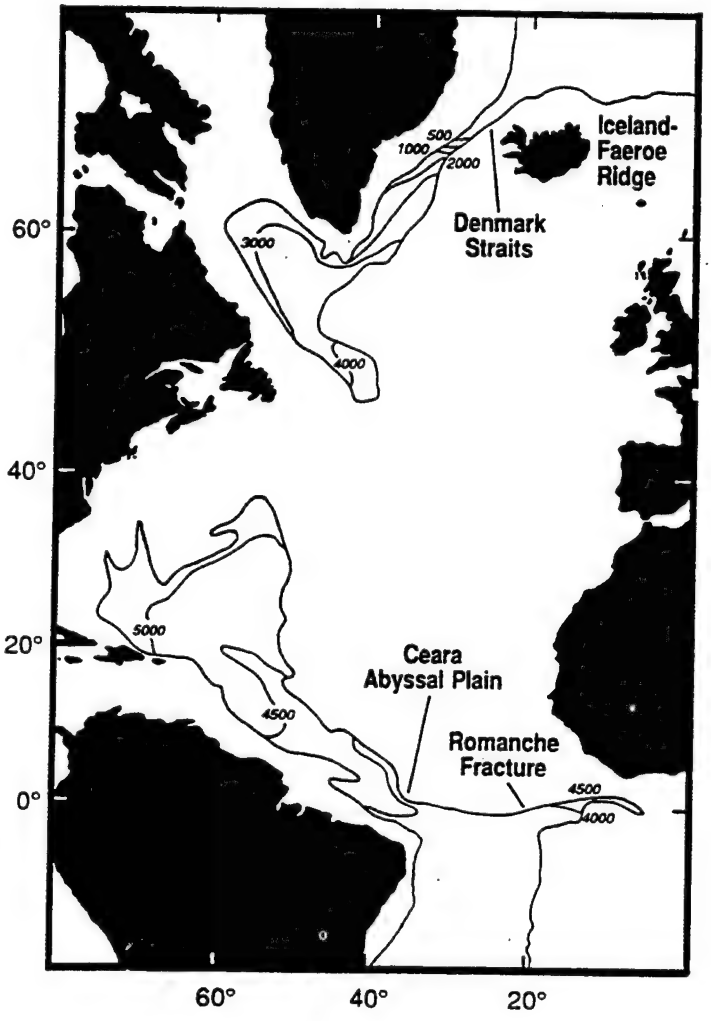

Figure 2 Plan view of the depth of the 1.7° potential temperature surface in the western North Atlantic. The transition from a level surface to a sloping surface reveals two sill flows.

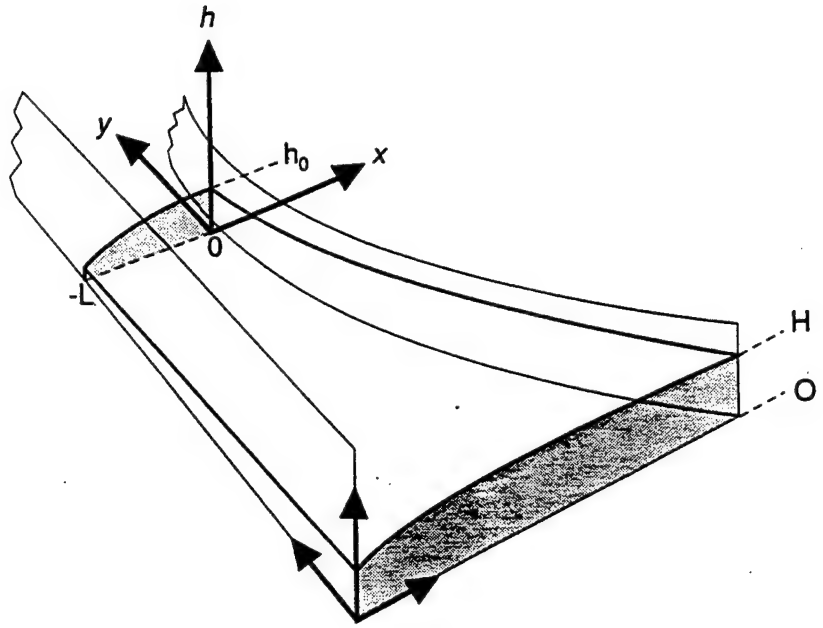

Figure 3 Sketch of the geometry of the constant potential vorticity problem. A reduced gravity current comes from $y = -\infty$ where the channel is very (infinitely) wide along a flat bottom to a point where the channel is width L.

The water originates from a reservoir of depth on the right wall H, that is wide enough so that the water is quiescent there. The origin of x is on the right wall looking down the flow. The surface height is given by $h(x)$. For a steady flow, the governing equations are

$$fv = g' \frac{dh}{dx} \tag{1}$$

$$\frac{\frac{dv}{dx} + f}{h} = \frac{f}{H} \tag{2}$$

where g' is the reduced gravity $\Delta\rho g/\rho$ and the approximation of gradual

flow[3] is applied. The equation can be solved by eliminating v as

$$h = H - Ae^{-x/R} - Be^{x/R}, \tag{3}$$

then with the geostrophy (1)

$$v = \frac{g'}{fR}(Ae^{-x/R} - Be^{x/R}), \tag{4}$$

where $R \equiv \sqrt{g'H}/f$ is the Rossby radius of deformation.

Applying the Bernoulli's theorem on the stream line along $x = 0$ i.e. right hand wall looking downstream, yields

$$\begin{aligned} v_0 &= \sqrt{2g'(H - h_0)} \\ &= \frac{g'}{fR}(A - B) \text{ (with Eq.(4))}, \end{aligned} \tag{5}$$

and

$$h_0 = H - A - B. \tag{6}$$

These can be solved for A and B, then the physical quantities in this problem are given in terms of one parameter h_0.

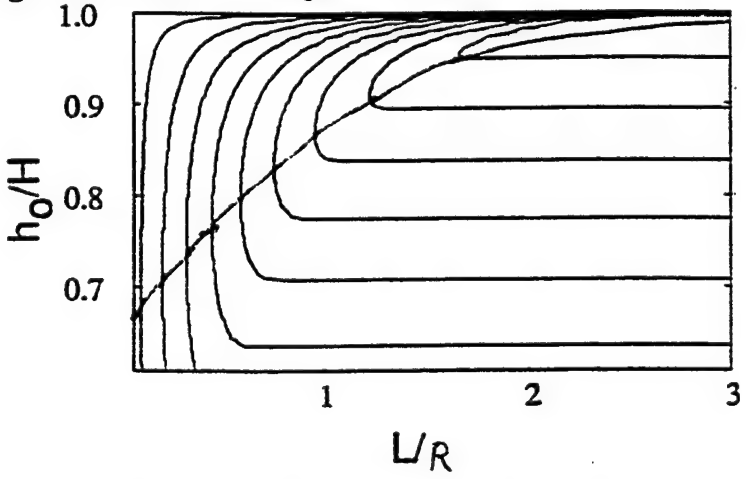

Figure 4 Contours of flux as a function of the normalized depth of the fluid on the right-hand wall and normalized channel width.

[3] $\frac{dv}{dx} \gg \frac{du}{dy}$

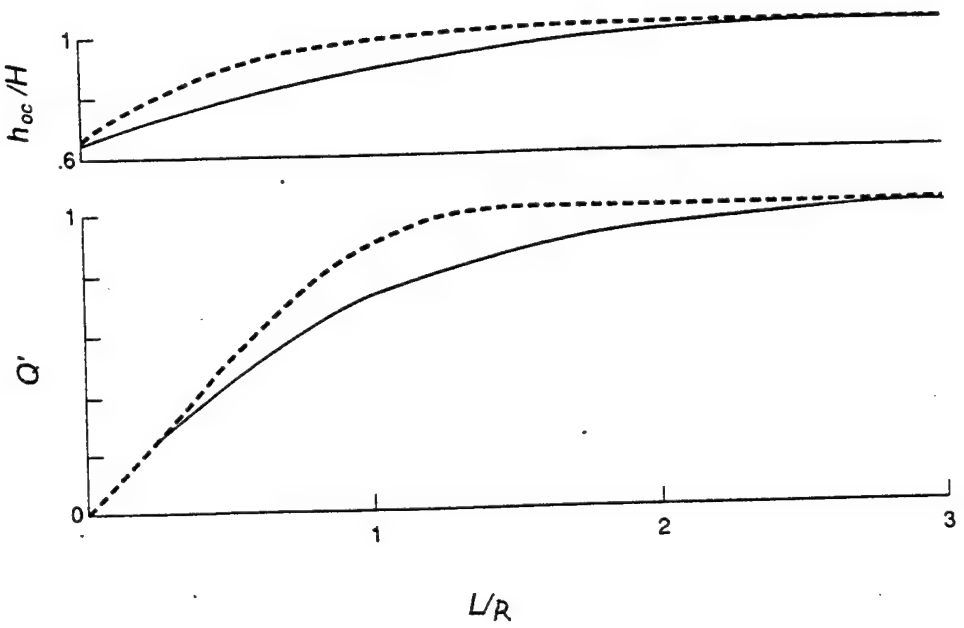

Figure 5 Flux and critical depth as a function of channel width for constant potential vorticity (solid) and zero potential vorticity (dashed).

To determine h_0, a hydraulic rule is employed: For a given energy the transport Q is maximized. This assertion of the maximization is equivalent to the condition of the controlled flow; that is, the variation of the sill height causes the change in the transport. The transport Q can be expressed in terms of h_0 when geostrophy is assumed. Figure 4 is a contour of Q as a function of the width of the constriction L and h_0. The curve connects the maximum of h_0 for given L.

This problem can also be solved for a very deep reservoir ($H \gg O(h)$), which can be called the zero potential vorticity case, but the difference in the critical initial height h_{0c} and the transport Q turns out to be small, at most 22 % (Fig.5). Since the zero potential vorticity case is much simpler algebraically, the expression of the transport will be used, it has the form;

$$Q = \begin{cases} \frac{g\Delta\rho h^2}{2\rho f} & L > R \\ \left(\frac{2}{3}\right)^{3/2} L\sqrt{\frac{g\Delta\rho}{\rho}}\left(h - \frac{L^2}{8R^2}\right)^{3/2} & \text{otherwise} \end{cases} \tag{7}$$

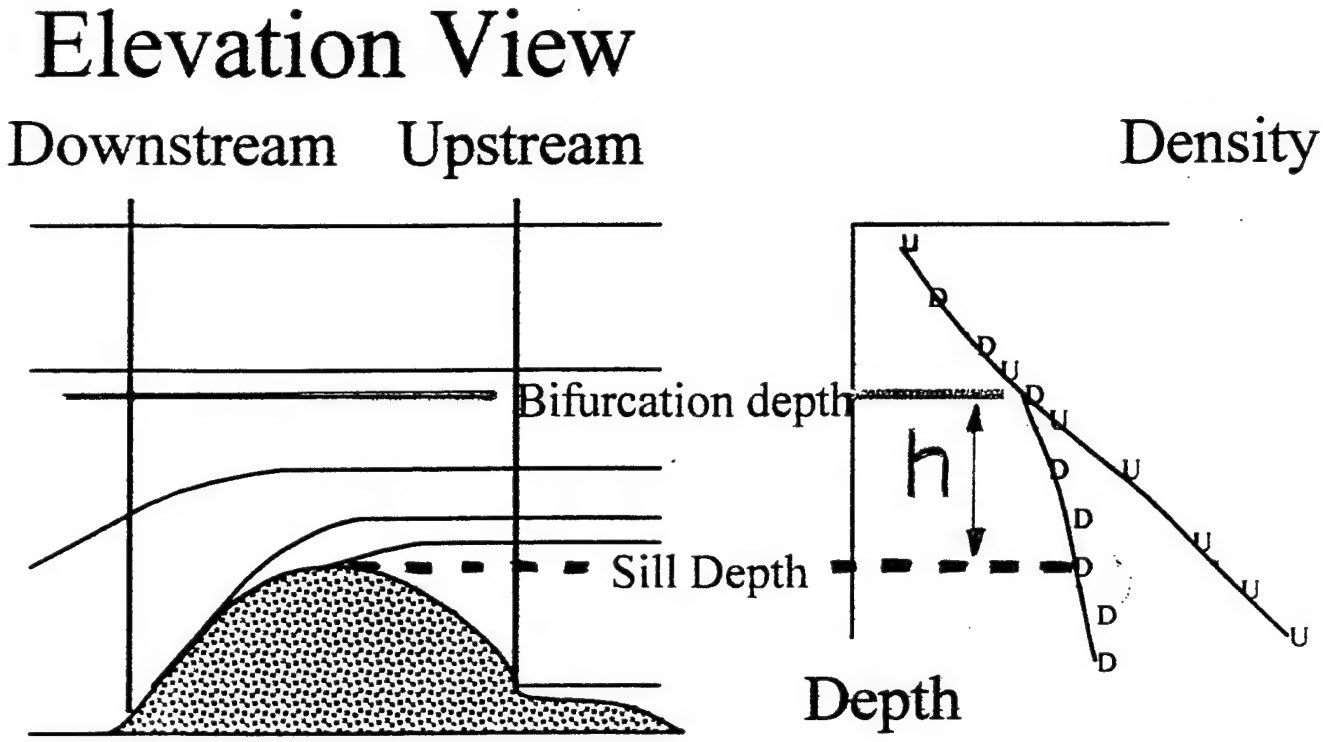

Figure 6 Methodology for determining $\Delta\rho$ and h. The density observations of both side of the sill are plotted on the same plane as functions of the depth.

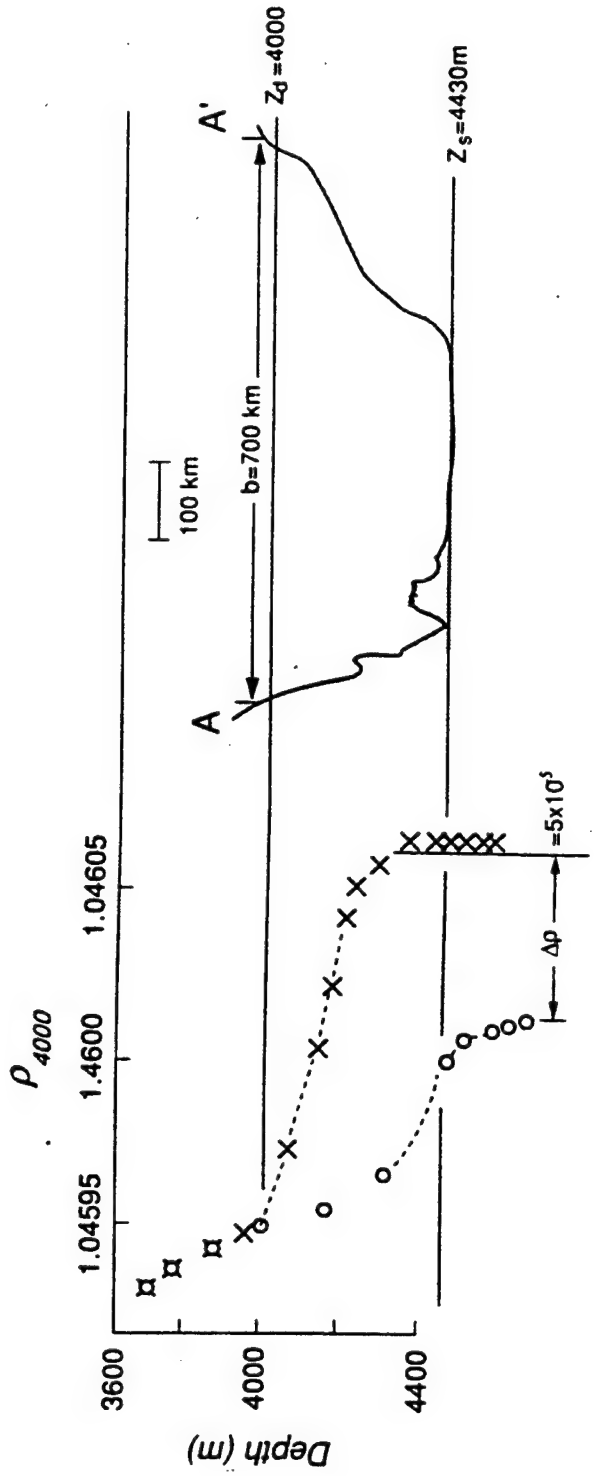

Figure 7 Estimation of $\Delta\rho$ and $H \equiv z_s - z_d$ for the Ceara Abyssal Plain.

Table 1: Data and predictions for Atlantic sills

Sill	$\Delta\rho/\rho$ $\times 10^4$	h (m)	L (km)	R (km)	Q Sv	Q_{obs} Sv	Cit.
Denmark Straits	3	580	350	14	3.8	2.9	Dickson et al.1990
Ceara Abyssal Plain	.5	430	700	65	4.6	2	Hall et al.1997
Vema Channel	1	1540	446	25	16.3	6	Speer&Zenk 1993
Discovery Gap	.1	600	80	4	.21	.21	Saunders 1987
Samoa Passage	.3	1050	240	34	7	6	Rudnik 1996
Vema Gap	.5	1000	9	35	3.3	2.1	McCartney et al 1991, Fischer et al.1997
Faroe Bank	5	400	20	15	3	1.9	Saunders 1990
Romanch Fracutre Zone	.47	380	20	369	2.2	1	Polzin et al.1996

3 Comparison of the theory with the observations

For the comparison of the above theory with the field observations, it is necessary to determine the depth at the sill h and the density difference of the upper and the lower layer from the observational data, along with the channel geometry and the Coriolis parameter. For that purpose, the measurements of the density at both side of the sill are made and plotted on the same plane (see Figure 6). The two datasets bifurcate at some depth, which we call the bifurcation depth. Thus we can define the depth at the sill h as the difference between the bifurcation depth and the real sill depth, and the density difference $\Delta\rho$ as the difference of the two densities at the sill depth. An example for the Ceara Abyssal Plain that connects the western North Atlantic and the western South Atlantic is shown in Figure 7. Table 1 is the result of the similar comparison made for the other sills in the Atlantic Ocean. Figure 8 compares the correspondence between the observation and the prediction. It is seen that the prediction by the theory always overestimates the observation, which is expected since the theory gives the upper limit for the transport because of the neglect of the effect of friction and the

artificial rectangular channel profile.

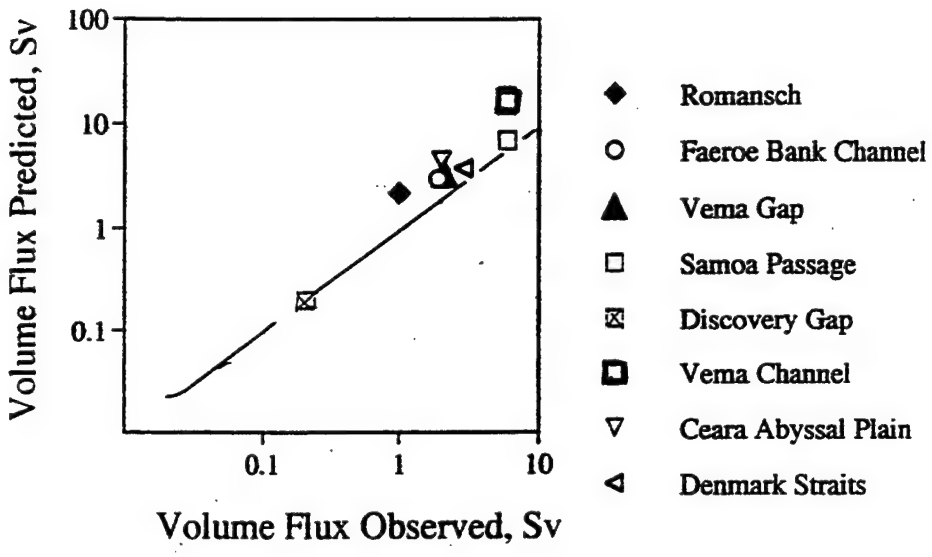

Figure 8 Comparison of the predictions and observations

4 Summary

A theory to estimate the transport with bathymetry and 2 hydrocasts is presented; the prediction overestimates the observation by 20 to 80 %, which is expected. In the comparison, the bifurcation depth of the density profile turns out to be a useful level of no motion. It is expected that the prediction is better than the observation with three or four current meters for a few weeks.

It is admitted that the method is a rough estimation and more effort to continue time series measurements, more studies of lateral velocity profiles, and more dynamic studies to incorporate the effect of friction, diffusion, and time-dependence must be made.

REFERENCES

WHITEHEAD, J.A. 1989 Internal Hydraulic Control in Rotaing Fluid – Applications to Oceans *Geopys.Astrophys.Fluid Dyn.* **48**, 169–192

Inter-basin Exchange Through Broad Channels and Gaps, Part I

Doron Nof

Notes by: Claudia Cenedese and Mary-Louise Timmermans.

1 Introduction

The exchange of surface water through broad gaps between oceans is an interesting oceanographic problem. Several important examples include the exchange between the Pacific Ocean and the Sea of Japan via the Toshima Strait, the flow between the Pacific and the Indian ocean via the Indonesian passages and flow through the Windward Passage in the Carribean and flow through the Unimack Pass between the North Pacific and the Bering Sea.

2 The non-rotating exchange problem

We will consider gaps that are too broad and flow speeds that are too low to be influenced by hydraulic control, yet too narrow to allow free flow through them. Consider the situation in which two infinitely large basins are separated by a thin wall which contains a gap of width several times the deformation radius, as in Figure 1. The basins differ in depth by an amount δ when a barrier is blocking the gap. At time $t = 0$, the barrier is removed and water flows through the gap. Radiating gravity waves are observed, as depicted in Figure 1(a), and after this initial period of adjustment, a steady state will be reached in the form of a barotropic inviscid solution as in Figure 1(b). The flow contracts as it goes through the gap reaching a steady flux of $Q = 1.22d\sqrt{2g\delta}H$, where H is the depth of the fluid and $2d$ is the width of the gap, and a uniform speed given by $\sqrt{2g\delta}$.

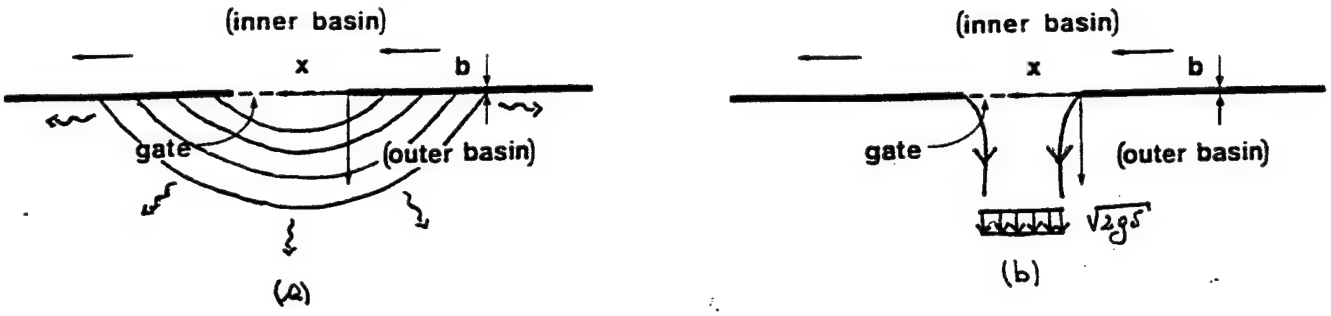

Figure 1: Schematic diagram of non-rotating exchange between two basins separated by a gap.

3 The rotating exchange problem

We will consider three cases. In case 1 and case 2, the initial geometry is identical. In case 1, Kelvin waves may only propagate along two walls in the flow domain and in case 2, they may propagate along three walls. In case 3, the geometry is slightly modified and Kelvin waves may propagate along all four walls in the flow.

3.1 Case 1

Here, we consider the same geometry as in §2, except that the inner basin now contains two layers - a shallow upper layer whose density is ρ and an infinitely deep lower layer whose density is $\rho + \Delta\rho$ where $\Delta\rho/\rho << 1$. The outer basin only contains one layer of density $\rho+\Delta\rho$, as shown in Figure 2. In this co-ordinate system, the y-axis is aligned in the direction perpendicular to the current and the x-axis lies in the direction of the flow. The sea level in the inner basin is higher than that of the outer basin by $H\frac{\Delta\rho}{\rho}$ and this difference is set up by the wind field. An imaginary gate initially blocks the gap that connects the two basins. When this gate is removed, Kelvin waves now take the place of the surface gravity waves of the non-rotating case. In this case, we assume that Kelvin waves can only propagate in regions 1 and 3 as shown in Figure 4. The final adjusted flow is as shown in Figure 3(a) and 3(b). Since the transport of light water through the gap is finite, the

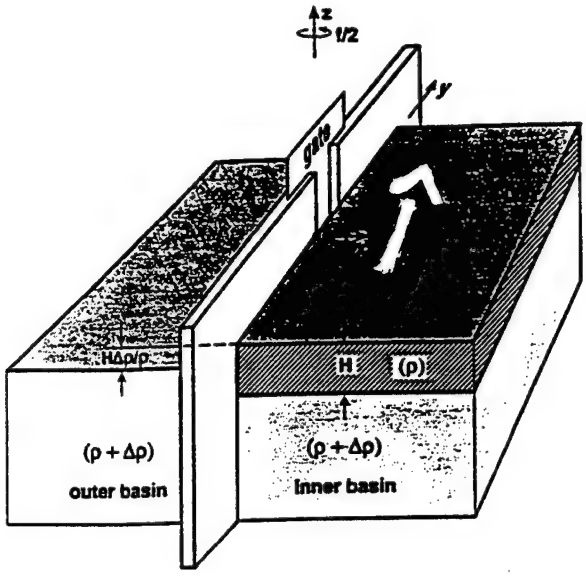

Figure 2: A schematic three dimensional view of the model for interbasin exchange for cases 1 and 2.

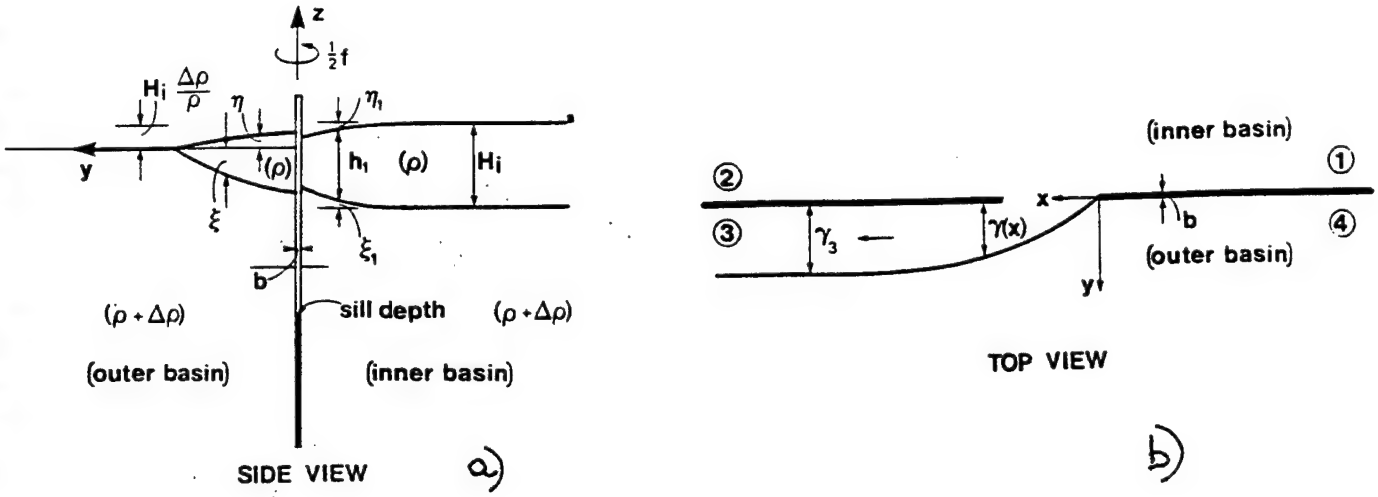

Figure 3: Schematic diagram of the final adjusted state in case 1.

current cross section in region 3 must also be finite so that the interface must intersect the free surface. Away from the gap, the flow is one dimensional and in geostrophic balance.

We assume that, within the inertial boundary current, the potential vorticity is uniform and equal to f/H_i where H_i is the undisturbed depth away from the wall. For such a current, the velocity U and the depth D are given by

$$U = U_w \exp\left(\frac{y}{R_d}\right), \tag{1}$$

and

$$D = H_i\left(1 - \frac{U_w}{fR_d}\exp\left(\frac{y}{R_d}\right)\right), \tag{2}$$

where R_d is the Rossby radius of deformation $= \left(\frac{\sqrt{g'H_i}}{f}\right)$ and the subscripts w correspond to the wall.

All regions away from the gap are governed by the potential vorticity equation and the geostrophic relationship given by

$$-\frac{\partial u}{\partial y} + f = h\frac{f}{H_i}, \tag{3}$$

and

$$fu = -g'\frac{\partial h}{\partial y}, \tag{4}$$

where $u \to 0$ as $x \to \infty$ and $h \to H_i$ as $x \to \infty$. These equations may be integrated to yield solutions

$$u = A\exp(y/R_d) + B\exp(-y/R_d), \tag{5}$$

and

$$h = H_i\left(1 - \frac{A}{fR_d}\exp(y/R_d) + \frac{B}{fR_d}\exp(-y/R_d)\right), \tag{6}$$

where A and B are constants. To determine A and B, we can use the Bernoulli equation

$$\frac{u^2}{2} + g'h = \text{constant} \tag{7}$$

and the momentum equation integrated over the region S outlined by the dashed line in Figure 4. Multiplication of the x-momentum equation by h

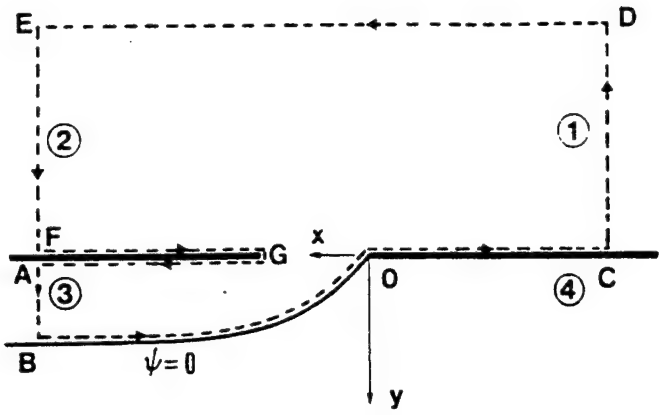

Figure 4: A diagram of the integration area for the momentum equation.

and integration over the region S gives

$$\int\int \left(hu\frac{\partial u}{\partial x} + vh\frac{\partial u}{\partial y} \right) dxdy - \int\int fvhdxdy = -g' \int\int h\frac{\partial h}{\partial x} dxdy. \quad (8)$$

which, by defining a streamfunction ψ as $\frac{\partial \psi}{\partial x} = vh$ and $\frac{\partial \psi}{\partial y} = -uh$, and using the continuity equation can be reduced to

$$\int\int \left[\frac{\partial}{\partial x}(hu^2) + \frac{\partial}{\partial y}(huv) \right] dxdy - \int\int f\frac{\partial}{\partial x} dxdy = -\frac{g'}{2} \int\int \frac{\partial}{\partial x}(h^2) dxdy. \quad (9)$$

Application of Stokes' theorem to (9) gives

$$-\oint huvdx + \oint hu^2 dy - \oint f\psi dy + \frac{g'}{2} \oint h^2 dy = 0. \quad (10)$$

The first term on the left hand side of this equation is zero because at least one of the three variables u, v and h vanishes on every portion of the boundary. Consequently, (10) reduces to

$$\oint \left(hu^2 + \frac{g'h^2}{2} - f\psi \right) dy = 0. \quad (11)$$

Since the flow is geostrophic, we have

$$fuh = -\frac{g'}{2}\frac{\partial}{\partial y}(h^2), \quad (12)$$

which, upon integration, becomes

$$f\psi = \frac{g'h^2}{2} + C, \quad (13)$$

where C is a constant of integration. $C = 0$ if we define $\psi \equiv 0$ where $h = 0$. This leads to

$$+ \oint hu^2 dy = 0. \tag{14}$$

(Note that if there were no rotation, then in place of (14), we would have $\oint (hu^2 + \frac{g'h^2}{2}) dy = 0$.) Finally, using the Bernoulli equation and equation (14), we can solve for the velocity u and depth h in regions one and three of Figure 5. In region three, these solutions are

$$u_3 = U_w \exp(y/R_d), \tag{15}$$

and

$$h_3 = H_i \left[1 - \frac{U_w}{\sqrt{g'H_i}} \exp(y/R_d) \right]. \tag{16}$$

In region one, the solutions are

$$u_1 = \sqrt{g'H_i} \exp(y/R_d), \tag{17}$$

and

$$h_1 = H_i (1 - \exp(y/R_d)). \tag{18}$$

We can also find the distance γ_3 (as shown in Figure 3(b)) from the outer wall, far downstream from the gap, at which the depth of the current vanishes. This distance is

$$\gamma_3 = \frac{\sqrt{g'H_i}}{f} \log \left[\frac{\sqrt{g'H_i}}{U_w} \right]. \tag{19}$$

The transport through the gap (and region three) is

$$T_3 = g'H_i^2 \left[1 - \frac{U_w^2}{\sqrt{g'H_i}} \right] / 2f. \tag{20}$$

3.2 Case 2

In this case, we relax the condition of no Kelvin waves in region 2 of Figure 3. We assume that the gap width is much larger than the Rossby radius of deformation and that the flow is semigeostrophic. Now, instead of integrating the momentum over a control volume, we use the front progression constraint which is valid only in the gap. From the x-momentum equation,

$$\frac{du}{dt} - fv = -g' \frac{\partial h}{\partial x}, \tag{21}$$

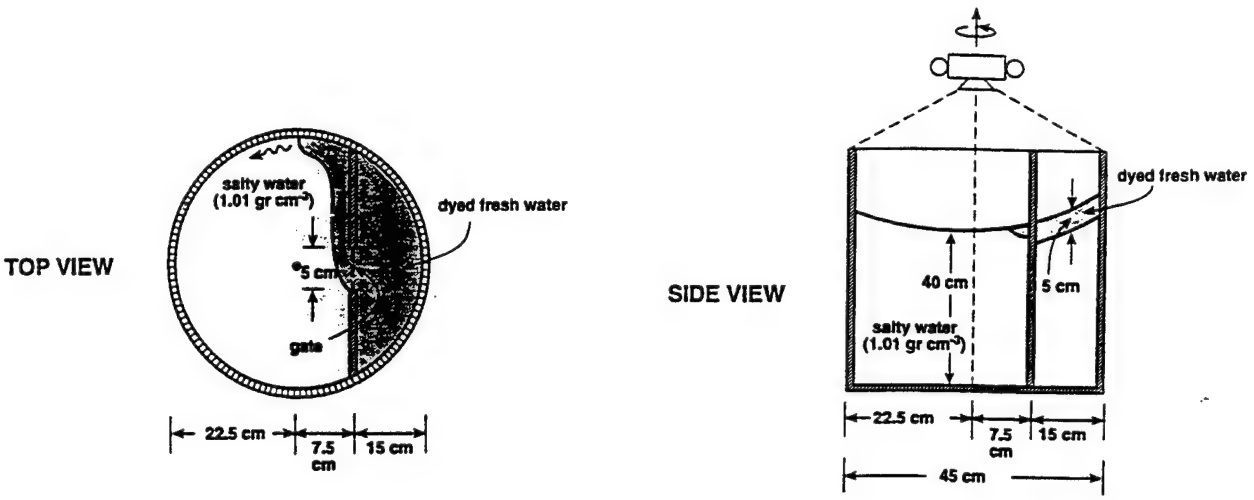

Figure 5: A sketch of the experimental apparatus.

and assuming that, in the gap, $\frac{\partial h}{\partial x} = 0$, this becomes

$$\frac{du}{dt} - f\frac{dy}{dt} = 0, \tag{22}$$

or

$$\frac{d}{dt}(u - fy) \equiv 0. \tag{23}$$

The velocity and depth can be found as in case 1, using equation (23) in place of equation (14). It is found that the transport through the gap T_3 is 0.4 times that of the transport upstream T_1.

3.2.1 Laboratory and Numerical Experiments

To examine the validity of the theory, a set of laboratory experiments were performed. The apparatus and flow pattern is illustrated in Figure 5. The light fluid penetrates into the outer basin upon removal of the gate. After a short time, a current is established in region 2. Kelvin waves reach region 2 by propagating along the boundary in a counterclockwise manner.

Numerical experiments were also performed and a comparison between the analytical (straight black lines) and numerical solution for the gap problem is shown in Figure 6.

3.3 Case 3

Now we relax the condition of zero depth in the outer basin so that the level in the inner basin is higer than that of the outer basin by an amount

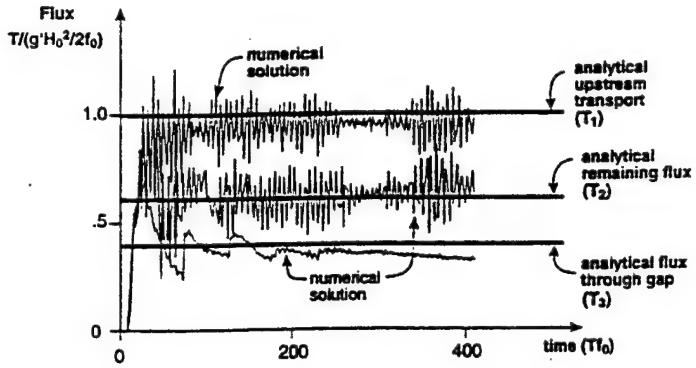

Figure 6: A comparison between the analytical and numerical solution for the rotating gap problem.

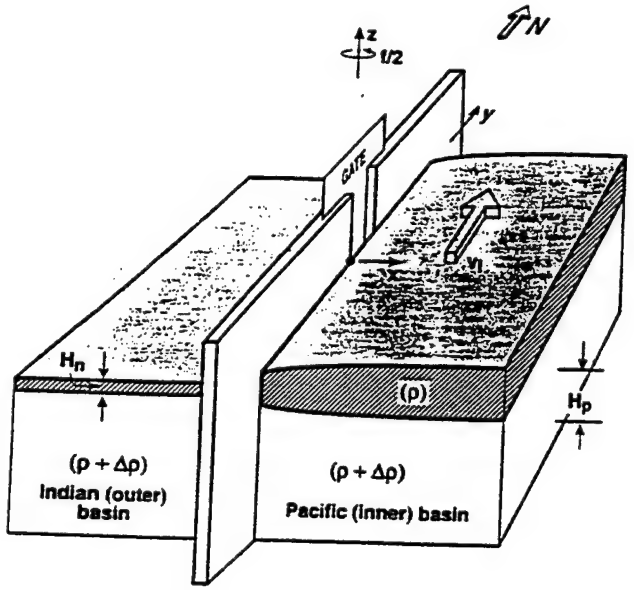

Figure 7: A schematic three dimensional view of the initial geometry for case 3.

$(H_p - H_n)\frac{\Delta\rho}{\rho}$, as shown in Figure 7. This difference is set up by the wind field. Again, the gap width is much greater than the Rossby radius of deformation. In this case, we allow Kelvin waves to propagate in all regions. The exchange process has two modes as illustrated in Figure 8. The first mode corresponds to the situation in which $H_p > H_n$ and the depth of the current near the wall is also greater than H_n. Under these conditions, the throughflow originates from the southern part of the inner basin and moves into the northern part of the outer basin. In the second mode, $H_p < H_n$, but the depth of the current near the wall in the inner basin is still larger than H_n. In this case, the throughflow originates in the northern part of the inner basin and penetrates into the southern part of the outer basin.

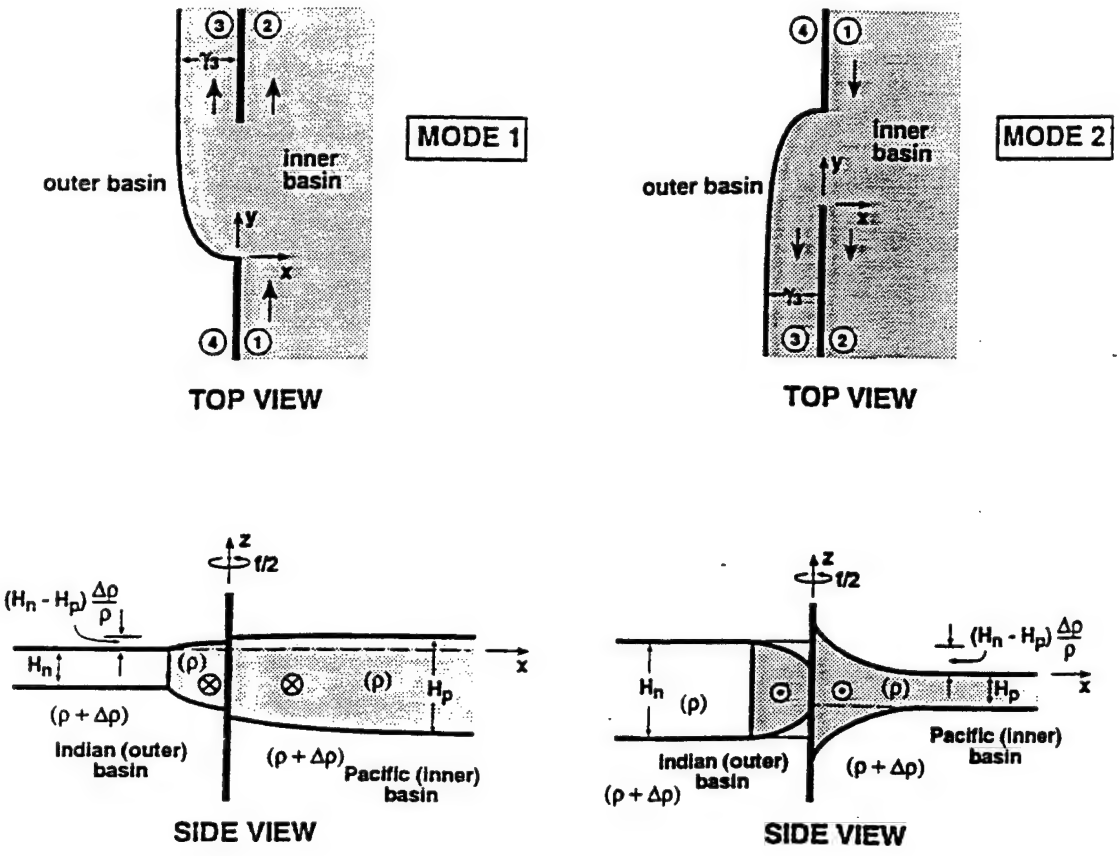

Figure 8: A schematic diagram for modes 1 and 2 in case 3.

References

[1] NOF, D. 1995 Choked flows from the Pacific to the Indian Ocean. *J. Physical Oceanog.* **25** 1369-1383.

[2] NOF, D. 1995 Choked flows and wind-driven interbasin exchange. *J. Marine Res.* **53** 23-48.

Inter-basin Exchange Through Broad Channels and Gaps, Part II

Lecturer: Doron Nof

Notes by: Jon Xinzhong Chen

1 The case with U turn

In the north hemisphere, when land is to the right looking downstream of a coastal current, flow into a gap will turn back after separating from the wall(see fig.1,2,3). The cause of the separation may be a vanishing wind stress curl over the ocean interior. In order to balance the momentum , eddies must be generated.

In the following, first we show that for U turn flow, the momentum is not in balance if there is no eddy generated; then we introduce the flow-force balance equation when eddy generation is considered; finally, we calculate the size and the generation period.

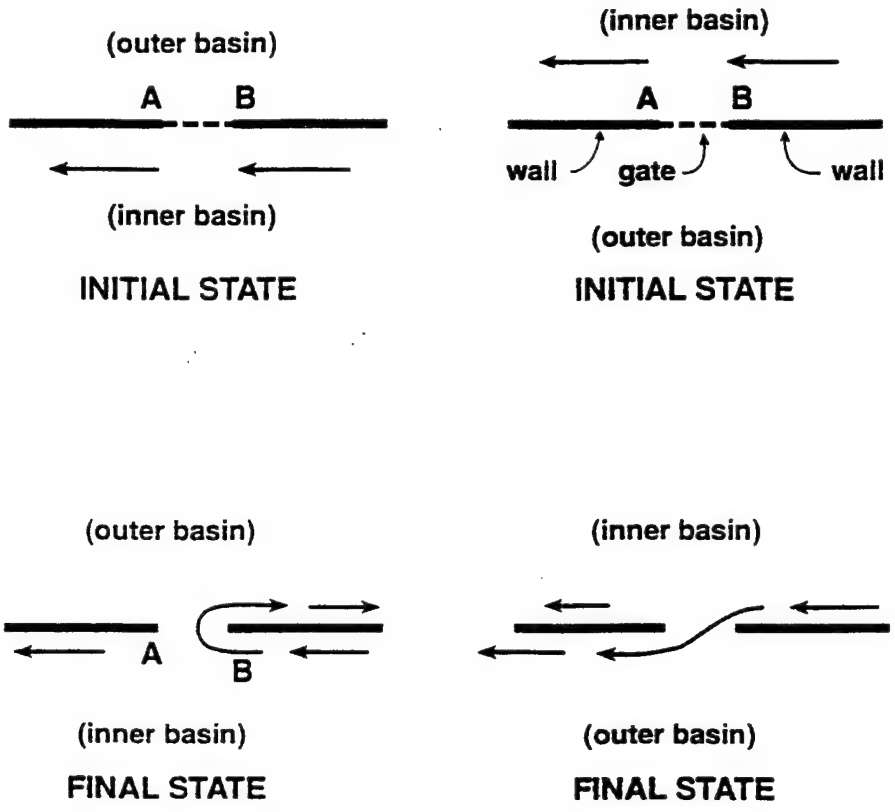

Fig.1, Schematic diagram for the two cases(the flows with U turn and without U turn)

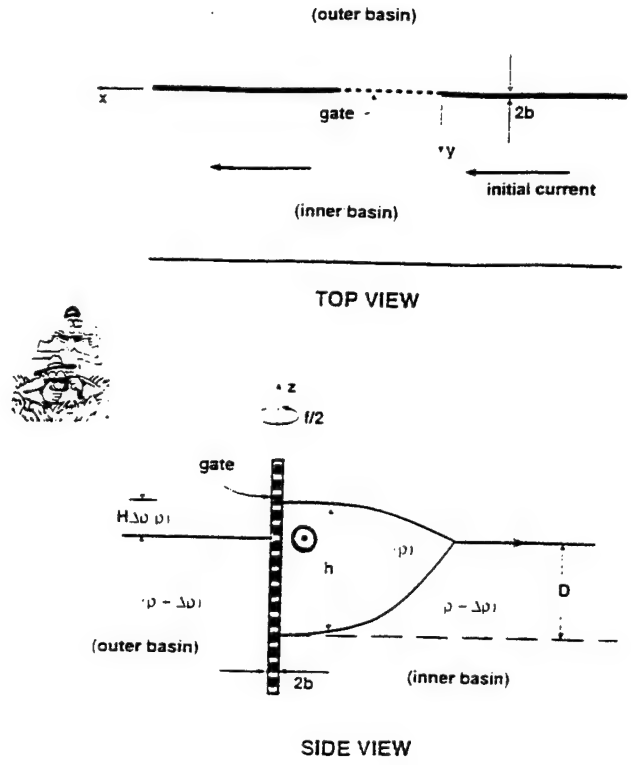

Fig.2, The initial state of the case with U turn.

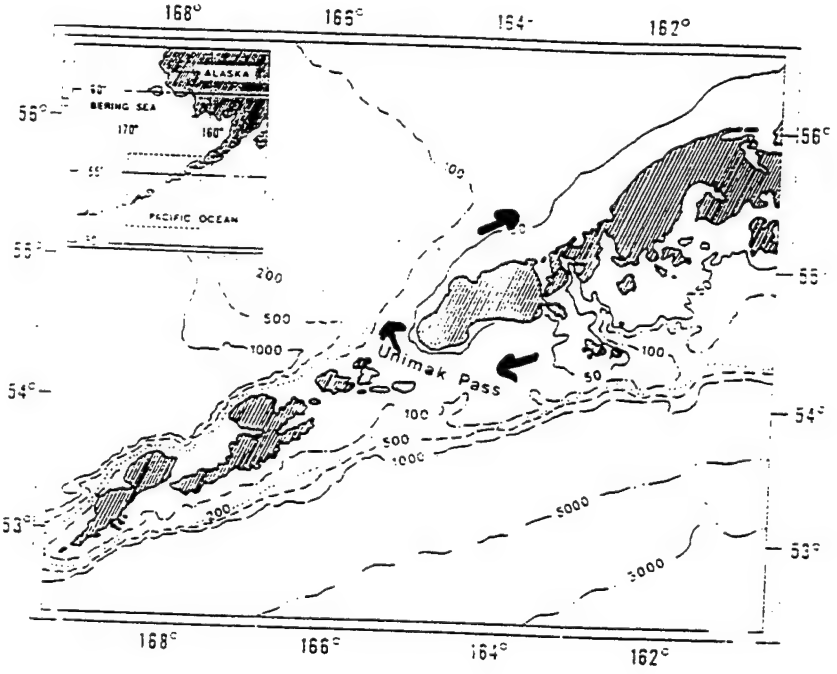

Fig.3, One example of flow with U turn.

1.1 Momentum balance without eddy generation

Suppose there is no eddy generation, then from fig.4, using continuity equation and stream function:

$$\psi_x = vh \tag{1}$$

$$\psi_y = -uh \tag{2}$$

Integrate momentum equation over the region bounded by ABCDEFG, we readily get the following relationship:

$$\int_0^L hu^2 dy + \beta \int_0^L (\int_y^L \psi dy) dy = 0 \tag{3}$$

where L is the combined width of the approaching and retroflecting current

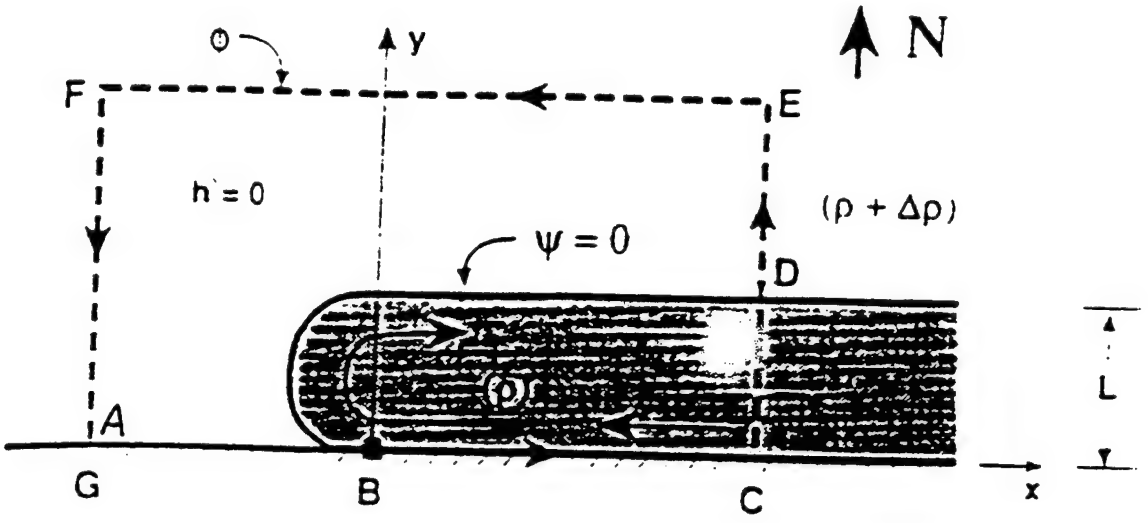

Fig.4 Schematic diagram of integrating boundary (without eddies)

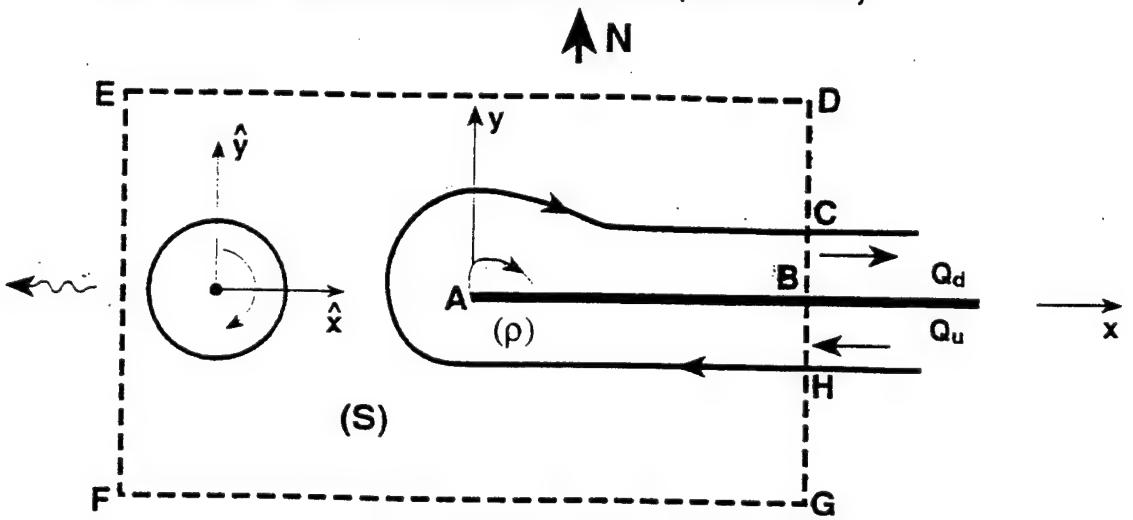

Fig.5 Schematic diagram of integrating boundary (with eddies)

It is easy to see the above condition cannot be satisfied because y and ψ are always positive along CD and the integration is done from small to large y. For most boundary currents, the second term is much smaller than the first term. The impossibility of satisfying this condition implies that there cannot be a steady state of the kind originally assumed because the integrated momentum imparted on the control volume cannot be balanced. The only way that the retroflected flow field can balance this momentum flux is by somehow creating a flow in the opposite direction. However, a light westward current with a finite cross section is impossible without a wall on the north side against which it can lean. We shall see that the balance can only be achieved by the generation of anticyclonic eddies, which propagate to the left due to β.

1.2 Momentum balance with eddy generation

Assuming T is the period of the eddy generation, the integrating area is shown in fig.5, then if we integrate the time-dependent x momentum equation(multiplied by h) and continuity equation(multiplied by u) from 0 to T over S region and add them together, we shall find the following equation:

$$\int_0^T \int_F^E (hu^2 + g'h^2/2)dydt - \int_F^E f\bar{\psi}dy = T\int_H^C (hu^2 - f\bar{\psi} + g'h^2/2)dy \qquad (4)$$

where,

$\bar{\psi}_y = -\int_0^T hudt$; $\bar{\psi}_x = \int_0^T hvdt$;

$\bar{\psi}$ is so-called time-integrated stream function, which is different from steady stream function ψ.

The above equation is our desired flow-force balance. Combined with time averaged continuity equation and potential vorticity equation, this equation will give us a closed system.

In an analogy to a rocket and spinning sprinkler, the right-hand side corresponds to the flow force exerted on the domain by the water entering and exiting on the right, the flow force is not balanced unless eddies are shed on the left. The term on the left-hand side corresponds to the flow force exerted by the eddies moving to the left out of the domain.

1.3 The size, migration rate of the eddy

Assume migration rate of eddies is C , using the following moving coordinate transformation(fig.6):

$dt = d\hat{t}$
$dy = d\hat{y}$
$dx = d\hat{x} + Cd\hat{t}$

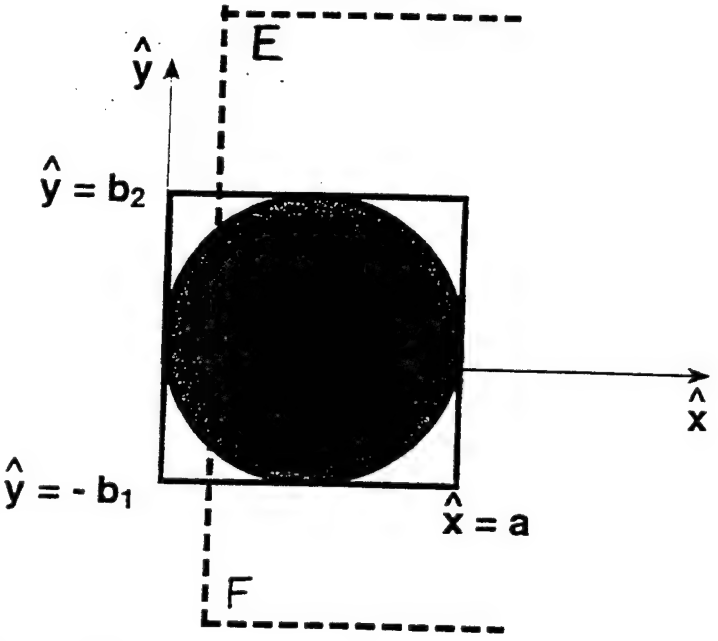

Fig.6, Transformation coordinate system for the eddy

After some manipulation, the flow-force balance equation is reduced to the following equation:

$$-c\int_{-\hat{b}_1}^{\hat{b}_2}\int_0^a h d\hat{x}d\hat{y} + \int_{-\hat{b}_1}^{\hat{b}_2}[f\int_{\hat{y}}^{\hat{b}_2}(\int_0^a h d\hat{x})d\hat{y}]d\hat{y} + \int_{-L_s}^0 f\int_{-\hat{b}_1}^{\hat{b}_2}(\int_0^a h d\hat{x})d\hat{y}d\hat{y}$$
$$= T\int_{-L_s}^{L_4} hu^2 dy + \beta T[-\int_{-L_s}^0\int_{-L_s}^y \psi dy dy + \int_0^{L_4}\int_y^{L_4}\psi dy dy] \quad (5)$$

The eddy scale is about $R_d/\epsilon^{1/6}$ with
$\epsilon \equiv \beta R_d/f_0$
We use expansion in $\epsilon^{1/6}$, set
$h = h^{(0)} + \epsilon^{1/6}h^{(1)} + \ldots$
where $R_d = (g'H)^{1/2}/f_0$.
finally, we get:
The radius of the eddy is:

$$R = \frac{2^{7/4}}{(5\pi)^{1/6}}\frac{R_d}{\epsilon^{1/6}} \quad (6)$$

The period is:

$$T = \frac{24(5\pi)^{1/6}}{2^{7/4}f_0\epsilon^{1/6}} \quad (7)$$

Both numerical simulation (fig.7) and experiment(fig.8) have confirmed this eddy formation mechanism.

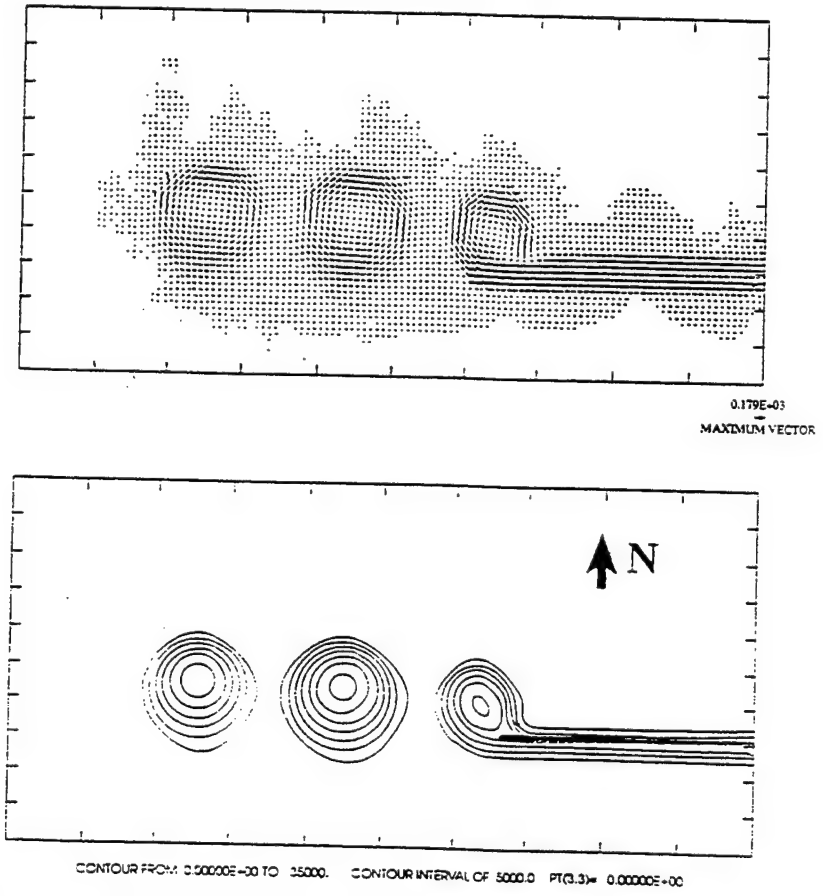

Fig.7, Numerical simulation of the generation of eddies.

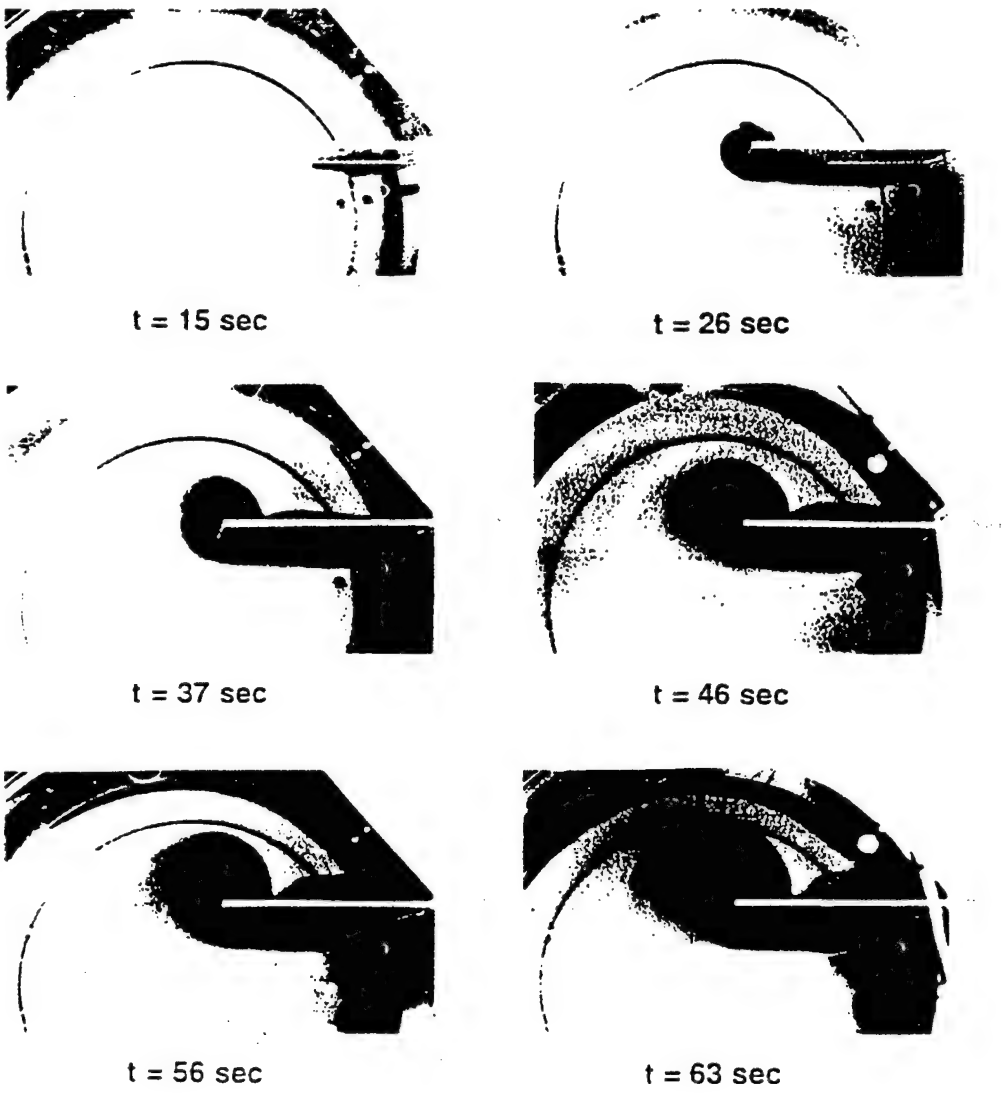

Fig.8, Experiment on the generation of eddies.

2 Island Rule

Suppose there is an island ADEF, the parallel coast points to the north, which is our y direction here (fig.9), then the vertically integrated equations read:

$$-fv = -\frac{1}{2}g'(h^2)_x + \tau^x/\rho \tag{8}$$

$$fu = -\frac{1}{2}g'(h^2)_y - Rv \tag{9}$$

The continuity equation, $v_x + v_y = 0$

Applying the x component equation to boundary 1 and boundary 2 (see Fig. 9), respectively, we get the following equations:

$$-f_1 T = -\frac{1}{2}g'(h_C^2 - h_D^2) + \int_D^C \tau^x/\rho dx = \int_D^C \tau^x/\rho dx \tag{10}$$

$$-f_2 T = -\frac{1}{2}g'(h_B^2 - h_A^2) + \int_A^B \frac{\tau^x}{\rho} dx = \int_A^B \frac{\tau^x}{\rho} dx \tag{11}$$

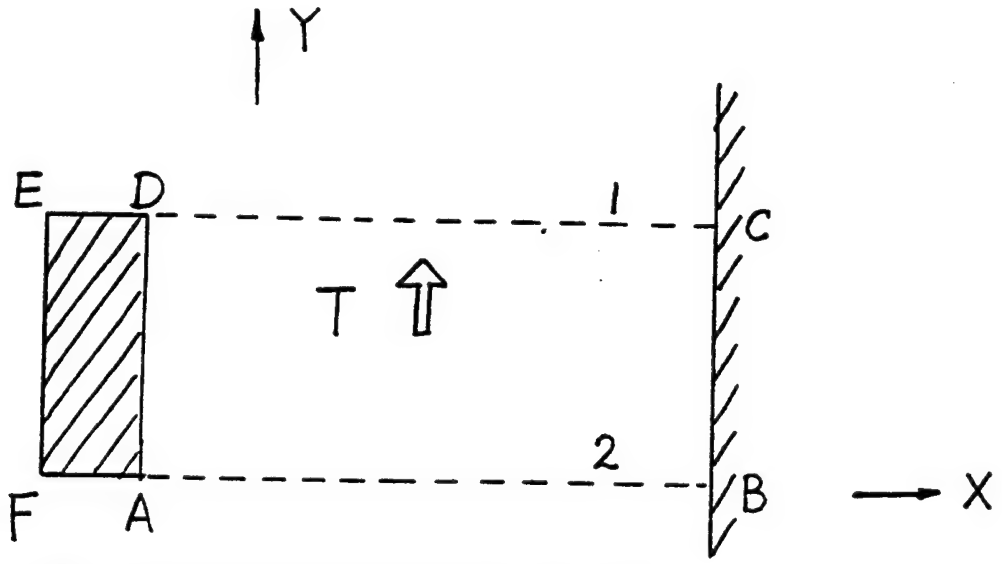

Fig.9, Schematic diagram of boundary in deriving island rule.

Along eastern boundaries, we have $\frac{\partial h}{\partial y} = 0$. So $h_C = h_B$ and $h_E = h_F$.
For "skinny" islands, $h_E = h_D$ and $h_F = h_A$.
Substract (11) from (10) to get,

$$T = \frac{\oint(\tau^x/\rho)dx}{(f_1 - f_2)}, \tag{12}$$

where T is volume transport across the channel. This is so-called island rule.
Now apply this formula to the ocean between Australia and South American:
As can be seen from fig.10, for the north boundary, $f_1 = 0$, so we have the following two equations:

$$0 = \frac{g'}{2}\int_D^C (h^2)_x dx - \int_D^C (\frac{\tau^x}{\rho})dx, \tag{13}$$

$$f_2 T_\omega = \frac{g'}{2}\int_A^B (h^2)_x dx - \int_A^B (\frac{\tau^x}{\rho})dx, \tag{14}$$

Then we get the transport is :

$$T_\omega = -\frac{1}{f_2}\oint \frac{\tau^x dx}{\rho}. \tag{15}$$

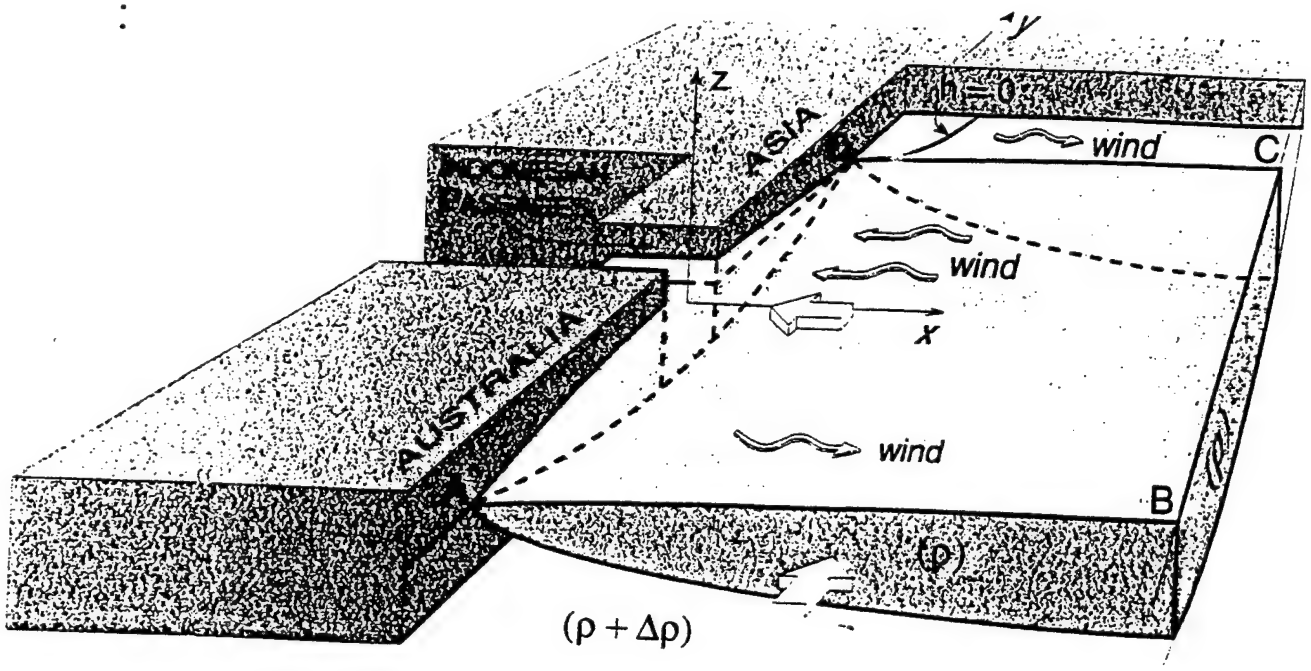

Fig.10, Schematic diagram of applying island rule to the ocean between Australia and South America.

From fig.10, it is easy to see that the right-hand side integral along the boundaries will be zero, then we get zero transport. This suggests us to add upwelling as Goldsbrough (1933) did,

$$v_x + v_y - \omega = 0 \tag{16}$$

then the transport will be:

$$T_{ind} = -\frac{1}{f_2}\oint \frac{\tau^l}{\rho} dl + \int\int \omega dx dy. \tag{17}$$

References

Nof,D. 1995: Choked flows from the Pacific to the India Ocean.J. Physical Oceanog.25 1369-1383.
Nof,D.1995 Choked flows and wind-driven interbasin exchange. J.Marine Res.53 23-48.
Nof,D. and T. Pichevin. 1996: The retroflection Paradox. . J. Physical Oceanog. 26 2344-2358.

Rotating channel exchange. Experiments and numerics.

Dan Ohlsen, Lecture 9.

Notes by: Annalisa Bracco

The problem of two layer exchange flow is investigated for the nonrotating case with or without friction or mixing as well the rotating case with and without friction.

1. Nonrotating inviscid Theory

A simplified model is used to investigate the transport between two basins connected by a channel assuming that the two-layer flow is steady, inviscid and there is not planetary rotation.

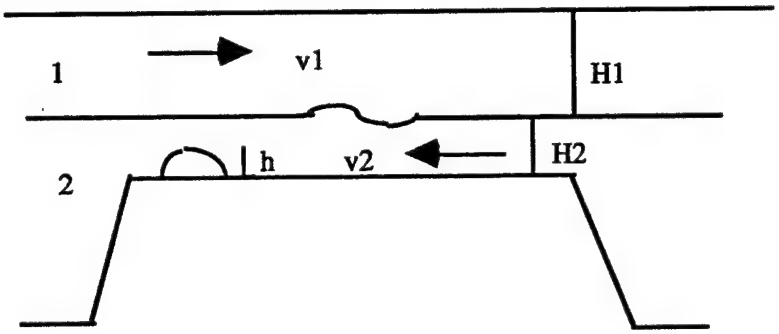

Figure 1 Section of the channel with two-layer flow.

The density of the light upper layer and the density of the dense lower layer are such that:

$$\rho_1 \leq \rho_2$$
$$\Delta\rho = \rho_2 - \rho_1 << \overline{\rho} \qquad (1.1)$$

where $\overline{\rho}$ is the average density. The condition for the Boussinesq approximation is satisfied, and guarantees that the location of the critical section in both layers is the same. We shall examine the response of the steady, linearized, long-wave interface to small variations in bottom topography. The interface deviation is denoted by η.
The velocity perturbation thus becames:

$$v_1' = \frac{v_1 \eta}{H_1}$$

$$v_2' = \frac{v_2 (h - \eta)}{H_2} \tag{1.2}$$

The linearized momentum equation along the y-axis

$$v \frac{\partial v}{\partial y} = -\frac{1}{\rho} \frac{\partial P}{\partial y} \tag{1.3}$$

using (1.2) gives:

$$\frac{\partial P_1}{\partial y} = -\rho_1 \frac{v_1^2}{H_1} \frac{\partial \eta}{\partial y}$$

$$\frac{\partial P_2}{\partial y} = -\rho_2 \frac{v_2^2}{H_2} \frac{\partial (h - \eta)}{\partial y} \tag{1.4}$$

Using the hydrostatic relation

$$\frac{\partial P_2}{\partial y} = \frac{\partial P_1}{\partial y} + g \Delta \rho \frac{\partial \eta}{\partial y} \tag{1.5}$$

and combining it with (1.4) we have:

$$\left[\rho_1 \frac{v_1^2}{H_1} + \rho_2 \frac{v_2^2}{H_2} - g \Delta \rho \right] \eta = h \rho_2 \frac{v_2^2}{H_2} \tag{1.6}$$

The critical flow occurs at the section where:

$$\frac{\rho_1 v_1^2}{g \Delta \rho H_1} + \frac{\rho_2}{g \Delta \rho} \frac{v_2^2}{H_2} = \frac{v_1^2}{g' H_1} + \frac{v_2^2}{g' H_2} = 1 = F^2 \tag{1.7}$$

F is the interfacial Froude number and g' is the gravitation acceleration reduced in proportion to the density difference across the interface.

In the simplest case $H_1 = H_2 = H$ so $v_1 = -v_2 = \frac{\Delta v}{2}$ and the relation:

$$F^2 = \frac{(\Delta v)^2}{2 g' H} = 1 \tag{1.8}$$

allows us to calculate the maximum value for the velocity Δv and the maximum rate of flow Q

$$Q = \int\int v dx dz$$

in the channel as

$$Q_{max} = \frac{\Delta v}{2} HL = \frac{1}{\sqrt{2}} H^{\frac{3}{2}} g'^{\frac{1}{2}} L \qquad (1.9)$$

where L is the length of the channel.

The application of this model of exchange flow which is probably studied the most is the Strait of Gibraltar. An outflow of dense, salty Mediterranean water formed by excess of evaporation, flows through the strait and is compensated by the light inflowing Atlantic surface water. Naturally, there are additional complications into actual region. The effect of tides is important and the maximal net exchange is achieved during some period of the tidal cycle.

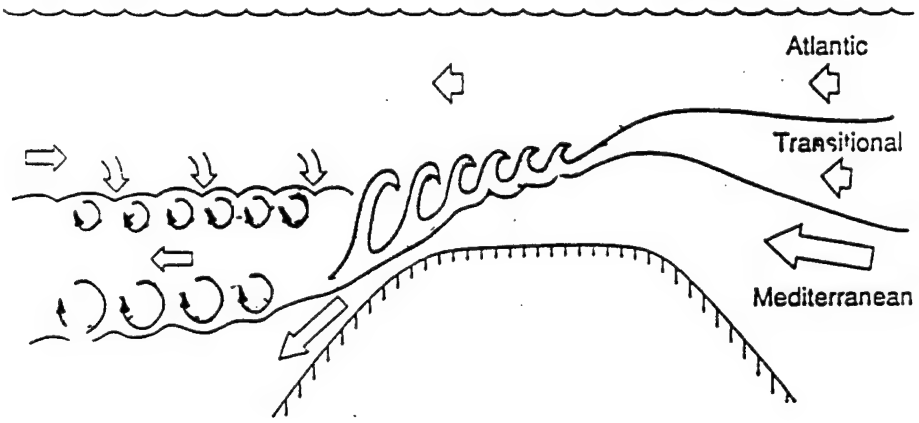

Figure 2 Section of the channel with outflow during neap tides.

In addition shear has to be taken into account (see section 2). It produces a 3-dimensional mixing which has an effect on the density of the outflow.

2. Nonrotating frictional theory

The geometry to be considered is the same horizontal two-layer channel aligned in the x-direction as before without rotation, but with a stratified laminar flow, where the shear instability generates Kelvin-Helmholtz short-waves and turbulence mixing at late time. The Reynolds number is not large, so viscosity may tend to limit the intensity of the turbulence. The Richardson number takes the form:

$$R_i = -\frac{\frac{g}{\rho}\frac{\partial \rho}{\partial z}}{\left(\frac{\partial v}{\partial z}\right)^2} \tag{2.1}$$

In a stratified laminar flow, the traditional $R_i = 1/4$ is expected. There is also some evidence that in the atmosphere turbulence decays for $R_i > \frac{1}{5}$.

In the ocean we expect both velocity and density profiles to have the same interfacial thickness since the flow is turbulent.
So if we define:

$$l = \frac{\Delta \rho}{\left(\frac{\partial \rho}{\partial z}\right)_{max}}; \qquad l_v = \frac{\Delta v}{\left(\frac{\partial v}{\partial z}\right)_{max}}$$

then

$$l \approx l_v \tag{2.2}$$

In this case the Richardson number becomes:

$$R_i = \frac{gl}{(\Delta v)^2}\frac{\Delta \rho}{\rho} = \frac{1}{2H}\frac{1}{F^2} \tag{2.3}$$

The volume flux compared to the previous section is reduced by the shear:

$$Q_R = Q\left(1 - \frac{1}{4H}\right) = Q\left(1 - \frac{R_i F^2}{2}\right) \tag{2.4}$$

where

$$\frac{5}{6} \le \left(1 - \frac{R_i F^2}{2}\right) \le \frac{9}{10}$$

for R_i =0.2 to 0.3.

3. Inviscid rotating theory

A theory for inviscid rotating hydraulic two-layer exchange flow which is steady, hydrostatically driven and geostrophic, was developed by Whitehead, Leetmaa and Knox in 1974.In the limit of zero potential vorticity upstream ($\frac{\partial v}{\partial x} = -f$) for two-layer the integrated equations become:

$$\begin{aligned} v_1 &= -fx + c_1 \\ v_2 &= -fx + c_2 \end{aligned} \tag{3.1}$$

where c_1 and c_2 are integration constants and f is the Coriolis parameter. The velocity profile across the channel is linear and the shear is invariant with respect to x.

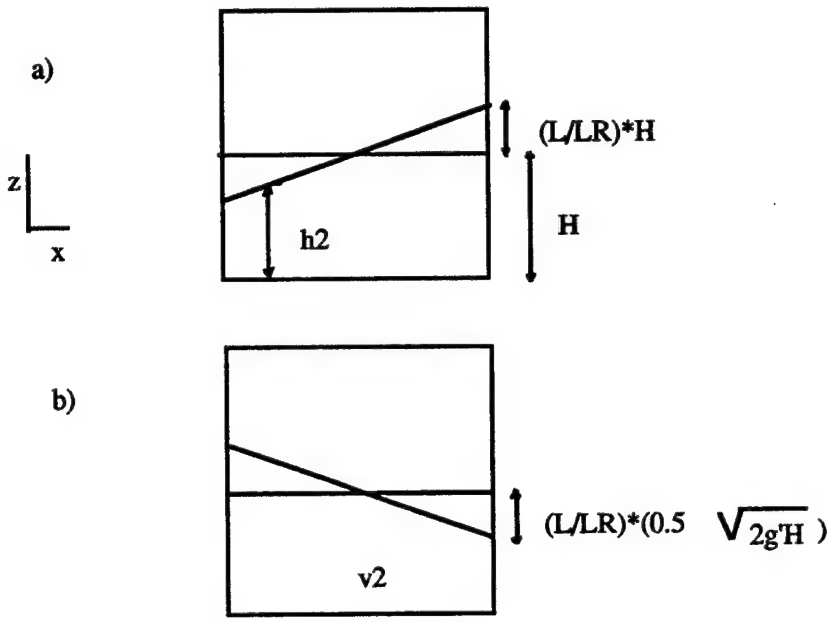

Figure 3 a) Cross section of rotating channel.
b) Velocity cross section.

Using the thermal wind equation

$$f(v_2 - v_1) = g' \frac{\partial h_2}{\partial x} \tag{3.2}$$

we obtain

$$h_2 = \frac{f(c_2 - c_1)}{g'} x + D \tag{3.3}$$

which expresses a linear height change. Assuming $\Delta\rho << \overline{\rho}$ the volume continuity equation can be applied. The integration constant D thus becomes:

$$D = -\frac{Hc_1}{c_2 - c_1}. \tag{3.4}$$

Finally the Bernoulli energy equation for $F^2 = \frac{(\Delta v)^2}{2g'H} = 1$ gives

$$c_2 - c_1 = \sqrt{2g'H} \tag{3.5}$$

and assuming the maximum volume transport $Q = Q_{max}$, c_2 is determinated by

$$c_2 = \frac{1}{2}\sqrt{2g'H} \tag{3.6}$$

The equation (3.3) becomes

$$h_2 = f\sqrt{2H/g'} \cdot x + H \tag{3.7}$$

and using the expression for the Rossby radius

$$L_R = \frac{\sqrt{2g'H}}{f}$$

we obtain

$$h_2 = H\left(1 + \frac{2x}{L_R}\right)$$

and (3.8)

$$v_2 = \frac{1}{2}\sqrt{2g'H}\left(1 - \frac{2x}{l_R}\right)$$

For an attached flow $(L_R > L)$ the volume transport Q in the bottom layer is

$$Q = \int_{-L/2}^{L/2} v_2 h_2 dx = \frac{1}{2}\sqrt{2g'H} \cdot LH\left[1 - \frac{1}{3}\frac{L^2}{L_R^2}\right] \tag{3.9}$$

If $L_R \leq L$ (separated flow) Q can be required to be continous at $L_R = L$ and

$$Q = \frac{2}{3}\frac{g'H^2}{f}. \tag{3.10}$$

The inviscid rotating hydraulic control theory applies to the strong steady outflow of Arctic Intermediate and Norwegian Sea Deep Water into the Atlantic through the Faroe Bank Channel.
For this flow the internal Rossby radius of deformation L_R is about the same size as the channel width and the internal Rossby number approches 1, thus the effects of rotation are important.

The theory in the approximation of a motionless upper layer allows a resonable prediction of the measured transport.
A regional hydrographic survey reveals considerable mixing along the channel, resulting in downstream changes of water properties.
Vertical density and velocity profiles in the center of the sill indicate that the outflow and the inflow mix at the pycnocline that separates them. The isopycnals are spreaded out on the shallow side and sharpened on the deep side.
To explain the observations Johnson and Sanford (1992) suggest that the cross-stream Ekman flow in the inflow on the deep side at the channel wall and at the bottom in the inflow meet at the pycnocline and then flow out into the interior.

a)

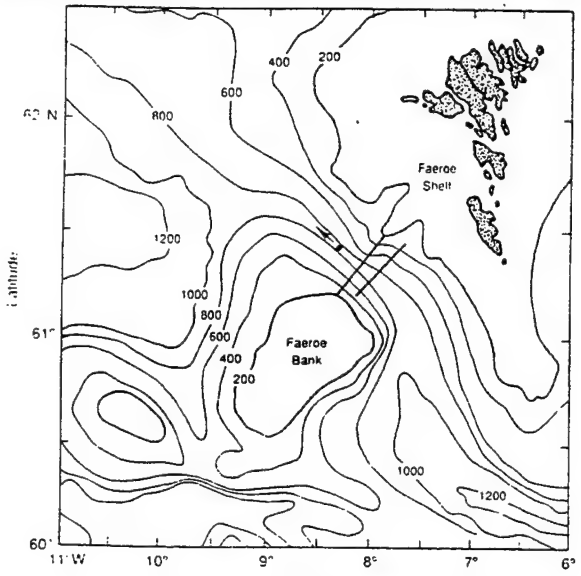

b)

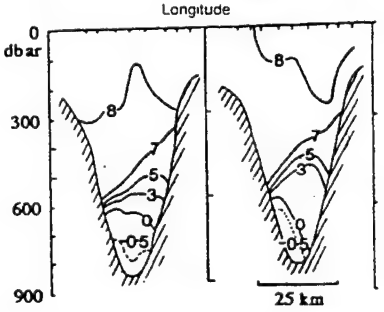

Figure 4 a) The bathymetry of the Faroe Bank Channel. The straigh line closest to the arrows gives the location of the section profiles in panel b).
b) Section profile of potential temperature. The isotherms spread to the northeast, probably owing mixing through shear instabilities. The outflow velocities increases toward bottom.

There is an analogous situation in the South Atlantic through the Vema Channel, where Lower Circumpolar Deep Water flows northward.
The calculation of the rate of transport through this channel from inviscid rotating reduced-gravity theory overestimates the observed transport. Significant friction at the bottom and mixing at the pycnocline is invoked to explain the observation data.

4. Frictionally modified rotating experiment

In predictions and experiments, friction and rotation together limit exchange more than both cases considered separately. In the ocean exchanges are generally overpredicted , so friction is needed. Here an existing and complete theory for rotating frictional two-layer exchange is adapted to a laboratory experiment.
The experimental apparatus consists of a tank, of approximately 120 cm long, 30 cm in wide and 40 cm high, partitioned in the middle by a vertical dam.

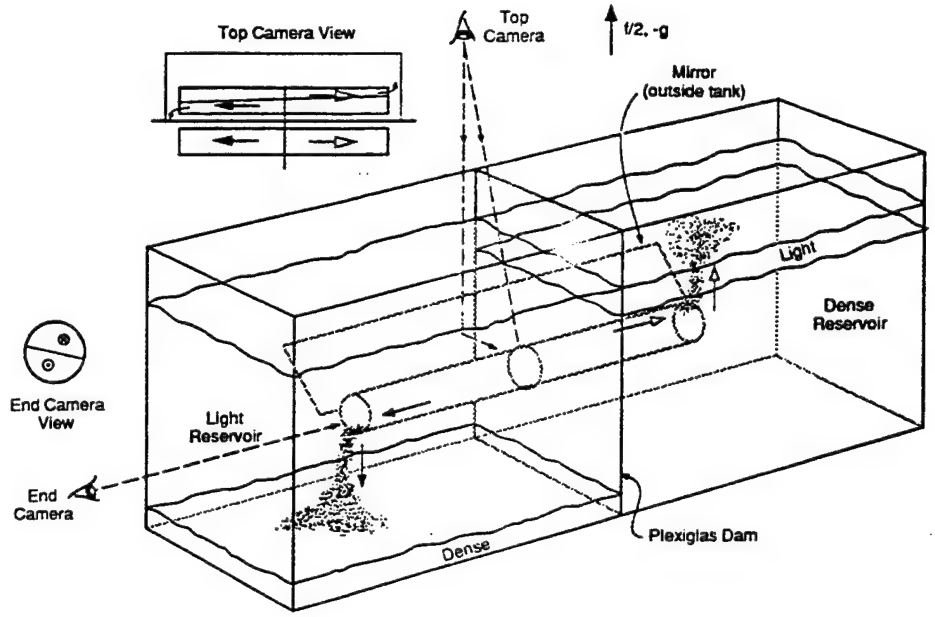

Figure 5 Experiment schematic. The dense outflow (solid arrows) flows over the tube bottom into the light water reservoir. The light inflow (open arrows) flows through the upper part and enters the dense water reservoir.

The two reservoirs are connected by a channel of circular section located at mid-depth, and the tank is centered on a rotating table at a constant rate. Fluids of different densities (different salinity, same temperature) are separated by the dam at the start of experiment.
When the channel is opened the dense outflow moves inside the lower portion of the tube toward the light water. The inflow flows in the opposite direction inside the upper part of the tube. Vertical profiles of salinity are measurated throughout the run so that the experiment could be stopped before the fluids, entering each reservoir, fill them to such level that flow back reentering the tube toward their original reservoirs.
The internal Rossby radius of deformation is about the tube diameter.
The tube diameter, the Coriolis parameter and the density difference between the inflow and the outflow are such that the Rossby number is near unity and assuming that the exchange is subject to hydraulic control, the Froude number approches unity too.

This configuration is intended to represent straits such as the Faroe Bank and Vema Channel discussed before including friction. The experiment shows Ekman layers are appended to the top and bottom of each layer of the channel and thick Stewartson layers to their sides. These Ekman layers drive a cross channel secondary circulation. This secondary cross-channel circulation reduces exchange by moving fluid that is put down at the boundaries and interface into the interior. The interface in the rotating experiment has a cross-channel tilt since the exchange is geostrophic to first order.
The flow is visualized injecting dyed water in various location in the inflow and in the outflow or using disodium fluorescein to reveal mixing between the fluids within the channel.

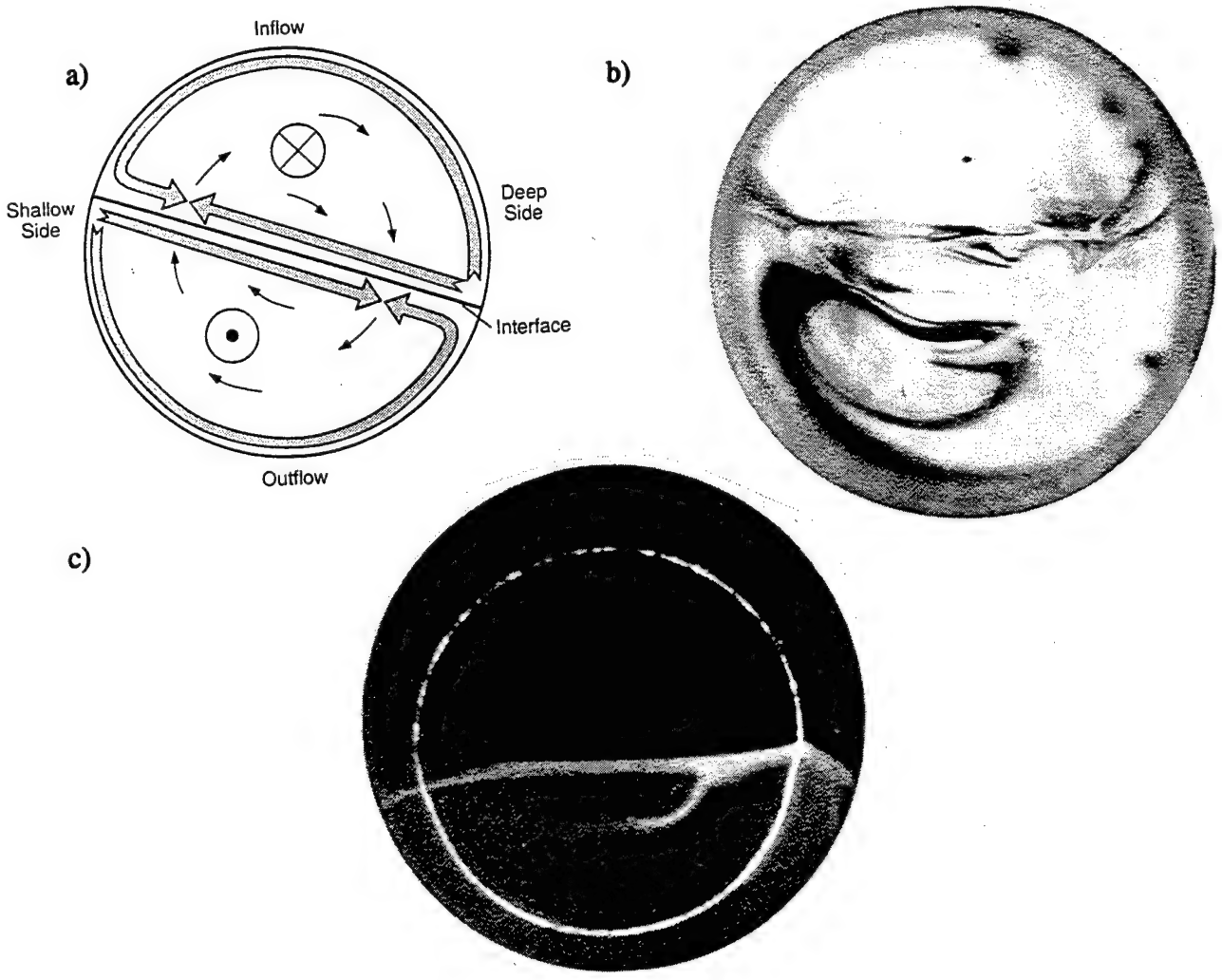

Figure 6 End views of the channel. The region - a) schematic, b) with dye streak, c) of fluorescence - shows mixing at the interface and reveals the presence of interfacial Ekman layers. The fluorescent tail extends down from the interface near the deep side and curls towards the shallow side marking the boundary between the secoundary circulation.
(Figure 6b viewed from the end opposite Figure 6a and 6c)

a) b)

Figure 7 Lateral section of the channel with fluorescein in the outflow for the nonrotatung (a) and rotating (b) case.

Finally the problem of a rotating frictional Hydraulic Channel Exchange is investigated using a numerical model with a $2\frac{1}{2}$ dimensional code and a finite-difference model.
The goal is to calculate velocity and density in the channel in the (y, z) plane for $\frac{\partial}{\partial x} \equiv 0$ except $\frac{\partial P}{\partial x} = -\frac{\Delta \rho g z}{L}$ (idrostatic pressure gradient).
The resolution of the simulation is 256*256 grid points.
The integrated equations are:

$$
\begin{aligned}
u_z + vu_y + wu_z - fu &= -\frac{P_x}{\rho_0} + \nu\left(u_{yy} + u_{zz}\right) \\
v_z + vv_y + wv_z + fu &= -\frac{P_y}{\rho_0} + \nu\left(v_{yy} + v_{zz}\right) \\
w_z + vw_y + ww_z &= -\frac{P_z}{\rho_0} + \nu\left(w_{yy} + w_{zz}\right) - g\frac{\Delta\rho}{\rho} \\
v_y + w_z &= 0 \\
\Delta\rho_t + v\Delta\rho_y + w\Delta\rho_z &= k\left(\Delta\rho_{yy} + \Delta\rho_{zz}\right)
\end{aligned}
\qquad (4.1)
$$

where ν and k are diffusive coefficients.

The cross-channel velocities shows clearly the separation of an Ekman layer at the interface and solid boundary Ekman layers at the top and the bottom of the channel.

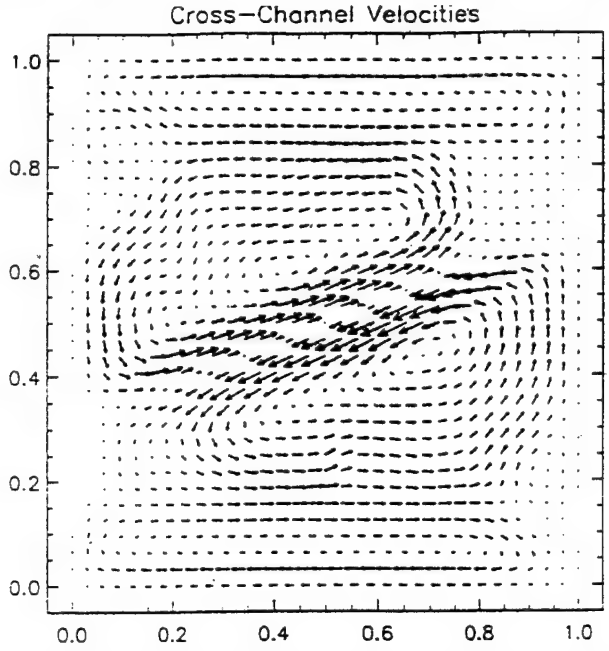

Figure 8 Cross-channel velocities for numerical simulations (256*256 grid points)

Two sets of experiments and simulations are done varing g' with a fix Coriolis parameter and varing f with fix g'.

It is possible evalue the rate Q/Q_{max} for different initial conditions.

Both experiment and simulations show that a realistic evaluation of the rate of the hydraulic exchange in a basin have to take into account friction and rotation. The secoundary circulation reduces the exchange by injecting water with retarded velocities out from the boundary into the interior.

References

Anati, D. A., Assaf, G. & Thompson, R. O. Ry. 1977 Laboratory models of sea straits. *J. Fluid Mech.*, **81**, 341 - 351

Hart, J. E., 1971 Instability and secoundary motion in a rotating channel flow. *J. Fluid Mech.*, **45**, 341 - 351

Johnson, D. A., McDowell, S. E., Sullivan, L. G. & Biscaye, P. E. 1976 Abyssal hydrography, nephelometry, currents and benthic boundary layer structure in the Vema Channel. *J. Geoph. Res.*, **81**, 5771 - 5786

Johnson, D. A. & Ohlsen, D. R. 1994 Frictionally modified rotating hydraulic channel exchange and ocean outflows. *J. Phys. Oceanog.*, **24**, 66 - 78

Johnson, D. A. & Sanford, T. B. 1992 Secoundary circulation in the Faroe Bank Channel outflow. *J. Phys. Oceanog.*, **22**, 927 - 933

Sauders, P. M., 1990 Cold outflow from the Faroe Bank Channel. *J. Phys. Oceanog.*, **20**, 29 - 43

Stommel, H. & Farmer, H. 1952 Abrupt change in width in two-layer open channel flow. *J. Mar. Res.*, **11**, 205 - 214

Bounding Rotating Hydraulic Flows

Peter Killworth

Notes by: *Chris Hills & Jeff Parsons*

The fluid flow across a sill is a very frequently occuring natural phenomenon. Within a single ocean there may be several hundred topographical sills. The flow of fluid (*e.g.* sea water) across one of these sills is a well studied problem and can be treated in a variety of ways. A frequent assumption used to simplify these approaches is that of zero (or constant) potential vorticity. However, this has the in-built assumption that $v_x \sim f$ or, in other words $\Delta v \sim Lf$ where v, f are the usual velocity and angular velocity and L is some length scale. We shall consider the flows over sills in a far more general context allowing us to deal more realistically with the speeds involved in oceanographic flows and demonstrate that we may construct bounds for these flows and that the bounds are attained. It is fundamental that the bounds we create and the flows which attain them are hydraulically controlled!

To begin with we shall consider the maximum bound for the flow over a sill as a function of the upstream energy, $\mathcal{E}$. Our geometry is as shown in figure 1, where $d(x,y)$ is the height of the sill, $h(x,y)$ the depth of fluid, u and v the cross- and down-stream velocities associated with the directions x and y.

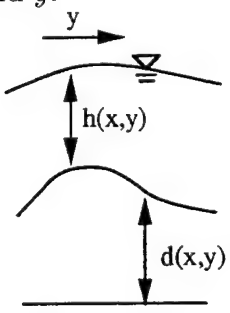

Figure 1.

We take all quantities to vary *slowly* along the sill and use the assumptions of semi-geostrophy,

$$v \gg u, \qquad \partial/\partial x \gg \partial/\partial y, \qquad u\partial/\partial x \sim v\partial/\partial y. \tag{1}$$

Using (1), the equations of motion become,

$$\begin{aligned} -fv &= -g'(h+d)_x, \\ uv_x + vv_y + fu &= -g'(h+d)_y, \end{aligned} \tag{2}$$

where g' is the relative gravity for our $1\frac{1}{2}$-layer model. From these equations we see that

we may define the standard 'stream function' ψ, and potential function ϕ so that,

$$uh = -\psi_y, \qquad vh = \psi_x,$$
$$\phi = h + d. \tag{3}$$

The first integral gives a familiar energy equation,

$$\tfrac{1}{2}v^2 + g'\phi = B(\psi), \tag{4}$$

and potential vorticity,

$$q = \frac{f + v_x}{h} = B'(\psi) \geq 0. \tag{5}$$

To obtain our upper bound we use the fact that the energy is usually a designate of the flow – if we continually increase the energy the flow increases unboundedly. Therefore we define,

$$\mathcal{E} = \max_x \left\{ g'(h_\infty + d_\infty) + \tfrac{1}{2}v_\infty^2 \right\}, \tag{6}$$

where the subscript ∞ indicates far upstream and the maximum is taken over the cross-stream direction. Then we find that B is bounded by the equation,

$$g' d_{\min} \leq B(\psi) \leq \mathcal{E}, \tag{7}$$

so that

$$d_{\min} \leq \phi \leq \mathcal{E}/g', \tag{8}$$

where the subscript *min* indicates the minimum over the cross-stream width.
We now proceed to bound the flux $\mathcal{F}$ over a fixed cross-section (see figure 2). The fluid flux across a downstream position y is given by,

$$\mathcal{F} = \int_{x_0}^{x_1} hv\mathrm{d}x = \frac{g'}{f}\int_{x_0}^{x_1} (\phi - d)\phi_x \mathrm{d}x = \frac{g'}{f}\left\{ \tfrac{1}{2}\left(\phi_1^2 - \phi_0^2\right) - \int_{x_0}^{x_1} d\phi_x \mathrm{d}x \right\}. \tag{9}$$

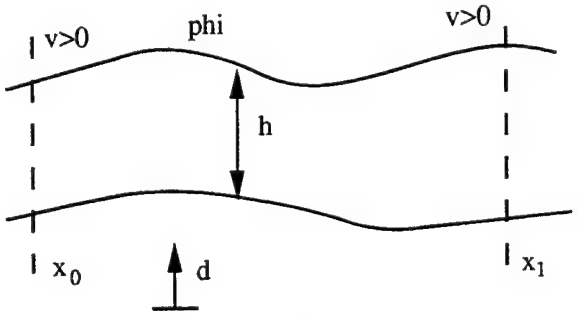

Figure 2.

An upper bound on this flux is found in the following manner. We alter the flow and contour in three stages: a) excise backflow at the ends, b) extend the flow to the left, and c) excise any internal maxima. By this procedure the flux is increased at each stage without changing the upstream conditions.

a) excise backflow at the ends

We move the points x_0, x_1 so that on the neighbouring height surface ϕ $(= h + d)$, $\phi_x > 0$. This trivially makes $v > 0$ and therefore increases the flux to $\mathcal{F}' > \mathcal{F}$.

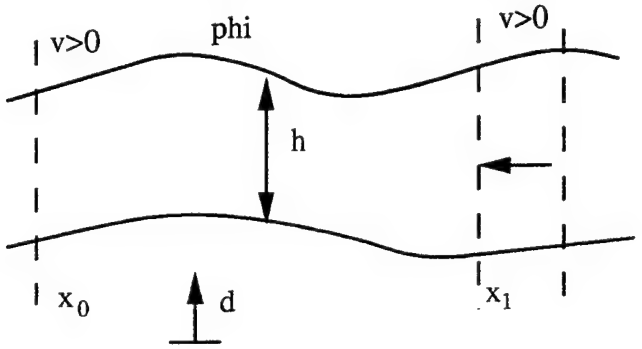

Figure 3.

b) extend the flow to the left

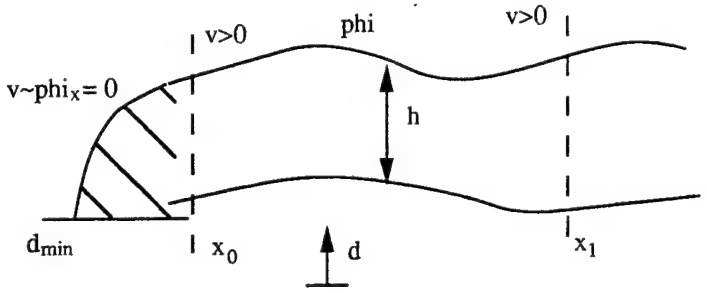

Figure 4.

We have included an additional positive flux – $\mathcal{F}'' > \mathcal{F}'$.

c) excise internal maxima

We remove the maxima of the function ϕ in the manner shown in figure 5.

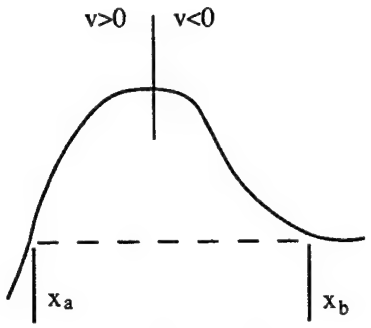

Figure 5.

Modifying ϕ in this manner gives,

$$\begin{aligned} g'\phi_b &= B(\psi_b), \\ \tfrac{1}{2}v_a^2 + g'\phi_a &= B(\psi_a), \qquad (\phi_b = \phi_a), \\ B(\psi_a) - B(\psi_b) &= \tfrac{1}{2}v_a^2 > 0, \\ B'(\psi) \geq 0 \quad &\Longrightarrow \quad \psi_a - \psi_b > 0, \\ \mathcal{F}''' &> \mathcal{F}''. \end{aligned} \tag{10}$$

Thus, by construction we have found that $\mathcal{F}$ may be bounded by,

$$\begin{aligned} \mathcal{F} &\leq \frac{g'}{f}\left\{\tfrac{1}{2}\left(\phi_1^2 - \phi_0^2\right) - d_{\min}(\phi_1 - \phi_0)\right\}, \\ &= \frac{g'}{f}(\phi_1 - \phi_0)\left\{\tfrac{1}{2}(\phi_1 + \phi_0) - d_{\min}\right\}. \end{aligned} \tag{11}$$

We now maximise $\mathcal{F}$ with respect to ϕ_1. Taking the partial derivative with respect to ϕ_1 we find the maximum occurs when $\phi_1 = \mathcal{E}/g'$ and that,

$$\mathcal{F} \leq \frac{g'}{2f}\left(\mathcal{E}/g' - d_{\min}\right)^2. \tag{12}$$

Taking the approximation of $\mathcal{E} \sim g'(h_\infty + d_\infty)$ (*i.e.* the kinetic energy far upstream is negligible) we have,

$$\mathcal{F} \leq \frac{g'h_u^2}{2f}, \tag{13}$$

, where h_u is the difference between the maximum upstream surface height and the lowest point on the sill. This flux is known to be attainable in channel flow.
We now wish to investigate bounding flows for *particular* geometries. First we non-dimensionalise using $\mathcal{E}^{\frac{1}{2}}, f, g'$: *i.e.* $v \sim \mathcal{E}^{\frac{1}{2}}, x\&y \sim \mathcal{E}^{\frac{1}{2}}/f, h, d\&\phi \sim \mathcal{E}/g', \psi \sim \mathcal{E}^2/g'f$. We have the following relations,

$$v = \phi_x, \quad \tfrac{1}{2}v^2 + \phi = B(\psi), \quad (1 + v_x)/h = B'(\psi), \tag{14}$$

giving,

$$\phi_{xx} = -1 + \xi, \qquad \text{where} \quad \xi = hq \geq 0. \qquad (-\text{relative vorticity}) \tag{15}$$

To maximise the flux we again follow three distinct stages: a) remove left-hand backflow, b) remove right-hand backflow, and c) excise intermediate backflow. These processes are summarised in figure 6.

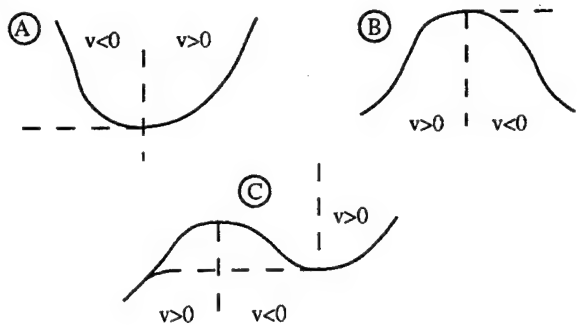

Figure 6.

We increase the flux at each stage in a similar manner to that described above, *e.g.* case C involves replacement of the existing flow with a combination of resting fluid and zero potential vorticity fluid (see Killworth [1]).

Assume now that our bottom topography is such that $\partial d/\partial x < 0$ for $x < x_{\min}$ and $\partial d/\partial x > 0$ for $x > x_{\min}$ and consider $\xi = \xi(x)$ as a function of $h(x)$ and $\psi(x)$. We define

$$\Pi(x) = \int_{x_b}^{x_a} (d - d_{\text{left}}) \mathrm{d}x. \tag{16}$$

Then for case A, $\Pi(x_a) = 0$ and $\Pi(x_a) < 0$ in case B; in general we may take $\Pi(x_a) \leq 0$. Note that x_a is determined by maximising $\mathcal{F}$ for a given ξ. We shall now take case A. Then,

$$\begin{gathered} \phi = 1, \quad \phi_x = 0 \qquad \text{at} \quad x_a, \\ \phi_{xx} = -1 + \xi, \\ \implies \quad \phi_x = -(x - x_a) + \eta, \quad \implies \phi = 1 - \tfrac{1}{2}(x - x_a)^2 + \zeta, \end{gathered} \tag{17}$$

, where

$$\eta = \int_{x_a}^{x} \xi(x') \mathrm{d}x' \leq 0, \qquad \zeta = \int_{x_a}^{x} \int_{x_a}^{x'} \xi(x'') \mathrm{d}x''. \tag{18}$$

Now consider perturbing x_a by a small amount, δ to $x_a + \delta$. then we have,

$$\begin{gathered} \mathcal{F} = \int_{x_b}^{x_a} \psi_x \mathrm{d}x = \int_{x_b}^{x_a} \phi_x (\phi - d) \mathrm{d}x, \\ \text{so} \qquad \delta\phi_{xx} = 0 \quad \implies \delta\phi_x = \text{constant}, \end{gathered} \tag{19}$$

where δk indicates the perturbation in a function k. We may now express the change in flux as follows,

$$\begin{aligned}
\delta\mathcal{F} &= \delta\left\{\int_{x_b}^{x_a}\phi_x(\phi-d)\mathrm{d}x\right\},\\
&= \int_{x_b}^{x_a}\left\{\delta\phi_x(\phi-d)+\phi_x\delta\phi\right\}\mathrm{d}x,\\
&= [\phi\delta\phi]_{x_a}^{x_b} - \delta\phi_x\int_{x_b}^{x_a} d\mathrm{d}x,\\
&= -d_b\delta\phi_b - \delta\phi_x\int_{x_b}^{x_a} d\mathrm{d}x, \qquad (19)
\end{aligned}$$

using that the upper end remains unchanged. But we also have, using the definition of x_a,

$$\delta\phi_b = -\int_{x_b}^{x_a}\delta\phi_x\mathrm{d}x, \qquad \text{and} \quad 0=\delta\phi_x\int_{x_b}^{x_a}(d-d_b)\mathrm{d}x \implies \Pi(x_a)=0. \qquad (20)$$

We have now determined x_a, and further consider $\xi\to\xi+\delta\xi$. This gives,

$$\begin{aligned}
\delta\phi_{xx} = \delta\xi, \qquad \delta\phi = \delta\phi_x = 0 \quad \text{at} \quad x = x_a,\\
[\delta\psi]_{x_b}^{x_a} &= \delta\left\{\int_{x_b}^{x_a}\phi_x(\phi-d)\mathrm{d}x\right\},\\
&= \left\{\int_{x_b}^{x_a}(\delta\phi_x(\phi-d)+\phi_x\delta\phi)\mathrm{d}x\right\},\\
&= [\phi\delta\phi]_{x_b}^{x_a} - \int_{x_b}^{x_a} d\delta\phi_x\mathrm{d}x,\\
&= -\phi_b\delta\phi_b - \int_{x_b}^{x_a} d\delta\phi_x\mathrm{d}x. \qquad (21)
\end{aligned}$$

But,

$$\phi_b = d_b, \qquad \text{and} \quad \delta\phi_b = \int_{x_b}^{x_a}\delta\phi_x\mathrm{d}x. \qquad (22)$$

So we have,

$$\begin{aligned}
[\delta\psi]_{x_b}^{x_a} &= \int_{x_b}^{x_a}(d_b-d)\delta\phi_x\mathrm{d}x,\\
&= -\int_{x_b}^{x_a}\Pi_x\delta\phi_x\mathrm{d}x = -[\Pi\delta\phi_x]_{x_b}^{x_a} + \int_{x_b}^{x_a}\Pi\delta\phi_{xx}\mathrm{d}x. \qquad (23)
\end{aligned}$$

The resulting change in flux is therefore found to be,

$$\delta\mathcal{F} = \int_{x_b}^{x_a} \Pi(x')\delta\xi(x')\mathrm{d}x'. \tag{24}$$

However, $\Pi(x_a) \leq 0$ and Π is increasing to x_a, thus $\Pi(x') < 0$. This implies that the maximum flux occurs when $\xi = 0$; *i.e.* at zero potential vorticity with possible areas of resting fluid (as in the excision treatment above).
Thus we have found the vorticity distribution which gives the maximum flux, $\mathcal{F}$. To compute this however is extremely difficult, except in the case of straightforward topography (*e.g.* parabolic or 'V'-shaped). The solutions for these cases *do* include areas of resting fluid on the right looking downstream. However, there are many complications and extensions which may be added to this theory, including mixing for non-ideal fluids, barotropic modes, non-slowly varying sills, non-steady flows and hydraulic jumps across the sills.

References.

(1)KILLWORTH, P.D. **1994**, On Reduced-Gravity Flow Through Sills,*Geophys. Astrophys. Fluid Dynamics*, **75**, 91-106

Eddy-shedding from a boundary current around a cape over a sloping bottom

By CLAUDIA CENEDESE

University of Cambridge

1. Introduction

In the last 10 years several surveys in the Canary Basin of the eastern Atlantic have shown the presence of Mediterranean water in lens-shaped vortices called "Meddies". These eddies were observed to form primarly near Cape St.Vincent (Bower *et* al., 1995) and to rotated anticyclonically (Armi & Zenk, 1984; Pingree & Le Cann ,1993). The continuous Mediterranean outflow through the Strait of Gibraltar develops into a coastal current along the coast of Spain and Portugal and provides the water found within the Meddies. The mechanism by which this continuous outflow breaks into discrete coherent vortices is not clear.

Meddies are characterised by their high salinity and temperature relative to the surrounding water and have a radius of approximately 50 km, a vertical extent of about 1 km and a core depth in the range 1100-1200 m. The azimuthal velocity of these lenses is approximately 0.2 m s^{-1} at radii between 30 and 45 km. Their main direction of propagation is generally southward and they are observed to be long lived structures (Armi *et al.*, 1988). Two dimensionless parameters, the Rossby number $R_0 = \frac{\zeta}{f}$ and the Burger number $B = \frac{f^2 R^2}{g'h}$ are important for this kind of flow. A low Rossby number suggests that the flow is in quasi-geostrophic balance, whereas a Burger number of order of unity indicates that the buoyancy forces and the Coriolis forces are in balance (the horizontal scale of the motion is of the same order of magnitude as the Rossby radius of deformation). For the Meddies described before $R_0 \approx 4\ 10^{-2}$ and $B \approx 2$.

The evolution and translation of eddies on a sloping bottom or a β-plane is a problem of particular importance because of its relevance to the transport of properties and energy within the ocean. The completely barotropic problem of an isolated eddy on the β-plane was performed by Stern (1975) who showed how equilibrium requires a coupled cyclone-anticyclone system called a "modon". A model of cold eddies migrating on a sloping bottom was given by Nof (1983), the eddy was predicted to travel to the west with a characteristic velocity given by $U_d = \frac{g's}{f}$ where g' is the reduced gravity given by $g' = g(\rho_1 - \rho_2)/\rho_1$, s is the slope of the bottom and f is the Coriolis parameter. Water in the lens circulated anticyclonically and the deep upper layer was motionless. Later experimental and theoretical studies by Mory (1985), Mory *et* al. (1987) and Whitehead *et* al. (1990) and Linden (1991)

indicated that similar eddies can be produced on a sloping bottom in laboratory experiments but that the eddies were qualitatively different from the Nof solution. The eddies produced in the laboratory always presented an active upper layer characterised by a strong cyclonic circulation. A more general expression for the westward drift was given by Cushman-Roisin *et* al. (1990) and all the previous results can be expressed as asymptotic limits to this single solution.

In a recent theoretical study Pichevin & Nof (1996) showed how the flow-force associated with any steady current that curves around a cape cannot be balanced without generating and shedding eddies.

In this paper we discuss laboratory experiments which elucidate the mechanism of formation and westward drift of anticyclonic baroclinic vortices from a buoyant surface current flowing along a side boundary and around a cape. The buoyant vortices are influenced by a sloping bottom through an active lower layer and vortex stretching. The lower layer in turn influences the upper layer vortex through advecion of vorticity, leading to motion the upper layer eddy along the depth contours. The motion along the bottom slope is related to westward motion on a planetary β-plane.

The experimental apparatus is described in §2 and the eddy shedding and drift mechanism is discussed in §3 and §4 respectively. Qualitative results are presented in §5 and quantitative results are given in §6. The conclusions of the work are discussed in §7.

2. The experiments

A sketch of the apparatus is shown in figure 1. The experiments were conducted in a transparent glass square tank of depth 60 cm with a square base measuring 61 cm. This was mounted on a 1m diameter, rotating turntable with a vertical axis of rotation, the tank being centred on the vertical rotation axis. A sloping bottom simulated the β-effect for the ambient fluid. The tank was filled with salty water of density ρ_2. When viewed as modelling a planetary β-plane the shallowest part of the environment corresponds to the "northern" shore of the topographic β-plane. East is to the right looking onshore, west is to the left, and south is the deepest end. A vertical sheet of perspex 20 cm long and 1 cm wide was placed perpendicular to the eastern wall of the tank in order to model the effect of a "cape". The depth of the salty water at the cape, h_0, varied between 14.0 and 24.7 cm. A reservoir R_1 of fresh dyed water of density $\rho_1<\rho_2$ was connected to a nozzle via a peristaltic pump and a plastic tube. The nozzle was covered by a piece of sponge. This source was located against the eastern wall of the tank, a few millimetres under the free surface and 14 cm from the cape. The outlet was directed up the slope so that the turbulent jet of buoyant water would reach the cape and there develop into a buoyancy-driven current along the cape. The jet was forced by a constant flow rate Q = 8.68 cm^3s^{-1}. Mixing between the source and the surrounding waters occurred along the interface of the two layers. However, the mixing was confined between the jet and the cape. The buoyancy forces are described by the parameter $g' = g(\rho_1-\rho_2)/\rho_1$, where g is the gravitational acceleration. In the experiment g' was fixed at approximately 0.60 cm s^{-2}. This value was determined by sampling the water in the current downstream of a region near the source where a significant amount of mixing occurred. The Coriolis parameter f was varied from 0.224 s^{-1} to 1.366 s^{-1} and the slope, s, of the bottom had three different values: s=0.26, 0.38, 0.50, 0.62, 0.76. The dimensionless Rossby number of the vortices, defined as the absolute value of the ratio of the relative vorticity and the Coriolis parameter, ranged from 0.4 to 0.9. The Rossby radius of deformation $R = (g'h_v)^{0.5} f^{-1}$ based on the vortex depth, varied from 1.2 cm to 10.4 cm.

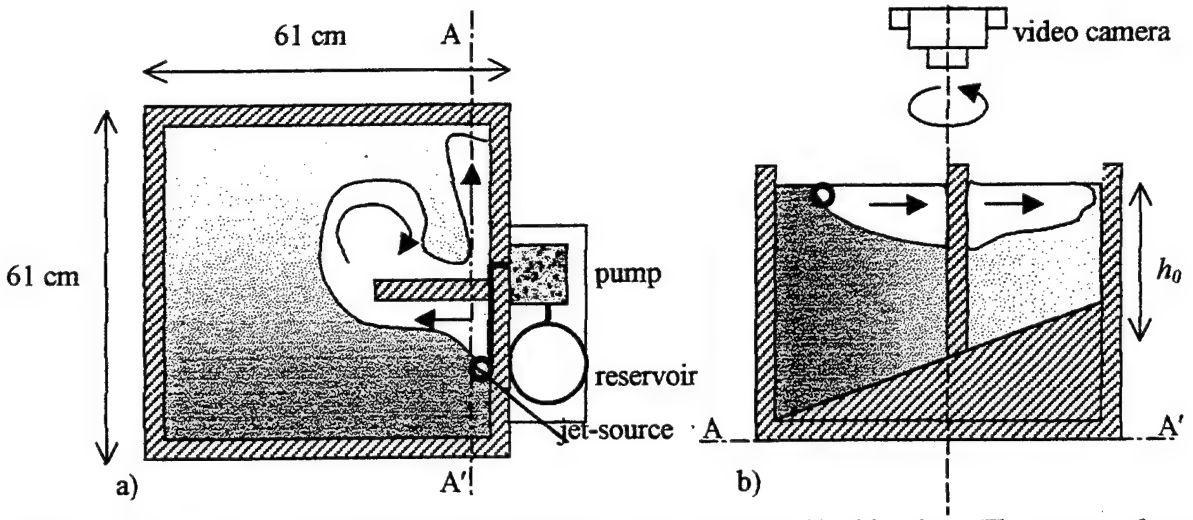

Figure 1. A sketch of the experimental apparatus. a) Top view, b) side view. The arrows denote the flow direction.

A video camera was mounted above the tank and fixed to the turntable so that velocity measurements were obtained in the rotating frame. The current was made visible by having the source water dyed by food colouring and by adding buoyant paper pellets on the surface. The lower layer flow was seen by injecting dyed tracer with a syringe positioned in the southeast side of the cape. A measure of the upper layer depth is given by the reduction in intensity of light transmitted through the dyed upper layer from the white base. The velocities were measured by tracking the paper pellets. The motion of dye was also observed from the side.

3. Eddy shedding mechanism

In order to understand the mechanism involved in the detachment of an eddy from the current and its consequent shedding we calculated the timescales of the formation of an eddy from a buoyant current flowing around a cape and compared it with a timescale for the drift of the eddy.

The formation timescale t_f is defined as the time for the volume V of the eddy to be filled by buoyant fluid flowing at a flowrate Q. The eddy is considered to be a paraboloid and hence its volume can be expressed as

$$V = \frac{\pi R^2 h_v}{2} = \frac{\pi g' h_v^2}{2f^2}, \qquad (1)$$

where the radius of the vortex is equal to the Rossby radius of deformation $R = \frac{\sqrt{g'h_v}}{f}$ and h_v is the maximum depth of the vortex. In order to calculate the time for filling the volume V two approximations are introduced. First, the maximum depth of the vortex is considered to be equal to the maximum depth of the current. Second, the maximum current depth at the wall is calculated assuming that the current is in geostrophic balance. The first approximation will be experimentally verified

later. Indicating with the subscript c and v quantities related to the current and to the upper layer vortex respectively, the geostrophic balance for the current gives

$$Q = \int_0^x v h_c dx' = \int_0^x \frac{g'}{f} h_{cx} h_c dx \approx \frac{g' h_c^2}{2f}. \tag{2}$$

Consequently,

$$h_c \approx h_v = \sqrt{\frac{2fQ}{g'}}. \tag{3}$$

Using (1) and (2) the formation time is then given by

$$t_f = \frac{V}{Q} \approx \frac{\pi}{f}. \tag{4}$$

The timescale for the westward drift of the eddy over a length equal to the radius of the vortex is calculated assuming that the westward drift velocity U_d scales with the long Rossby wave speed and therefore is given by $U_d = \frac{g's}{f}$, (Nof, 1983). Hence

$$t_d = \frac{R}{U_d} = \frac{1}{s}\sqrt{\frac{h_v}{g'}}. \tag{5}$$

In order to have a vortex forming at the cape, and then detaching from it as a result of a westward drift, the timescale for the formation of the vortex and the timescale for the westward drift have to be of the same order of magnitude ($t_f \cong t_d$) so that, using (4) and (5) we can find

$$\frac{h_v}{R} = \pi s. \tag{6}$$

More generally we define $s' = \frac{h_v}{R}$, *the slope associated with the interface displacement generated by* the vortex, which can also be expressed as a function of the variables using (3) and the usual expression for the Rossby radius R:

$$s' = \frac{(2Q)^{1/4} f^{5/4}}{g'^{3/4}}. \tag{7}$$

Equation (6), from this simple scale analysis, shows that in order to have formation and westward drift of the eddy the slope of the topography must be of the same order of magnitude as the slope of the vortex interface displacement.

Two other possible situations can occur when t_f is bigger or smaller than t_d so that

$$t_f < t_d \quad \Rightarrow \quad s < \frac{s'}{\pi},$$
$$t_f > t_d \quad \Rightarrow \quad s > \frac{s'}{\pi}. \tag{8}$$

In the first case the formation process is faster than the drift process. Consequently, the eddy grows to its final volume V and then drifts westward. In the second case the time for the formation of the vortex is longer than the time necessary for its drift, so that some fluid from the vortex can drift westward before the formation process of the vortex is completed. Therefore the vortex takes even longer to reach its final volume V and can not drift sufficiently rapidly as a coherent structure but instead remains attached to the cape.

4. Mechanism for westward drift

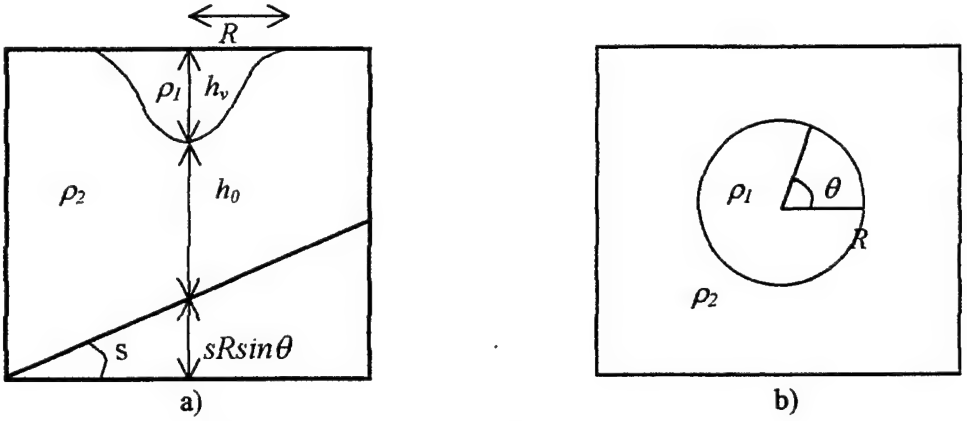

Figure 2. Schematic diagram of the eddy over a sloping bottom.

Consider a buoyant vortex at the free surface of a homogeneous layer having a sloping bottom topography as sketched on figure 2 where in polar coordinates the depth of the ambient fluid underneath the vortex is $h = h_0 - sR\sin\theta - h_v$. A first approximation of the resulting flow can be obtained by neglecting the effect of friction at the density interface, the free surface and the tank bottom. The inviscid flow, both inside and outside the vortex, is governed by the principle of conservation of potential vorticity. Assuming hydrostatic balance the cyclostrophic equations are

$$u\frac{\partial u}{\partial r} + \frac{v}{r}\frac{\partial u}{\partial \theta} - \frac{v^2}{r} - fv = -\frac{1}{\rho}\frac{\partial p}{\partial r} = -g'\frac{\partial h}{\partial r},$$
$$u\frac{\partial v}{\partial r} + \frac{v}{r}\frac{\partial v}{\partial \theta} + \frac{vu}{r} + fu = -\frac{1}{r\rho}\frac{\partial p}{\partial \theta} = -\frac{g'}{r}\frac{\partial h}{\partial \theta}, \tag{9}$$

and the continuity equation is

$$\frac{\partial(ruh)}{\partial r} + \frac{\partial(vh)}{\partial \theta} = 0, \tag{10}$$

where u and v are the radial and azimuthal velocities respectively.

4.1 Lower layer vortex

The upper layer vortex formation squashes the fluid column underneath so that, in order to conserve potential vorticity, the fluid in the column will start rotating clockwise in an anticyclonic motion. Consider a circular vortex with azimuthal velocity v_2 and same radius R as the vortex in the upper layer (figure 2). In the absence of a zonal drift and assuming the radial velocity to be negligible the continuity equation becomes

$$\frac{\partial(v_2 h)}{\partial\theta} = 0, \tag{11}$$

and applying this to the north (N) and south (S) sides of the eddy yields

$$v_{2N} h_N = v_{2S} h_S, \tag{12}$$

where

$$\begin{aligned} h_N &= h_0 - sR - h_{vN}, \\ h_S &= h_0 + sR - h_{vS}. \end{aligned} \tag{13}$$

Since the same fluid circulates around the eddy without loss of mass and $h_N \neq h_S$ we conclude that $v_{2N} \neq v_{2S}$. The Coriolis forces associated with these two velocities will no longer balance each other and, assuming the vortex shape is unchanged, a westward zonal drift U_{2d} is required in order to reach an equilibrium. The vortex will initially move southward for an inertial lengthscale proportional to the velocity difference. This motion will induce a Coriolis force westward. Consequently, the vortex will be deflected westward until the Coriolis force associated with the westward drift velocity balances the net Coriolis force associated with the difference between v_{2N} and v_{2S}. This transient regime takes place for a timescale of the order of one inertial period. After reaching a steady balance the Coriolis forces in the north and south side must equilibrate

$$f(v_{2N} - U_{2d}) = f(v_{2S} + U_{2d}), \tag{14}$$

that gives

$$v_{2N} = v_{2S} + 2U_{2d}. \tag{15}$$

Substituting (15) into (12) yields

$$(v_{2S} + 2U_{2d}) h_N = v_{2S} h_S, \tag{16}$$

$$U_{2d} = \frac{v_{2N}(2sR + h_{vN} - h_{vS})}{2(h_0 - sR - h_{vN})}. \tag{17}$$

4.2. Lower and upper layer interaction

We will assume that the lower layer vortex interacts with the upper layer vortex through advecion of vorticity (Griffiths & Hopfinger, 1986). The lower layer vortex drifts westward as discussed in §4.1 and its vorticity field induces the drift of the upper layer vortex at the same speed $U_{1d} = U_{2d}$. Any small departure of the upper layer vortex from a configuration concentric with the lower layer motions will

be removed through advection by the lower layer velocity field. This process is similar to the "axisymmetrization" of vortices in a fluid of uniform depth and subjected to a uniform f, but in the present case the vortex an a slope will not be circular.

In order to calculate the westward velocity U_{2d} we will use conservation of potential vorticity in both layers. In the top layer we assume that the eddy is generated by an inflow from the coastal current having zero potential vorticity and, consequently, the vorticity is given by $\zeta_v = -f$. In the lower layer

$$\frac{f}{h_0 - sr\sin\theta} = \frac{f+\zeta_2}{h_0 - sr\sin\theta - h_v}, \tag{18}$$

and the relative vorticity becomes

$$\zeta_2 \cong -\frac{fh_v}{h_0}\left(1+\frac{sr\sin\theta}{h_0}-\frac{h_v}{h_0}\right). \tag{19}$$

Assuming $s<<1$ and $h_v<<1$ (19) yields

$$\zeta_2 = -\frac{fh_v}{h_0}. \tag{20}$$

If we consider that the vortices in the lower and upper layer have approximately the same radius then the ratio of the two vorticities gives a scale of the ratio of the azimuthal velocity in the two layers. The ratio of the two velocities is then given by

$$\frac{\zeta_2}{\zeta_v} \approx \frac{v_2}{v_v} = \frac{h_v}{h_0}. \tag{21}$$

Integration of the vorticity in the upper layer leads to the azimuthal velocity $v_v = -\frac{1}{2}fR$ and using (21) and (17) the westward velocity drift is given by

$$U_{2d} = \frac{1}{2}\frac{g's}{f}\left(\frac{h_v}{h_0}\right)^2. \tag{22}$$

This result is similar to the westward drift introduced in §3 (Nof,1983), but is multiplied by ½ and by the square of the ratio between the upper and lower layer depths.

The drift velocity (22) depends on the sign of the vorticity in the lower layer. For an anticyclonic vortex the drift speed is directed westward as discussed in §4.1, whereas for a cyclonic vortex the drift speed is directed eastward. This is in contradiction with the laboratory observations of a westward drift. A different explanation is required for this behaviour.

4.3. Drift due to induced vorticity

A vortex on a slope will advect fluid columns both upslope and downslope regardless of the sign of the vorticity and regardless of whether or not the vortex is drifting. Conservation of potential vorticity dictates that the columns advected upslope and downslope acquire anticyclonic and cyclonic relative vorticity, respectively. The vorticity ζ' of these columns is given by

$$\zeta' = \mp \frac{sRf}{h_0}, \tag{23}$$

These regions of positive and negative vorticity form a dipolar contribution to the velocity field which can then induce motion "westward" along the slope. Writing the azimuthal velocity associated with the induced vorticity as v', we have $v' = \frac{1}{2}\zeta' R$. The westward drift of the vortex due to the induced dipolar vorticity component is given by

$$U_{2d} = 2v' = \frac{g's}{f}\left(\frac{h_v}{h_0}\right). \tag{24}$$

The two different drift mechanisms discussed above can be added together to give a total westward speed for an anticyclonic vortex:

$$U_{2dTOTAL} = \frac{g's}{f}\left[\frac{h_v}{h_0} + \frac{1}{2}\left(\frac{h_v}{h_0}\right)^2\right], \tag{25}$$

and for a cyclonic vortex equal to

$$U_{2dTOTAL} = \frac{g's}{f}\left[\frac{h_v}{h_0} - \frac{1}{2}\left(\frac{h_v}{h_0}\right)^2\right]. \tag{26}$$

Bjerknes & Holmboe (1944), Rossby (1948) and Cushman-Roisin *et* al. (1990) gave similar arguments to find the westward drift for an eddy on a slope.

5. Qualitative results

In our experiments the buoyant current generated by the jet on the eastern wall propagated upslope (northward) until it encountered the cape. It rounded the cape and turned eastward after separating from the corner and reattaching to the cape some distance from the tip. Providing the current had a large enough volume flux, an anticyclonic vortex grew where the current separated and, under some conditions, it eventually detached from the cape and drifted westward. Some experiments carried out with a different type of source providing less volume flux than the jet source, and some experiments with lower flowrate showed that the formation mechanism of the eddies was inhibited and the current reattached at the cape without forming a region of closed streamlines at the cape.

We first varied only the slope s and the Coriolis parameter f in order to observe eddy shedding as discussed in §2. The influence of lower layer depth and of bottom topography was investigated for some of these experiments. A different orientation of the cape relative to the direction of bottom slope was investigated in order to simulate different geographical situations.

5.1. Eddy-shedding

Experiments were carried out with different slopes and for each of those we varied the Coriolis parameter in order to investigate different values of the dimensionless parameter s'/π (7) as showed in figure 3. The lower layer depth was kept constant and approximately equal to 15 cm. For $s > s'/\pi$ the

current separated and formed an anticyclonic vortex that started slowly growing at the cape. Some of the fluid within the vortex leaked out and drifted westward along an isobath; consequently, the formation time of the vortex was very long and no shedding was observed at the early stage of the flow. When the value of the slope was 0.75 the eddy was observed to detach after a timescale much longer than for the regime characterised by $s \lesssim s'/\pi$. The detachment also involved the destruction of the anticyclonic eddy due to baroclinic or shear instabilities growing at the front of the eddy. For all other values of the slope the vortex did not detach or breakup and remained approximately at its initial position at the cape. For $s \lesssim s'/\pi$ the current flowing around the cape formed an eddy after it separated from the wall. Before the current reattached to the cape the flow streamlines were observed to pass through a bifurcation point. After this point the streamlines in the outer edge of the current reattached

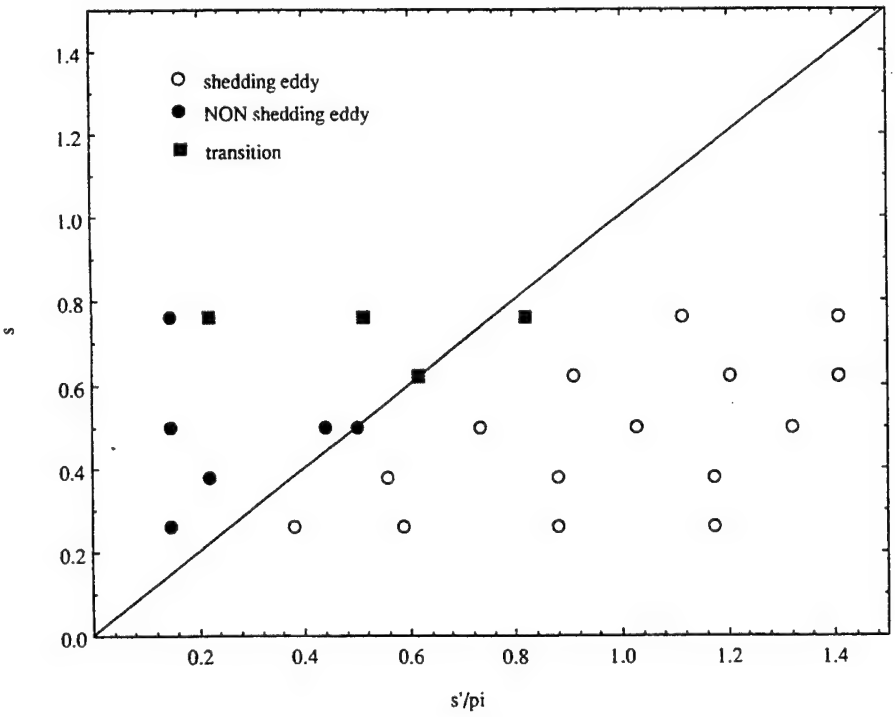

Figure 3. Regime diagram illustrating the eddy-shedding region for $s \lesssim s'/\pi$. No eddy-shedding was observed for $s > s'/\pi$. The squares indicate experiments were the eddy-shedding occurred after time scales much longer than in the region where $s \lesssim s'/\pi$.

to the cape, strongly influenced by depth contours, while the streamlines in the inner part of the current closed on themselves at the end of the cape. The closed streamlines indicated the presence of the anticyclonic vortex (figure 4 a)), and this grew in size due to the continuous inflow from the current. After this transient regime the bifurcation point moved westward along the cape until it reached the tip of the cape. The vortex then separated from the current and from the cape (figure 4 b),c),e)). The current streamlines then re-established their previous path around the cape, separated and reattached downstream, starting the whole process again and leading to the production of a new vortex (figure 4 c),d),e)). After each eddy detached from the current it drifted westward approximately following isobath contours. The vortex generally lost its axisymmertic shape and coherency and could

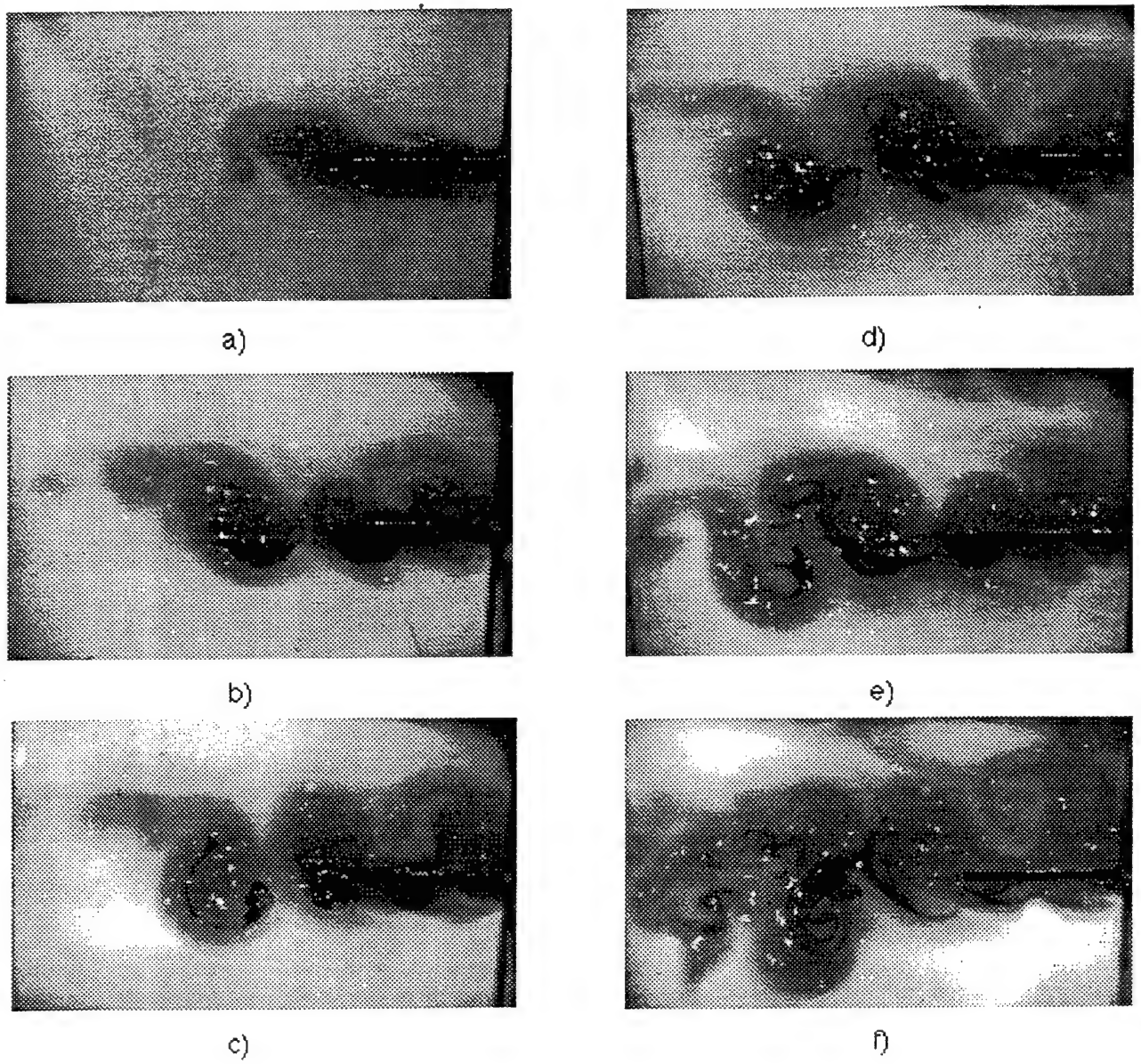

Figure 4. Formation (a) and westward drift (b,c,d,e) of anticyclonic baroclinic vortices from a buoyant surface current flowing along a side boundary and around a cape (f =0.963 s^{-1}, s =0.62, h_0 =14.8 cm). The anticyclone was unstable (e) and formed two spiral arms as a result of the generation of cyclonic vorticity in the lower layer by baroclinic instability. The lower layer flow was seen by injecting dyed tracer in the southeast side of the cape.

be destroyed before reaching the western wall of the tank as a result of two different kinds of processes (which will be discussed in §5.5).

5.2. The influence of depth

The depth of the lower layer plays two important roles in the shedding process. First it determines the relative squashing of the lower layer fluid column underneath the anticyclonic upper layer eddy. Consequently, it determines the magnitude of the relative vorticity in the lower layer. Second, the topographic β-effect depends on the lower layer depth through the relation $\beta = \frac{sf}{h_0}$. In this section we will discuss only the influence of h_0 on the eddy shedding mechanism under the assumption that the β-effect associated with the bottom slope remains unchanged. Sets of two experiments were carried out with the same value of the Coriolis parameter but varying the lower layer depth and the slope to give

$$\beta = \frac{s_A f}{h_{0A}} = \frac{s_B f}{h_{0B}}, \tag{27}$$

where the subscripts A and B label the two different experiments with h_0 =15 cm and h_0=25cm respectively. The value of the dimensionless parameter s'/π depends only on f for a given flowrate and reduced gravity, and for both experiments s'/π was chosen to be smaller than s in order to observe the shedding of eddies. The flow structure of experiment A has already been discussed in §5.1. During experiment B the vortex formed at the cape but it did not detach and had a similar appearance as the flow case presented in §5.1 for $s < s'/\pi$. In the two experiments the westward drift was forced by the same topographic β-effect. Therefore the different behaviour observed was caused by the increase of the lower layer depth and the relative decrease of the lower layer column squashing.

5.3. The influence of topography

Within the context of the homogeneous (one-layer) model there is a dynamical equivalence between the variation of the Coriolis parameter with latitude, the β-effect, and variation of depth in the presence of constant f (for small bottom slopes and geostrophic flow). Hence β plays the same role in potential vorticity dynamics as $\frac{fs}{h_0}$. The relative magnitudes of the relative vorticity gradient and the planetary vorticity gradient are measured by the parameter $\frac{U}{\beta L^2}$, where U and L are characteristic velocity and length scale, respectively.

In order to investigate the importance of the planetary β-effect on the formation and drift of eddies in the oceans we performed some experiments with values of the slope that reproduced in the laboratory a flow dynamically equivalent to a flow influenced by the planetary variation of the Coriolis parameter. To calculate the value of the slope we assumed that the ratio of the relative vorticity gradient and the planetary vorticity gradient is the same in both the laboratory experiments and the oceans:

$$\frac{U_{2d}}{\beta_{LAB} R^2} = \frac{U_{ocean}}{\beta_{plan} L_{ocean}^2}, \tag{28}$$

where $\beta_{LAB} = \frac{sf}{h_0}$. Meddies have been observed (Armi & Zenk, 1984) drifting at a velocity U_{ocen}=5 cm s^{-1} and have a radius of approximately 50 km. Considering $\beta_{plan} = 1.57 \cdot 10^{-13} cm^{-1} s^{-1}$ (corresponding to latitude 45° and a planetary radius of 6370 km), U_{2d}=0.174 cm s^{-1}, R=12 cm, f=1.366 s^{-1} and h_0=15 cm the value of the slope from (28) is given by s=0.05. We carried out two experiments with s=0.05 and s=0.10 and compared them with the corresponding experiments with the same value of f and a larger value of the slope. For both values of the slope a vortex was observed forming at the cape by the usual mechanism. However, it did not detach, nor drift from the cape, and behaved in a similar way to the case presented in §5.1 for $s < s'/\pi$.

5.4 The influence of the "cape" position

Experiments were performed with different orientations of the cape relative to the direction of bottom slope in order to obtain a more complete view of possible scenarios along real coastlines. We first positioned the cape perpendicular to the western wall of the tank with a buoyant coastal current encountering the cape from the north. After encountering the cape the current flowed around it and then turned westward separating from the corner and reattaching itself to the cape. An anticyclonic vortex formed at the cape in the same way as in the previous experiments and it was observed to remain in its initial position for $s < s'/\pi$. For $s \geq s'/\pi$ the eddy migrated westward and merged with the current flowing around the cape and along the western wall. No eddies were observed to cross the tank in the westward direction. Nor did eddies shed when the cape was positioned orthogonal to the southern wall. In this geometry some fluid from the current leaked westward just before going around the cape. Consequently the vortex did not form completely or shed from the cape.

In other experiments the cape was oriented perpendicular to the northern wall with a current flowing westward. This geometry, where the cape was perpendicular to the isobaths, was an attempt to simulate a peninsula on a shelf with a strong off-shore slope. The resulting flow showed similar behaviour to those described in §5.1 with the eddies migrating westward along isobaths for values of $s \geq s'/\pi$. It appears that the results for the geometry with the cape positioned perpendicular to the eastern wall apply to this case as well.

5.5 Instability processes

Instability was observed to influence the formation and drift of eddies as well as the flow of the boundary current along the side boundary and around the cape. These instabilities are expected to range from those that were almost purely baroclinic and driven by the release of potential energy, to those that are almost purely barotropic and which drew on the kinetic energy in the basic shear flow. However, the appearance of the amplified disturbances is expected to be very similar for both types of instability and therefore it was difficult to determine which one was occurring or dominant. As observed by Griffiths and Linden (1981), these instabilities led both vortex splitting and rapid radial spreading of the water of the upper layer eddy. At an early stage of the instability cyclonic rings, or "spiral arms", of buoyant fluid were produced, indicating the presence of cyclonic vortices in the lower layer.

Experiments showed that anticyclonic eddies were destroyed by instabilities as a result of two different processes. In one case the boundary current was observed to become unstable along the

southern side of the cape, with backward breaking wave crests. The buoyant fluid started meandering and anticyclonic vorticity was generated to conserve potential energy. As a consequence of the meandering of the upper layer current, the lower layer water in the wave troughs was stretched and acquired cyclonic vorticity. The cyclonic motion trapped some of the buoyant fluid and formed visible cyclonic arms that give the appearance of backward breaking waves. When each of these cyclonic vortices reached the tip of the cape they interacted with the anticyclonic vortex generated at the tip by the current. The two different structures began moving westward as a dipole in which the anticyclonic initially had the greater intensity. Thus the anticyclone advected the cyclone slightly southward to deeper water so that the lower layer cyclone was stretched, further increasing its intensity. Eventually the intensity of the cyclone overcame the anticyclone intensity and it entrained fluid from the anticyclone, elongating and destroying it.

Another process occurred when we could not observe any instability of the current. In these cases the anticyclonic vortex drifted westward without any obvious lower layer cyclonic vorticity generated by the current. However, the anticyclone was unstable and formed two spiral arms as a result of the generation of cyclonic vorticity in the lower layer by baroclinic instability (figure 4 d),e)). One of the cyclonic vortices was advected southward by the anticylone and increased its intensity until it became strong enough to tear the anticyclone apart as in the other cases.

6. Quantitative results

The width of the boundary current flowing around the cape was equal to one to two times the Rossby radius of deformation. The separation and reattachment of the current from the cape generated a vortex with a radius two or three time bigger than the Rossby radius of deformation. The westward drift speed was measured for the experiments in which $s \geq s''/\pi$ and in figure 5 it is plotted against the predicted drift speed (25) calculated in §4.3. It was observed that for $s = s''/\pi$ the drift velocity was of the same order of magnitude as the theoretical drift speed U_{2d} while for $s > s''/\pi$ the measured velocity is bigger than U_{2d}. The higher speed can be explained considering that for $s > s''/\pi$ the vortices form faster than the time necessary to move westward. Consequently two anticyclonic vortices start strongly interacting at the cape before they start drifting. Suppose the two vortex centres lie on the same isobath and that their contours touch each other. The anticyclone on the right will advect the vortex on the left with a northward velocity, moving it slightly upslope. The lower layer columns will then be squashed even more and will increase their azimuthal velocity in accordance with the conservation of potential vorticity. Equation (17) shows how an increase of the azimuthal velocity v_{2N} gives an increase of the westward velocity U_{2d}. Similarly v' will increase and intensify the westward drift of the main vortex. This simple explanation can justify the increase in speed observed in the experiments for $s > s''/\pi$.

Figure 6 shows the measured drift velocity normalised by the theoretical velocity U_{2d} and plotted against the ratio $s''/(s\pi)$ of the eddy interface slope and the bottom slope. The ratio $s''/(s\pi)$ gives an indication of the interaction occurring between two anticyclonic vortices at the cape. A ratio equal 1 corresponds to weak interaction; the interaction between the vortices is stronger for larger values of $s''/(s\pi)$.

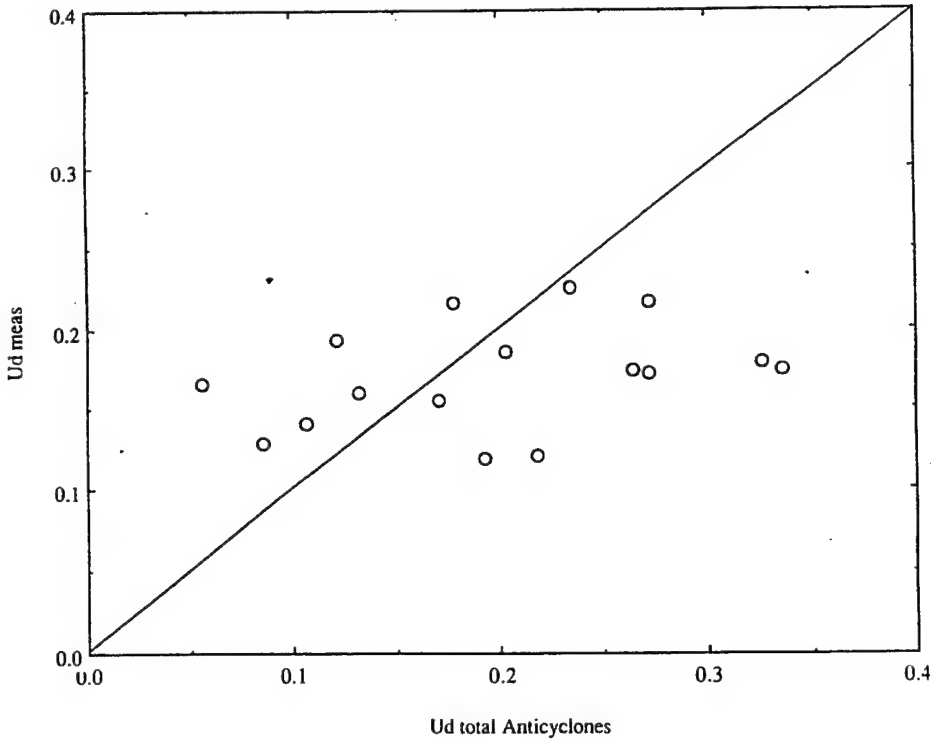

Figure 5. The westward drift speed measured for the experiments in which $s \geq s'/\pi$ and plotted against the predicted drift speed (25) calculated in §4.3.

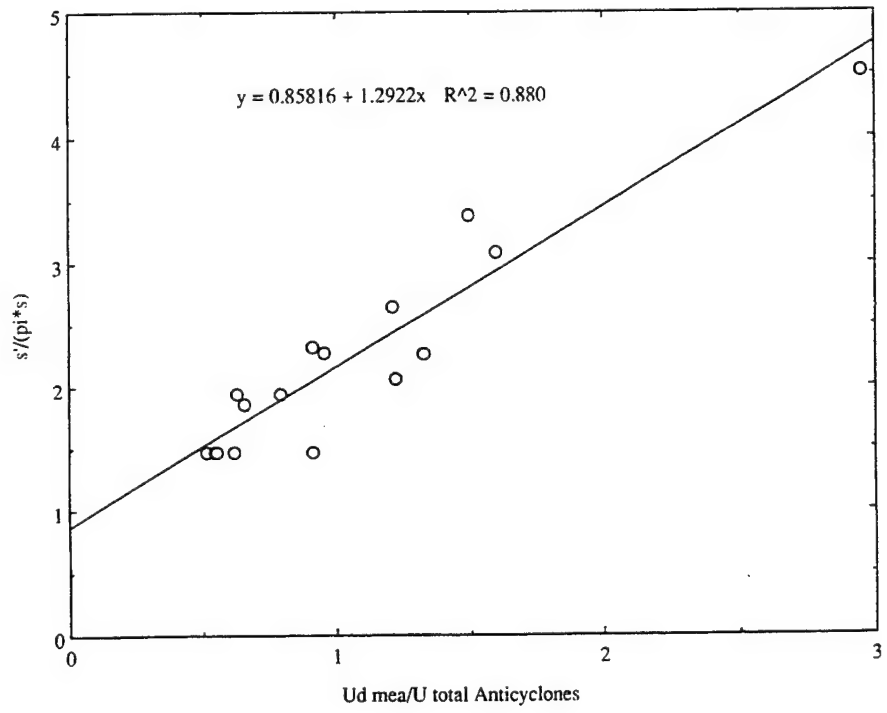

Figure 6. Measured drift velocity normalised by the theoretical velocity U_{2d} plotted against the ratio $s'/(s\pi)$ of the eddy interface slope and the bottom slope.

7. Discussion and conclusion

Laboratory experiments were performed to investigate a buoyant current flowing along a side boundary and around a cape over a sloping bottom. They showed how a vortex can be generated from the current where it separates and reattaches to the cape and that, under some conditions, the eddy is able to detach from the cape and drift westward following isobaths. Two important timescales regulate the flow: the time that the current takes to generate a vortex, t_f, and the time, t_d, that the vortex takes to drift westward for a distance equal to its radius. When these two timescales are of the same order of magnitude the eddy was observed to translate westward with approximately the same theoretical speed found in §4. For $t_f < t_d$ vortices were observed to drift at a higher speed than the predicted. This was attributed to an interaction between two consecutive anticyclonic vortices. The interaction resulted in a northward shift of the vortex and an increase of its azimuthal velocity, and consequently of its westward drift speed. For $t_f > t_d$ the vortex was able to form at the cape but it was not observed to detach and drift westward. The influence of the depth of the lower layer, h_0, on the flow was investigated. The eddy drift was observed for h_0=14 cm, whereas an increase of the lower layer depth to 25 cm completely inhibited the detachment and drift of the vortex from the cape. The theoretical westward speed, U_{2d}, depends on the depth of the lower layer: the deeper the lower layer the slower the drift. The experiments, on the other hand, indicate that for sufficiently small values of the westward speed the whole process no longer takes place. The large values of the slope s required in the experiments in order to obtain the detachment and drift of the vortex indicate that the phenomena will occur on a planetary β-plane only when the variation of the Coriolis parameter wit latitude is reinforced by a topographic β-effect. This suggests that only peninsulas or capes on a sufficiently steep shelf can cause the detachment and drift of a vortex from a boundary current.

Different orientations of the cape with respect to the isobaths show that eddies always drift westward if the geometry allows this, and the behaviour of the drifting eddies is similar for different orientation of the cape. Finally we investigated the lost of coherence and destruction of the anticyclonic eddies before they could reach the western wall of the tank. An active (shallow) lower layer led to instability of both the boundary current and the anticyclonic eddy. Cyclones were generated in the lower layer. These were advected to deeper water by interaction with the anticyclonic eddies, increasing their intensity until they destroyed the anticyclones. The precise nature of the instability was difficult to determine because both baroclinic and barotropic instabilities presents many features in common.

This study suggests that the formation, detachment and drift of an eddy from a current flowing around a cape is a delicate process that takes place only if the water depth is not too large and the topography is steep enough. The orientation of the cape must also allow the westward motion of the vortex (i.e. the coastline is not directly westward of the cape). These conditions appear to be satisfied, for example, in the Canary Basin, where the Mediterranean outflow from the Gibraltar Straits flows along the coast of Spain and around Cape St.Vincent. Observations of Meddies in that region suggest that an eddy-shedding process similar to that observed in the laboratory experiments take place.

Acknowledgements

I wish to thank the staff of the GFD summer program for providing a stimulating environment during the summer, and especially Jack Whitehead, George Veronis and Ross Griffiths for their

suggestions and advise. A special thanks to John Salzig for providing assistance and help any time I needed making the experiments possible.

References

Armi L. *& al.* 1988 The history and decay of a Mediterranean salt lens. *Nature* **333**, 649-651.

Armi L. & Zenk W. 1984 Large lenses of highly saline Mediterranean water. *J. Phys. Oceanogr.* **14**,1560-1576.

Bjerknes J. & Holmboe J. 1944 On the theory of cyclones. *J. Meteor.* **1**, 1-22.

Bower A.S., Armi L. & Ambar I. 1997 Lagrangian observations of meddy formation during a mediterranean undercurrent seeding experiment. Submitted to *J. Phys. Oceanogr.*

Cushman-Roisin B., Chassignet E.P. & Tang B. 1990 westward motion of mesoscale eddies. *J. Phys. Oceanogr.* **20**,758-768.

Griffiths R.W. & Linden P.F. 1981 The stability of vortices in a rotating, stratified fluid. *J. Fluid Mech.* **105**, 283-316.

Griffiths R.W. & Hopfinger E.J. 1986 Experiments with baroclinic vortex pairs in a rotating fluid. *J. Fluid Mech.* **173**, 501-518.

Griffiths R.W. & Hopfinger E.J. 1987 Coalescing of geostrophic vortices. *J. Fluid Mech.* **178**, 73-97.

Linden P.F. 1991 Dynamics of Fronts and Eddies. *Proceeding of Enrico Fermi Summer School* 313-351.

Mory M. 1985 Integral constraints on bottom and surface isolated edies. *J. Phys. Oceanogr.* **15**,1433-1438.

Mory M., Stern M.E. & Griffiths R.W. 1987 Coherent baroclinic eddies on a sloping bottom. *J. Fluid Mech.* **183**, 45-62.

Nof D. 1983 The translation of isolated cold eddies on a sloping bottom. *Deep-Sea Res.* **30**, 171-182.

Pedlosky J. 1979 *Geophisical Fluid Dynamics.* Springer. 624 pp.

Pichevin T. & Nof D. 1996 The eddy cannon. *Deep-Sea Res.* **43**, 1475-1507.

Pingree R.D. & Le Cann B. 1993 Structure of a meddy (Bobby 92) Southeast of the Azores. *Deep-Sea Res.* **40**, 2077-2103.

Rossby C.G. 1948 On displacements and intensity changes of atmospheric vortices. *J. Mar. Res.* **26**, 175-187.

Stern M.E. 1975 Minimal properties of planetary eddies. *J. Mar. Res.* **33**, 1-13.

Whitehead J.A., Stern M.E., Flierl G.R. & Klinger B.A. 1990 Experimental observations of baroclinic eddies on a sloping bottom. *J. Geophys. Res.* **95**, 9585-9610.

The rotating hydraulic jump from an axisymmetric jet

Chris Hills

Department of Applied Mathematics and Theoretical Physics,
Cambridge University, Cambridge CB3 9EW

Introduction.

The problem of an axisymmetric, radial hydraulic jump is a familiar one arising naturally when an incident jet spreads out over a perpendicular flat plate, *e.g.* when filling a sink from a tap. The apparent simplicity of this arrangement, however, belies the complications of mixing, viscous boundary layers and the jump itself. But, this geometry provides a good framework to consider the treatment of such shocks and jumps. The problem of the jet and subsequent radially spreading flow has been analysed in the non-rotating case, principally by Watson [1] and Bowles & Smith [2]. Experimentally results are provided by the works of Watson [1] and Craik *et al.* [3].

In his treatment of a vertical jet falling onto a rigid surface, Watson first considers a fully inviscid flow, and then further introduces a viscous boundary layer with flow adjustment regions. We will be studying the problem in the context of a rotating co-ordinate system where the incoming jet and plate are fixed relative to the axes. We will follow the framework of Watson's study allowing us to guage the effects of rotation on the formation of the hydraulic jump.

Description and notation.

We shall consider the problem of a vertical jet of constant velocity, U and radius a, falling under gravity onto a horizontal, flat plate as shown in figure 1. To exploit symmetry, we take cylindrical polar co-ordinates, (r, θ, z), at the centre of the point of impact and for simplicity we assume a constant angular velocity of $f/2$ about the z-axis for our frame of reference. The fluid motion is taken to be incompressible. Then the governing, Navier-Stokes, equations of motion and the equation of conservation of mass, in this co-ordinate frame, become

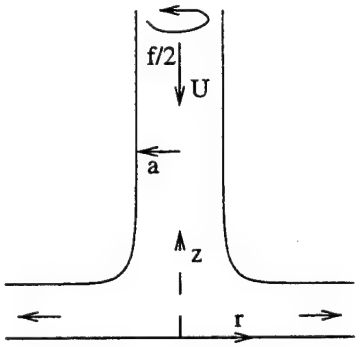

Figure 1.

$$\frac{\mathrm{D}\mathbf{u}}{\mathrm{D}t} + \mathbf{f} \times \mathbf{u} + \tfrac{1}{4}(\mathbf{f} \times (\mathbf{f} \times \mathbf{r})) = -\nabla p/\rho + \mathbf{g} + \nu \nabla^2 \mathbf{u},$$
$$\nabla . \mathbf{u} = 0, \qquad (1)$$

where $\mathbf{g} = (0, 0, -g)$ is the gravitational body force per unit mass, $\mathbf{u} = (u, v, w)$, ν, p and ρ are the standard velocity, kinematic viscosity, pressure and (constant) density variables and we have used $\frac{\mathrm{D}}{\mathrm{D}t} \equiv \frac{\partial}{\partial t} + \mathbf{u}.\nabla$ to denote the material time derivative. Although it is not strictly necessary to use the rotating form of the momentum equations (1a), we shall

use this formulation for convenience and consistency with later work, but throughout a change of co-ordinates back into the inertial frame is straightforward. In component form, equations (1a) now become, using our assumption that $\mathbf{f}$ is aligned with the z-axis,

$$\begin{aligned}(\mathbf{u}.\nabla)u - \frac{v^2}{r} - fv - \tfrac{1}{4}f^2 r &= -\frac{1}{\rho}\frac{\partial p}{\partial r} + \nu\left(\nabla^2 u - \frac{2}{r^2}\frac{\partial v}{\partial \theta} - \frac{u}{r^2}\right),\\ (\mathbf{u}.\nabla)v + \frac{uv}{r} + fu &= -\frac{1}{\rho r}\frac{\partial p}{\partial \theta} + \nu\left(\nabla^2 v + \frac{2}{r^2}\frac{\partial u}{\partial \theta} - \frac{v}{r^2}\right),\\ (\mathbf{u}.\nabla)w &= -\frac{1}{\rho}\frac{\partial p}{\partial z} + \nu\nabla^2 w - g, \end{aligned} \tag{2}$$

writing $\mathbf{u}.\nabla \equiv u\frac{\partial}{\partial r} + \frac{v}{r}\frac{\partial}{\partial \theta} + w\frac{\partial}{\partial z}$ and allowing only steady solutions ($\partial/\partial t \equiv 0$). For our analysis we shall consider, for the most part, fluid of low kinematic viscosity allowing a large Reynold number ($Re = UL/\nu$), inviscid approximation away from the surface of the plate.

We now consider more closely the structure of the flow up to and including the jump. We shall use the term 'jump' to indicate a sharp change in depth of fluid and fluid velocity over a short radial distance which formally we shall treat as a discontinuity. We may then, in a similar manner to Watson [1], anticipate five regions separating different flow regimes:

i) uniform in-flow from tap, $\mathbf{u} = (0, 0, -U)$. This satisfies the equations of motion and the requirement of constant mass flux.

ii) adjustment area between the viscous boundary layer, region (iii), and essentially inviscid region away from the source *i.e.* $r \gg a$

iii) thin viscous boundary layer where viscosity plays a defining role

iv) boundary layer expands, as depth decreases, to encompass the whole of the *thin* layer of fluid up to the jump

v) region outside the jump where fluid is slower and the inviscid assumption once again becomes valid

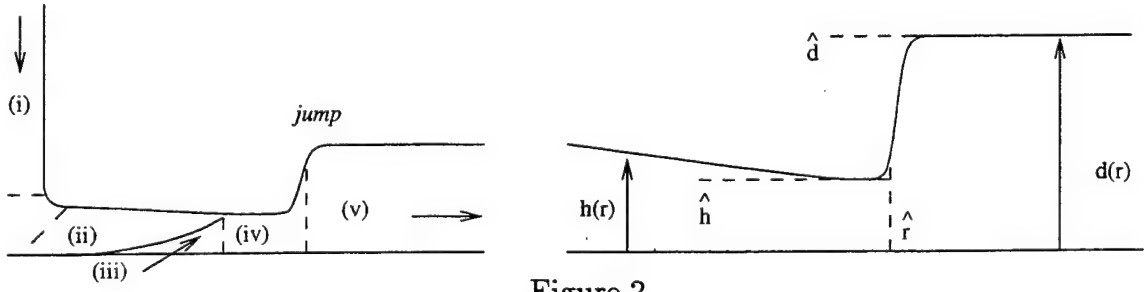

Figure 2.

Figure 2, shows these regions, where we use $h(r)$ to indicate the (inside) depth of fluid, $d(r)$ the depth outside the jump, $\hat{r}$ the radial position of the jump and hats to indicate the function values evaluated at $r = \hat{r}$. Finally we may introduce a convenient constant of the motion, the volume flux Q. Clearly conservation of mass dictates that, since density

is constant,

$$Q = \pi a^2 U = \begin{cases} \int_0^{2\pi} \int_0^{h(r)} u r \mathrm{d}z \mathrm{d}\theta, & r < \hat{r}, \\ \int_0^{2\pi} \int_0^{d(r)} u r \mathrm{d}z \mathrm{d}\theta, & r > \hat{r}. \end{cases} \tag{3}$$

Inviscid flow.
The majority of the fluids we consider will behave essentially inviscidly with viscous effects only playing an important role in thin boundary layers where vertical scales become sufficiently small (and thus the z-derivatives involved in the dissipative terms are of comparable size to inertial effects). Clearly, for our physical apparatus, a thin layer *will* be formed between the faster moving outer fluid and the plate as the fluid spreads out as outlined above. But as a first approximation and useful precursor to a boundary layer analysis, we consider the fully inviscid flow which will exist away from the incoming jet to which the boundary flow must adjust and limit the effect of viscosity to the formation of the discontinuity. Formally we take the limit $\nu \to 0$ to yield the Euler equations of motion. In addition, we take the flow over the plate to be laminar with $w = 0$, and exploit the axisymmetry of our system to assume no θ-dependance throughout: $\partial/\partial\theta \equiv 0$. Our system of equations (2), in these approximations, become

$$\begin{aligned} u\frac{\partial u}{\partial r} - \frac{v^2}{r} - fv - \tfrac{1}{4}f^2 r &= -\frac{1}{\rho}\frac{\partial p}{\partial r}, \\ u\frac{\partial v}{\partial r} + \frac{uv}{r} + fu &= 0, \\ \frac{\partial p}{\partial z} &= -\rho g. \end{aligned} \tag{4}$$

Integrating equation (4c) immediately, and imposing the physical condition that p is constant on the free surface, $z = h(r)$, we have that inside the jump,

$$p = \rho g(h(r) - z), \tag{5}$$

where p is now the pressure relative to the atmospheric pressure. Therefore, equations (4a,b) are independent of z, so that $u = u(r)$, $v = v(r)$. Expression (4b) becomes a homogeneous linear equation for v, which we solve to obtain,

$$v = A/r - fr/2, \tag{6}$$

where A is a constant. It should be noted that this equation simply represents a conservation of angular momentum with the second term on the right hand side arising from the rotation of our co-ordinate frame. Substituting for the pressure and azimuthal velocity in

our final equation of motion we obtain a differential equation for u which when integrated gives,

$$u^2 = -2gh - A^2/r^2 + B, \tag{7}$$

where once again B is a constant of integration. Equation (7) should be recognised as a statement of Bernoulli's theorem (derived by integrating the momentum equation) with B playing the role of a Bernoulli constant. In addition, we have due to our axisymmetry that, from (3),

$$Q = 2\pi urh, \qquad \text{or} \qquad h = a^2U/2ur. \tag{8}$$

We now have a complete solution of the iniviscid equations of motion for the velocity and pressure fields. To determine the unknown constants we must make a further assumption. As discussed above, we expect the invisicd solution to be valid in a region both away from the plate and the incoming jet. However, we must apply the condition of matching the velocity profile of the invisicd solution to the incoming jet at a point where the free surface meets the jet. We can see from figure 2 that this region is likely to adjust the quickest and agree most closely to the laminar approximation. Therefore, we impose $u(a) = U$, and $v(a) = 0$, which may be thought of the condition that, as the fluid on the outside of the jet turns the 'corner', instantaneously no energy is lost. We now find that,

$$A = fa^2/2, \qquad B = U^2 + ga + f^2a^2/4, \tag{9}$$

since $h(a) = a/2$ from (8). Thus we have from (6), (7) and (8b) a full solution of our inviscid flow, involving cubic equations for u and h.

To better understand the form of our solution we consider the asymptotic limit of the velocity for $r \gg a$. Assuming $u \sim r^{-\alpha}$ at large radii, a balance of scales in equation (7) gives that $\alpha = 0, -1$. Therefore we expect two types of profile, one where the velocity becomes uniform, the other where it decreases like $1/r$. We investigate this by forming a series solution for u in terms of the asymptotic series r^{-n}. Substituting and equating coefficients we find,

$$\begin{aligned}
u_1 &= B^{1/2} - \frac{ga^2U}{2Br} - \frac{4B^2A^2 + 3g^2a^4U^2}{8B^{5/2}r^2} + O\left(\frac{1}{r^3}\right), \\
h_1 &= \frac{a^2U}{2B^{1/2}r} + \frac{ga^4U^2}{4B^2r^2} + O\left(\frac{1}{r^3}\right), \\
\text{or} \qquad u_2 &= \frac{ga^2U}{Br} + \frac{(ga^2U)^4 + B^4A^2}{B^4ga^2Ur^2} + O\left(\frac{1}{r^3}\right), \\
h_2 &= \frac{B}{2g} - \frac{(ga^2U)^4 + B^4A^2}{2B^2g^3a^4U^2r^2} + O\left(\frac{1}{r^3}\right),
\end{aligned} \tag{10}$$

for $r \gg a$. These are conjugate solutions, the first representing supercritical flow the second, subcritical flow. We shall concentrate first on the observed regime inside the jump – supercritical flow.

It can be seen from (10a,b) that, to first order, the velocity is constant and the depth decreases inversely with r. This justifies, to some extent, a further approximation of discarding the h-derivative in the r-momentum equation as negligibly small. It should be noted that this approximation removes the subcritical branch from the solution. In this approximation we have the simplified relations,

$$u^2 = C - A^2/r^2, \qquad v = A/r - fr/2,$$
$$h^2 = a^4U^2/4(Cr^2 - A^2),$$
$$A = fa^2/2, \qquad C = U^2 + f^2a^2/4, \tag{11}$$

which in the limit $f \to 0$ reduces to the profile of Watson [1]: $u = U$, $h = a^2/2r$.
Figure 3 shows plots of the calculated velocity and height distributions for various values of f, highlighting the effects of rotation and the h-derivative on the solutions. On the

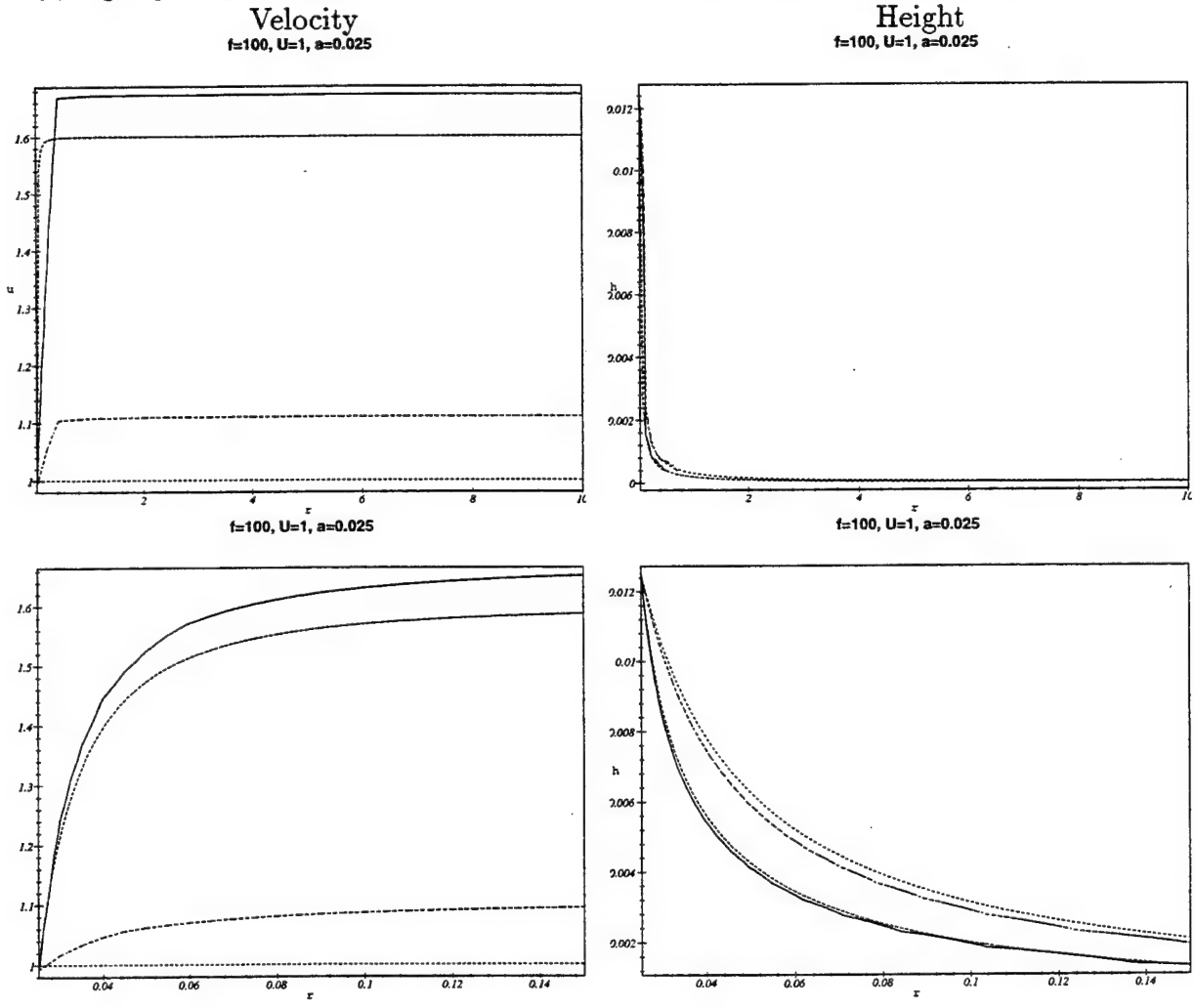

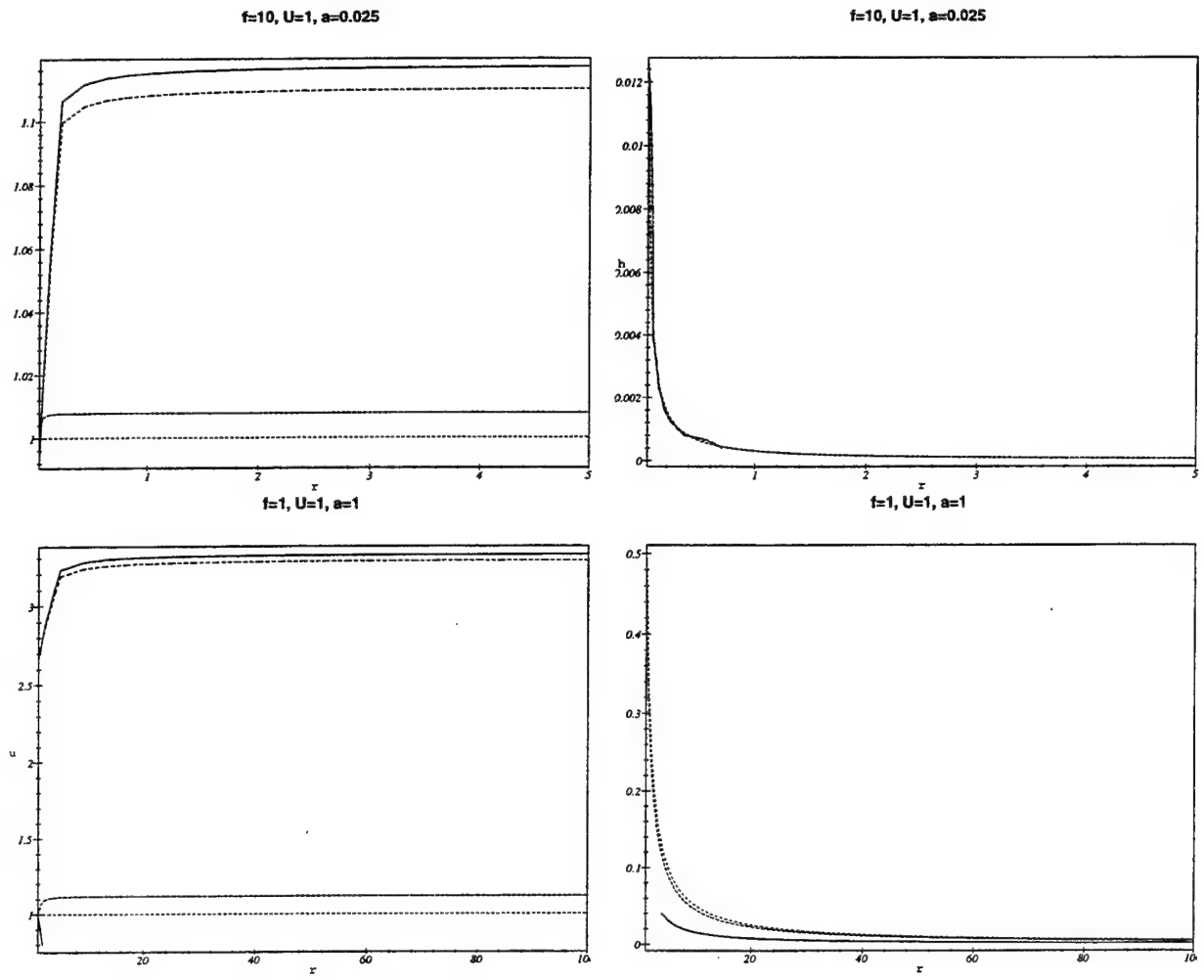

Figure 3.

left hand side, for the velocity profiles, the top (solid) curve represents the full solution including both rotation and the effects of h-derivative. The bottom, uniform, velocity profile is that determined by Watson by neglecting both of these terms. In between, we can see the curves representing the addition of rotation and the h-derivative, respectively, as the velocity increase above that of the Watson set-up.

It is clear from these plots that although the influence of rotation can be significant, the angular velocity of our frame, $f/2$, must be considerable (or the jet diameter large) for a measurable long-term difference. However, the inclusion of an h-derivative makes a much greater impact upon the value of the limiting, uniform flow the system settles to at large radii – still being 10% at $f = 1$. The principal contribution to this difference occurs near the jet, where the change in h is most rapid. Since h is inversely proportional to ru the order of the height profiles is reversed and the differences are far less pronounced.

The observations above are strongly supported by taking the appropriate limits of f and a in the asymptotic series (10). The series also highlight the 'uniform' nature to which the velocity settles. Figure 4 demonstrates the speed of convergence of these series and the

numerical proximity of the aymptotic series to the full analytic solution.

Velocity Height

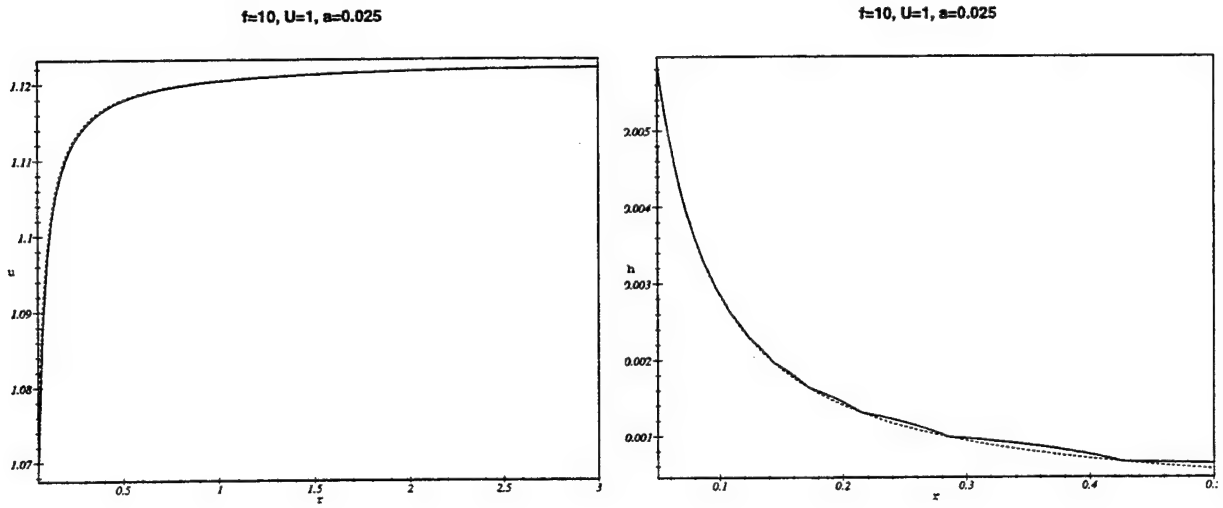

Figure 4.

The conjugate solution.

As we observed above, equation (7) is effectively a cubic and therefore we expect three solutions. One of these can be immediately discounted as unphysical, giving negative heights and velocities. The two remaining solutions represent the super and subcritical flows discussed earlier, termed conjugate. For example, we may plot as before the velocity and height profiles, but this time using the subcritical branch.

Velocity Height

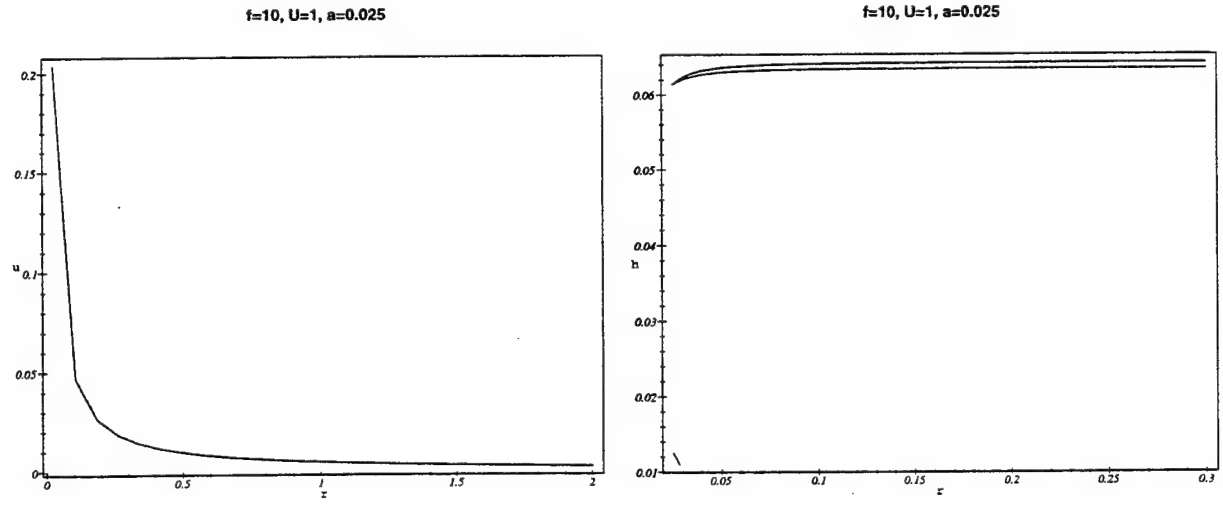

Figure 5.

We can see that now (as predicted by the series solution) the height profile approaches a uniform limit and the velocity decays inversely with r. This therefore is the solution that

is appropriate after the flow has jumped! For each flow rate Q we may determine both a supercritical and a subcritical flow and it is the transition from one solution to the other that is observed at the hydraulic jump. This is clearly demonstrated in figure 6a, where we can see that for a particular Q, we have for any value of r and 'Bernoulli' constant, B, two possible depths of fluid. We note that not necessarily all values of B shown are physical and only values for which there exist real U, a such that $Ua^2 = 1$ are attainable.

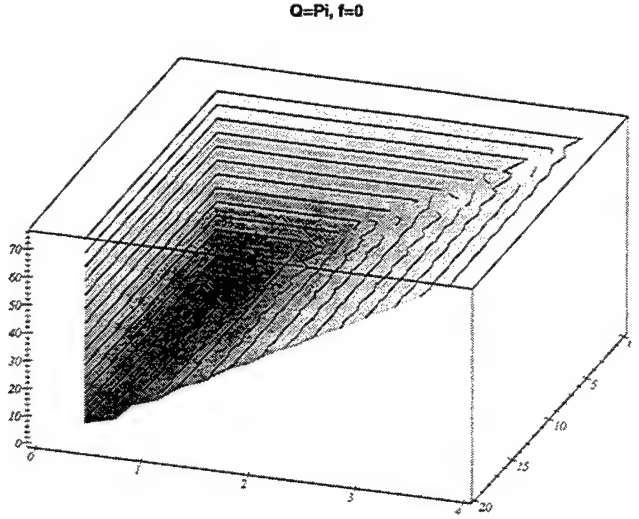

(a) the possible super and subcritical height profiles (horizontal axis) for various values of the Bernoulli constant, B(vertical axis), against the radius r(into the page),

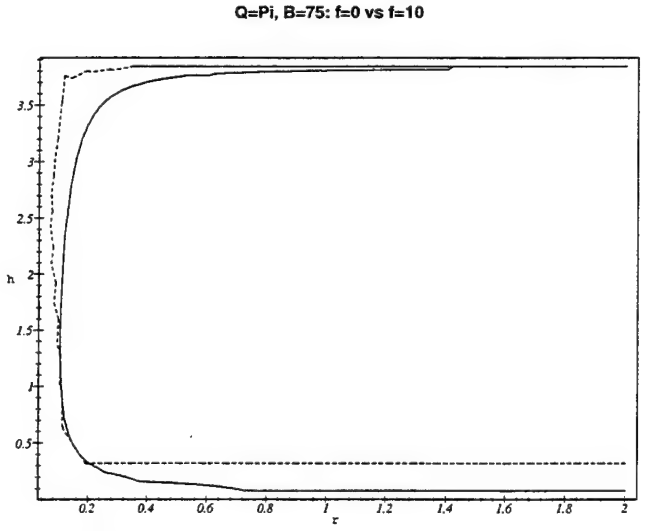

(b) a particular height profile showing both branches for B=75.

Figure 6.

Figure 6b compares the effect of rotation (solid curve) on the two possible height profiles

for a given Q and B.

The jump conditions.

It is observed that as the fluid spreads out radially from the jet as a thinner and thinner layer the flow eventually jumps from a supercritical fast-thin layer to a subcritical slow-thick layer. In order to determine conditions for the position of the jump, which can be checked experimentally or numerically, we might consider two distinct approaches: a) by maintaining a mass, momentum and angular momentum balance across the jump and b) by considering the characteristic wave speed of the flow, c, compared to the actual flow speed, u.

The method of characteristics is well developed in respect of shocks and jumps. By this method the governing equations are rewritten in terms of new variables, R, so that along characteristic curves defined by $\frac{\mathrm{d}r}{\mathrm{d}t} = c$, the R are invariant. The R are termed *Riemann invariants* and c the *characterstic wave speeds*. These speeds represent the rate at which information may travel through the fluid in the form of waves. Therefore, by tracing the values of the Riemann invariants along the characteristics we may construct a solution in the whole of the phase space. It is clear that if two independant characteristic curves meet, however, their respective values of R will conflict and it is at these points that a shock is formed. In general, however, this can only be determined numerically – analytically we find the somewhat redundant condition that the flow must be supercritical $u > (gh)^{1/2}$ for a steady jump to form *i.e.* both characteristic wave speeds are positive.

Mass, momentum and angular momentum balance: We consider a small cross-section of the jump , of radius $2\delta r$ about $\hat{r}$ as shown in figure 7, in the manner of Watson [1]. Assuming conservation of momentum across the jump we have that the rate of destruction of momentum across the jump is equal to the total 'thrust' due to pressure across the jump. But the pressure inside the jump is given by (5) and similarly $p = \rho g(d(r) - z)$ outside the jump. So that the thrust of pressure across our annular cross-section is given by,

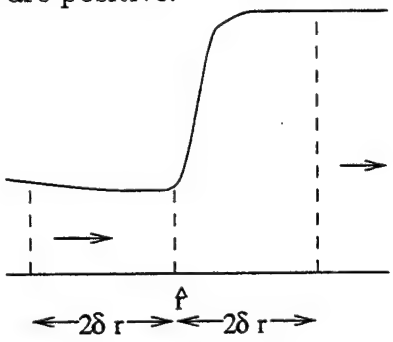

Figure 7.

$$\int_0^{2\pi}\int_0^{\hat{d}} \rho g(d(\hat{r}) - z)\hat{r}\,\mathrm{d}z\mathrm{d}\theta - \int_0^{2\pi}\int_0^{\hat{h}} \rho g(h(\hat{r}) - z)\hat{r}\,\mathrm{d}z\mathrm{d}\theta = \pi\rho g\hat{r}(\hat{d}^2 - \hat{h}^2). \tag{12}$$

The transport of momentum for the annulus can also be found:

$$\int_0^{2\pi}\int_0^{\hat{d}} \rho u(\hat{r}_-)^2\hat{r}\,\mathrm{d}z\mathrm{d}\theta - \int_0^{2\pi}\int_0^{\hat{h}} \rho u(\hat{r}_+)^2\hat{r}\,\mathrm{d}z\mathrm{d}\theta = 2\pi\rho\hat{r}(U_-^2\hat{h} - U_+^2\hat{d}), \tag{13}$$

where $U_\pm$ are the fluid velocities either side of the jump at $\hat{r} \pm \delta r$. Equating these we have,

$$\tfrac{1}{2}g\left(\hat{d}^2 - \hat{h}^2\right) = \left(U_-^2\hat{h} - U_+^2\hat{d}\right). \tag{14}$$

An additional condition also comes from considering conservation of mass (*i.e.* Q remains constant across the jump). So that,

$$U_- = a^2 U/2\hat{r}\hat{h}, \qquad U_+ = a^2 U/2\hat{r}\hat{d}. \tag{15}$$

We determine $\hat{h}$ by evaluating the height profile above at $\hat{r}$ and thus have a relationship between $\hat{r}$ and $\hat{d}$,

$$\tfrac{1}{2}g\left(\hat{d}^2 - \hat{h}^2\right) = \left(\frac{a^2 U}{2\hat{r}}\right)^2 \left(\frac{1}{\hat{h}} - \frac{1}{\hat{d}}\right). \tag{16}$$

Discarding the trivial solution $\hat{d} = \hat{h}$ we can plot the profiles of $\hat{d}$ against $\hat{r}$. In figure 8, the upper, solid line shows this profile for the full rotating solution the lower curve representing Watson's solution.

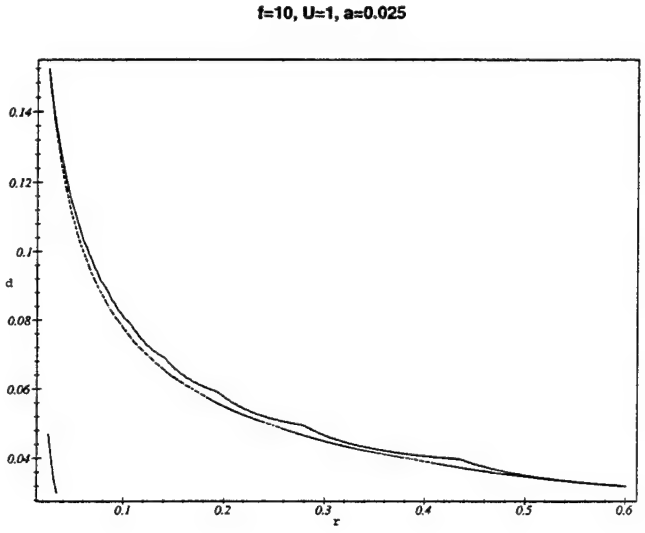

Figure 8.

Equation (16) may now be used to yield a lower bound on the jump radius $\hat{r}$. As we have discussed, the jump occurs where the flow changes from a shallow, supercritical flow to a deeper subcritical flow. Therefore, we expect that $\hat{d} > \hat{h}$ and, using (16),

$$g\hat{h}^3 < \tfrac{1}{2}g(\hat{d} + \hat{h})\hat{d}\hat{h} = \left(\frac{a^2 U}{2\hat{r}}\right)^2. \tag{17}$$

Therefore, substituting for the height profile of (7) and (8) we have a bound on $\hat{r}$. In the simple case of the Watson profile, $h = a^2/2r$, we find

$$\hat{r} > ga^2/2U^2. \tag{18}$$

We may also determine the azimuthal velocity profile (which could also jump) for $r > \hat{r}$ by considering the conservation of angular momentum. It is clear that the transport of

angular momentum into the jump must equal that away from the jump. But, the transport of angular momentum into the jump is given by,

$$\int_0^{2\pi}\int_0^{\hat{h}} \rho U_- v_-(\hat{r})\hat{r}^2 \mathrm{d}z\mathrm{d}\theta = 2\pi\rho U_- \hat{h}\hat{r}^2 v_-(\hat{r}) = \rho Q \hat{r} v_-(\hat{r}). \tag{19}$$

Since Q is conserved across the jump, we must have that $v_+(\hat{r}) = v_-(\hat{r})$. But the azimuthal velocity profile outside the jump is still given by (6) and thus, matching the unknown constant at $\hat{r}$, we have shown that the azimuthal velocity does **not** jump!
Therefore, outside the jump we return to our invisicd solution, (6) and (7), and use the matching conditions above, for $r = \hat{r}$, to determine the unknown constants and therefore provide a full invisicd solution for all r.

Determining the jump radius.
The conditions of the previous section do not determine a unique position for the jump given an initial inflow: equation (16) expresses a relationship between the jump radius, $\hat{r}$, and the depth of fluid just past the jump, $\hat{d}$. However, an interesting and practical application of this condition may be considered. Physically, the jump represents the transition of the radial outflow from supercritical to subcritical flow. Therefore, by introducing a ridge (or weir) at some fixed radius R, we may by the principles of hydraulic control, fix the subcritical flow upstream of the weir. Then, using our inviscid solutions (6) and (7) we may fully determine the subcritical flow from the upstream weir depth and velocity, d_w, U_w. (Note that only one of U_w, d_w is independent, as we must still impose our flux condition: $Q = 2\pi R d_w U_w$). Indeed for a thin weir, (*i.e.* so that r can be taken to be constant) we may use the methods of one dimensional weir analysis to show that the critical depth of fluid over the weir is $(Q^2/4g\pi^2R^2)^{1/3}$ – the critical point on the curve specifying $H - k$ in terms of the fluid depth across the weir for a fixed Q, where H is the Bernoulli head and k is the height topography of the weir. Therefore, d_w is found by solving the cubic,

$$\frac{Q^2}{8g\pi^2R^2d_w^2} + d_w = k_{\max} + \tfrac{3}{2}\left(\frac{Q^2}{4g\pi^2R^2}\right)^{1/3}, \tag{20}$$

where $k_{\max}$ is the height of the weir. In this manner, from a prescribed inflow and weir topography we may find a unique jump radius with which to test our inviscid theory. However, care must be exercised in choosing the our parameters: we require that the ridge does act as a weir and *controls* the flow. For example, the super and subcritical flows are given by taking the appropriate roots (as explained above) of,

$$u^2 = \begin{cases} -2gh - f^2a^4/4r^2 + U^2 + ga + f^2a^2/4, & r < \hat{r}, \\ -2gd - f^2a^4/4r^2 + U_w^2 + 2gd_w + f^2a^4/4R^2, & r > \hat{r}, \end{cases}$$
$$h = a^2U/2ur \quad r < \hat{r}, \qquad \text{and} \qquad d = a^2U/2ur \quad r > \hat{r}, \tag{21}$$

which determine our $U_{\pm}$, $\hat{h}$, $\hat{d}$ in equation (16). Numerically, for $U = 1\text{ms}^{-1}$, $a = 2.5\text{cm}$, $g = 9.81\text{ms}^{-1}$, $R = 25\text{cm}$, $f = 10\text{s}^{-1}$ we have,

$\hat{r}$=2.6cm, $\hat{h}$=1.195cm, U_-=1.006ms^{-1}, $\hat{d}$=14.965cm, U_+=0.080ms^{-1}, d_w=15.070cm, U_w=0.008ms^{-1},

$\hat{r}$=9cm, $\hat{h}$=0.317cm, U_-=1.095ms^{-1}, $\hat{d}$=8.560cm, U_+=0.041ms^{-1}, d_w=8.573cm, U_w=0.015ms^{-1},

$\hat{r}$=10cm, $\hat{h}$=0.285cm, U_-=1.096ms^{-1}, $\hat{d}$=8.140cm, U_+=0.038ms^{-1}, d_w=8.151cm, U_w=0.015ms^{-1},

$\hat{r}$=11cm, $\hat{h}$=0.258cm, U_-=1.101ms^{-1}, $\hat{d}$=7.777cm, U_+=0.037ms^{-1}, d_w=7.785cm, U_w=0.016ms^{-1},

$\hat{r}$=24.5cm, $\hat{h}$=0.115cm, U_-=1.109ms^{-1}, $\hat{d}$=5.271cm, U_+=0.024ms^{-1}, d_w=5.271cm, U_w=0.024ms^{-1}. (22)

By comparing such numerical calculations we find that, as verified by experiment, for a fixed weir height, $\hat{r}$ increases with rotation rate and flux. Also we find that for the same volume flux and weir, the thinner the jet the further out the jump.

Numerical calculation.

In order to verify the relations derived above for this idealised situation, a numerical simulation might be run using the time-dependent equations. In order to demonstrate this approach, we made use of a numerical channel flow model, adding a circular ridge to the bottom topography ensuring axisymmetry. The flow was initiated at each time-step so that a constant flux was maintained through the circle $r = a$ (*i.e.* $u = Ur/a$ for $r < a$) and h taken to be $a/2$ (constant) for $r < a$. The evolution of the fluid was followed as the flow evolved in time and the jump formed. We would not expect exact agreement with our theory as any numerical calculation must have a degree of dissipation (numerical viscosity) but we should find a close comparison with the above results. At present no data has been collected but an example of the steady jump, is shown in figure 9.

Laboratory experiments.

An experiment was performed to qualitatively verify the predictions of our inviscid theory, graphically demonstrate the extent of the effects of rotation and highlight further areas of interest and investigation. A square tank of side 21in was placed on a rotating table, inside which there was a circular perspex plate of diameter 20in. Removable weirs of heights 2cm and 1cm could be affixed at diameter 17in. Water was continually pumped from the tank into a vertical pipe of varying diameters ($\frac{1}{8}$in, $\frac{1}{4}$in, $\frac{3}{8}$in and $\frac{1}{2}$in) to produce a jet of constant flux and the whole apparatus rotated. Experiments demonstrated the following principal behaviour:

i) Bore diameter - bore diameter did not seem to have a measurable effect for the flow rates and sizes we used, however, the flow due to larger pipes seemed to be more stable.

ii) Rotation rate - the greater the rotation rate the greater the value of $\hat{r}$. In fact, the addition of rotation can introduce a hydraulic jump into a flow which when not rotating is engulfed in the subcritical regime. Using our apparatus we managed to attain angular velocities up to $f = 2$.

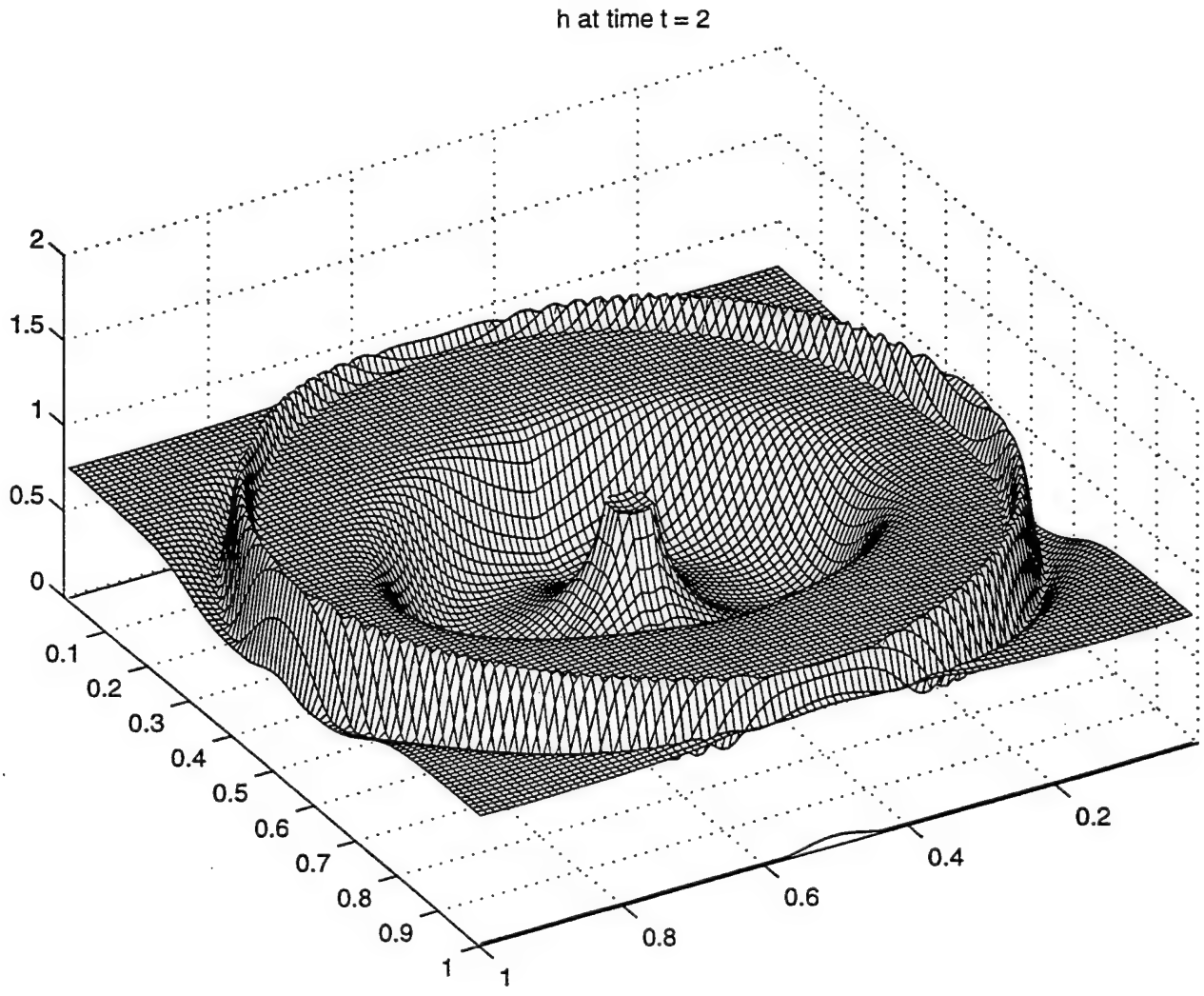

Figure 9.

iii) Flow rate - the greater the flow rate the greater the diameter of the jump. By reducing the flow rate sufficiently the subcritical flow created by the weir can collapse to engulf the incoming jet so that rotation is required to re-introduce the hydraulic jump.

iv) Weir height - the higher the weir the smaller the jump radius. The weir by controlling the 'downstream' flow parameters dramatically stabilised the flow, including reinforcing axisymmetry. In the absence of a weir the flow becomes very thin and more difficult to quantify and for our scale of apparatus the hydraulic jump rarely formed inside the radius of our disk.

v) Tilted - an interesting variation of the standard problem was also tried. The plate was tilted at an angle so that not only does gravity now play a role in the radial momentum equation but also the axis of rotation is not aligned with the z-axis. This resulted in the hydraulic jump becoming deformed to an 'elliptical' shape and no longer being centered below the jet. Also this allowed the possibility for slow enough flow rates for the higher part of the surface to become dry. Frequently the flow formed two regions a supercritical 'slip-way' off the plate and a horseshoe shaped halo of subcritical fluid surrounding it with the hydraulic jump occuring in between. As before, rotation and increased flux increased the jump radius.

A more precise experiment could be employed to compare analytic and experimental data, although in some regimes departure from axisymmetry, the measurement of depths and the introduction of air due to turbulent mixing at the interface could make accurate measurement difficult.

The viscous boundary layer.

It is clear from the above analysis that the layer of spreading fluid quickly becomes thin and that viscous forces are likely to play a significant role. It therefore becomes necessary to consider the problem in the context of boundary layer theory, *i.e.* $H \ll L$ for typical height and length scales H and L respectively. Clearly, we may no longer assume independence with respect to the vertical co-ordinate z and since $z \ll r$ we expect z-derivatives to dominate. The conservation of mass gives, still taking our system to be axisymmetric ($\partial/\partial\theta \equiv 0$),

$$\frac{1}{r}\frac{\partial}{\partial r}(ru) + \frac{\partial w}{\partial z} = 0. \tag{23}$$

Therefore, to maintain a balance of scales, we have that the magnitude of the velocities u, w satisfy,

$$u/r \sim w/z. \tag{24}$$

We may now write down the balance of first order terms in the momentum equations,

using $\nabla.\mathbf{u} \sim u\partial/\partial r + w\partial/\partial z$ and $\nabla^2 \sim \partial^2/\partial z^2$,

$$u\frac{\partial u}{\partial r} + w\frac{\partial u}{\partial z} - \frac{v^2}{r} - \frac{f^2 r}{4} - fv = -g\frac{\partial h}{\partial r} + \nu\frac{\partial^2 u}{\partial z^2},$$
$$u\frac{\partial v}{\partial r} + w\frac{\partial v}{\partial z} + \frac{uv}{r} + fu = \nu\frac{\partial^2 v}{\partial z^2}. \tag{25}$$

The boundary conditions we must satisfy now include the adherence condition on $z = 0$ and the no-stress condition on the surface:

$$u = v = w = 0 \qquad \text{on} \qquad z = 0,$$
$$\frac{\partial u}{\partial z} = \frac{\partial v}{\partial z} = 0 \qquad \text{on} \qquad z = h,$$
$$2\pi r \int_0^{h(r)} u\mathrm{d}z = Q. \tag{26}$$

Watson employs a similarity solution in order to solve the boundary layer equations in his configuration, where $v \equiv 0$ and $f = 0$. However, the addition of rotation considerably complicates the equations and the method of solution is no longer clear. The effects of the inclusion of the azimuthal velocity and extra terms in the momentum equations due to rotation need further consideration.

Further work.

i) Weir analysis – the upstream conditions created by the presence of the weir should be further investigated, taking into account the axisymmetric topology

ii) Experimentation – a more accurate experimental apparatus, might be employed to give quantitative results and a measure of the suitability of the inviscid approximation to the flow.

iii) Numerical – data could be collected to test the nearly inviscid theory and viability of the steady approximation. In addition any instability should e highlighted.

iv) Stability – the stability of the calculated flow regime might be investigated including the susceptability of the hydraulic jump to linear wave-like instabilities.

v) Viscosity – a more detailed analysis of the viscous regime and the adjustment of the essentially inviscid flow to the viscous boundary layer could be performed.

vi) Tilt – a treatment of the tilted regime described in the experimental section might raise interest in the form of new flow regimes and instabilities.

References.

[1] WATSON E J, 1964 *The radial spread of a liquid jet over a horizontal plane,* JFM **20,** 481-499

[2] BOWLES R I & SMITH F T, 1992 *The standing hydraulic jump: theory, computations and comparisons with experiments,* JFM **242,** 145-168

[3] CRAIK *et al.*, 1981 *The circular hydraulic jump,* JFM **112,** 347-362

Acknowledgements.
The above project was suggested and supervised by Ted Johnson whose help and encouragement throughout was invaluable.
I am also very grateful to John Salzig, whose speedy efforts made the laboratory experiments possible and so successful. In addition the work of Eric Chassignet to produce the numerical simulations using the code of Karl Helfrich is greatly appreciated.
Finally, I would like to thank all the fellows and staff of the GFD programme at Woods Hole Oceanographic Institution for their considerable support and assistance on this project, and for making the summer such an enjoyable one.

Fluid Intrusion in a Rotating Channel

Allen C. Kuo

1 Introduction

It has been argued that climatological change may depend in part on flows in the deep oceanic basins (Watts & Hayder 1983). A key to understanding these flows is knowledge of the transports between them, i.e. knowledge of sill flow. This report examines, analytically and numerically, a related (initial value) problem: the breaking of a dam in a channel under the influence of rotation. We briefly review past work.

One of the first attempts at understanding sill flow in the geophysical context was made by Whitehead, Leetma & Knox (1974). They applied existing *steady* hydraulic theories and incorporated rotational effects to study sill flow in the zero potential vorticity limit. They were able to calculate mass transports in terms of the rotation rate and the difference in depth between the upstream reservoir and the sill height. Gill (1977) provided a more general theory for hydraulics type flows under the influence of rotation and extended steady, rotating hydraulic theory to constant, not necessarily zero, potential vorticity flow. Pratt (1983), using numerical means and the characteristics formalism, contributed to our understanding of *time-dependent* rotating hydraulics.

Two simplifying approximations exist in the theoretical work mentioned above: the assumption of constant potential vorticity and the assumption of geostrophic along-sill/channel flow (semi-geostrophy). Here, we continue to use these approximations to study the time-dependent intrusion of a fluid mass in a constant width channel under the influence of rotation. Dam break initial conditions are used. The characteristic method and simple wave theory are applied to obtain an analytical solution. The nature of the flow is investigated as a function of the width of the channel. (Stern, Whitehead & Hua 1982 considered the infinite width case). Formal validity of the semigeostrophic equations is expected in the limit of narrow channel width and long times; numerical computations of the full equations of motion bear out this idea. Differences and similarities between theory and computations are examined as the flow evolves. Lastly, steady state solutions are found and the associated mass transports are calculated.

We note that the related and important problem of transients in the hydraulic control process, due to changes in channel width or topography, is not investigated here.

2 Mathematical Problem Formulation

The non-dimensional model equations used in this study which govern a rotating, inviscid, homogeneous, "shallow-layer" layer of a fluid flowing beneath a deep, inactive upper layer of fluid (a $1\frac{1}{2}$ layer model) can be found in Pratt & Whitehead. Repeated here, they are:

$$\delta^2\left(\frac{\partial u}{\partial t}+u\frac{\partial u}{\partial x}+v\frac{\partial u}{\partial y}\right)-v=-\frac{\partial d}{\partial x} \tag{1}$$

$$\frac{\partial v}{\partial t}+u\frac{\partial v}{\partial x}+v\frac{\partial v}{\partial y}+u=-\frac{\partial d}{\partial y}-\frac{\partial h}{\partial y} \tag{2}$$

$$\frac{\partial d}{\partial t}+\frac{\partial}{\partial x}(ud)+\frac{\partial}{\partial y}(vd)=0, \tag{3}$$

The layer thickness d is scaled by D, x (cross-channel length scale) by the deformation radius $\sqrt{gD}/f$, y (along-channel length scale) by an arbitrary length scale L, u by gD/fL, v by a linear gravity wave speed $\sqrt{gD}$, and time by $(L/\sqrt{(gD)})$. Notice that we have included a y (but not x) dependent topographic term h here, scaled by D, for generality but topographic effects are ignored in the initial value problem studied here. The hope is that this effect will be incorporated in a future study.

We wish to investigate the breaking of a dam in an infinitely long channel of width w and hence, the following initial and boundary conditions:

$$
\begin{aligned}
u(x,y,t=0) &= 0 \\
v(x,y,t=0) &= 0 \\
d(x,y,t=0) &= \begin{cases} 1 & y<0 \\ 0 & y>0 \end{cases} \\
u(x=\pm w/2,y,t) &= 0
\end{aligned}
$$

The following diagram shows the lower layer of fluid in a section of the channel at $t = 0$:

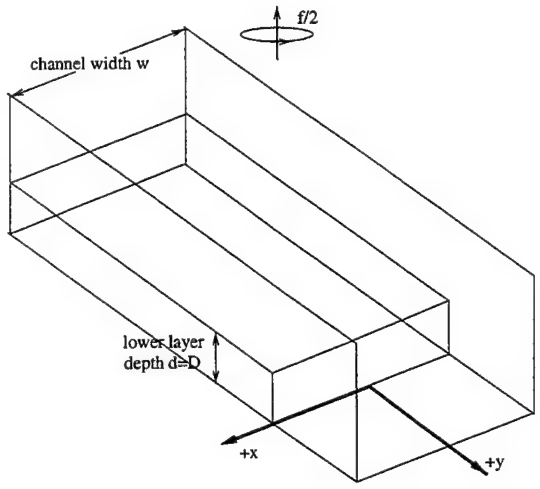

Figure 1: Initial conditions.

3 Semigeostrophic Approximation

The parameter $\delta \equiv \frac{\sqrt{gD}}{fL}$ which appears in Eq. (1) is the ratio of the width to length scale of the flow (or equivalently the u scale to the v scale). We henceforth narrow our focus by considering flows such that variations are much greater cross-channel than along-channel so that $\delta << 1$. Formally then, we may neglect the acceleration terms in Eq. (1), thus making the so-called semigeostrophic approximation.

The validity of the semigeostrophic approximation is questionable in the short instances after the "dam" breaks. But should the channel be narrow, we may expect that the constraining effects of the side walls to be significant enough to suppress strong u velocities; δ remains small. At the other extreme, complete breakdown of the theory should occur for very wide channels where a strong positive u velocity will develop shortly after the dam breaks.

In either case, since we expect a rarefaction type of solution, validity of the approximation should increase in time. Formally we might say that semigeostrophic theory is valid in the limits $w \to 0$ and $t \to \infty$. Comparison of the solution with numerical computations will show this to be the case and that good agreement can be found for channels as wide as two deformation radii.

Having argued for the approximation, we use it. The approximation allows us to solve for the cross-channel structure of d and v, but in addition, we need the following dimensionless potential vorticity equation (neglecting the $O(\delta^2)$ relative vorticity term):

$$
q = \frac{1 + \frac{\partial v}{\partial x}}{d}, \tag{4}
$$

The potential vorticity q has been nondimensionalized by $\frac{f}{D}$. Because of our initial conditions, q is constant initially. Dimensionally, $q = \frac{f}{D}$; nondimensionally, $q = 1$.

Since many of the formulas and equations derived or used in this paper are not dependent on the initial conditions, we will not take $q = 1$ until necessary to solve this particular problem. This will allow us to give expressions having greater generality than would otherwise be the case. We still assume q to be constant, but not necessarily equal to unity. Its value is set from upstream conditions: assuming an upstream reservoir/source of potential depth (see Pratt & Whitehead) D_∞, this implies that $q = D/D_\infty$ nondimensionally.

Solving the two equations (1) and (4) yields:

$$d(x,y,t) = q^{-1} + \hat{d}(y,t)\frac{\sinh[q^{\frac{1}{2}}x]}{\sinh[\frac{1}{2}q^{\frac{1}{2}}w]} + (\bar{d}(y,t) - q^{-1})\frac{\cosh[q^{\frac{1}{2}}x]}{\cosh[\frac{1}{2}q^{\frac{1}{2}}w]}, \tag{5}$$

$$v(x,y,t) = q^{\frac{1}{2}}\hat{d}(y,t)\frac{\cosh[q^{\frac{1}{2}}x]}{\sinh[\frac{1}{2}q^{\frac{1}{2}}w]} + q^{\frac{1}{2}}(\bar{d}(y,t) - q^{-1})\frac{\sinh[q^{\frac{1}{2}}x]}{\cosh[\frac{1}{2}q^{\frac{1}{2}}w]}, \tag{6}$$

The above solution is written in terms of two unknown integration constants: $\bar{d}$ and $\hat{d}$. $\bar{d}$ is the average of the sidewall depths across the channel. $\hat{d}$ represents half the difference in sidewall depths. The solution for the u velocity can be obtained diagnostically from Eq. (2).

For large enough velocities v, the flow may detach from the assumed rectangular channel (the left wall in the Northern hemisphere). The above profile must be modified since the above solution assumes symmetry of the channel walls across the line $x = 0$. It is not difficult to show that in this case:

$$d(x,y,t) = q^{-1} + \bar{d}(y,t)\frac{\sinh[q^{\frac{1}{2}}(x - x_c(y,t))]}{\sinh[\frac{1}{2}q^{\frac{1}{2}}w_e(y,t)]} + (\bar{d}(y,t) - q^{-1})\frac{\cosh[q^{\frac{1}{2}}(x - x_c(y,t))]}{\cosh(\frac{1}{2}q^{\frac{1}{2}}w_e(y,t))}, \tag{7}$$

$$v(x,y,t) = q^{\frac{1}{2}}\bar{d}(y,t)\frac{\cosh[q^{\frac{1}{2}}(x - x_c(y,t))]}{\sinh[\frac{1}{2}q^{\frac{1}{2}}w_e(y,t)]} + q^{\frac{1}{2}}(\bar{d}(y,t) - q^{-1})\frac{\sinh[q^{\frac{1}{2}}(x - x_c(y,t))]}{\cosh[\frac{1}{2}q^{\frac{1}{2}}w_e(y,t)]}, \tag{8}$$

Here, the two integration constants are now $\bar{d}$ and the width of the separated flow w_e. Also, $x_c \equiv w - w_e(y,t)$.

In summary, the mathematical problem has been reduced to finding, as functions of y and t, the integration constants $\bar{d}$ and $\hat{d}$ for the case of attached flows, and $\bar{d}$ and w_e for the case of separated flow. The first-order quasilinear partial differential equations governing these quantities, as well as their initial conditions, are given in the next two sections.

4 Reduced Equations: Attached Flow

The governing equations for $\bar{d}$ and $\hat{d}$ can be found in Pratt (1984). We simply repeat them here.

$$q^{\frac{1}{2}}T^{-1}\frac{\partial \hat{d}}{\partial t} + \frac{\partial \bar{B}}{\partial y} = 0 \tag{9}$$

$$2q^{-\frac{1}{2}}T\frac{\partial \bar{d}}{\partial t} + \frac{\partial Q}{\partial y} = 0 \tag{10}$$

where $Q = 2\bar{d}\hat{d}$ is the flow rate, $\bar{B} = \frac{1}{2}q(T^{-2}\hat{d}^2 + T^2(\bar{d} - q^{-1})^2) + \bar{d} + h$ is the y-averaged Bernoulli function, and $T \equiv \tanh(w/2)$ is a measure of the width of the channel.

Initial conditions for these equations are:

$$\hat{d}(y, t = 0) = 0 \tag{11}$$

$$\bar{d}(y, t = 0) = \begin{cases} 1 & y < 0 \\ 0 & y > 0 \end{cases} \tag{12}$$

The assumption of semigeostrophy has reduced the problem of finding 3 unknowns in 3 independent variables to 2 unknowns in 2 independent variables y and t.

5 Reduced Equations: Separated Flow

The governing equations for $\bar{d}$ and w_e can be found in Pratt & Whitehead. We repeat them here.

$$\frac{\partial(q^{1/2}T_e^{-1}\bar{d})}{\partial t} - \frac{1}{2}\frac{\partial w_e}{\partial t} + \frac{\partial \bar{B}}{\partial y} = 0 \tag{13}$$

$$\frac{\partial(q^{1/2}T_e(\bar{d}-q^{-1}))}{\partial t} + \frac{1}{2}\frac{\partial w_e}{\partial t} + \frac{1}{2}q\frac{\partial Q}{\partial y} = 0 \tag{14}$$

where

$$Q = 2\bar{d}^2 \tag{15}$$

is the time dependent transport which depends on y,

$$\bar{B} = \frac{1}{2}q[T_e^{-2}\bar{d}^2 + T_e^2(\bar{d}-q^{-1})^2] + \bar{d} + h \tag{16}$$

is the cross-channel averaged Bernoulli function, and

$$T_e \equiv \tanh(w_e/2) \tag{17}$$

Strictly speaking, at $t = 0$, the above equations are not applicable so we do not give initial conditions. "Initial conditions" are obtained by a matching procedure with the solution in the attached region.

6 Solution to IVP

6.1 Solution: Overview

We first give an outline of our solution methodology. It is helpful to imagine finding the solution in the y–t plane, indicated schematically below:

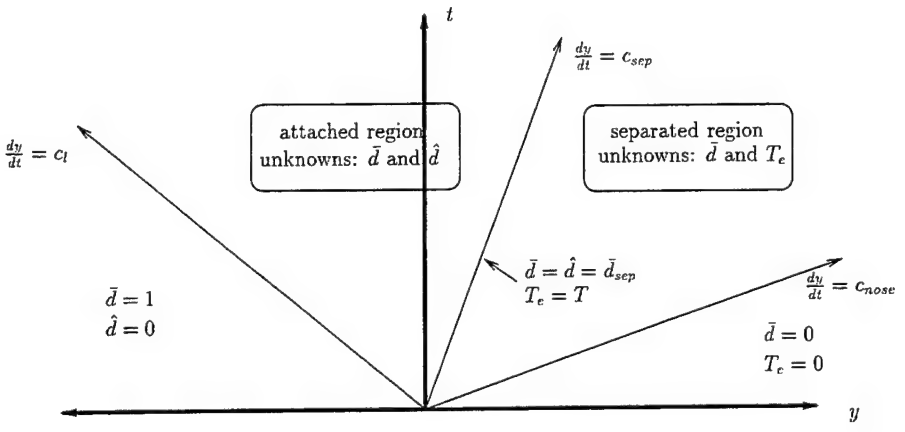

Figure 2: Schematic characteristic diagram showing the two regions where the solution is sought. $\bar{d}$, $\hat{d}$, T_e, c_l, c_{sep} and c_{nose} are all to be found. Note that we have chosen to solve for T_e rather than w_e in the separated region for the sake of mathematical convenience.

There are two regions where the solution is sought- the attached region and the separated region. We first solve the problem in the attached region. The relevant unknowns here are $\bar{d}$ and $\hat{d}$. This region is delimited on the left by some line in y–t space which represents the propagation of

information about the actual dam break upstream. The slope of this line we term c_l and is to be determined. The region is delimited on the right by assuming that there exists a line in y–t space where $\bar{d} = \hat{d} \equiv \bar{d}_{sep}$. If such is the case, then by definition of $\bar{d}$ and $\hat{d}$, the depth of the fluid must be zero on one wall (which must be the left wall in the northern hemisphere), implying separation. The slope of this line is a measure of the speed of the separation point c_{sep}, to be determined.

To the right of this line is the separated region where T_e and $\bar{d}$ are sought. (Note that we have chosen to solve for T_e rather than w_e for the sake of mathematical convenience.) We postulate that this region is delimited on the right by a line in y–t space where $\bar{d} = 0$, in analogy with the one dimensional dam break problem. The slope of this line is a measure of the speed of the nose of the fluid intrusion, which we call c_{nose} and is to be found.

It is not clear that the (characteristic) lines delimiting the two regions are straight. We will argue that this is in fact the case through simple wave theory (Stoker 1955, Whitham 1974). It is precisely this feature of the characteristic lines that makes the reduced problem mathematically tractable.

In the following two subsections, we describe in detail how the solution to Eqns. (9), (10), (13), and (14) are found for $\bar{d}$, $\hat{d}$ and T_e. We urge the reader to skip these detail-filled subsections on first reading and go on to the results of Section 7.

6.2 Solution: Attached Region

We solve Eqns. (9) and (10) with initial conditions (11) and (12) by using the method of characteristics.

First, we write the equations in this region in standard quasilinear form

$$\mathbf{u}_t + \mathbf{A}\mathbf{u}_y + \mathbf{B} = 0 \tag{18}$$

with $\mathbf{u}$ representing the vector of dependent variables:

$$\mathbf{u} = \begin{pmatrix} \bar{d} \\ \hat{d} \end{pmatrix}$$

$\mathbf{A}$ and $\mathbf{B}$ are given by:

$$\mathbf{A} = \begin{pmatrix} q^{1/2}\hat{d}T^{-1} & q^{1/2}\bar{d}T^{-1} \\ q^{1/2}T^3(\bar{d} - q^{-1}) + q^{-1/2}T & q^{1/2}\hat{d}T^{-1} \end{pmatrix}$$

$$\mathbf{B} = \begin{pmatrix} 0 \\ q^{-1/2}T\frac{\partial h}{\partial y} \end{pmatrix}$$

At this point, matters are simplified if we take $\frac{\partial h}{\partial y} = 0$. Then, a straightforward diagonalization of Eq. (18) yields the interpretation that on the characteristic lines in y–t space given by:

$$\frac{\mathrm{d}y}{\mathrm{d}t} = c_{\pm}^{attach} \equiv q^{1/2}\hat{d}T^{-1} \pm \bar{d}^{1/2}[1 - (1 - q\bar{d})T^2]^{1/2} \tag{19}$$

the following differential relationship holds:

$$\frac{\mathrm{d}\hat{d}}{\mathrm{d}\bar{d}} = \mp(q\bar{d})^{-1/2}T[1 - (1 - q\bar{d})T^2]^{1/2} \tag{20}$$

The above equation may be integrated immediately to yield the following relationship between $\bar{d}$ and $\hat{d}$ on the characteristic lines:

$$R_{\pm} = q^{1/2}\hat{d}T^{-1} \pm \left(\bar{d}^{1/2}[1 - (1 - q\bar{d})T^2]^{1/2} + \frac{(1 - T^2)}{q^{1/2}T}\log\left[2(q\bar{d})^{1/2}T + 2[1 - (1 - q\bar{d})T^2]^{1/2}\right]\right) \tag{21}$$

(Compare the above expression with the one obtained by Pratt (1984)).

At this point, we specialize to our particular initial conditions and take $q = 1$. $R_{\pm}$, the integration constants of Eq. (20) (the Riemann invariants), can be found as a function of the width parameter T by evaluating Eq. (21) at $t = 0$ when $\bar{d} = 1$ and $\hat{d} = 0$:

$$R_{\pm} = \pm\left[1 + \left(\frac{1 - T^2}{T}\right)\log(2T + 2)\right] \tag{22}$$

Below is a plot of the relationship between $\bar{d}$ and $\hat{d}$ as given by the "plus" Riemann invariant for several choices of the channel width. Note that where $\hat{d} > \bar{d}$, the Riemann invariants are no longer relevant since the flow would be separated.

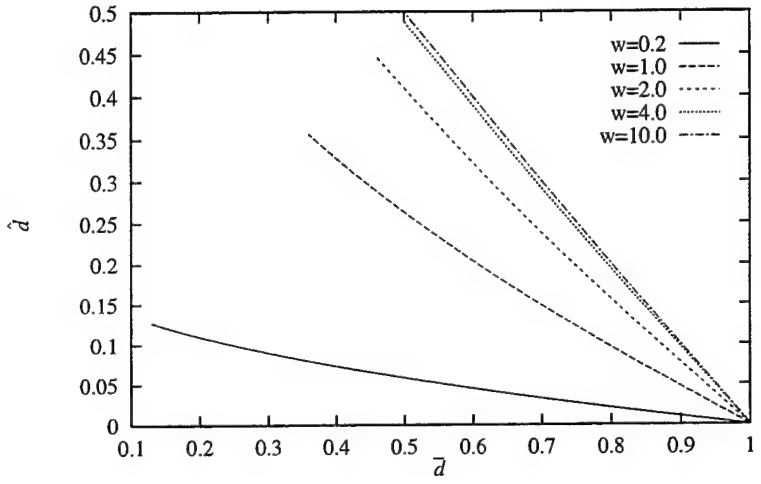

Figure 3: "Plus" Riemann invariant for the case of attached flow.

Now, we may apply simple wave theory to this problem. Two solutions are possible depending on whether one chooses R_+ or R_- as a constant initially (at this point, they both seem to be constant at $t = 0$!). In the next two paragraphs, we argue on physical grounds that R_+ is the correct choice of constant at $t = 0$.

We consider the solution to the dam break problem at an infinitesimal time Δt after the "dam" breaks. In this case, we might expect that under gravity, an infinitesimal "slumping", indicated schematically in Fig. 4 below, to occur. If either $R+$ or R_- were chosen constant for all $y < 0$ at $t = 0$, then the relationship (21) between dependent variables will hold for all time in the attached region of Fig. 2. Specifically, at $t = \Delta t$, we can evaluate $\hat{d}$ given a $\bar{d}$. "Physically", we expect it to be greater than or equal to zero, corresponding to a velocity v in the positive y direction. We shall show that taking R_- as a constant at $t = 0$ is "unphysical" since it leads to a negative v velocity.

Inspect Eq. (20). The positive sign corresponds to R_- and implies that as $\bar{d}$ decreases, $\hat{d}$ decreases. As one travels along the y axis in the positive direction starting where $\bar{d} = 1$, $\hat{d}$ must eventually decrease from zero, i.e. it is negative, which implies a negative v velocity. *q.e.d.*

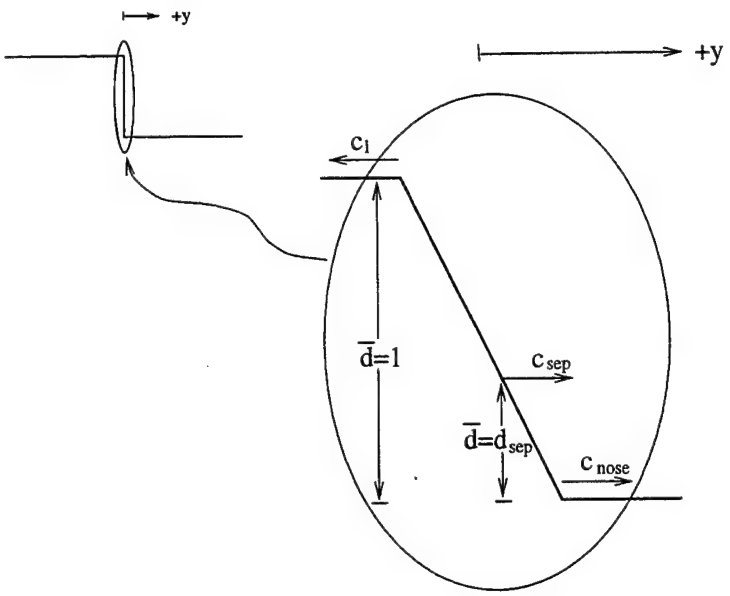

Figure 4: Schematic diagram of $\bar{d}$ at an infinitesimal time Δt after the "dam" breaks. Assuming that the perfectly discontinuous initial condition at $t = 0$ can be approximated by this condition at $t = \Delta t$, one can argue more plausibly for the simple wave solution in the unseparated regime.

The discontinuous structure of the initial conditions is difficult to comprehend. It is more helpful to think of the above qualitative schematic as an initial condition for $\bar{d}$- we might imagine that as $\Delta t \to 0$, the solution to the initial value problem (IVP) with initial conditions (IC) given by Eqns. (11) and (12) converges to the solution of the IVP with the IC indicated schematically above. A similar qualitative schematic could be drawn for $\hat{d}$ and would show an increase from zero to a maximum value at the point where $\bar{d} = \bar{d}_{sep}$ is indicated. Beyond that point, conditions on T_e must be specified.

Now, with R_+ argued to be the correct choice of constant at $t = 0$, we invoke simple wave theory (Whitham 1974) which implies that c_-^{attach} is constant on the characteristic lines defined by $dy/dt = c_-^{attach}$. This implies a set of straight line characteristic given by $y/t = c_-^{attach}$. With this fact, the solution for $\bar{d}$ and $\hat{d}$ as a function of y/t and the width parameter T in the attached region of Fig.2 is given by the solution of the equation for the characteristic lines and the R_+ equation (21):

$$y/t = \hat{d}T^{-1} - \bar{d}^{1/2}[1-(1-\bar{d})T^2]^{1/2} \tag{23}$$

$$1+\left(\frac{1-T^2}{T}\right)\log(2T+2) = \hat{d}T^{-1} + \bar{d}^{1/2}[1-(1-\bar{d})T^2]^{1/2} + \frac{(1-T^2)}{T}\log\left[2\bar{d}^{1/2}T + 2[1-(1-\bar{d})T^2]^{1/2}\right] \tag{24}$$

The problem of solving the partial differential equations (10) and (9) has thus been reduced to the problem of solving simultaneously two transcendental algebraic equations. The algebra problem is solved numerically. It is necessary, though, to first find in what region of y–t space the numerical solution is valid. In others words, we need to find to find c_l and c_{sep} of Fig. 2. (It will be necessary to determine $\bar{d}$ at the point of flow separation, $\bar{d}_{sep}$, before one can obtain c_{sep}.)

To find c_l, which represents the leftmost tip of the leftward propagating disturbance, we assume continuity and solve Eq. (23) using the condition/definition that on $y/t = c_l$, $\hat{d} = 0$ and $\bar{d} = 1$. We see that c_l=-1 regardless of the width. Just as in the nonrotating dam break problem, the tip of the rarefaction region travels at the linear gravity wave speed (it can be viewed as an infinitesimal disturbance).

Next, we find $\bar{d}_{sep}$ as a function T. This is done by solving Eq. (24) taking $\bar{d} = \hat{d} = \bar{d}_{sep}$; the numerically computed solution is shown in Section 7. But we can give a qualitative idea of the

dependence on T by examining the limiting form of $\bar{d}$ in the wide and narrow channel limits.

For the narrow channel limit, take $T = 0$ in Eq. (24) where it is then seen that $\bar{d}_{sep} = 0$. This makes sense, since we would expect the two dimensional nature of the flow, caused by rotation, to be suppressed to one dimension as the channel narrows; flow separation becomes less of an effect. The region of flow separation should be gradually reduced until the point of flow separation coincides with the nose of the fluid, which from the nonrotating dam break problem is known to be zero.

In the wide channel limit, $T = 1$, implying $\bar{d} = .5$. This limit is not as obvious as the previous. In any case, we expect a monotonic increase in $\bar{d}$ from 0 to .5 as T ranges from 0 to 1 since there is no reason to expect maxima or minima.

Finally, we find the speed of the separation point c_{sep} as a function of T by solving Eq. (23) under the conditions that $\bar{d} = \hat{d} = \bar{d}_{sep}$ for $y/t = c_{sep}$. This yields the dependence of c_{sep} on $\bar{d}_{sep}$, whose dependence on T was given above.

Once again, we may obtain a qualitative understanding of how c_{sep} varies with T. As stated above, when $T = 0$, $\bar{d} = 0$. This implies from Eq. (23) that $c_{sep} = 2$. This is consistent with the argument presented above about how the separation point becomes the point of the nose of the fluid intrusion as the channel narrows. At $T = 1$, $\bar{d} = .5$, implying $c_{sep} = 0$: the separation point is motionless. In general, we might expect c_{sep} to decrease monotonically from 2 to 0 as T increases from 0 to 1.

6.3 Solution: Separated Region

As in the attached case, we obtain the solution in the separated region using the method of characteristics. Unlike the attached case, we will not obtain an explicit expression for the Riemann invariants since the differential equations satisfied on characteristic lines appear intractable.

As before, we cast Eqns. (13) and (14) into standard quasilinear form

$$\mathbf{p}_t + \mathbf{C}\mathbf{p}_y + \mathbf{D} = 0 \tag{25}$$

where $\mathbf{p}$ represents the vector of dependent variables:

$$\mathbf{p} = \begin{pmatrix} \bar{d} \\ T_e \end{pmatrix}$$

Also, $\mathbf{C} \equiv \mathbf{E}^{-1}\mathbf{F}$ and $\mathbf{D} \equiv \mathbf{E}^{-1}\mathbf{G}$. $\mathbf{E}$, $\mathbf{F}$ and $\mathbf{G}$ are given by:

$$\mathbf{E} = \begin{pmatrix} q^{1/2}T_e & q^{1/2}(\bar{d} - q^{-1}) + q^{-1/2}(1 - T_e^2)^{-1} \\ q^{1/2}T_e^{-1} & -q^{1/2}\bar{d}T_e^{-2} - q^{-1/2}(1 - T_e^2)^{-1} \end{pmatrix}$$

$$\mathbf{F} = \begin{pmatrix} 2q\bar{d} & 0 \\ q\bar{d}T_e{}^{-}2 + qT_e{}^{2}(\bar{d} - q^{-1}) + 1 & -q\bar{d}^2T_e{}^{-3} + qT_e(\bar{d} - q^{-1})^2 \end{pmatrix}$$

$$\mathbf{G} = \begin{pmatrix} 0 \\ \frac{\partial h}{\partial y} \end{pmatrix}$$

Matrix multiplication gives the elements of the matrix $\mathbf{C}$

$$\begin{aligned} c_{11} &= \frac{3q\bar{d} + T_e^2 + (q\bar{d} - 1)T_e^4}{2q^{1/2}T_e} \\ c_{12} &= \frac{(q\bar{d} - 1)^2T_e^4 - (q\bar{d})^2}{2q^{3/2}T_e^2} \\ c_{21} &= \frac{q^{1/2}(T_e^2 - 1)^2(q\bar{d} - (1 - q\bar{d})T_e^2}{2(q\bar{d} + (1 - q\bar{d})T_e^2)} \\ c_{22} &= \frac{(1 - T_e^2)(q\bar{d} - (1 - q\bar{d})T_e^2)}{2q^{1/2}T_e} \end{aligned}$$

and the column vector $\mathbf{D}$

$$\mathbf{D} = \frac{\partial h}{\partial y}\left(\frac{T_e(T_e^2-1)}{2(q\bar{d}+(1-q\bar{d})T_e^2)}\right)\cdot\begin{pmatrix} -q^{1/2}(\bar{d}-q^{-1}) - q^{-1/2}(1-T_e^2)^{-1} \\ q^{1/2}T_e \end{pmatrix}$$

Multiplication of Eq. (25) by the left eigenvector matrix $\mathbf{S^{-1}}$ of $\mathbf{C}$ yields:

$$\mathbf{S}^{-1}\mathbf{p}_t + \mathbf{\Lambda}\mathbf{S}^{-1}\mathbf{p}_x + \mathbf{S}^{-1}\mathbf{D} = 0$$

The elements of $\mathbf{S^{-1}}$, which we call $\hat{s}_{ij}$, are:

$$\begin{aligned}
\hat{s}_{11} &= \frac{1}{\det \mathbf{S}} \\
\hat{s}_{12} &= \frac{1}{\det \mathbf{S}}\left(\frac{c_{12}}{c_{11}-c_-}\right) \\
&= \frac{1}{\det \mathbf{S}}\left(\frac{-q^2\bar{d}^2 + (1-2q\bar{d}+q^2\bar{d}^2)T_e^4}{qT_e\left(q\bar{d}+T_e^2+(q\bar{d}-1)T_e^4+2(q\bar{d})^{1/2}T_e[1-(q\bar{d}-1)T_e^2]^{1/2}\right)}\right) \\
\hat{s}_{21} &= -\hat{s}_{11} \\
\hat{s}_{22} &= -\frac{1}{\det \mathbf{S}}\left(\frac{c_{12}}{c_{11}-c_+}\right) \\
&= \frac{1}{\det \mathbf{S}}\left(\frac{q^2\bar{d}^2 - (1-2q\bar{d}+q^2\bar{d}^2)T_e^4}{qT_e\left(q\bar{d}+T_e^2+(q\bar{d}-1)T_e^4-2(q\bar{d})^{1/2}T_e[1-(q\bar{d}-1)T_e^2]^{1/2}\right)}\right)
\end{aligned}$$

$\det \mathbf{S}$ need not be calculated since it cancels out of the equation.
The diagonal $\mathbf{\Lambda}$ matrix is given by:

$$\mathbf{\Lambda} = \begin{pmatrix} c_+^{sep} & 0 \\ 0 & c_-^{sep} \end{pmatrix}$$

where

$$c_\pm^{sep} \equiv q^{1/2}\bar{d}T_e^{-1} \pm \bar{d}^{1/2}[1-(1-q\bar{d})T_e^2]^{1/2} \tag{26}$$

Notice that the above equation is just Eq. (19) with $\hat{d}$ replaced by $\bar{d}$ and T replaced by T_e.

At this point, it is necessary to take $\frac{\partial h}{\partial y} = 0$ implying $\mathbf{D} = \mathbf{0}$; otherwise, the interpretation of conserved quantities on characteristic lines is lost and an explanation becomes tedious. Doing so, we have the following two relationships between $\bar{d}$ and T_e (corresponding to the plus and minus Riemann invariants) that must hold on the characteristic lines $\frac{\mathrm{d}y}{\mathrm{d}t} = c_\pm^{sep}$:

$$\begin{aligned}
\frac{\mathrm{d}T_e}{\mathrm{d}\bar{d}} &= -\frac{\hat{s}_{11}}{\hat{s}_{12}} \\
&= \frac{qT_e\left(q\bar{d}+T_e^2+(q\bar{d}-1)T_e^4+2(q\bar{d})^{1/2}T_e[1-(q\bar{d}-1)T_e^2]^{1/2}\right)}{q^2\bar{d}^2-(1-2q\bar{d}+q^2\bar{d}^2)T_e^4} \qquad (27) \\
\frac{\mathrm{d}T_e}{\mathrm{d}\bar{d}} &= -\frac{\hat{s}_{21}}{\hat{s}_{22}} \\
&= \frac{qT_e\left(q\bar{d}+T_e^2+(q\bar{d}-1)T_e^4-2(q\bar{d})^{1/2}T_e[1-(q\bar{d}-1)T_e^2]^{1/2}\right)}{q^2\bar{d}^2-(1-2q\bar{d}+q^2\bar{d}^2)T_e^4} \qquad (28)
\end{aligned}$$

Were we able to solve these nonlinear differential equations analytically, the constant of integration would yield the two Riemann constants (as in the previous attached flow case).

Now, we specialize to our problem and take $q = 1$. Solutions for $\bar{d}$ and T_e in the separated flow region of Fig. 2 are obtained in principle by the simultaneous solution of Eq. (27) and the characteristic equation $y/t = c_-^{sep}$.

The solution to the differential equation (27) is obtained numerically by assuming the solution is continuous across the line $y/t = c_{sep}$ shown in Fig. 2. In other words, the numerical integration is started with $\bar{d} = \bar{d}_{sep}$ and $T_e = T$ and stepped backward in $\bar{d}$ until $\bar{d}$ is a very small number which we call the nose of the fluid intrusion. A plot of these "plus" Riemann invariant (the integral curves of Eq. (27)) is shown below for a few values of the channel width:

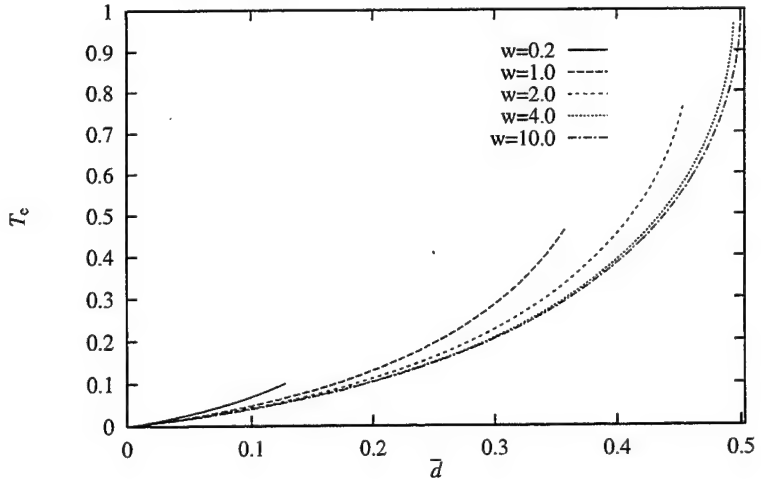

Figure 5: "Plus" Riemann invariant for the case of separated flow.

The above diagram suggests that T_e is zero where $\bar{d}$ is zero for all T, implying that the nose of the separated region is not only of zero height, as might be expected, but also of zero width. Note too that T_e goes to zero more quickly than $\bar{d}$ implying that the width of the nose becomes narrower more quickly than the thickness of the nose does. Being slightly more quantitative, it can be shown that w_e approaches zero at roughly twice the rate that $\bar{d}$ does for all channel widths.

With T_e obtained numerically as a function of $\bar{d}$, it is a simple (numerical) matter to solve for each variable individually as a function of the similarity variable y/t from the characteristic equation $y/t = \bar{d}T_e^{-1} - \bar{d}^{1/2}[1-(1-\bar{d})T_e^2]^{1/2}$. Notice that the characteristic lines are straight in the separated region, which follows from the relation between $\bar{d}$ and T_e given by (27) and assumed to be true at an infinitesimal time after the dam breaks.

The speed of the nose of the intrusion depends on T. This can be seen by taking the limit $\bar{d} \to 0$ in the characteristic equation. We have $c_{nose} = \lim_{y\to 0} \frac{\bar{d}}{T_e}$. The limit is indeterminate and must be resolved via the differential equation (27) as $\bar{d}$ approaches zero- this too is indeterminate and in fact should not be able to be resolved simply since the ratio must depend on specific initial conditions, that is, on $\bar{d}_{sep}$ and T. The inverse of the slope of the lines in Fig. (5) at $\bar{d} = 0$ measures the speed of the nose.

7 Results

In this section, we present our analytical results. Additionally, we will compare and contrast our results, all based on the semigeostrophic approximation, with results from numerical simulations of the full 2-D shallow water equations in a channel (Eqns. (1), (2), and (3) with $\delta = 1$). Before presenting the results, we comment briefly on the numerical scheme.

The finite difference scheme used here is based on "flux-corrected transport." (see Leveque 1992) It allows one to achieve second order accuracy in space by adding a correction to a first order upwind scheme. The time stepping is accomplished via Strang splitting which gives second order accuracy in time. The equations are cast in conservation law form so that the finite difference formulation obeys discrete forms of mass and momentum conservation. A small $O(10^{-10})$ layer depth is required in the simulations upstream of the dam at $t = 0$.

The first plot shows the value of $\bar{d}$ at the separation point, $\bar{d}_{sep}$, as a function of the width parameter T:

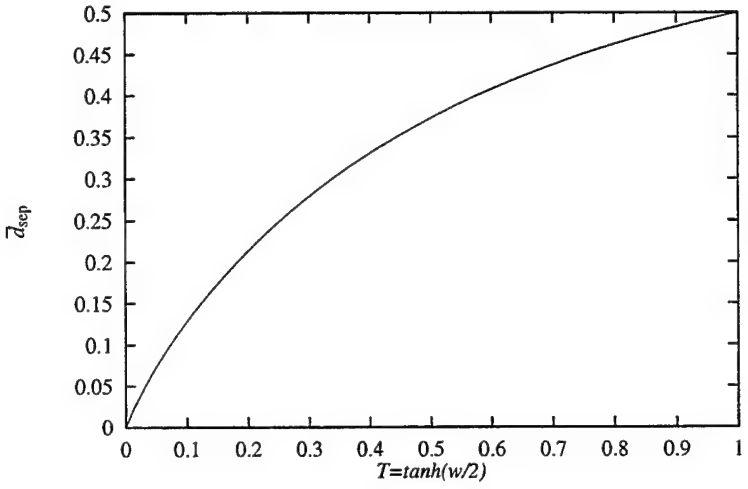

Figure 6: Dependence of $\bar{d}$ at the separation point on the width parameter T. $T = .46$ corresponds to $w = 1$.

Notice that $\bar{d}_{sep}$ (and d) approaches zero as the channel narrows because the separation point becomes the nose of the fluid intrusion in this limit. Also, as the channel width approaches infinity, the value of $\bar{d}$ approaches 0.5. As we will show later, the configuration of the flow in this case has the separation point being stationary at $y = 0$ where $d = 1$ for all x except in a left (looking downstream) wall boundary layer where d goes to zero. Note though that we expect a breakdown of the semigeostrophic equations in this limit.

Now that we have the value of $\bar{d}_{sep}$, we plot the speed of the separation point c_{sep} and the speed of the nose of the fluid intrusion c_{nose} as functions of T:

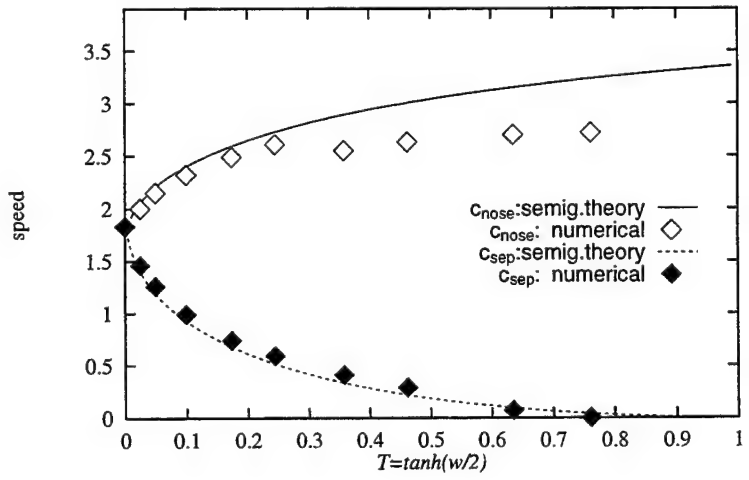

Figure 7: Dependence of the separation point speed and speed of a point very close to the speed of the nose, on the width parameter T. Semigeostrophic theory is presented along with the full numerical simulation results. $T = .46$ corresponds to $w = 1$

To avoid confusion, we have used the label "c_{nose}" in the above plot. Strictly speaking, it is the speed of a point located $\Delta x/2$ away from the right hand wall (looking downstream) and having depth $d = .001$. The grid spacing Δx ranged, as determined from the numerical simulations, from

0.01 for the case of narrow channels to 0.025 for the case of the $w = 2$ channel. Δy, the along-channel grid spacing, was held fixed at 0.05.

Comparison between the numerics and the theory was carried out by noting that the numerical simulations were formulated in conservation law form. This fact implies that the cell centered values of the numerical simulation data represent an integral average of the data over the cell (the "cell average"- see for example Leveque 1992). Therefore, we obtain data points from the semigeostrophic theory by averaging the speed of points having d=.001 at $x = w/2$ and $x = w/2 - \Delta x$, the only assumption being linear interpolation across the cell. In Fig. 7, the theoretical nose speed curve was plotted using $\Delta x = .025$.

We expect agreement between theory and numerics as the channel width narrows; the fact that the separation point speed matches so well for all values of T is thus quite surprising. In general we attribute discrepancies between the theory and the numerics to resolution effects and slight numerical viscosity rather than to a failure of semigeostrophic theory *for the case of the nose speed* for the following reasons.

The theory predicts an ever-thinning nose solution; the numerics can never reproduce this effect accurately for fixed resolution. Numerical viscosity probably comes into play at this scale. In addition, the cross-channel resolution decreases in the simulations as the width is increased. With regards to comparing results from different theories, we might expect discrepancies in the depth and velocity fields but the fastest Poincare waves in the simulation should still be comparable in speed to the fastest waves in the semigeostrophic theory.

The "real" nose speed as obtained from semigeostrophic theory is shown below. Here, we have taken speeds at the right hand wall $x = w/2$ for four successively smaller values of d. The plot demonstrates numerical convergence and suggests an upper bound on the nose speed of approximately four.

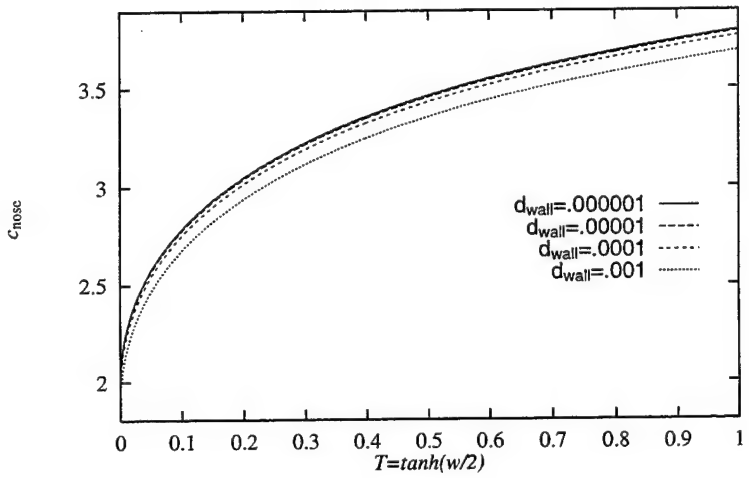

Figure 8: Nose speed dependence on the width parameter T, from semigeostrophic theory. The four lines represent the velocity on the right (looking downstream) wall (d_{wall}) of points having four successively smaller values of depth.

Viscosity and lateral mixing would of course tend to smear and slow down this thinning nose solution.

Next, the full solution of the equations for $\bar{d}$, $\hat{d}$ and T_e are plotted below as a function of the similarity variable y/t and for four values of the width parameter T.

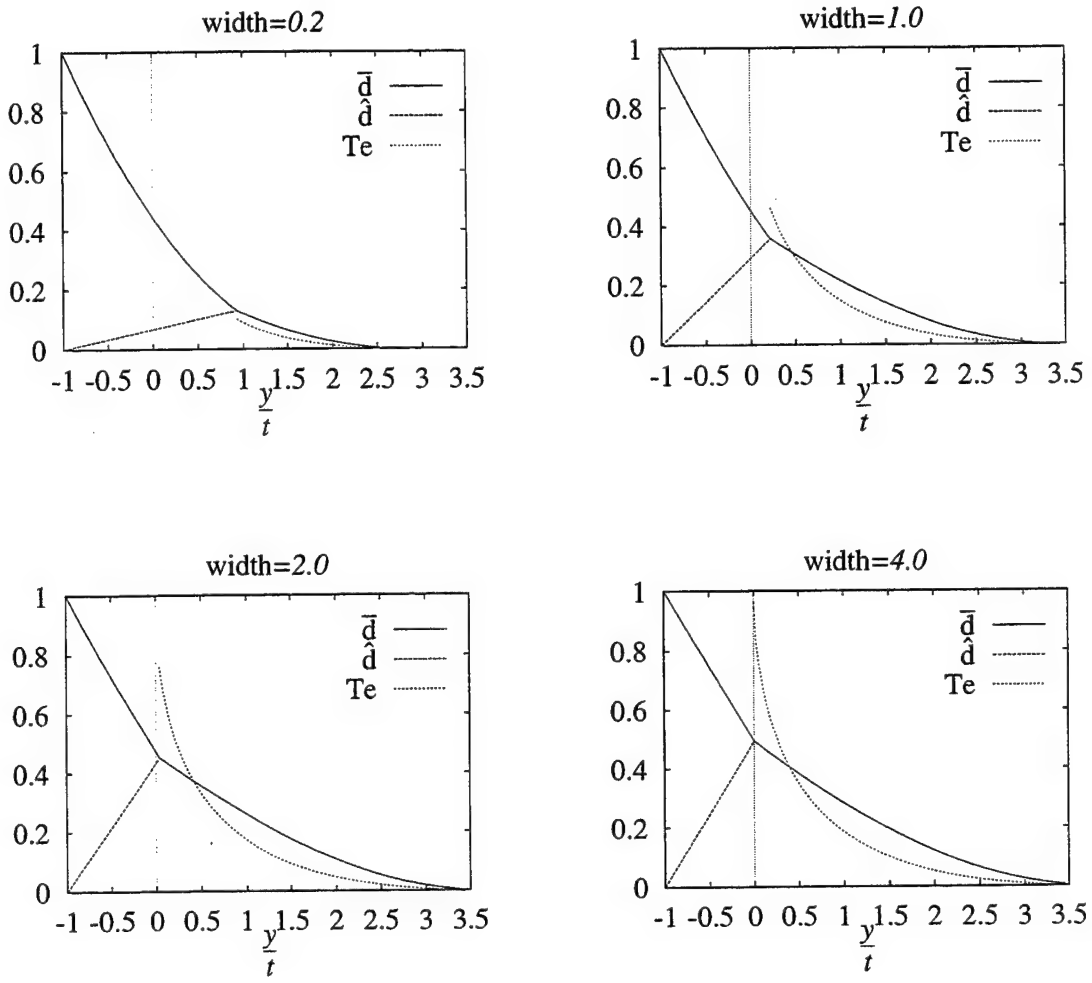

Figure 9: Solutions for $\bar{d}$, $\hat{d}$ and T_e in both the attached and separated regions. Four values of the width were taken: 0.2, 1.0, 2.0 and 4.0. The flow is critical at $y = 0$, subcritical for $y < 0$ and supecritical for $y > 0$.

The above plot can be interpreted as giving the y-dependence of $\bar{d}$, $\hat{d}$ and T_e at unit time. The discontinuous nature of $\bar{d}$ increases as w increases which is probably related to the breakdown in semigeostrophic theory in the large w limit.

Next, we compare contour plots of the depth field from semigeostrophic theory and from the numerical simulations. This is done at a fixed time $t = 10$ and for two cases of the channel width, $w = 0.2$ and $w = 2.0$. The figures are plotted separately then overlain. The contours were selected at eleven discrete levels: $d = 0.001,\ 0.1,\ 0.2, ..., 0.9,\ 0.999$. Note that the cross-channel scale is magnified greatly with respect to the along-channel scale.

(a)

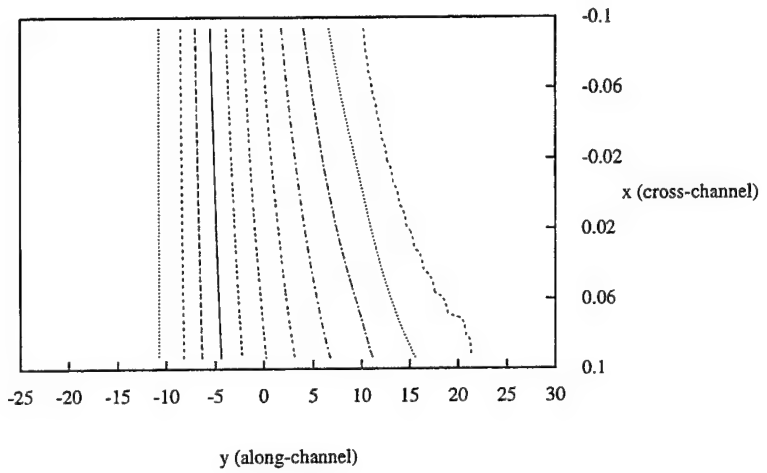

(b)

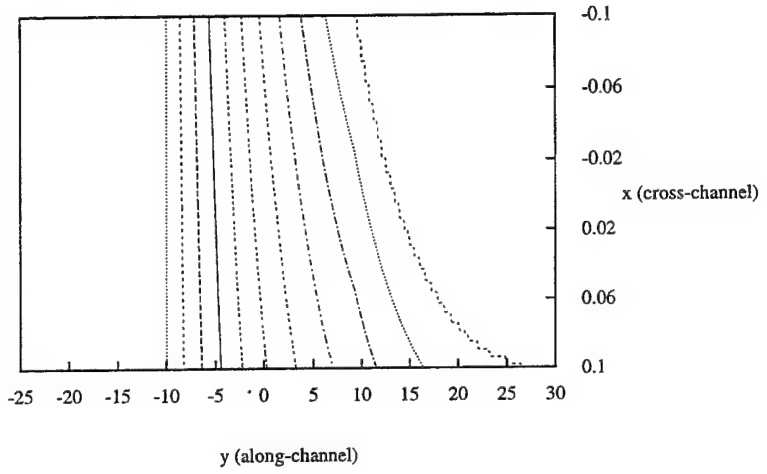

(c)

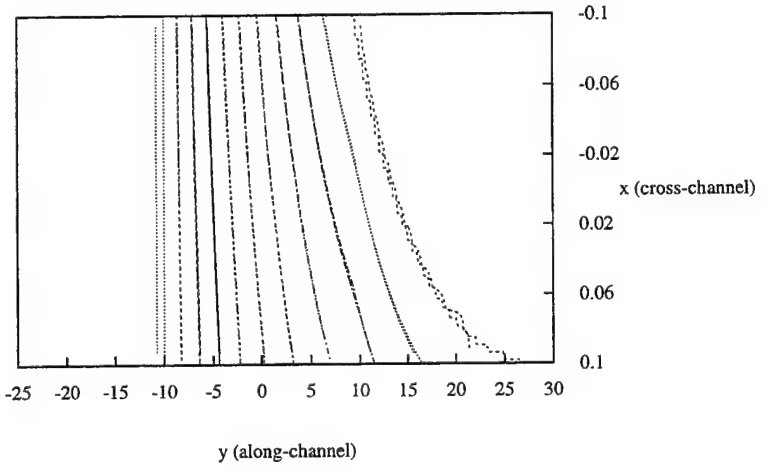

Figure 10: Contour plots of the layer depth d at $t = 10$ for channel width $w = 0.2$ (a) numerical simulation (b) semigeostrophic theory (c) both plots superimposed

(a)

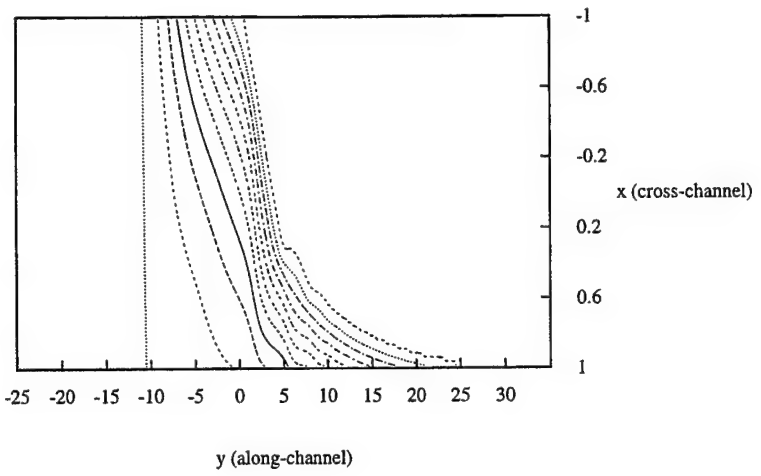

(b)

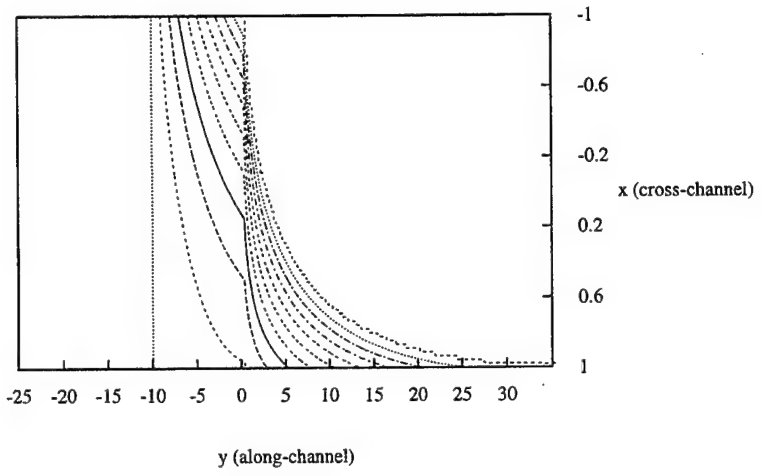

(c)

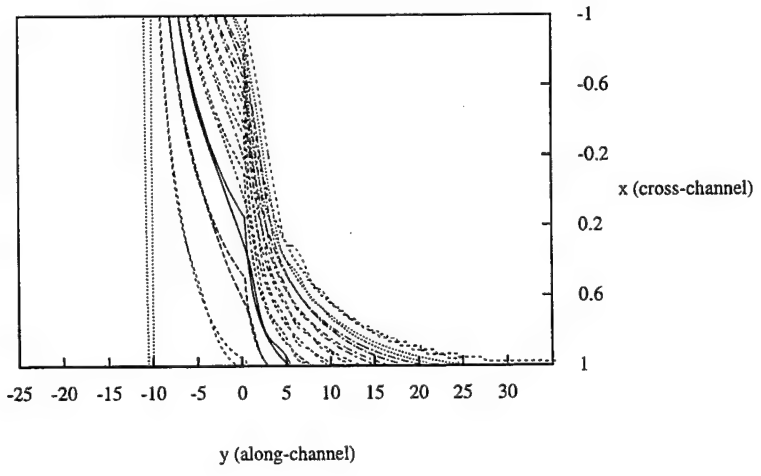

Figure 11: Contour plots of the layer depth d at $t = 10$ for channel width $w = 2.0$ (a) numerical simulation (b) semigeostrophic theory (c) both plots superimposed

The agreement shown in Figs. 10(c) and 11(c) is somewhat surprising. The full 2-D system admits Poincare waves; it is not clear that at a fixed time, the depth field in the numerical simulations should not be more oscillatory in nature.

As expected, the solutions tend to agree more for small w. (It can also be shown that the solutions agree more at longer times.) Notice also that the solutions are more similar near the sidewalls. This may be explained by noting that near the walls, we expect u to go to zero and the semigeostrophic approximation to increase in validity. Near $y = 0$, the discontinuous nature of the theoretical solution becomes more apparent as the channel width increases (Fig. 11 (b)). Agreement between the two solutions is worst in this region because a strong negative u velocity must develop in this region for wide channels. This velocity is prevented from forming in the theory.

As the channel gets wider, the "generalized Kelvin wave" (see Pratt & Whitehead) nature of the solution becomes more apparent. Comparing Figs. 10 and 11, the signature of these waves is given by the increased deviation from the vertical of the contour lines near the sidewalls. In the infinitely wide channel limit, one expects two independently propagating Kelvin waves to appear along both channel walls (Pratt & Whitehead).

For visualization purposes, we plot in 3-D the depth field d for a $w = 1$ channel at three different times (next page). Note again that the cross-channel scale is magnified greatly with respect to the along-channel scale.

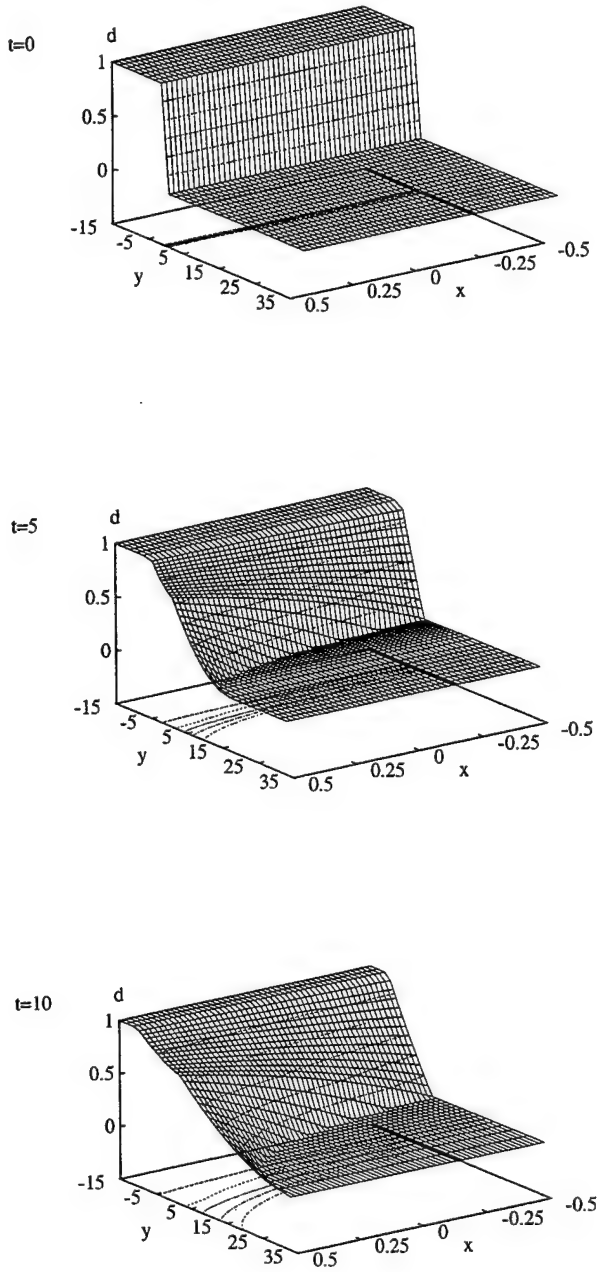

Figure 12: Full solution for the layer depth d at three different times $t = 0, 5$ and 10. Here, the channel width equals the deformation radius.

7.1 Results at Steady State

One might inquire into the steady state solution of this rotating dam break problem. By steady solution, we mean the solution at any fixed position y as $t \to \infty$. Because of similarity, this is equivalent to the solution evaluated at $y = 0$ at any time t. (It thus follows that as $t \to \infty$, the flow at any position y approaches criticality.) Below, we plot the steady values of $\bar{d}$ and $\hat{d}$ as a function of T.

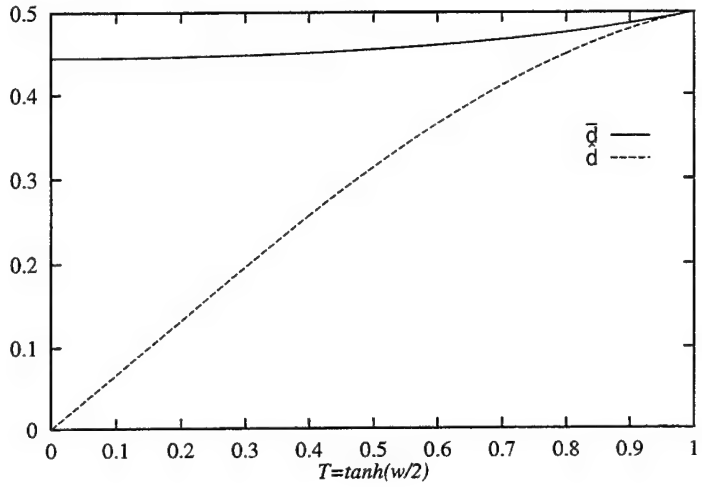

Figure 13: Long time values of $\bar{d}$ and $\hat{d}$ as a function of T

Recall from the nonrotating dam break problem (Stoker 1955) that the steady state depth d is $(2/3)^2 \approx .44$. Notice that the solution for $\bar{d}$ agrees with the nonrotating case in the limit $T \to 0$.

With the steady state values of $\bar{d}$ and $\hat{d}$ known, it is instructive to plot the full depth profile d. Below, we do so for two cases of the channel width: $w = 1$ and $w = 10$.

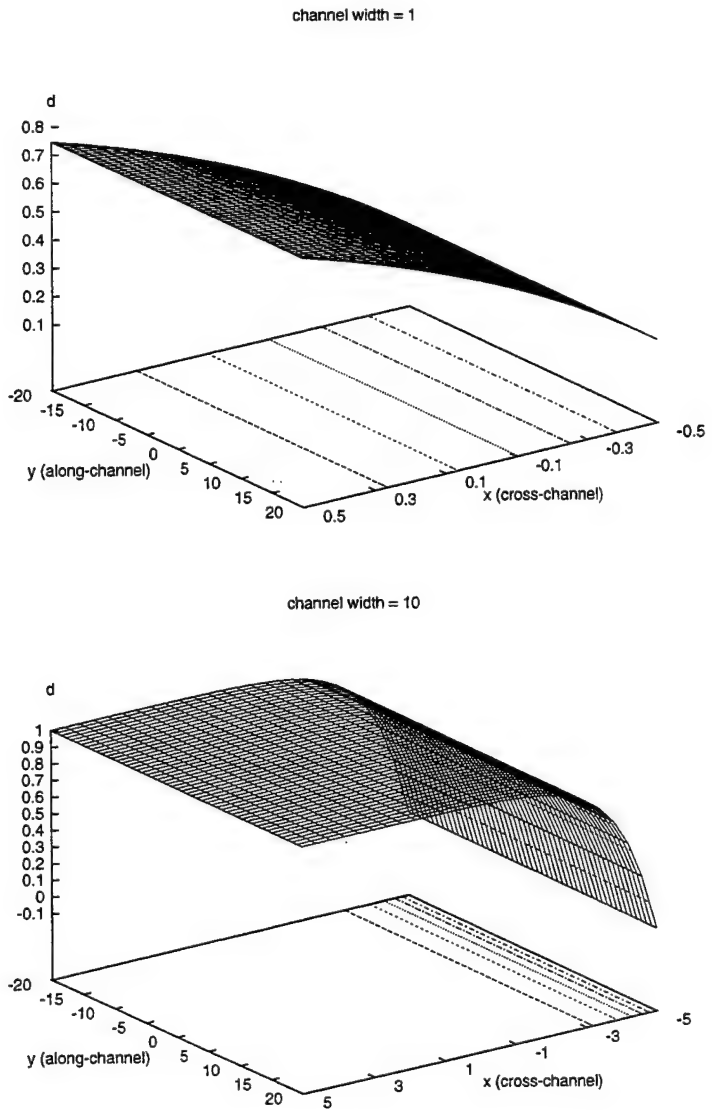

Figure 14: Long time depth field d for two cases of channel width. The initial discontinuity was at $y = 0$. Note the x and y scales.

Stronger curvature in d implies stronger velocity v by geostrophy. Notice that as the channel broadens, the transport becomes confined to a sidewall boundary layer of deformation radius width.

With the steady values of $\bar{d}$ and $\hat{d}$, it is also possible to calculate the mass transport $Q = 2\bar{d}\hat{d}$. We plot it below.

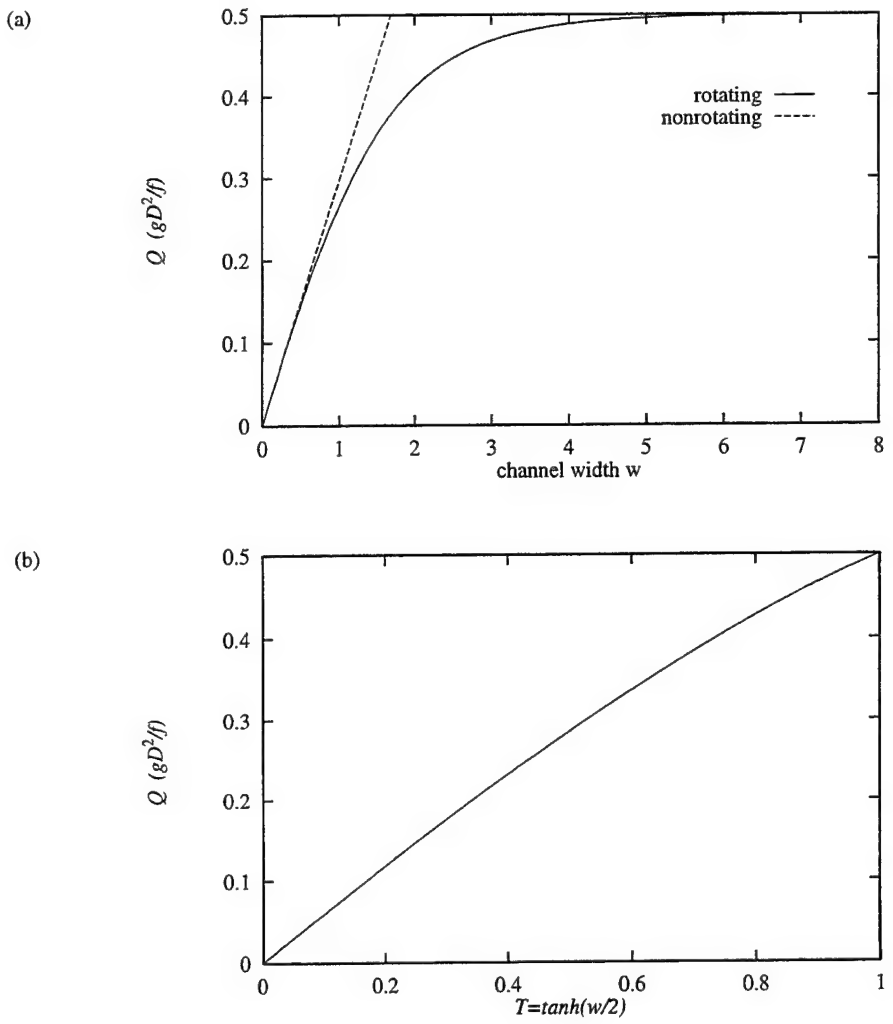

Figure 15: Transport Q at asymptotically steady state as a function (a) the channel width w and (b) $T \equiv \tanh w/2$

First examine Fig. 15 (a). In the narrow channel limit, the rotating solution should approach the nonrotating 1D solution of Stoker (1955). In this case, the depth and velocity approach constants at long times so that the transport is simply a linear function of width- specifically, $Q = dvw = (2/3)^2(2/3)w$. This is the general behavior seen in the plot above for channels widths smaller than the deformation radius. Beyond this width, rotational influences set in. The graph shows that increases in the width beyond this point have less and less of an effect on the transport.

One might have guessed that the transport would taper off, in analogy with the results of Whitehead, Leetma & Knox (1974). They showed that the effect of rotation on hydraulically controlled flows is to reduce the transport. In any case, in the infinite width limit, one could expect the flow not to feel the effects of the channel width. The only length scale the flow can have in that case is the deformation radius, in which case the transport must approach a constant.

Fig. 15 (b) is instructive in that plotting Q vs. T yields an almost linear relationship. Perhaps this would be obvious if one was looking for a function that increases linearly and then tapers off to a maximum value. In any case, Gill's (1977) introduction of the parameter T proves useful.

8 Conclusions

In this study, we have used a semigeostrophic approximation to study time dependent effects in rotating channel as a function of the width of the channel. Additionally, we have gained a general idea of the long time mass transports involved in such flows.

In the problem considered here, it is not obvious how one could solve for the final geostrophically balanced state given only the initial conditions (channel width) and the full set of governing equations; the potential vorticity conservation methods that Rossby (1937) outlined for doing so fail in this case. Here, we have resorted to considering the time dependent equations in order to connect the initial and final states. It is tempting to conjecture that the steady state results presented here are equivalent to the steady state results of the full shallow water equations in the channel, for at the steady state the mathematical equations are identical. If this could be proven, then the characteristic method would have indirectly solved a nontrivial two dimensional geostrophic adjustment problem. Since one system admits Poincare waves while the other filters them out, it would also imply that Poincare waves do not have a strong influence in the final state, in this problem at least.

We note that a net v velocity could have been added in to the initial conditions without destroying the analytic tractability of the problem. It is not immediately obvious that this effect can be scaled away.

Topographic and sidewall influences, well known to be able to strongly alter the mass flux, have not been studied here. It appears such problems are not amenable to analytical techniques; numerical and experimental methods must be brought to bear in those cases.

Acknowledgments

I would like to thank Karl Helfrich and Larry Pratt for taking the time to advise me this summer, Joe Keller and George Veronis for help on a nonlinear ODE, Vitaly Sheremet for pointing out the breakdown of semigeostrophic theory and Katsurou Katsumata for his computer expertise. Dr. Helfrich provided all of the numerical simulation results.

References

GILL, A. E. 1977 The hydraulics of rotating-channel flow. *J. Fluid Mech.* **80**, 641-671.

LEVEQUE, R. J. 1992 *Numerical Methods for Conservation Laws.* Birkhauser, 214 pp.

PRATT, L. J. 1983 On inertial flow over topography. Part 1. Semigeostrophic adjustment to an obstacle. *J. Fluid Mech.* **131**, 195-218.

PRATT, L. J. & WHITEHEAD, J. A. *Hydraulic Phenomena in Rotating Fluids.* to appear.

ROSSBY, C. G., 1937 On the mutual adjustment of pressure and velocity distributions in certain simple current systems I. *J. Mar. Res.*, **1**,15-28.

STERN, M. E., WHITEHEAD, J. A. & BACH-LIEN, H., 1982 The intrusion of a density current along the coast of a rotating fluid. *J. Fluid Mech.* **123**, 237-265.

STOKER, J. J., 1958 *Water waves*, John Wiley, 567 pp.

WATTS, R. G. and HAYDER, M. E. 1983 Climatic fluctuations due to deep-ocean circulation. *Science* **219**, 387-388.

WHITEHEAD, J.A., LEETMAA, A. & Knox, R.A. 1974 Rotating hydraulics of strait and sill flows. *Geophys. Fluid Dyn.* **6**, 101-125.

WHITHAM, G., B., 1974: *Linear and Nonlinear Waves.* John Wiley, 636 pp.

Annalisa Bracco
Universita' degli Studi di Torino

Boundary layer separation in the Surface Quasi-Geostrophic equations

GFD 1997

Introduction

The 3D dynamics of quasigeostrophic flow with uniform potential vorticity reduces to the evolution of potential temperature on horizontal boundaries.
This work provides an application of surface quasi-geostrophic equations (SQG here) in a simple oceanic continuously stratified model with a tilted upper boundary.
One of the most striking features of the oceanic circulation is the observed separation of western boundary current. The outcropping mechanism provides one of the simplest explanations of separation of western boundary current in wind-driven gyres of opposite signs. Assuming that the effects of the friction and inertia are confined to regions of a boundary layer character, the separation latitude is shown to depend on the degree of stratification. Recent models of the wind driven circulation in a closed basin solve the two dimensional quasi-geostrophic or the shallow water equations with layers outcropping with vertical discretization in constant density layers: the separation latitude and the resulting circulation is strongly dipendent from the stratification choice.
Using the SQG equations we can study the problem of the separation of the western boundary currents in a continuously stratified model, where the outcropping of the interior flow can occurs "continuously" and the separation latitude is non dictated by the choice of vertical coordinate.
The goal of this project is to study a semplified model and compare the dynamics in the SQG approximations with the homegeneous case

1. Equations of motion: Surface Quasi-Geostrophic dynamics

We want consider the problem of 3-Dimensional flows driven by the dynamics of upper boundaries, the internal dynamics being the vanishing potential vorticity.
In the limit of small Rossby number $(R_o = U/f_oL << 1)$, the quasi-geostrophic approximation of the equations of motion on the β-plane in the Boussinesq version and in a nondimensional form are:
(see Pedlosky, 1964 for a complete derivation)

$$\partial_t q = -J(\psi, q + \beta y) \tag{1.1.a}$$

with the condition on the streamfuncion of no-normal flow at a rigid horizontal boundary $z = z_1, z_2$ (being the upper and the lower boundaries).
At a flat boundary the condition of no normal flow is:

$$\partial_t \theta = -J(\psi, \theta), \qquad z = z_1, z_2 \tag{1.1.b}$$

In presence of a surface with elevation where $z = \eta(x,y)$ is the equation for the surface in a non dimensional form, the boundary condition on ψ becomes:

$$\partial_t \theta = -J\left(\psi, \theta + \frac{b}{DR_o}\eta\right), \quad z = z_1, z_2 \tag{1.1.c}$$

where we assumed that

$$q \equiv \left(\partial_{xx} + \partial_{yy} + \rho_s \partial_z \rho_s \varepsilon \partial_z\right)\psi \tag{1.2}$$

is the 3-dimensional potential vorticity.
The streamfunction ψ rapresents the pressure field related to the horizontal velocity field in the usal way $(u,v) = (-\psi_y, \psi_x)$ and $\psi_z \equiv \theta$ is the potential temperature.
S=S(z) is the stratification parameter definited by:

$$\frac{1}{S(z)} = \varepsilon = \frac{f_o^2 L^2}{gkD} = \frac{f_o^2 L^2}{N^2 D^2} \tag{1.3}$$

$f_o/2$ is the Coriolis parameter and rapresents the characteristic value of the normal component of the earth's rotation.

L is the characteristic horizontal length, D the vertical scale, $N(z)=\left(\frac{g}{\theta}\frac{\partial\theta}{\partial z}\right)^{1/2}$ is the Brunt - Väisälä frequency, ρ_s is a function of z and may be defined as the global average of ρ at each level z and b is the characteristic amplitude of the topographic variation.
In the oceans, where the compressibility effect on fluid elements is negligible, the Brunt - Väisälä frequency is given in term of the equilibrium density distribution:

$$N=\left(-\frac{g}{\rho}\frac{\partial\rho}{\partial z}\right)^{1/2}$$

and the basic density field may be considered roughly constant.
Assuming N constant, the factor ε may be subsumed into a rescaled vertical coordinate $z'=\varepsilon^{1/2}z$. (We will retain the notation z for the rescaled z').
A familiar special case of 3-dimensional flow is obtained by assuming $\theta=0$, z = z_1, z_2. In this context we have a flow of " Charney type ", where the dynamical effect of upper and lower boundaries was neglected. In other words the flows are confined within isoentropic surfaces with uniform pressure and temperature.
The complementary problem is that of Surface quasi-geostrophic flow, or flow of " Eady type " (Eady, 1949), in which it is assumed that q = 0. The interior equation (1.1.a) is identically satisfied and the flow is driven by the dynamics of upper and lower boundaries.

We are interested in this second case applied to a ocean basin, assuming that the flow is confined in a closed horizontal basin with infinite depth, in the approximation of zero potential vorticity at the interior, uniquely driven by the upper boundary.
Typical scales relevant to the North Atlantic Ocean may be $U=O(2*10^{-2}ms^{-1})$, $L=O(10^3Km)$, $f_o=2\Omega\sin\phi_o=O(10^{-4}s^{-1})$ on mid-latitudes.
Introducing a tilted surface with elevation $z=-\lambda y$ the equations take the form:

$$\partial_t\theta=-J(\psi,\vartheta-\Lambda y)+F \qquad z=0$$

$$\theta\equiv\partial_z\psi \qquad (1.4)$$

$$\left(\partial_{xx}+\partial_{yy}+\partial_{zz}\right)\psi=0 \qquad z<0$$

(1.4)

$$\psi_z \to 0 \text{ as } z \to -\infty$$

where

$$\Lambda = -\frac{\lambda N}{f_o L R_o} \tag{1.5}$$

F is the total heating rate and may be considered a given forcing function and Λ is the nondimensional topographic variation that reproduces the beta - effect in two dimensional flows.

In terms of spectral amplitude in an infinite period domain with infinite depth $\psi = \mathrm{Re}\left[\hat{\psi}\exp(ikx + ily - i\omega t)\right]$ for a two dimensional flow. The vertical structure which satisfies the system (1.8) is $\exp\left(\sqrt{k^2+l^2}z\right)$ and $\hat{\theta} = \sqrt{k^2+l^2}\hat{\psi}$.

This model supports linear waves travelling westwards with the dispersion relation

$$\omega = -\frac{\Lambda k}{\sqrt{k^2+l^2}} \tag{1.9}$$

These waves decay away from the surface as exp(kz) and are dynamically identical to topographic edge waves.

2. Linear problem.

a) The time dependent, inviscid, unforced case. Free modes of the system

The aim is to show how the interior and the western boundary layers develop in a basin governed by the linear version of the SQG equations.

The geometry of our model consist in a flat basin of stratified fluid confined to a closed domain with $0 \le x \le L$, $0 \le y \le L$ with depth in a general case $0 \ge z \ge -B$.

Before examing the forced problem it is of interest to discuss the free modes of the system.

The linear, non - dimensional, inviscid equations are:

$$q = \nabla^2\psi = 0 \qquad (0 \le x \le L;\ 0 \le y \le L;\ -B < z < 0;\ t \ge 0) \tag{2.1.a}$$

$$\partial_t\psi_z - \Lambda\psi_x = 0 \qquad (0 \le x \le L;\ 0 \le y \le L;\ z = 0;\ t \ge 0) \tag{2.1.b}$$

$$\psi = 0 \qquad (x = 0, L;\ y = 0, L;\ z = 0;\ t \geq 0) \tag{2.1.c}$$

$$\psi_z = 0 \qquad (z = -B) \tag{2.1.d}$$

Because of the form of the equations (2.1) without loss of generality we can assume a periodic behaviour with y:

$$\psi(x,y,z) = \phi(x,z)\sin(ly)$$

using L/π as scale for the north-south coordinate.
The operator ∂_{yy} can be replaced by $-l^2$ where l is the north-south wavenumber. The equation (2.1.a) becomes :

$$\nabla^2\phi - l^2\phi$$

$$(0 \leq x \leq L;\ 0 \leq y \leq L;\ -B < z < 0;\ t \geq 0)$$

and equations (2.1.b, 2.1.c, 2.1.d) are invariant on ϕ.
The system supports propagating wave solutions of the form:

$$\phi = \mathrm{Im}\left\{A\cosh\left[\sqrt{k^2+l^2}\,(z+B)\right]\exp(ikx - i\Lambda\omega t)\right\} \tag{2.2}$$

with the dispersion relation

$$\omega = -\frac{k}{\sqrt{k^2+l^2}}\coth\left(\sqrt{k^2+l^2}B\right) \tag{2.3}$$

The phase speed in the x - direction is

$$C_{px} = -\frac{1}{\sqrt{k^2+l^2}}\coth\left(\sqrt{k^2+l^2}B\right) \tag{2.4}$$

The x - component of the group velocity is given by:

$$C_{gx} = -\frac{l^2 \coth\left(\sqrt{k^2+l^2}B\right)}{\left(\sqrt{k^2+l^2}\right)^3} + \frac{Bk^2}{\left(k^2+l^2\right)\sinh^2\left(\sqrt{k^2+l^2}B\right)} \qquad (2.5)$$

and the y - component:

$$C_{gy} = -\frac{kl}{k^2+l^2}\left(\frac{\coth\left(\sqrt{k^2+l^2}B\right)}{\left(k^2+l^2\right)^{3/2}} - \frac{B}{\sinh^2\left(\sqrt{k^2+l^2}B\right)}\right) \qquad (2.6)$$

We can consider the behaviour of the wave solutions in the particular limit of D –> ∞ which represents a strongly stratified ocean. In this case z scale as $\frac{fL}{N}z'$ and

$$\omega \rightarrow -\frac{k}{\sqrt{k^2+1}}$$

$$C_{px} \rightarrow -\frac{1}{\sqrt{k^2+1}} \qquad (2.7)$$

$$C_{gx} \rightarrow -\left(\frac{1}{\sqrt{k^2+1}}\right)^3$$

The phase speed and the group velocity are always positive. The waves are unidirectional: all the information and the energy from the eastern boundary is trasmitted westwards while there is no possibility to propagate information eastwards.

This behaviour contrasts with the wavelike solutions for the planetary wave equation in a basin. In that case the energy from the western boundary can be trasmitted eastwards by short waves. The inviscid system is does not achieve a steady state.

In our model the linear unforced system develops a steady state in the interior and a finite time singularities along the western boundary, corresponding to a front.

Choosing the north - south wavenumber equal to one, appers that long waves travel faster and both speed decrease to zero decreasing wavelength.

Instead for the homogeneus model, D –> 0, the phase speed increases indefinitely with increasing wavelength and decrease to zero for short waves.

b) Time independent, forced, viscous, case.

In the homogeneous model in the prossimity of the surface the dominant contributions to the frictional forces in dimensional form can be rapresented as:

$$\frac{A_v}{f_o D^2}\frac{\partial^2 u}{\partial z^2} = \frac{E_v}{2}\frac{\partial^2 u}{\partial z^2}$$
$$\frac{A_v}{f_o D^2}\frac{\partial^2 v}{\partial z^2} = \frac{E_v}{2}\frac{\partial^2 v}{\partial z^2} \qquad (2.8)$$

where A_v is the vertical turbulent viscosity coefficient and E_v is the Ekman number associated with vertical mixing. Estimates of A_v for the ocean suggest values from $1cm^2s^{-1}$ to $10^3 cm^2s^{-1}$.

It shown that the homogeneous model of the Ekman layer remains valid for a stratified fluid. In case of infinite depth the vertical scale D is replaced by $\frac{fL}{N}$.

In our model further assume a vertical dissipation in the form of eq. (2.8).

We choose the forcing resulting from an applied wind stress

$$F = W \cdot \bar{k} \cdot \mathrm{curl}\bar{\tau} \qquad (2.9)$$

$\bar{\tau}$ is the wind stress and W in our non dimensional coordinates is $\frac{\tau_o N}{\rho_s U^2 f_o}$.

τ_o is the maximum wind stress value (typically $\tau_o = 10^{-1} Nm^{-2}$).

For an ocean driven by a zonally simmetric wind stress:

$$\bar{\tau} = \left[\cos\left(\frac{\pi y}{L}\right), 0\right]$$
$$\mathrm{curl}\tau = -\frac{\partial \tau^x}{\partial y} = \sin\left(\frac{\pi y}{L}\right) \qquad (2.10)$$

We are interested in particular in the behaviour of the western boundary layer. In the non dimensional form the linear time independent equation for the SQG dynamics becomes

$$\frac{E_v^{1/2}}{2R_o}\left(\frac{\partial^2\psi}{\partial x^2}+\frac{\partial^2\psi}{\partial y^2}\right)+\Lambda\psi_x=-W\sin\left(\frac{\pi y}{L}\right) \tag{2.11}$$

The linear problem reduces to the system which was originally solved by Stommel. An analitical solution can be found with the boundary condition that the cost be a streamline, which is satisfied setting $\psi = 0$ on $x = 0, L$ and $y = 0, L$.

The result is shown in Fig. (2.1). There is an intense crowding of streamlines toward the western border of the basin and the displacement of the center of the anticyclonic gyre toward the west. This westward intensification of the wind-driven ocean currents is the conseguence of the variation of the Coriolis parameter with latitude.

Eq. (2.11) expresses a balance between planetary vorticity, frictional vorticity and wind stress. On the western side of the ocean where current speed and current shear are strong, frictional and platenary vorticity tendencies are also great. Whereas in the eastern part, where currents are weak and diffuse, these terms are orders of magnitude smallers. Instead the wind stress tendency is the same all over the ocean.

If we neglect the frictional terms under the condition $\frac{E_v^{1/2}}{2R_o} << 1$, the interior circulation, reduce to the Sverdrup relation

$$\Lambda v = \text{curl}\tau \tag{2.12}$$

On the western boundary where the frictional effects are non negligible, eq. (2.11)becomes to lowest order:

$$\frac{E_v^{1/2}}{2R_o}\frac{\partial^2\phi_b}{\partial\lambda^2}+\Lambda\frac{\partial\phi_b}{\partial\lambda}=0 \tag{2.13}$$

where we wrote the original equation in term of the interior ψ plus a boundary layer correction function

$$\psi_b = \psi(x,y)+\phi_b(\lambda,y)$$

The solution is clearly:

$$\phi_b(\lambda,y)=C(y)\exp\left(-\frac{2\Lambda R_o}{E_v^{1/2}}\lambda\right) \tag{2.14}$$

$\frac{E_v^{1/2}}{2R_o\Lambda}$ times the scale of the basin is the frictional boundary layer thickness.

3. The nonlinear time dependent problem.

The fully nonlinear, time dependent problem is studyed with a numerical experiment. Results from numerical calculations of wind-driven ocean circulation in the SQG model with explicit bottom friction and surface heating are presented. The lateral friction is instead supposed to be zero everywhere in order to minimaze the influence of frictional boundary layers (Munk layers) and holds the model to become dynamically unstable.
The integrated equation is

$$\partial_t \psi_z + J(\psi, \psi_z - \Lambda y) = \frac{E_v^{1/2}}{2R_o}\left(\partial_{xx}\psi + \partial_{yy}\psi\right) + F \qquad (3.1)$$

with $\psi = \psi(x,y,0)$ and the boundary condition $\psi = 0$ on $x = 0, L$ $y = 0, L$.
$\psi_z - \Lambda y$ may be defined as the absolute temperature.
Our ocean model is a square basin of length 1000 Km and infinite depth. It is driven by an imposed heating in the form of a wind stress curl in both single and double gyre configurations.
For a single anticyclonically forced subtropical gyre

$$\bar{\tau} = \left[W\cos\left(\frac{y\pi}{L}\right), 0 \right] \qquad (3.2.a)$$

for the antisymmetrically forced double gyre

$$\bar{\tau} = \left[W\cos\left(\frac{2\pi y}{L}\right), 0 \right] \qquad (3.2.b)$$

giving a counterclockwise gyre north of the wind stress curl zero and an anticyclonically gyre to the south. This configuration of the wind stress holds the formation of an intergyre boundary and a jet. We saw that the Sverdrup dynamics implies that the interior meridional drift must return in intense western boundary layer currents. These currents can be unstable and in the classical homogeneous model conditions for instability in the ocean are easily verified in jet regions.

a) The numerical model.

A finite difference approximation of eq. (3.1) is integrated forward in time with a first order Adams-Bashforth scheme from an initial state at rest everywhere $(\theta = \psi = 0, \forall x, y)$ on a square grid of length π.

At each time step ψ is calculated from θ using a spectral method, variables being expanded as a sine series. ψ automatically satisfies the boundary conditions at $x = 0, \pi$ and $y = 0, \pi$ and

$$\hat{\psi}_{k,l} = -\frac{1}{\sqrt{k^2 + l^2}} \hat{\theta}_{k,l} \tag{3.3}$$

Our model describes a stratified ocean with infinite depth and a forcing acting on a finite layer thikness.

The Jacobian is finite differenced using a third order upwinding scheme, which introduces an implicit friction term on θ on the form:

$$\mu = U_{max} (\Delta x)^3 \nabla^4 \psi_z$$

where U_{max} is the maximum velocity at each time step and Δx is the grid space. This term helps to dissipate the enstrophy that builds up at small grid scales.

For numerical simulations the dimensional parameters have the value:

$$L = 10^6 \, m$$
$$\beta_o = 2 \cdot 10^{-11} \, m^{-1} s^{-1}$$
$$\rho_s = 10^3 \, Kg \cdot m^{-3}$$
$$f_o = 10^{-4} \, s^{-1}$$

A_v is choosen to obtain the frictional boundary layer thickness between one and three grid points, in the range $75 \div 10^3 \, cm^2 s^{-1}$.

When the nonlinear effects become important the thickness of the boundary layer is controlled by inertial effects.

We shall consider flows which have nonlinear and frictional effects of varying degrees. Our interest is in those flows which are strongly nonlinear, the linear case reproducing the same behaviour of the homegeneous model.

A measure of effects of nonlinearity is given by W, the amplitude of the forcing. The nonlinearity can be increasing increasing W increasing the value of the maximum wind stress, τ_o.

The integrated equation is rescaled so that the coefficient arising from the latitudinal variation in slope is equal to one and eq. (3.1) becomes:

$$\partial_t\theta + J(\psi,\theta+y) = \nu\nabla^2\psi + w' \,\mathrm{curl}\bar{\tau} \qquad (3.4)$$

In this rescaled form w' = 1 corresponds to a maximum wind stress $\tau_o = 10^{-1}\mathrm{Nm}^{-2}$.

The equation is integrated with a variable timestep which garantees the CFL number less or equal to 0.2.

b) Single gyre configuration

Fig. (3.1.a - b - c) show the streamfunction and the potential temperature field of a single gyre at different evolution times. Fig. (3.1.c) is after reaching a steady state, where steady means that the maximum velocity and the mean square velocity differed by less than 5% from their values at the previous time step.

The resolution is 256*256 grid points, ν is equal to 0.0125, the minimum value required to resolve the frictional boundary layer, and w' is equal to 2.

There is a north-south asymmetry produced by the northward advection of potential temperature. A thin, strong jet appears along the length of the northern wall. With the increasing of time the jet flows southward on the eastern boundary producing a weak eastern boundary current and modifing the interior configuration in the north. The nonlinear boundary current does not penetrate the interior except at the north-west corner.

If the inertial effect decrease in magnitude (w' = 1) and the inertial boundary thickness is of the same order of the frictional boundary, (Fig. 3.2), the jet along the northern wall becomes narrow.

With w' = 4 (Fig. 3.3.a - b) the jet is broad, but there is no significant variation in the thick of the western boundary, where most of the energy is confined.

We compared these results with the classical homogeneous ocean model, where the flow is confined in a square, flat, bottomed basin governed by the barotropic vorticity equation in the beta-plane approximation and it is driven by the same imposed wind-stress curl with identical friction retard.

The integrated equation is

$$\partial_t q + J(\psi, q + \beta y) = -W \sin\frac{\pi y}{L} - \frac{E_v^{1/2}}{2R_o}\nabla^2\psi \qquad (3.5)$$

where ψ is the two dimensional streamfunction and q the potential vorticity ($q = \nabla^2\psi$).
In our nondimensional form

$$\beta = \frac{\beta_o L^2}{U}$$

$$W = \frac{\tau_o L}{\rho U^2 H}$$

where H is the depth of the homogeneous layer.
For the mesoscale in the ocean $\beta_o = 10^{-11} m^{-1} s^{-1}$.
In the rescaled form eq. (3.5) becomes

$$\partial_t q + J(\psi, q + y) = -w' \sin\frac{\pi y}{L} - \nu\nabla^2\psi \qquad (3.6)$$

where w'=1 corresponds to a maximum value of the wind stress $\tau_o = 10^{-1} Nm^{-2}$ with a layer depth 500 m.
Fig. (3.4) shows the evolution toward a steady state of a single gyre for w' = 1 and ν = 0.0125. The flow is sufficiently nonlinear to resemble a Fofonoff free basin mode.
The maximum streamfunction in the domain measures the transport of the gyre quantifying the degree of spin-up. If the interior was in linear Sverdrup balance, ψ_{max} would be unity in this particular case, being w' and β equal to 1. Pedlosky (1979) describes this spin-up as a perturbation involved ignoring lateral frictional boundary layers. In the single gyre circulation the interior velocities exceed Sverdrup prediction in order to accomplish the necessary dissipation through the vertical friction. In the SQG simulations with the same frictional coefficient and forcing the degree of spin-up is one-sixth of the presente case. It means that the frictional terms (explicit and implicit) are more active in the SQG system in order to dissipate the energy accumulated at the western boundary and avoid a singularity formation.

c) Double-gyre configuration

Fig. (3.5.a - b) shows the instantaneous ψ maps for a numerical experiment with ν = 0.0125, w' = 2 and 256*256 grid points. In Fig. (3.5.b) the flow has reached a statistically steady steady state. The boundary current south the zero wind stress curl line (ZWCL) flows north and the one north the ZWCL flows south. They become unstable forming a midlatitude short jet with a ring penetrating south of the ZWCL.

The circulation is dynamically unstable and in the double-gyre problem this leads to a degree of spin-up smaller than in the one-gyre case, because the vertical friction is coupled to lateral temperature exchange between gyres, but the difference between the two configuration is less than in the homogeneous case. The explanation is probably still in the singular character of the waves propagation..

A region of recirculation exists in prossimity of the ZWCL at the western wall where the isolines of total temperature are distorted. The jet becomes stronger and it extends quite far into the interior. The ZWCL assumes an oscillatory behaviour following the jet contours. Like in the homogeneous model is useful to consider ψ in the context of the T contour. In the region of linear Sverdrup balance T runs west-east along latitude circles T = -y. At the western boundary T contours are attached to the western lateral wall: the flow must pass across T contours from lower to highter values and in the prossimity of the midlatitude, because the gradient of T are strong, a region of significant recirculation is formed. The ZWCL follows almost exactly the T = 0 contour. The T countours are non firmly attached to the coast at their reference latitude (= -y). In a sufficiently nonlinear boundary current they can be drown almost parallel to the streamlines.

The solution reached a quasi steady state. In Fig (3.6) w' is equal to 4 and ν is 0.008 (512*512 grid points): there is a strong circulation along the ZWCL and the increasing of the recirculation zones. Increasing the viscosity we attend the progressive reduction of the recirculation zone and the development of a shorter and more symmetric double-gyre configuration, with a more linear behaviour of the ZWCL which remains in prossimity of the midlatitude.

Increasing the resolution it is possible to study the previous cases using as viscosity coefficient ν =0.006. The nonlinear effects are dominant on the frictional ones.

For w' = 1 (Fig. 3.7.a - b) a strong circular anticyclonically eddy forms at the midlatitude on the western boundary and slowly propagates eastward, surrounded by a thin and stretched cyclonically recirculation zone moving south. The ZWCL turns south following the cyclonically eddy and return at the midlatitude following the anticyclonically one. The evolution on time shows the formation of a strong and complex recirculation zone with cyclonically and anticyclonically eddy near the western boundary.

Setting w' = 2 (Fig. 3.8.a - b) the separation region appears elongated and the two recirculation zones north and south the ZWCL are almost symmetric at the formation time. Evolving in time the anticyclonically recirculation zone becomes bigger and moves north penetrating the interior with the formation of a circular eddy not attached to the western boundary.

Acknowledgements

Rick Salmon and Ted Johnson can not be thanked enough for all them help through this project (in particulary during the last week for their moral support too).
I would also thank all the GFD staff (professors, visitors, fellows) for providing a GREAT summer.
A special thanks to Lee Campbell for providing coffee and goodies every morning.

References

ANDERSON, T. L. D. & GILL, A. E. 1975 Spin-up of a stratified ocean, with apllications to upwelling. Deep-sea Res. **22**, 583-596.

ANDERSON, T. L. D. & KILLWORTH, P. D. 1977 Spin-up of a stratified ocean, with topography. *Deep-sea Res.* **24**, 709-732.

BLUMEN, W. 1978 Uniform potentail vorticity flow: Part I. Theory of wave interactions and two-dimensional turbulence. *J. Atm. Scien.* **35**, 774-783.

CHASSIGNET, E. P. & BLECK, R. 1993 The influence of layer outcropping on the separation of boundary currents. Part I: The wind-driven experiments. *J. Phis. Ocean.* **23**, 1485-1507.

CHASSIGNET, E. P., BLECK, R. & ROOTH, C. G. H. 1995 The influence of layer outcropping on the separation of boundary currents. Part II: The wind- and Buoyancy-driven experiments. To apper in J. *Phis. Ocean.*

EDDY, E. J. 1949 Long waves and cyclon waves. *Tellus* **1**, 33-52

HOYER, J.-M. & SADOURNY, R. 1982 Closure modeling of fully developed baroclinic instability. *J. Atm. Sci.* **39**, 707-721.

JOHNSON, E. R. 1985 Topographic waves and evolution of coastal currents. *J. Fluid Mech.* **160**, 499-509.

JOHNSON, E. R. & DAVEY, M. K. 1990 Free surface adjustment and topographic waves in costal currents. *J. Fluid Mech.* **219**, 273-289.

MARSHALL, J. C. 1984 Eddy-mean-flow interaction in a barotropic ocean model. *Quart. J. R. Met. Soc.* **110**, 573-590.

PAGE, M. A. & JOHNSON, E. R. 1991 Nonlinear western boundary current flow near a corner. *Dyn. Atm. and Oceans* **15**, 477-504.

PEDLOSKY, J. 1964 The stability of currents in the atmosphere and the ocean: Part I. *J. Atm. Sci.* **21**, 201-219.

HELD, I. M., PIERREHUMBERT, R. T., GARNER, S. T. & SWANSON, K. L. 1995 Surface quasi-geostrophic dynamics. *J. Fluid Mech.* **282**, 1-20.

VERONIS, G. 1966 Wind-driven circulation - Part II. Numerical solutions of the non-linear problem. *Deep-sea Res.* **13**, 31-55.

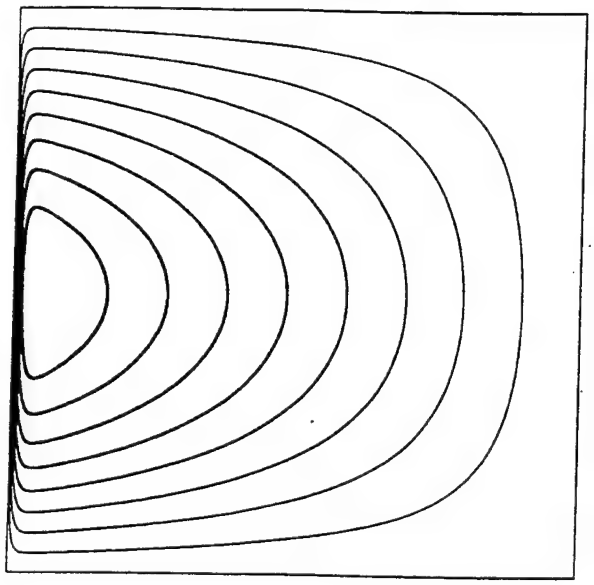

Fig. 2.1 ψ contours for a the single gyre in the linear, time dependent problem.
$\psi_{max} = 0.917$ with $\Lambda = 1$, $w' = 0.01$ and $\nu = 0.02$.

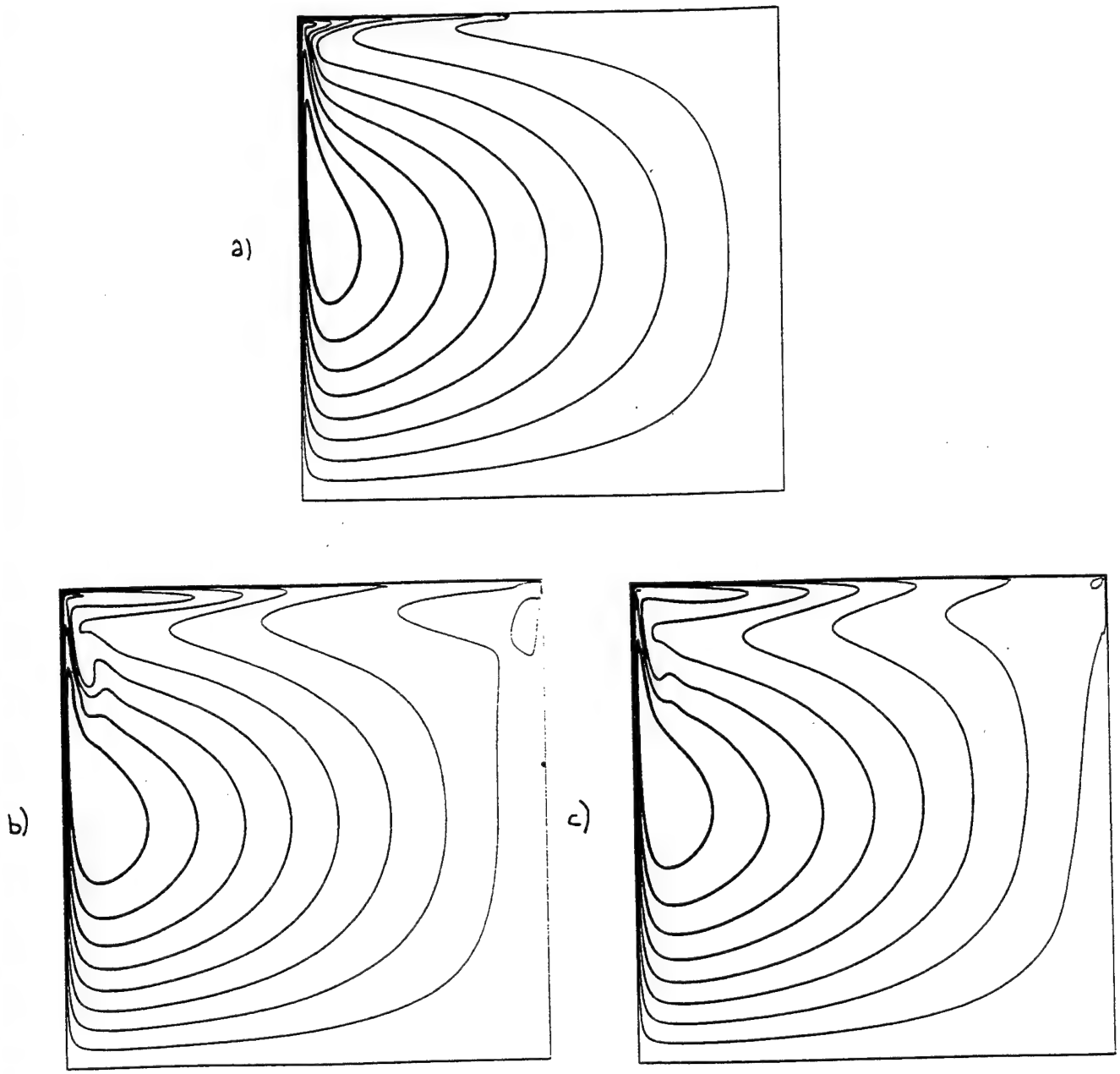

Fig. 3.1 Evolution of a single gyre configuration with w' = 2, $\nu = 0.0125$. a) ψ countours at numerical time t = 0.055, $\psi_{max} = 5.725$. b) ψ countours at t = 0.055, $\psi_{max} = 5.249$. c) ψ countours at t = 0.434 (steady state), $\psi_{max} = 5.198$.

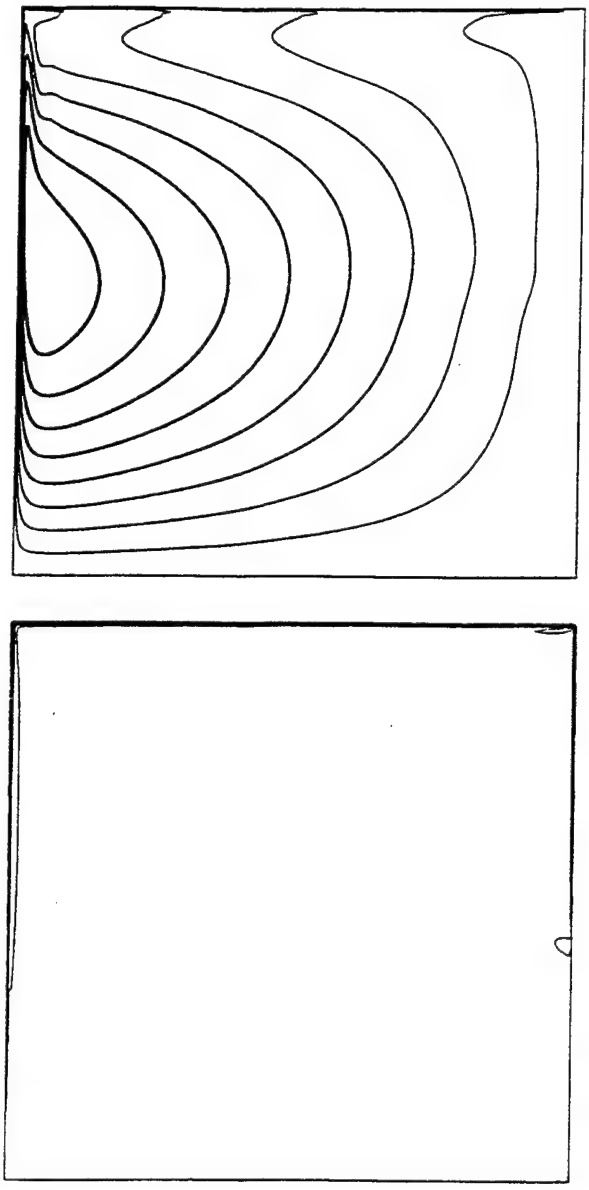

Fig. 3.2 Evolution of a single gyre configuration with $w' = 1$, $\nu = 0.0125$. ψ countours and θ contours at $t = 0.253$ (steady state), $\psi_{max} = 2.676$.

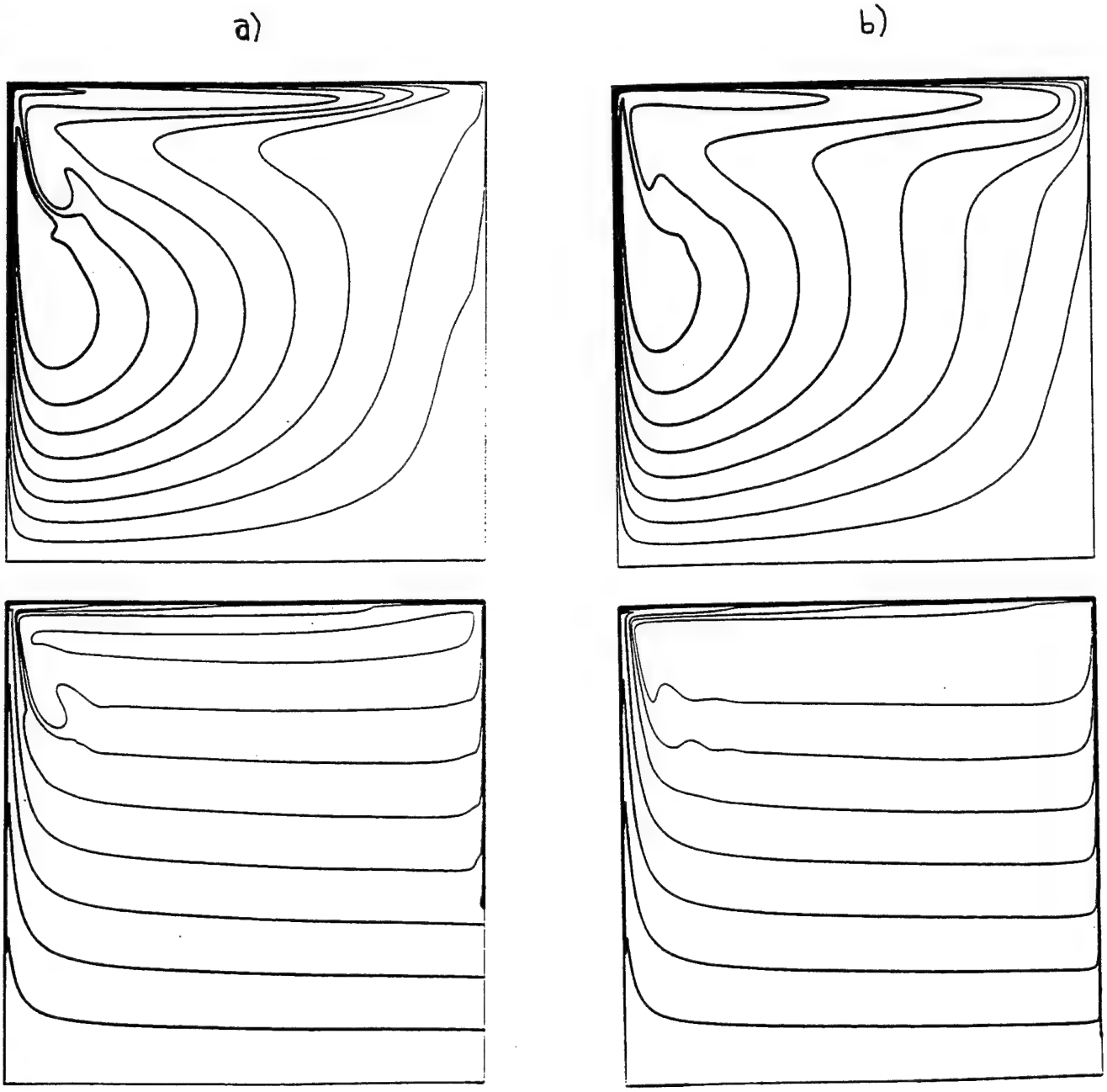

Fig. 3.3 Evolution of a single gyre configuration with w' = 4, $\nu = 0.0125$. a) ψ contours and T = (θ - y) contours at t = 0.105, $\psi_{max} = 10.432$. b) ψ contours and T = (θ - y) contours at t = 0.166 (steady state), $\psi_{max} = 11.252$.

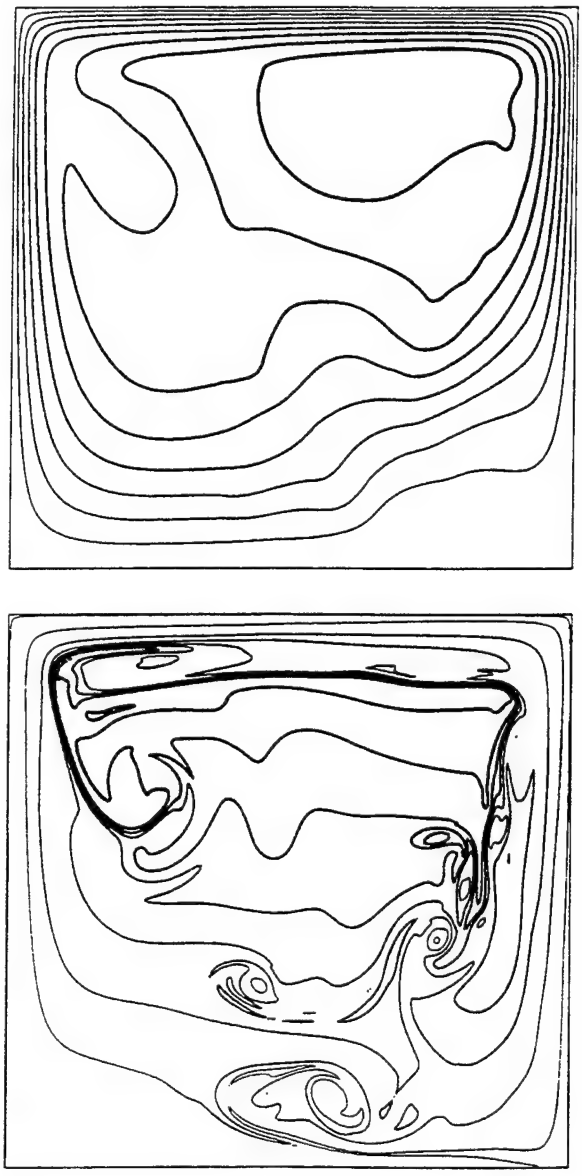

Fig. 3.4 Evolution of a single gyre configuration for the homogeneous case with w' = 1, $\nu = 0.0125$. ψ contours and $\zeta = (q + y)$ contours at t = 0.695, ψ_{max} = 12.65

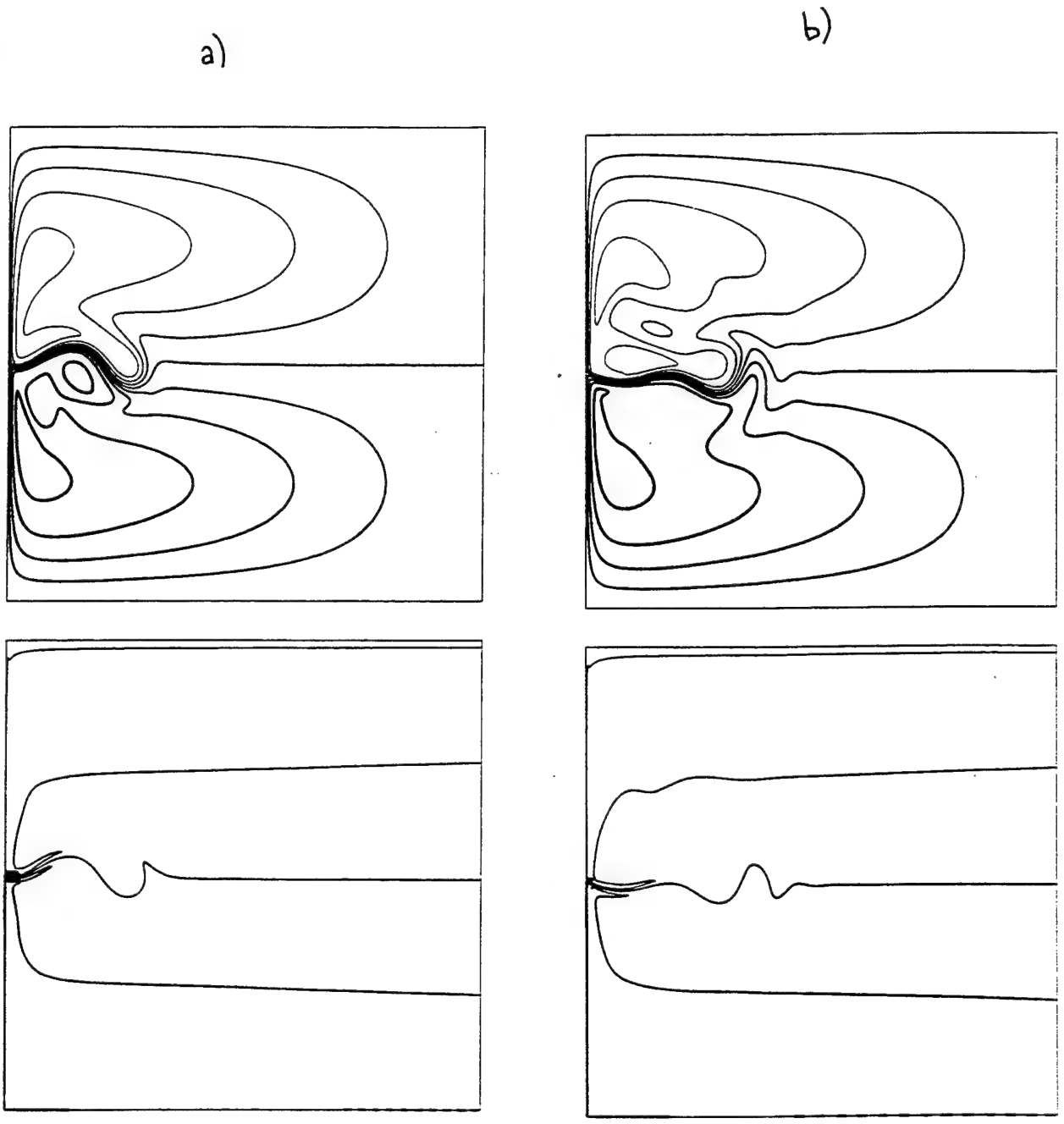

Fig. 3.5 Evolution of a double gyre configuration with w' = 2, $\nu = 0.0125$. a) ψ contours and $T = (\theta - y)$ contours at t = 0.109, $\psi_{max} = 4.936$. b) ψ contours and $T = (\theta - y)$ contours at t = 0.212 (steady state), $\psi_{max} = 5.039$.

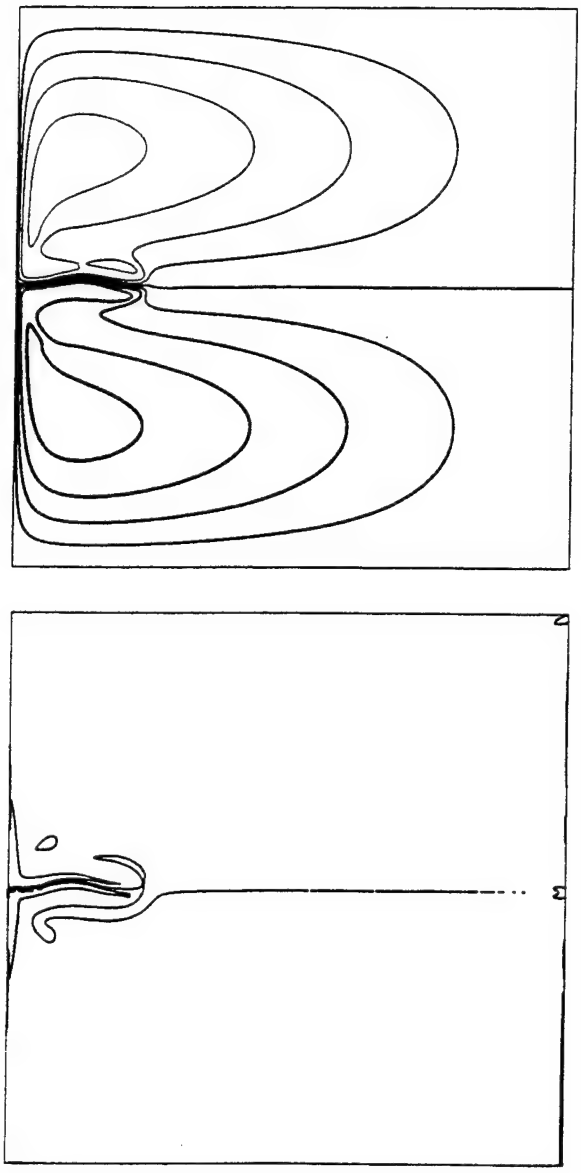

Fig. 3.6 Evolution of a double gyre configuration with w' = 4, $\nu = 0.008$. ψ contours and θ contours at t = 0.04, $\psi_{max} = 12.4$

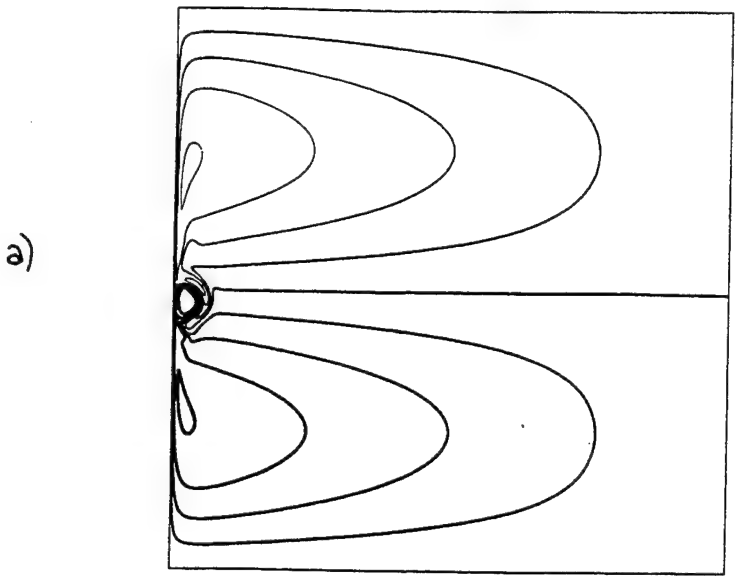

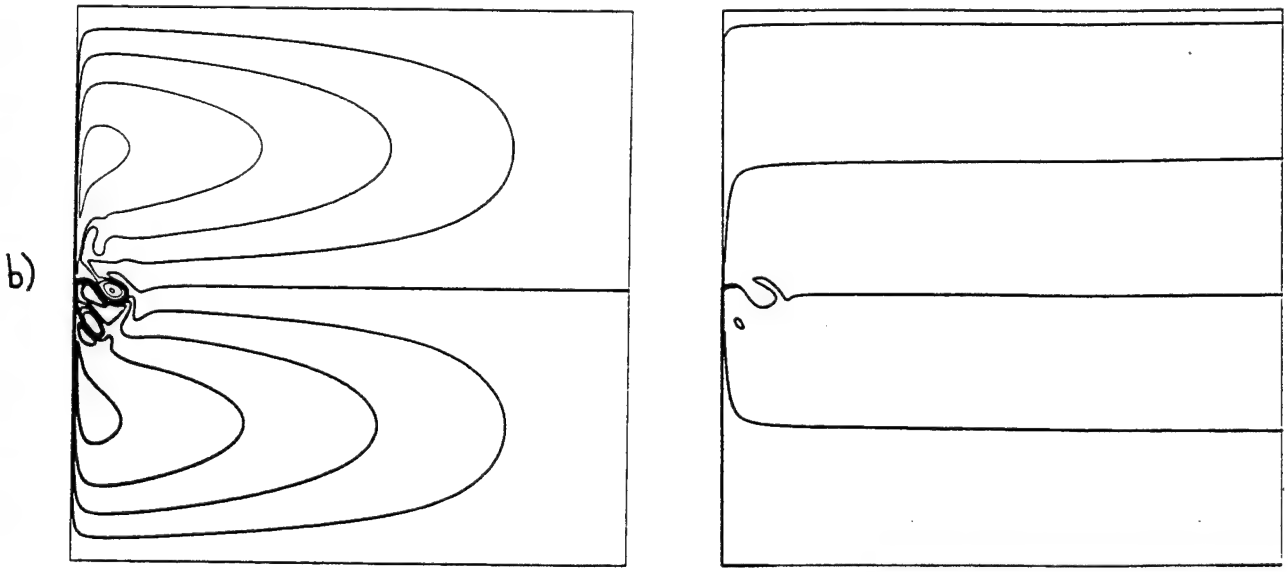

Fig. 3.7 Evolution of a double gyre configuration with w' = 1, $\nu = 0.006$. a) ψ contours at t = 0.044, $\psi_{max} = 3.010$. b) ψ contours and $T = (\theta - y)$ contours at t = 0.08 , $\psi_{max} = 2.791$.

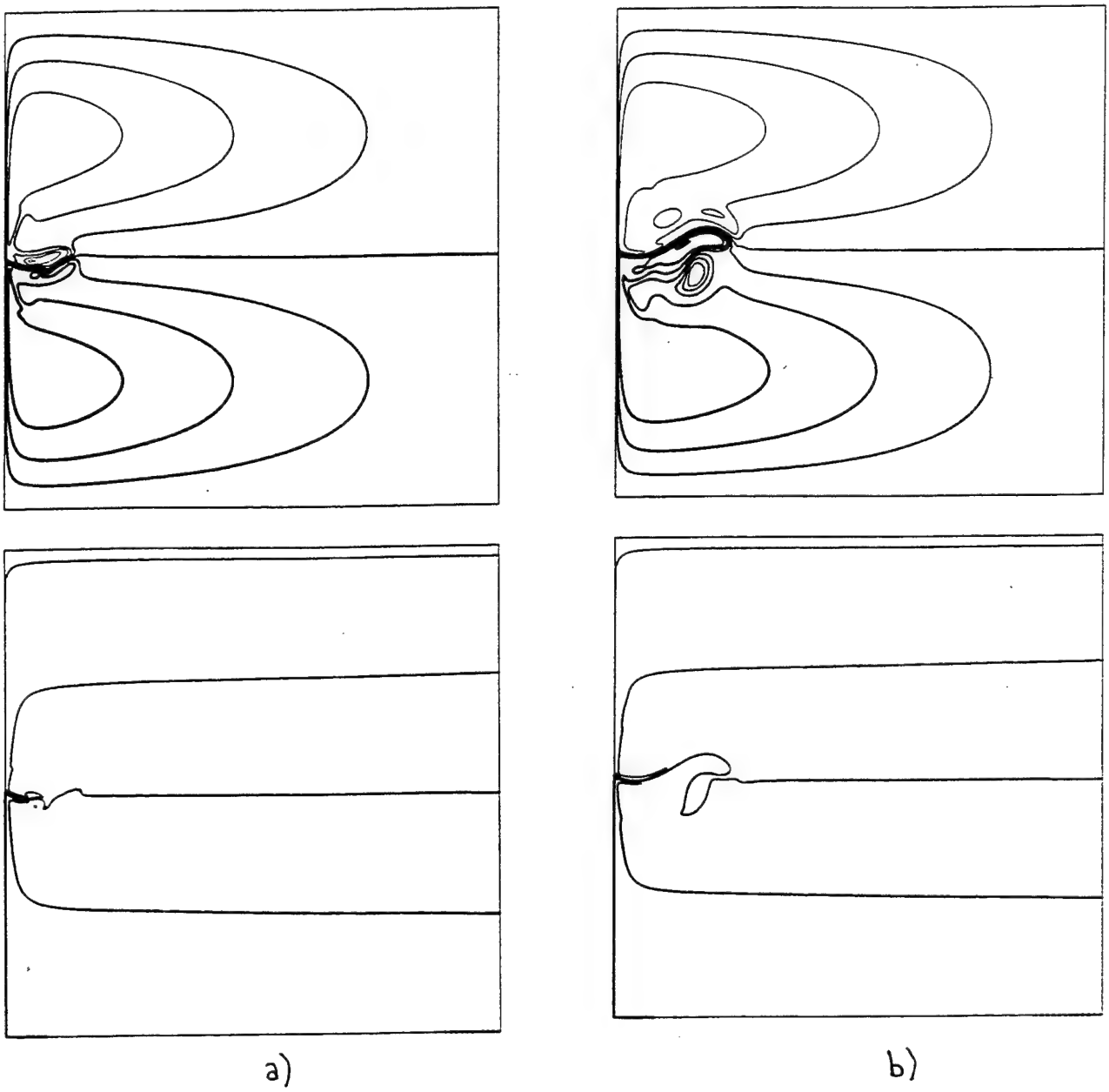

Fig. 3.8 Evolution of a double gyre configuration with $w' = 2$, $\nu = 0.006$. a) ψ contours and $T = (\theta - y)$ contours at $t = 0.037$, $\psi_{max} = 8.119$. b) ψ contours and $T = (\theta - y)$ contours at $t = 0.070$, $\psi_{max} = 7.236$.

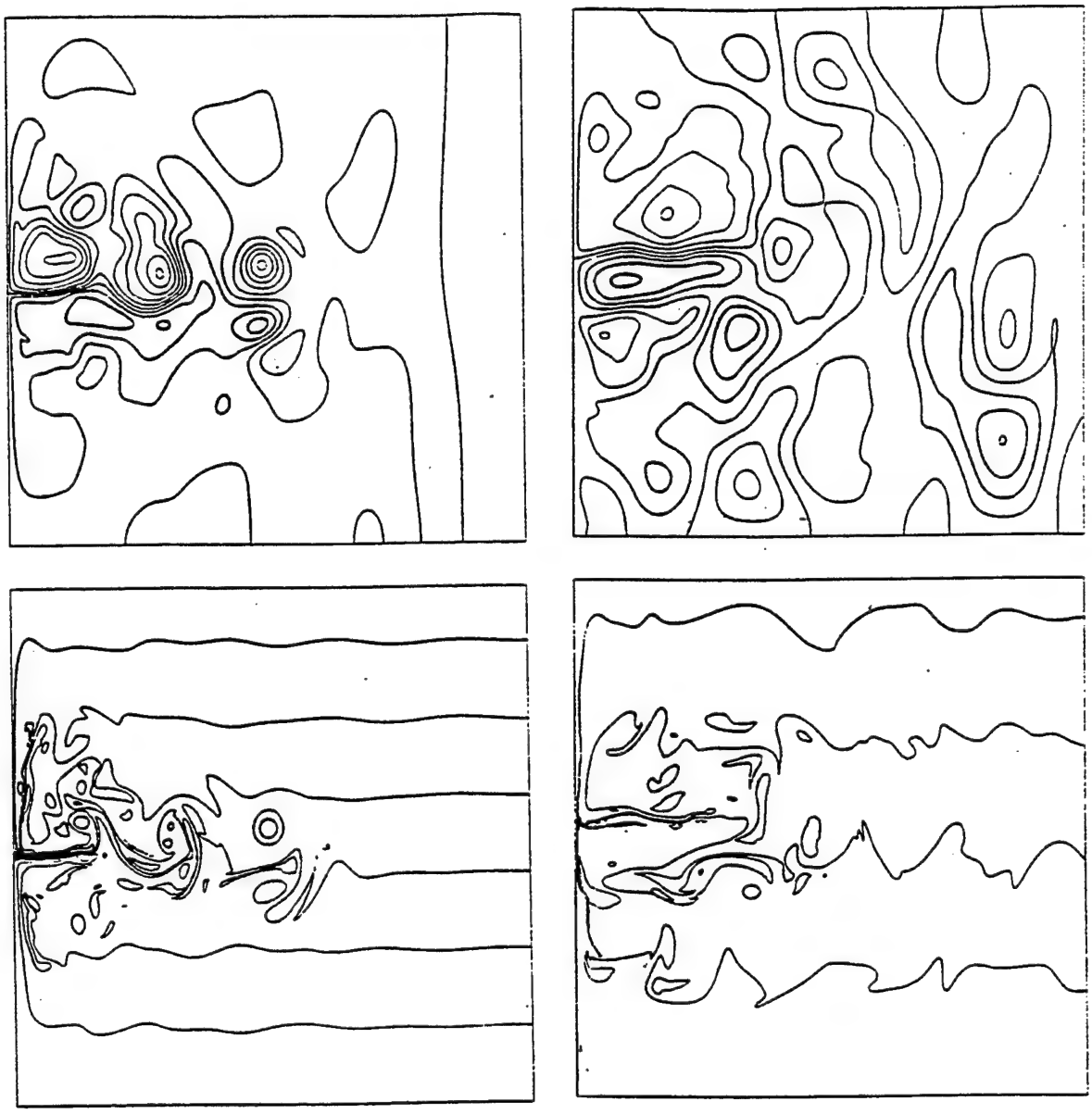

Fig. 3.9 Evolution of a double gyre configuration in the homegeneous model with w' = 0.2, $\nu = 0.025$. a) Ψ contours and $q = (\omega - y)$ contours at $t = 0.997$, $\Psi_{max} = 0.988$. b) Ψ contours and $q = (\omega - y)$ contours at $t = 2.270$, $\Psi_{max} = 1.234$.

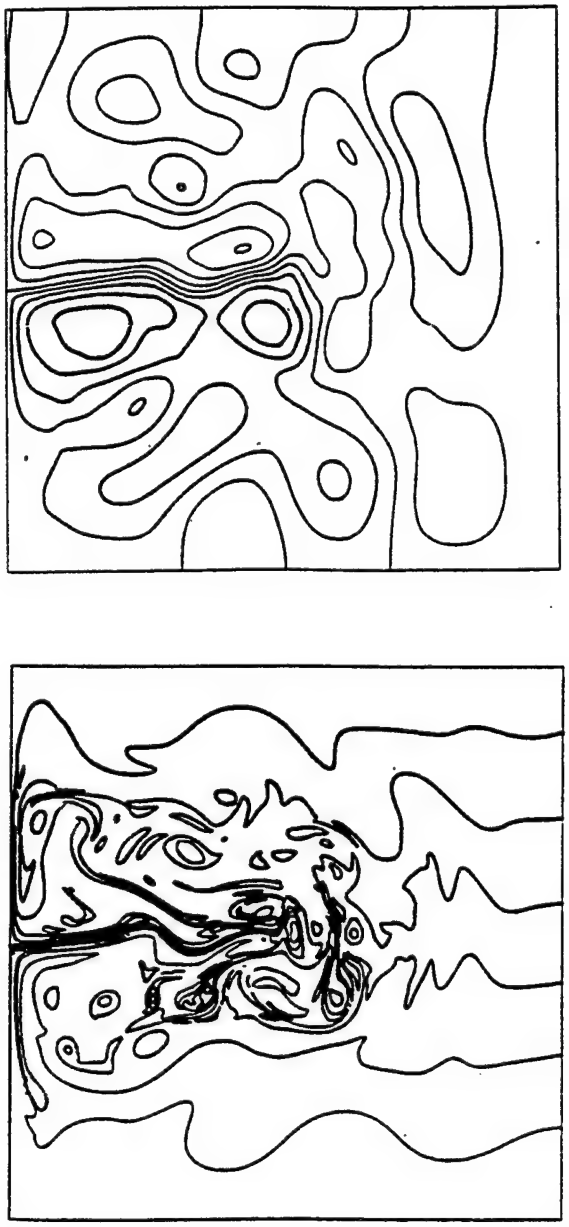

Fig. 3.10 Evolution of a double gyre configuration in the homegeneous model with w' = 0.5, $\nu = 0.0125$. Ψ contours and $q = (\omega - y)$ contours at t = 1.00, $\Psi_{max} = 2.533$.

Hydraulic control and mixing in a semi-enclosed reservoir

Mary-Louise Timmermans

1 Introduction

The problem of mixing in a reservoir that is connected by a narrows to a larger reservoir is of importance in a range of applications, including flow between a sea or fjord connected to the ocean by a strait or natural ventilation in buildings [2]. We examine the relationship between the mixing taking place in the small reservoir and the hydraulically controlled flow between the reservoirs. This situation was first investigated by Stommel and Farmer [6], who considered an estuary opening into the ocean through a narrow strait. Figure 1 illustrates the simplistic case of no bottom topography and reservoirs with vertical sides. The estuary is the basin on the right in this schematic diagram. If there is no mixing between the river outflow and the ocean water in the estuary, then the entirely fresh upper layer flows out through the strait while the lower layer remains stationary. If the two layers are mixed vertically in the estuary, then the thickness of the upper mixed layer increases and the density difference between the upper and lower layers is decreased. The mixing drives an exchange flow between the estuary and the ocean because there is now a return flow of the dense lower layer into the estuary. Under the assumption that the two-layer flow is critical at the narrowest section of the channel, Stommel and Farmer showed that the salinities and exchange rate are independent of the magnitude of the mixing beyond a particular value of the mixing. This limiting case is referred to as *overmixed*. Thus, in the overmixed limit, the density difference between the layers as a result of mixing is limited by the exchange process between the estuary and the ocean, rather than by the mixing process itself.

One application of this problem is the exchange of Mediterranean and Atlantic water through the Strait of Gibraltar. In the Mediterranean, unlike an estuary, where there is a buoyancy source of low density water, there is a buoyancy loss as a result of evaporation which leads to dense water formation. Bryden and Stommel [1] argued that mixing in the Mediterranean Sea is sufficiently intense that it has reached the overmixed limit and the overmixing criterion may be applied to the exchange flow through the Strait of Gibraltar. That is, they showed that the salinity differences between Atlantic and Mediterranean water and the exchange flow between basins is limited by the hydraulic control at the strait and not by the mixing

processes operating in the Mediterranean. This simplifies the problem because it is then only necessary to know that the basin is overmixed and the problem is fully determined without the exact amount of mixing needing to be specified.

The present work emphasises the importance of the magnitude of the mixing on the exchange rather than simply assuming that the basin is overmixed. This is of oceanographic significance because not all basins in nature are overmixed. For example, Hunkins and Whitehead [3] hypothesized that the surface water of the Arctic Ocean is greatly undermixed. The Arctic Ocean consists of an upper layer of low salinity water that prevents circulation in the shallow depths. If there were more mixing of this low salinity water, the thickness of the upper buoyant layer would be greater and the exchange flow between the Arctic Ocean and the Greenland Sea through Fram Strait would increase, while salinity differences between the surface and deep regions of the Arctic Ocean would decrease. Thus, the exchange depends on the magnitude of the mixing, and hence the basin is not overmixed.

In this study, we investigate, both theoretically and experimentally, the two-way exchange for mixing conditions in the smaller reservoir that vary from small mixing to the overmixed limit. In most exchange flow problems, either the basin is assumed to be overmixed, or the density difference between the two flowing layers is given. However, it is not always possible to specify arbitrarily the density difference between layers. In §2, a two-layer hydraulic model is described in which the mixing is modelled as turbulent plumes. Laboratory experiments designed for comparison with the theory are described in §3 and the results are given in §4.

2 Theory

2.1 Governing Equations

We consider a steady, frictionless two-layer flow through a channel connecting a small basin from a larger basin, as illustrated in Figure 1. The channel is assumed to be much narrower than the internal Rossby radius of deformation and therefore rotation is not considered. Initially, both reservoirs contain unstratified salt water and a small steady flux of fresh water is added to the smaller basin. The equation of continuity is

$$Q_1 - Q_2 = Q_0, \tag{1}$$

where Q_0 is the volume flux of fresh water into the small basin, Q_1 is the volume flux of the upper layer out of this basin and Q_2 is the volume flux of the lower layer into the basin. Conservation of salinity may be expressed as

$$Q_1 s_1 - Q_2 s_2 = 0, \tag{2}$$

where s_1 and s_2 are the salinities of the upper and lower layers. This assumes a simple relationship between the salinity of the currents through the narrows, which is valid

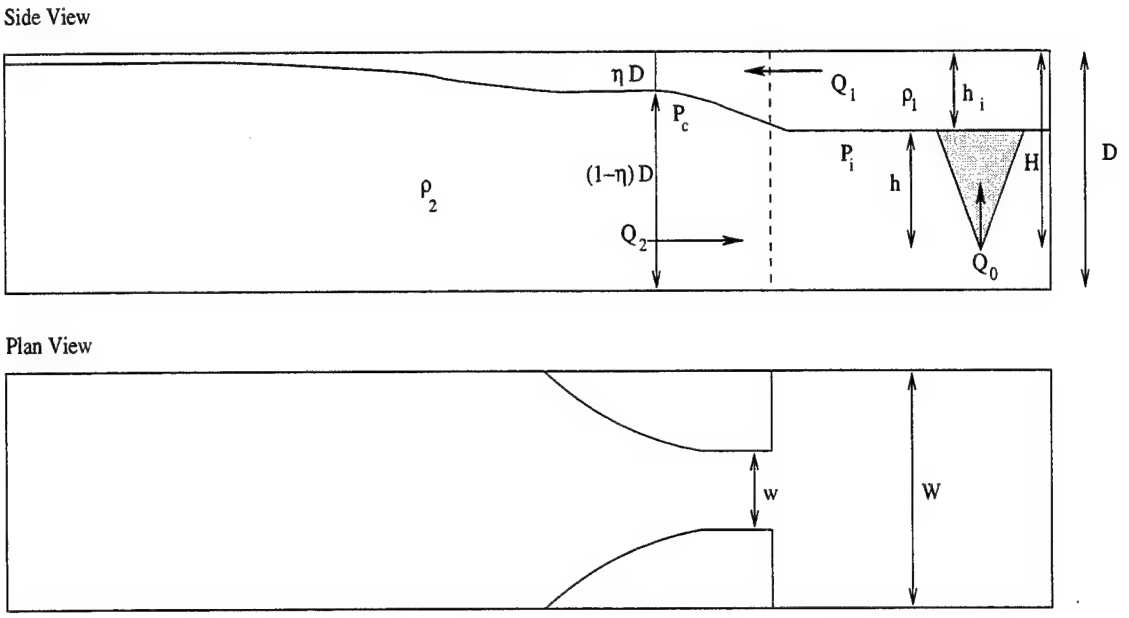

Figure 1: Two layer flow through a transition in width. Fresh water influx into the salt water surroundings in the smaller reservoir results in a flow of lighter mixed water, of density ρ_1, out of this reservoir in an upper layer of depth ηD in the transition, and a relatively dense (density ρ_2) inflow in a lower layer of depth $(1-\eta)D$.

in the laboratory situation, but may be more complicated in nature. Combining equations (1) and (2) yields

$$Q_1 = \frac{Q_0 g_0'}{g'}, \tag{3}$$

and

$$Q_2 = \frac{Q_0 g_0'}{g'} - Q_0, \tag{4}$$

where $g' = g\beta(s_2 - s_1)$ is the reduced gravity since we have assumed that the density difference is proportional to the salinity difference and β is a constant. g_0' (given by $g\beta s_2$) is the reduced gravity prior to any mixing between the input fresh water, and the unmixed salt water. For no mixing ($g'/g_0' = 1$), the entirely fresh upper layer is the only active layer. It is apparent from equations (3) and (4) that for large mixing, when the salinity differences become very small ($g' \to 0$), Q_1 and Q_2 become very large in the absence of frictional effects. This is impossible because the potential energy of the system is proportional to g', and hence decreases rapidly as $g' \to 0$. But, the potential energy is the only source of kinetic energy for Q_1 and Q_2, and thus the fluxes cannot become arbitrarily large as $g' \to 0$. Hence, a limiting minimum g' and a maximum in the exchange flow is implied by the equations, and further mixing in the reservoir cannot alter these limits. This is the overmixing limit.

We assume that the flow passes through critical conditions at the narrowest point in the channel. Using the steady state momentum equations and the equations of mass continuity in each layer, it can be shown [5], in the Boussinesq approximation, that the exchange flow is hydraulically critical at locations where

$$F_1^2 + F_2^2 = 1, \tag{5}$$

where $F_i^2 = \frac{u_i^2}{g' d_i}$ is the Froude number for layer i, u_i is the speed of the flow in this layer and d_i is the thickness of the layer in the narrowest part of the channel. Here, $i = 1$ denotes the upper layer and $i = 2$ denotes the lower layer. The volume flux of layer i is given by $Q_i = u_i d_i w$ where w is the width of the narrowest section of the channel.

It is convenient to express all quantities in non-dimensional form. We non-dimensionalize widths by w, depths by the total depth D of the channel and volume fluxes by $g_0'^{\frac{1}{2}} D^{\frac{3}{2}} w$. Hence, after introducing a fraction η such that $d_1 = \eta D$ and $d_2 = (1 - \eta)D$ (we assume that the free surface deflection is zero), equation (5) becomes,

$$\frac{\tilde{Q}_1^2}{\eta^3} + \frac{(\tilde{Q}_1 - \tilde{Q}_0)^2}{(1-\eta)^3} = \frac{g'}{g_0'}, \tag{6}$$

where the tilde over a quantity implies that it is non-dimensional. Eliminating $\tilde{Q}_1$ from this equation, we obtain

$$\mathcal{F}(\tilde{g}', \eta) = \frac{1}{\eta^3} + \frac{(\tilde{g}' - 1)^2}{(1-\eta)^3} - \frac{\tilde{g}'^3}{\tilde{Q}_0^2} = 0, \tag{7}$$

where $\tilde{g}' = \frac{g'}{g_0'}$ which lies in the range between 0 (completely mixed) and 1 (no mixing). Equation (7) is a cubic in $\tilde{g}'$ which has a real root between 0 and 1 for a given value of η provided that $\tilde{Q}_0$ is less than some critical value $\tilde{Q}_c \approx \sqrt{6}(1-\eta)^{\frac{3}{2}}$, from the theory of cubic equations. In addition to this expression for hydraulic control, we will derive an equation for the mixing process taking place in the small reservoir.

In this study, the agency for vertical mixing is turbulent buoyant convection from a small source. The amount of mixing is progressively increased by extending the distance over which the buoyant plume rises vertically through the environment and hence increasing the amount of entrainment of salt fluid into the fresh plume. We consider an axisymmetric plume generated by an idealized point source below a finite source of buoyancy. The environment is assumed to be uniform and at rest. In homogeneous surroundings, the buoyancy flux B_0 (given by $Q_0 g_0'$) remains constant with height. We use the basic entrainment assumption that the mean inflow velocity U across the edge of the plume is proportional to the mean upward velocity W [4]. That is, $U = \alpha W$, where the constant of proportionality α is called the entrainment coefficient, which has an empirical value of about 0.1.

Morton et al. [4] found exact similarity solutions of the equations for conservation of mass, momentum and buoyancy in the case of an ambient fluid of uniform density. They applied conditions of zero radius and zero momentum flux at the source. The volume flux at a height h above the source is given by

$$Q = c(B_0 h^5)^{\frac{1}{3}}, \tag{8}$$

and the reduced gravity by

$$g' = \frac{(B_0^2 h^{-5})^{\frac{1}{3}}}{c}, \tag{9}$$

where c is an empirical constant which depends upon α. Non-dimensionalizing as before, these variables become

$$\tilde{Q} = c\left(\tilde{Q}_0 (D/w)^2 \tilde{h}^5\right)^{\frac{1}{3}}, \tag{10}$$

and

$$\tilde{g}' = \frac{\left(\tilde{Q}_0^2 (w/D)^2 \tilde{h}^{-5}\right)^{\frac{1}{3}}}{c}. \tag{11}$$

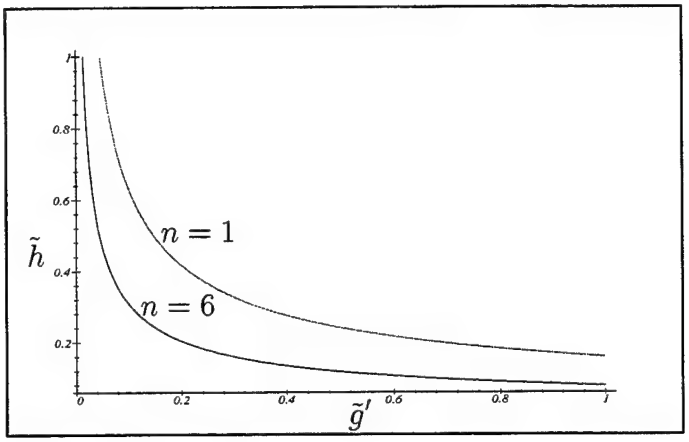

Figure 2: $\tilde{g}'$ as a function of the dimensionless height $\tilde{h}$ of the mixed layer above the plume source. Curves are plotted for one source (n=1) and 6 sources (n=6) for the same total buoyancy flux. The parameters used in the calculations were those of the experimental system: $g_0' = 0.23\ \mathrm{ms}^{-1}$, $w = 0.05$ m, $D = 0.37$ m, $Q_0 = 7{\times}10^{-6}\mathrm{m}^3\mathrm{s}^{-1}$.

In order to increase the volume flux for a given buoyancy flux, a number of buoyancy sources could be placed at the same vertical level in the reservoir. For example, consider n sources placed sufficiently far apart so that their plumes do not

interact, with each plume of buoyancy flux B_0/n. The volume flux at a height $\tilde{h}$ above the source is $n^{\frac{2}{3}}\tilde{Q}$, where $\tilde{Q}$ is given by equation (10), and the reduced gravity is

$$\tilde{g}' = n^{-\frac{2}{3}} \frac{\left(\tilde{Q}_0^2 (w/D)^2\right)^{\frac{1}{3}}}{c} \tilde{h}^{-\frac{5}{3}}. \tag{12}$$

This is the same $\tilde{g}'$ that would result from one plume of buoyancy flux B_0/n.

A short time after the fresh water flux is initiated, a steady state is achieved in which a mixed layer of uniform depth $\tilde{h}_i$ accumulates at a height $\tilde{h}$ above the source. Let $\tilde{H}$ be the non-dimensional depth of the nozzle opening below the top interface between fluid and air, (as shown in Figure 1) so that $\tilde{H} = \tilde{h} + \tilde{h}_i$ and the reduced gravity between mixed and ambient fluid is

$$\tilde{g}' = n^{-\frac{2}{3}} \frac{\left(\tilde{Q}_0^2 (w/D)^2\right)^{\frac{1}{3}}}{c} \left(\tilde{H} - \tilde{h}_i\right)^{-\frac{5}{3}}. \tag{13}$$

The vertical volume flux in the plume is equal to the volume flux in the upper mixed layer through the channel. The density of the mixed layer is equal to the density of the plume fluid at the interface between the two layers. Figure 2 shows $\tilde{h}$, the distance that the plume travels, as a function of the dimensionless reduced gravity for both 1 source and for 6 sources with the same total buoyancy flux.

Equation (13) introduces a new variable $\tilde{h}_i$, and hence, we require an additional relationship between $\tilde{h}_i$, η and $\tilde{g}'$. This equation is obtained by applying Bernoulli's principle just above and below the interface between the two layers,

$$P_i + \rho_1 g(D - h_i) = \frac{1}{2}\rho_1 u_1^2 + P_c + \rho_1 g(1-\eta)D, \tag{14}$$

and

$$P_i + \rho_2 g(D - h_i) = \frac{1}{2}\rho_2 u_2^2 + P_c + \rho_2 g(1-\eta)D, \tag{15}$$

where P_i is the pressure on the interface at depth h_i and P_c is the pressure in the narrowest part of the channel on the interface at depth ηD, as shown in Figure 1. The left sides of these expressions refer to the section in the small reservoir and the right sides refer to the narrowest section in the channel. We have assumed that there is no change in energy before and after the transition in width and we have neglected the velocities in the reservoir under the assumption that $w/W << 1$, where W is the width of the reservoir. Taking the difference of equations (14) and (15), and expressing the velocities in terms of volume fluxes, we obtain

$$2\tilde{g}'(\eta - \tilde{h}_i) + \frac{\tilde{Q}_1^2}{\eta^2} - \frac{\tilde{Q}_2^2}{(1-\eta)^2} = 0, \tag{16}$$

where we have made the Boussinesq approximation and expressed the variables in non-dimensional form. Eliminating $\tilde{Q}_1$ and $\tilde{Q}_2$, we obtain

$$\frac{2\tilde{g}'^3}{\tilde{Q}_0^2}(\eta - \tilde{h}_i) + \frac{1}{\eta^2} - \frac{1}{(1-\eta)^2}(\tilde{g}' - 1)^2 = 0. \tag{17}$$

Note that the derivative of this equation with respect to η is the expression for hydraulic control in the channel. We now have three equations, (7), (13) and (17), which we can solve for η, $\tilde{g}'$ and $\tilde{h}_i$. However, before obtaining a complete solution, it is useful to examine the limits of large and small mixing.

2.2 Limiting Cases

2.2.1 Large Mixing

Stommel and Farmer [6] used the critical condition in the contraction to derive the overmixing solution. This relationship (equation (7)) is plotted in Figure 3 for three different values of $\tilde{g}'$. The graph shows that, for a particular $\tilde{g}'$, there are two solutions to $\mathcal{F} = 0$ for η in the range between 0 and 1. One of these solutions corresponds to a thin upper layer and the other to a thin lower layer. In the present experimental configuration, the smaller solution for η is chosen as η increases from 0 to its limiting overmixed value. As mixing increases ($\tilde{g}'$ decreases), $\mathcal{F}$ increases for all η and at a particular $\tilde{g}'$, the two solutions coalesce. This point, for which a

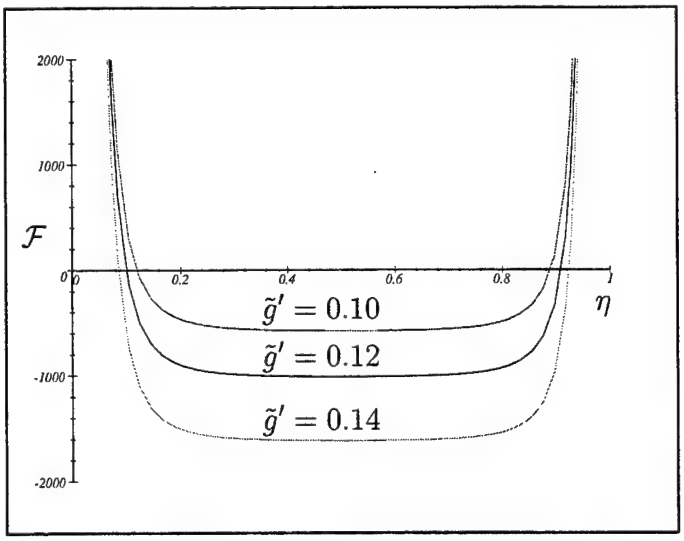

Figure 3: Equation (7) plotted as a function of η for three different values of $\tilde{g}'$ with $\tilde{g}'$ decreasing as the two solutions to $\mathcal{F}(\tilde{g}', \eta) = 0$ move closer. In the limit as $\tilde{g}' \to 0$, the real solutions cease to exist. The parameters used in the calculations were those of the experimental system.

double root occurs, is the overmixing solution of minimum $\tilde{g}'$ and it is given by

$$\tilde{g}' = \left(\frac{\tilde{Q}_0^2}{\eta^4}\right)^{\frac{1}{3}}. \tag{18}$$

In this limit, for small $\tilde{Q}_0$, $\eta = \frac{1}{2}$. That is, overmixing results in an interface at half of the depth in the contraction.

In a completely mixed reservoir, it is not possible to use Bernoulli's equation to link the mixed reservoir to the narrows, because the assumption of no dissipation no longer applies. We can see this because if there is no energy loss, then the rate of release of potential energy exactly balances the rate at which the kinetic energy of the motion increases. In this balance, the interface in the contraction is at half of the depth in the contraction. However, with increased mixing, there is more potential energy put into the system and therefore there must be dissipation, likely in the form of a jump, before the flow of the mixed layer reaches the contraction, and hence we cannot use Bernoulli's equation.

As the overmixed limit is approached, the interface height in the reservoir becomes (from equations (7) and (17))

$$\tilde{h}_i = 2\eta - \frac{1}{2}. \tag{19}$$

Hence, for small $\tilde{Q}_0$ ($\eta = \frac{1}{2}$), the overmixed limit is reached as soon as the interface height is at half of the depth of the reservoir. Thus, from the plume theory equation (13), we find that

$$\tilde{H} = \frac{1}{2} + c^{-\frac{3}{5}} \left(\frac{1}{2}\right)^{\frac{4}{5}} \left(\frac{w}{Dn}\right)^{\frac{2}{5}}. \tag{20}$$

We can find the minimum number of plumes required to reach the overmixed limit by setting $\tilde{H} = 1$ (i.e., the sources are placed at the bottom of the reservoir). Solving equation (20), we see that we need 5 plumes to reach the overmixed limit, given the present experimental parameters. Further increasing the number of plumes does not influence the exchange. Note that the strength of the source, Q_0, does not affect the number of plumes in the overmixed limit.

2.2.2 Small Mixing

Let us now consider small amounts of mixing ($\tilde{g}' \to 1$). In the limit as $\tilde{g}' \to 1$, from equations (7) and (17) we find $\eta = \tilde{Q}_0$ and the thickness $\tilde{h}_i$ of the upper layer in the small reservoir can be expressed as

$$\tilde{h}_i = \frac{3}{2}\eta. \tag{21}$$

This is simply the relationship between upstream and contraction depths in the one layer system. For small $\tilde{Q}_0$, small mixing results in a lower layer that is very much

thicker than the upper layer and hence there is only a very weak inflow in the lower layer, which is why we recover the one layer result. Equation (21) also holds for small η, even if $\tilde{g}'$ is also small, since again the inflow speed of the lower layer is very small. For small mixing, the depth of the sources below the surface is given by

$$\tilde{H} = \frac{3}{2}\eta + \left[\left(\frac{w}{Dn}\right)^{\frac{2}{3}} \frac{\eta}{c}\right]^{\frac{3}{5}}. \tag{22}$$

2.3 Solutions

Figure 4 shows the reduced gravity as a function of the interface height calculated from the equation for critical flow in the constriction (equation (7)) for different values of $\tilde{Q}_0$. When the net barotropic flow is weak ($\tilde{Q}_0 \to 0$), the solution is

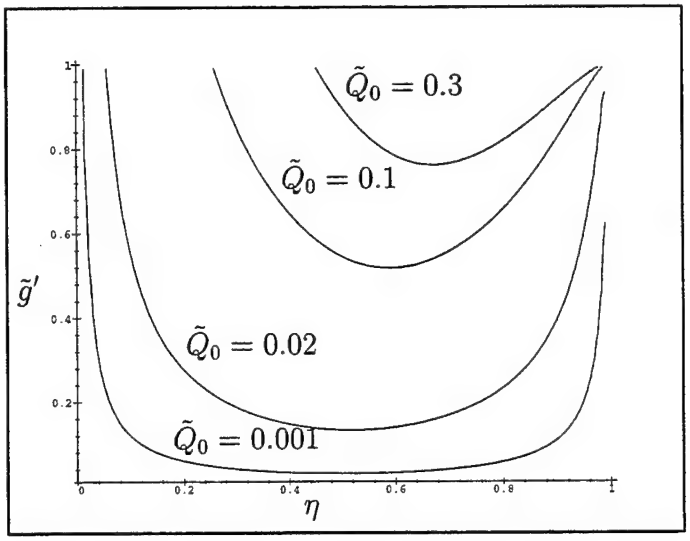

Figure 4: Solutions to equation (7) are plotted for various values of $\tilde{Q}_0$. The dimensionless reduced gravity $\tilde{g}'$ plotted as a function of η for $\tilde{Q}_0 = 0.001, 0.02, 0.1, 0.30$.

nearly symmetric about $\eta = \frac{1}{2}$ with the left side corresponding to a thin upper layer and the right side to a thin lower layer. However, when $\tilde{Q}_0$ is increased, a critical value is reached past which there are no real solutions to $\tilde{g}'$ for a given value of η.. That is, the flow is no longer controlled. Note that for $\tilde{Q}_0 = 1$, which has no physical solutions, the flow is unidirectional and the outflowing layer occupies the full depth of the channel. Figure 5 shows $\tilde{g}'$ as a function of the interface height η in the narrows. The intersection of the thick line (equation (7)) and the dashed lines (equations (13) and (17) for various values of $\tilde{H}$) are the possible values of η and $\tilde{g}'$

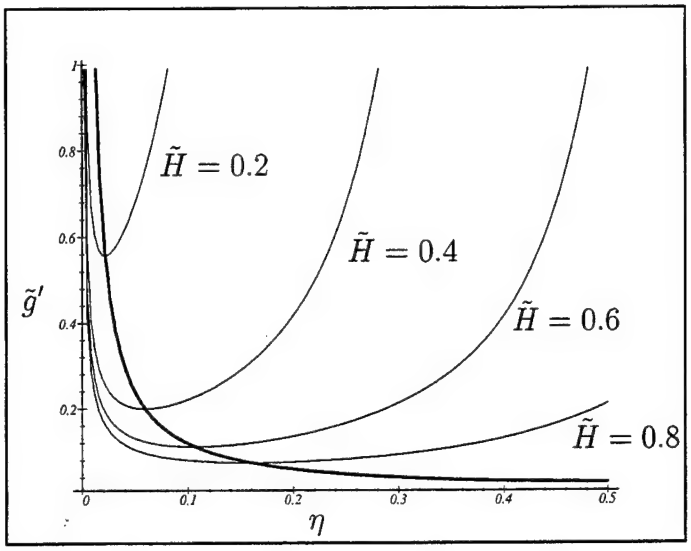

Figure 5: The dimensionless reduced gravity $\tilde{g}'$ plotted as a function of η. The thick line is the solution to equation (7), and the thin lines are the solutions to equations (13) and (17) for $\tilde{H} = 0.2, 0.4, 0.6, 0.8$. The parameters used in the calculations are those of the experimental system.

in the present experimental system. In §4, the numerical solutions will be compared with the laboratory results.

3 Laboratory Experiments

A test of the theory was carried out in a laboratory flume that was 5 m in length, 0.6 m high and 0.4 m wide. The flume was filled with salt water from the ocean. The reservoirs were formed by placing a perspex contraction in the flume so that the length of one reservoir was 0.4 m long and the other was 4.2 m long. The geometry is illustrated in Figure 1. The contraction was abrupt on the side joining the small basin, where it had a width of 5 cm. The channel, made of clear flexible plastic, widened over a length of 0.4 m onto the side of the larger reservoir. To produce vertical mixing, buoyant fresh water plumes were generated in the uniform salt water environment of the small basin. The initial reduced gravity g'_0 between the fresh water and the salt water was 0.23 m s^{-2}.

Experiments began by releasing fresh water from an upward pointing tube placed at some height H under the salt water surface. In order to increase the volume flux through the contraction for the same buoyancy flux, experiments were also performed with a varying number of sources placed at the same vertical level. In

all experimental runs, the total buoyancy flux from the source or sources was $B_0 = 1.6 \times 10^{-6}$ m^4 s^{-3}. [1] The fresh fluid ascended, forming a turbulent entraining plume which drove an exchange flow through the contraction. Approximately one to two minutes after the fresh water flux was initiated, a steady state two-layer system was achieved. The two layers were visualized by adding dye to the fresh water supplied at

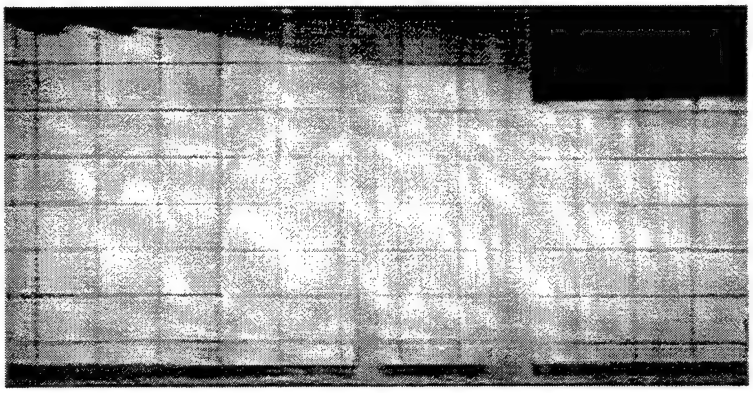

Figure 6: Vertical cross section of a typical experiment. Mixing takes place in the reservoir on the right. The narrowest part of the contraction is in the center and the flow in the upper layer is from right to left.

the source. In the upper layer, the fluid was mixed and less dense than the ambient, while in the lower layer, the fluid outside the plume was uniform dense ambient fluid. Water samples were taken to measure the density of the surface mixed layer. The samples, taken from various regions in the mixed layer, indicated that it was a well mixed layer. Once this steady state was reached, the exchange flow was observed for various values of H. Crystals of potassium permanganate were dropped into the contraction and their subsequent traces were observed. A total of 20 runs was conducted with varying values of H.

For the single plume experiments, the same outlet, of diameter 1 cm, was used each time. As the experimental source had a finite diameter, it was necessary to determine the position of the virtual point source below the nozzle opening. The position of the virtual source was determined experimentally by measuring the radius of the cone shaped plume as a function of height above the nozzle and extrapolating the resulting straight line to the apex of the cone. The relevant heights were then measured from this virtual source, which was determined to be 0.5 cm below the opening. When multiple sources generated the mixing, the outlets were each of diameter 0.5 cm and their virtual sources were taken to be at the nozzle openings.

[1] We have assumed pure buoyancy driven plumes and neglected any flux of momentum, because the lengthscale $L = M_0^{\frac{3}{4}}/B_0^{\frac{1}{2}}$ based on the momentum flux M_0 and the buoyancy flux B_0 at the source is only 0.5 cm, which is very much less than the height of the plume. Thus, buoyancy dominates over momentum, except in the region close to the source.

The vertical cross section of a typical experiment is shown in Figure 6. In the experiment shown here, 6 sources were placed at 16 cm below the surface in the small reservoir, which is on the right in the figure. The steady state level of the mixed layer has been reached and the flow of the upper dark layer is from right to left out of the smaller reservoir. The plumes are out of the picture to the right.

4 Results

In Figure 7(a), the position of the interface in the contraction as a function of the non-dimensional depth $\tilde{H}$ for several different single plume experiments is compared with the theoretical predictions. The interface height $\tilde{h}_i$ in the basin is plotted as a function of $\tilde{H}$ in Figure 7(b), and the relationship between the reduced gravity $\tilde{g}'$ and $\tilde{H}$ is shown in Figure 7(c). As can be seen from the experimental results, the completely undermixed case was difficult to achieve in the laboratory. There was always a slight upstream flow in the lower layer due to some unavoidable mixing across the interface. For small $\tilde{h}_i$ and η, the data is in agreement with the one layer relationship ($h_i = \frac{3}{2}\eta$). As the overmixed limit is approached ($\eta \to \frac{1}{2}$), the height of the interface $\tilde{h}_i$ in the small reservoir does not lie on the numerical curve. This dissagreement is a result of the incorrect assumption that the exchange flow is dissipationless in a well-mixed reservoir, as discussed in §2.2.1. Beyond the overmixed state, the present theory can no longer predict the height of the interface in the reservoir.

Experimental and theoretical predictions for multiple plumes are compared in Figure 8. By increasing the number of plumes, we increase the volume flux through the contraction while decreasing the density difference. The interface height should be approximately $n^{2/9}$ more than that for a single plume from a source at the same depth. This agrees with the experiments. Before the basin has reached the overmixed state, the experimental results for the interface height $\tilde{h}_i$ lie on the curve as expected. However, close to the overmixed limit, where $\tilde{H} \approx 1$ for 6 sources, and $\eta \approx \frac{1}{2}$, the value of $\tilde{h}_i$ deviates from the theoretical prediction, as in the single source case. This indicates that the basin is overmixed and the value of $\tilde{h}_i$ can no longer be predicted by the theory, although the exchange flow is not affected. The reduced gravity $\tilde{g}'$ as a function of $\tilde{H}$ (Figure 8(c)) shows the increased mixing for a given value of $\tilde{H}$ that is a result of increasing the number of sources.

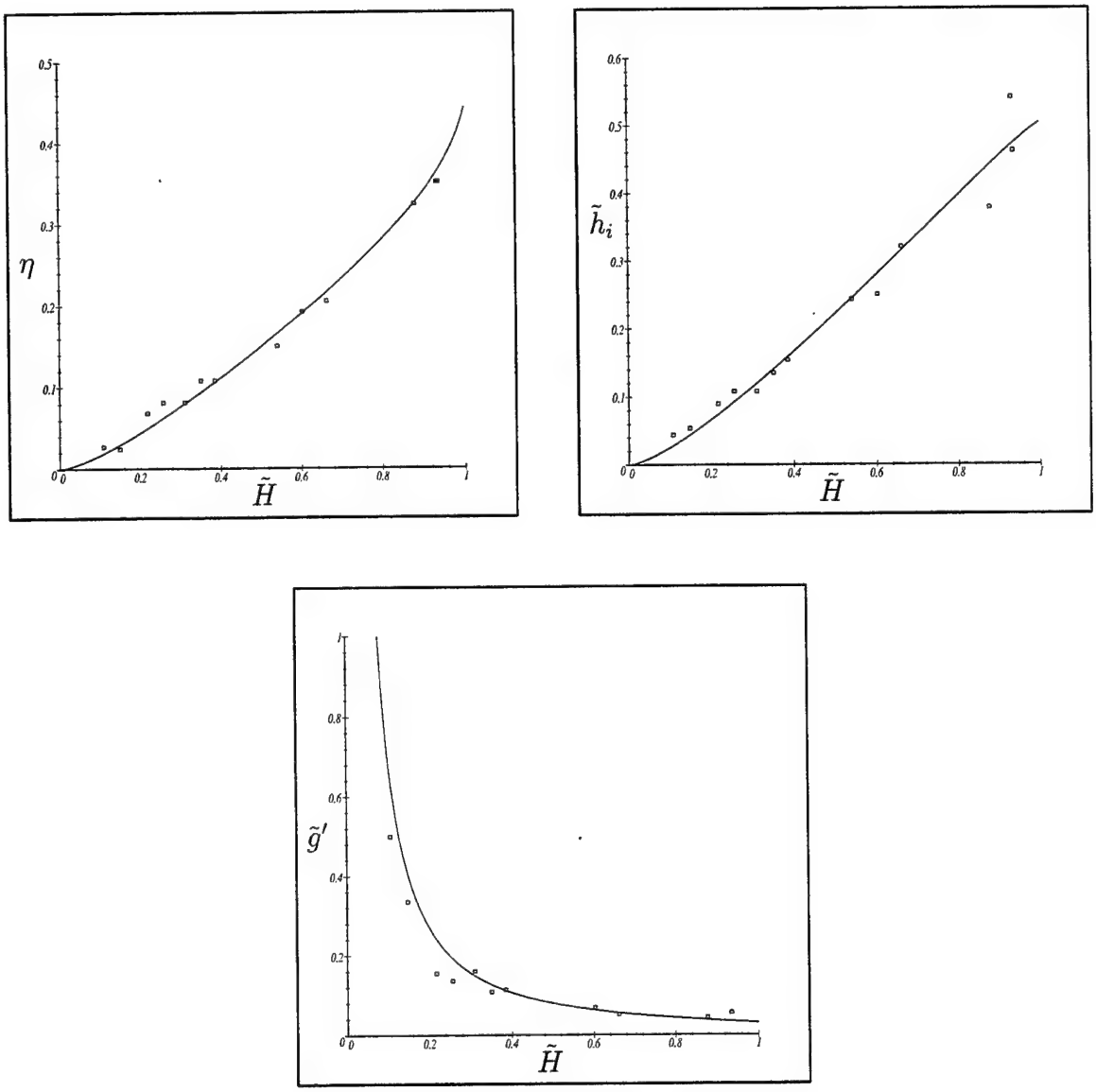

Figure 7: The relationship between the dimensionless depth $\tilde{H}$ of a single fresh water source and (a) the interface height η in the contraction, (b) the interface height $\tilde{h}_i$ in the basin and (c) the reduced gravity $\tilde{g}'$. The solid curves are the numerical solutions and the points are experimental results.

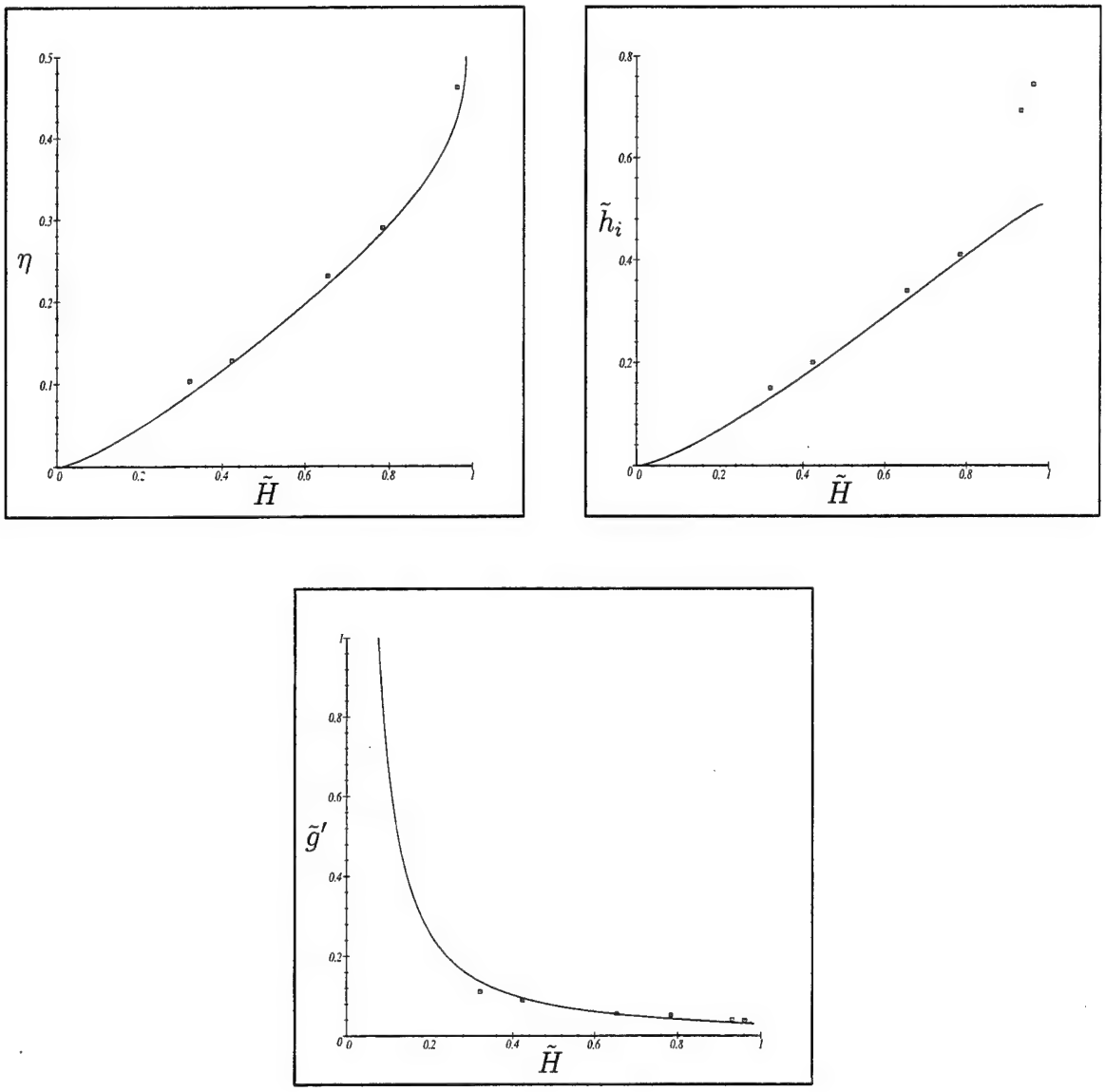

Figure 8: The relationship between the dimensionless depth $\tilde{H}$ of 6 sources at the same vertical level and (a) the interface height η in the contraction, (b) the interface height $\tilde{h}_i$ in the basin and (c) the reduced gravity $\tilde{g}'$. The solid curves are the numerical solutions and the points are experimental results

5 Conclusions

We have shown that for the simple geometry of a flat bottom and a transition in width, as shown in Figure 1, the exchange flow between two reservoirs can be determined as a function of the amount of mixing between the two flowing layers (as given by the dimensionless source depth $\tilde{H}$). Unlike in other exchange flow problems, where the density difference between the buoyant and dense layers is specified, we have fixed the amount of mixing between the layers. Theoretical calculations verified by experiment demonstrate, for small volume flux of fresh water $\tilde{Q}_0$, that as soon as the interface reaches half of the depth in the reservoir, the basin is overmixed and the overmixing criterion can be applied. Once this limit has been reached, the exchange flow is independent of the mixing.

There are numerous extensions to this work. In nature, the amount of mixing in an ocean basin may vary over time (for example, as a result of the tides). This will cause temporal variations in the exchange flow, and a time dependent hydraulic theory is therefore necessary. Similarly, varying strait geometries will greatly influence the hydraulic control and the exchange flow. A simple extension of the present problem of a narrows with a horizontal bottom would be the addition of a sill to the channel. Furthermore, in the present study, it was assumed that the strait was narrow compared to the Rossby deformation radius. It is possible that in wider channels the effects of rotation on the two-way flow may be strong and a rotating hydraulic control theory [7] must be applied.

I would like to thank Jack Whitehead for suggesting the project and for his encouragement and advice over the summer. Special thanks are also due to John Salzig for his invaluable assistance in the laboratory. I am most grateful for the interesting and helpful discussions with many other GFD staff and visitors.

References

[1] BRYDEN, H.L. & STOMMEL, H. M. 1984 Limiting processes that determine basic features of the circulation in the Mediterranean Sea. *Oceanol. Acta* **7,3** 289-296.

[2] DALZIEL, S. B. & LANE-SERFF, G.F. 1991 The hydraulics of doorway exchange flows. *Building and Environment* **26** 121-135.

[3] HUNKINS, K. & WHITEHEAD, J.A. 1992 Laboratory simulation of exchange through Fram Strait. *J. Geophys. Res.* **97, C7** 11,299-11,321.

[4] MORTON, B.R., TAYLOR, G. & TURNER, J.S. 1955 Turbulent gravitational convection from maintained and instantaneous point sources. *J. Fluid Mech.* **131** 195-218.

[5] STOMMEL, H. & FARMER, H.G. 1952 Abrupt change in width in two-layer open channel flow. *J. Mar. Res.* **11** 205-214.

[6] STOMMEL, H. & FARMER, H.G. 1953 Control of salinity in an estuary by a transition. *J. Mar. Res.* **12** 13-20.

[7] WHITEHEAD, J.A., LEETMAA, A. & KNOX, R.A. 1974 Rotating hydraulics of strait and sill flows. *Geophys. Fluid Dyn.* **6** 101-125.

An Experimental Investigation of a Coastally-Trapped, Surface Density Current

JEFF PARSONS
Department of Civil Engineering
University of Illinois

1. Introduction

The ultimate fate of rotationally-dominated plumes is of utmost importance to oceanographers as well as engineers and geologists. River plumes and oceanic outflows, like that of Mediterranean at the Straits of Gibraltar, typically have only slightly different densities than the surrounding water. Also because of their relatively low momentum and their large size they are commonly trapped by the topography and flow along the coast as surface gravity current (see Figure 1). Though considerable analysis (Stern, 1980; Griffiths and Linden, 1981; Stern *et al*, 1997) has been devoted to the stability of these currents, the effects of these instabilities on the propagation rate and ultimate fate of the front of a current have not been studied. Laboratory experiments provide the most effective way of understanding this process due to the complexities (*i.e.*, discontinuities) present in the flow. Scaling analysis will then provide the basis for interpreting the underlying mechanisms regulating the removal of the geostrophic current from the coast.

2. Dimensional Analysis

Five independent parameters exist in the experiments performed herein. They are the Coriolis parameter f the reduced gravitational acceleration of the current g' the volumetric flux of light fluid at the source Q the total flow depth H and the kinematic viscosity ν. From these parameters, two different scenarios can be posed to describe the development of the surface gravity current. If the current reaches a steady-state, these two behaviors will either be geostrophic (*i.e.*, a balance between rotationally-affected inertia and buoyancy) or viscous-dominated (*i.e.*, a balance between rotationally-affected viscosity and buoyancy).

Geostrophic balance (which occurs in the limit of zero viscosity; $\nu \rightarrow 0$) dictates that there are two significant length scales formed with f, Q and g'. From geostrophic balance and continuity the depth of the current at the wall D will be described by $\sqrt{2fQ/g'}$. Using this as a length, it is possible to form the Rossby radius $L = \sqrt{g'D}/f$ in terms of the independent parameters. Doing this we find $L = \left(2g'Q/f^3\right)^{1/4}$. Both the Rossby radius and geostrophically-expected depth can be made dimensionless with the total fluid depth, to form the two dimensionless lengths. An alternative third, but not independent, dimensionless parameter is the ratio of L/D. Dimensional

quantities are typically scaled in time by $1/f$ and in length by the Rossby radius L. The ratio of these results in a velocity scale of $\sqrt{g'D}$. All of these parameters can be found in relation to their physical interpretations in Figure 1 below.

If the flow is viscous-dominated, velocities will scale lengths with $\sqrt{\nu/f}$ and velocities with $\sqrt{\nu f}$. Effects of viscosity can also originate from the Ekman layer at the bottom of the tank. These effects will occur after the Ekman spin-up time which can be expressed by $t_{spin-up} = \sqrt{H^2/\nu f}$. Processes which see the transition from geostrophic to viscous-dominated behavior will be described the square of the ratio of the two velocity scales $g'D/\nu f$.

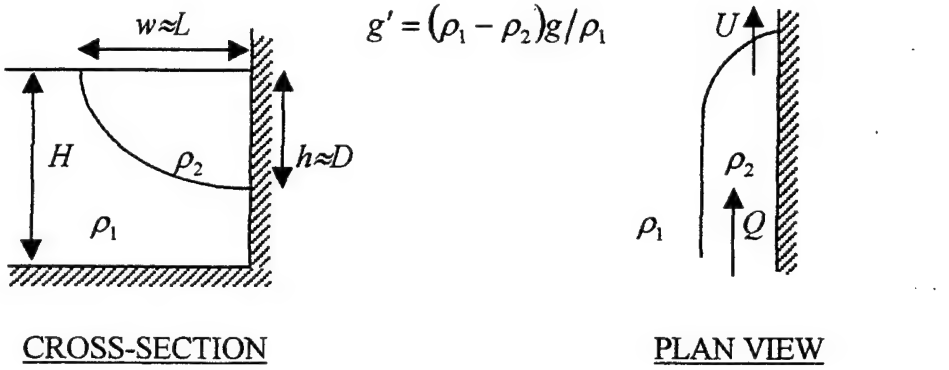

Figure 1 Definition diagram of a geostrophic coastal density current

Dependent variables in this problem are the nose propagation rate U and the seaward flux of light fluid q. These parameters are the oceanographically relevant parameters describing the ultimate size and shape of the plume. The depth h and width w of the current are also dependent variables. Deviations from the values shown in Figure 1 will most likely indicate that geostrophy is not the appropriate description of the flow.

3. Experimental Setup and Procedure

Experiments were performed in two different tanks. The first experiments were performed in a Perspex rectangular tank 174.4 cm long, 30.5 cm wide and 30 cm deep. With an external mirror mounted at a 45° angle with the floor of the tank, the width-averaged depth structure was visualized simultaneously with the horizontal behavior of the current. Because of limitations in the runout of the current, later experiments used a 2 m diameter Fiberglas (*i.e.*, not transparent) circular tank. The circular tank was not only larger, but allowed for runout distances of as much

as 6 m without topographic interruption (*i.e.*, without hitting a corner). Both tanks were covered with plastic wrap to curtail evaporation effects and prevent wind shear at the surface.

It should be noted that the reduced gravitational accelerations required for the blocking instabilities were extremely small, even for the large tanks used herein. Under reasonable rotation rates (*e.g.*, $f \leq 2$), the reduced gravitation acceleration needs to be less than 0.3. This, along with the small volume fluxes (around 1 cm^3/s) required for plume behavior at the source, severely hampered the parameter range that could be explored.

For the most part, the reduced gravitational acceleration and the total fluid depth were the parameters that were varied. This was done primarily to assess the effects of the instabilities on the total depth because it was thought that the compression of the lower layer played an important role in the activity of the blocking instabilities. However, as will be discussed at length below, viscosity played an important role in the flows herein and these variables were relatively insignificant. As a result, the Coriolis parameter was varied in the later experiments and resulted in a limited, but significant, spread in the data.

4. Experimental Results

4.1 Effect of instabilities on the nose propagation rate

Experimental results in terms of the parameters discussed above are shown for all of the experiments in Table 1. Experiments with a prefix M indicate experiments performed by Melvin Stern, Jack Whitehead and John Salzig in the rectangular tank. A prefix R indicates a rectangular box experiment run by the author, while C indicates a circular tank experiment.

More interesting, however, was the behavior of the velocity of the current nose with time. Two typical time series are shown in Figure 2 which illustrate the behavior of the dimensionless velocity and with dimensionless distance along the coast. Scaling of the velocity and the length was for a geostrophic current (see Dimensional Analysis above). As can be seen (roughly), the current initially has a velocity consistent with geostrophy (in the non-dimensionalization in the figure, this corresponds to a value of 1.0), but loses momentum until it reaches a constant value. Extreme early times were difficult to measure because of the small size and fast speed of the current. The transition to the slower velocity seen in these two experiments, as well as all others, was rapid and typically occurred on the $O(10)L$. Oscillations seen at large times in Experiment C1 were not due to experimental error, but rather to the formation trains of blocking instabilities and to the meandering phenomenon described below. Despite these oscillations, the mean velocity remains remarkably constant, even for the large runout lengths in the circular tank experiments.

Table 1 General experimental results

Experiment #	g' (cm/s^2)	H (cm)	Q (cm^3/s)	f (Hz)	U (cm/s)	Blocking instabilities	Nose meandering
M1	.10	22.0	1	1	.125	Y	Y
M2	.31	22.0	1	2	.123	L	N
R1	.09	13.8	1	1	.140	Y	N
R2	.14	14.1	1	1	.133	Y	Y
R3	.33	14.6	1	1	.129	Y	N
R4	.31	15.3	1	1	.118	Y	N
R5	.30	9.0	1	1	.114	L	N
R6	.10	9.6	1	1	.151	Y	Y
R7	.09	8.4	1	1	.088	N	N
R8	.06	7.8	1	1	.036	N	N
R9	.19	10.8	1	1	.190	L	N
C1	.12	30.0	1	1	.114	Y	Y
C2	.20	30.0	2	1	.093	Y	Y
C3	.20	30.0	2	1.8	.109	Y	Y
C4	.10	31.0	2	2	.238	Y	Y
C5	.16	30.0	2	0.6	.080	Y	Y

* L denotes limited blocking instabilities (or weak/damped instabilities as in Figure 3)

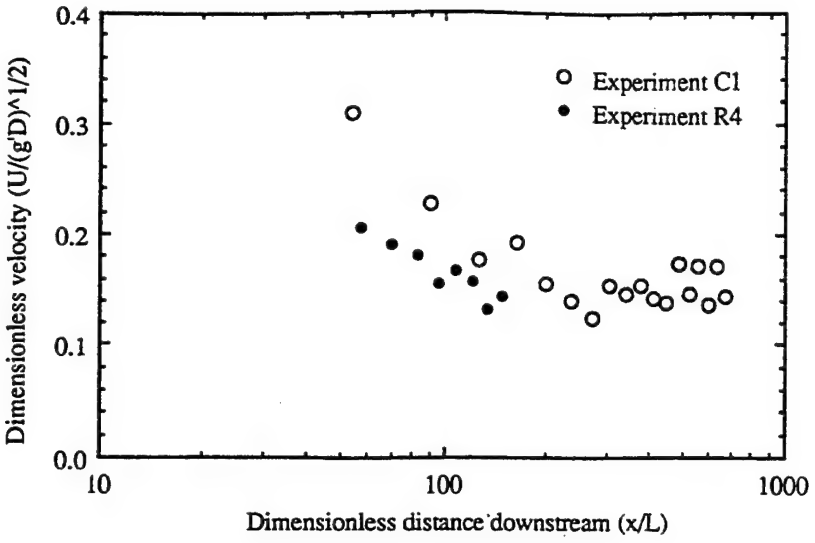

Figure 2 Nose velocity time series

Taking advantage of the quick and long-lasting steady-state, it was possible to assess the controlling parameters in this portion of the flow. By averaging the last four velocity measurements taken in the rectangular box experiments (measurements were taken every 10 cm for the entire length of the tank) and the velocity between 1.57 m and 3.14 m in the circular tank, it was possible to assign a characteristic velocity to each experiment. This characteristic velocity is the U in Table 1. Plotting the two velocity scales ($\sqrt{g'D}$, $\sqrt{vf}$) against U illustrates that the nose velocity is much more influenced by viscosity than geostrophy. Shown in Figure 3, the ratio of the velocity scaled with viscosity only yields in a 50% change in the resulting dimensionless parameter, while the geostrophic dimensionless varies by nearly a factor of four. The slight positive correlation between the two scales is most likely a result of the positive bias in the velocity of slowly adjusting fronts (*i.e.*, the velocity was measured in some experiments where the steady-state was not quite reached). It is important to note that the nose depth, though it could not be measured easily, even with the angled mirror, was also consistent with viscosity-dominated behavior (namely; $\sqrt{v/f}$, usually about 1 mm).

Despite the solid evidence presented above, strict scaling with viscosity does not yield pleasing results. Plotted in Figure 4 are the same data (for the strong instability experiments only), but with just velocity and viscous velocity scale. Ideally, these data would plot along a single line. However, due the lack of variation in f, the correlation is not quite clear. Future experiments could resolve this difficulty by additional runs with the f varied between 0.5 and 2.0 (the extremes of f possible with the rotating table used herein).

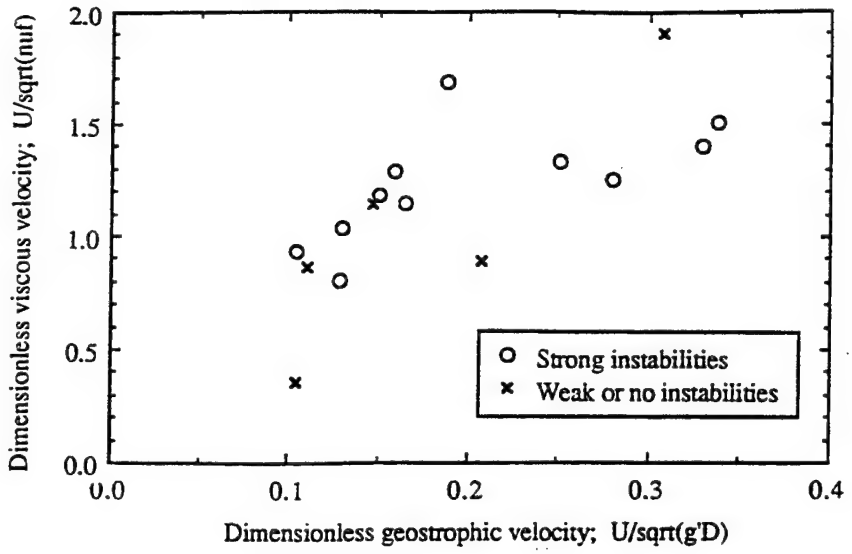

Figure 3 Comparison of the importance of the velocity scaling

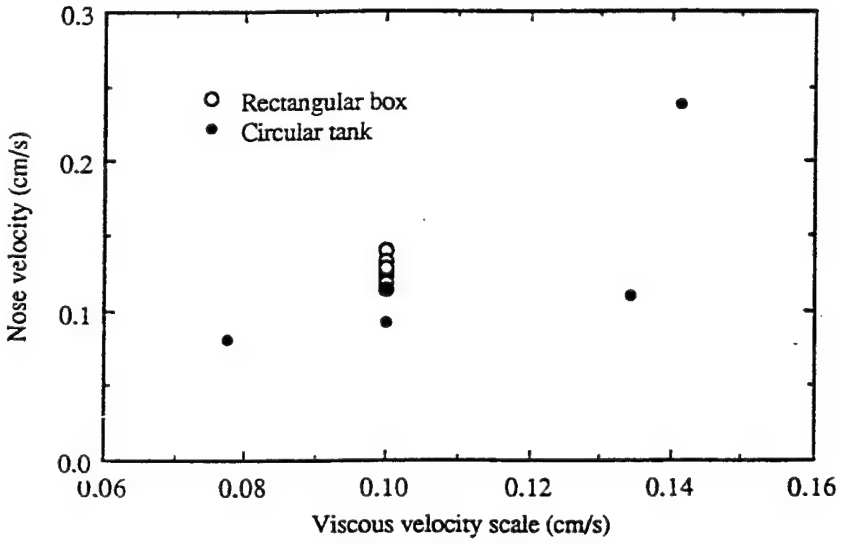

Figure 4 Collapse of nose velocity with viscosity-dominated velocity scale
*Experiments are only shown if they possessed strong instability formation.

Viscosity also effects the propagation velocity when the total fluid depth becomes increasingly shallow. In this case, the bottom Ekman layer begins to influence the entire flow structure and interferes with the development of the instabilities. This behavior is consistent with the numerical analysis of Stern *et al* (1997). Though the Ekman number (the ratio of the Ekman spin-up time to $1/f$) is small, the instabilities slow the actual velocity and increase the horizontal length scale. Also, because the velocity and length scales are easily predicted by the analysis above, it is possible to plot the expected effective time scale (the ratio of the instability length and velocity). Figure 5 illustrates these results. It should be noted that when there were

no instabilities, where the current was dominated by the bed, the propagation speed was proportional with the geostrophic velocity $\sqrt{g'D}$. This is illustrated in Figure 3. The actual velocities, however, were on the order of 1/5 the geostrophic velocity.

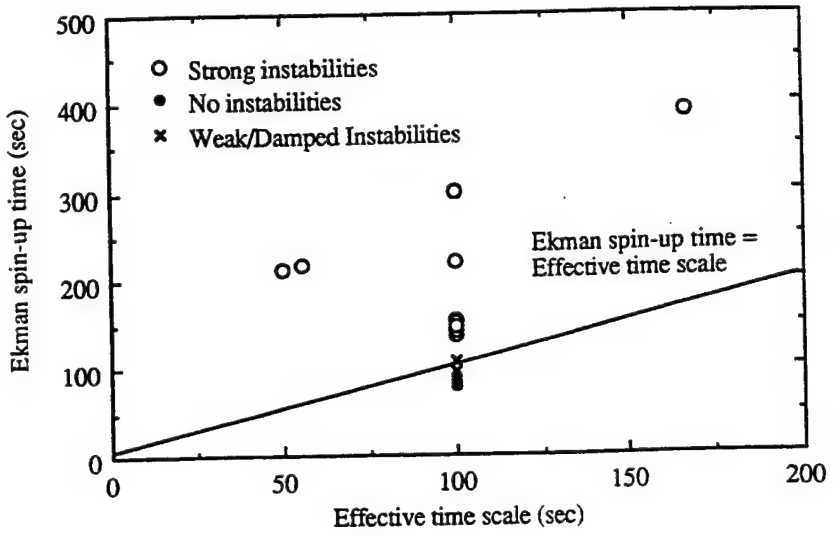

Figure 5 Effect of bottom Ekman spin-up time on blocking instabilities

4.2. Nose meandering

Interesting behavior occurred at times long after the fronts became viscous-dominated. At these large times, the nose meandered to and from the sidewall. This is illustrated in a photograph in Figure 6. The phenomenon was qualitatively similar to that of 'squirts'. Squirts, commented upon by Stern (1986) and first seen in river plumes off the coast of California by Mooers and Robinson (1984), are suspected to be caused by the compression of the current nose. Compression, or velocities behind the nose moving faster than the nose itself, causes the light fluid in the coastal current to 'squirt' away from the coast. Though this is a possible explanation of the behavior herein, a more likely explanation is given below (*i.e.*, the flows herein are viscous-dominated, rather than geostrophic like those of Stern, 1986).

Characteristics of the meandering, along with the proposed scaling, are shown in Table 2. As can be seen in the table, the formation length and amplitude of the meanders follow with the buoyant-viscous length scale of $g'D/vf$. Formation times should necessarily follow with this

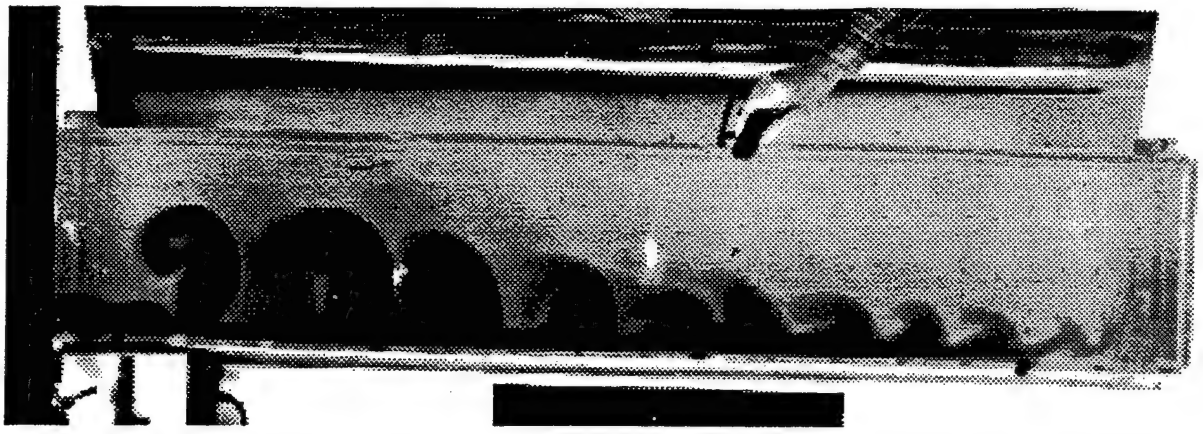

Figure 6 Photograph of nose meandering and blocking instabilities in Experiment M2

parameter because it describes the relationship regulating the two effects in this problem (*i.e.*, buoyancy and viscosity). Length scales of the meandering themselves might not necessarily follow the same relationship, but as is seen in the table and will be discussed below, this is indeed the case.

A possible explanation of the meandering follows from the idea that the viscous influence originates from two distinct viscous boundary layers; one due to the sidewall, the other from the surface. Figure 7 illustrates the development of the phenomenon, along with along with an analysis of controlling processes at each point. Essentially, it is thought that the sidewall preferentially slows the fluid near it, causing the light fluid away from the wall to overrun the fluid near the wall. This effect, however, could also be due to surface tension gradients (*i.e.*, meniscus effects). In turn, light fluid following this can flow more easily away from the wall than towards it, moving the nose offshore. However, once the flow realizes it is in rotation, it turns back towards the wall. It can do this by forming anticyclone (which is consistent with a small bulb of light fluid in rotation), which guides the fluid back to the coast. The ratio of the buoyancy and the viscosity and rotation (reflected in the dimensionless parameter in Table 2) would be the factors that regulate this process and was reflected in the results.

Care, however, should be exercised in extending this phenomenon to the field. The flow in question is extremely sensitive to external laboratory forcing. For example, evaporation effects, though they were tempered by the plastic wrap covering the tank, could be important. Visualizations indicated small flows due to this effect. Also, because the tank is not exactly rotating at the same frequency all the time, small changes could force instabilities such as these. The question of the importance of the surface tension on this phenomenon also has to be raised. However, most damaging to the fate of this phenomenon in nature are the long lengths of uniform (*i.e.*, no capes or peninsulas) coastline required for this phenomenon. Substituting the

Table 2 Characteristics of nose meandering

Experiment #	Formation length (m)	Meander Amplitude (cm)	Viscous-Buoyancy Parameter ($g'D/vf$)
M1	1.3	3	45
R2	1.5	3	53
R6	1.5	3	45
C1	2.5	4.5	69
C2	3.5	6	89
C3	1.5	4	47
C4	2.0	3.5	63
C5	2.5	8	103

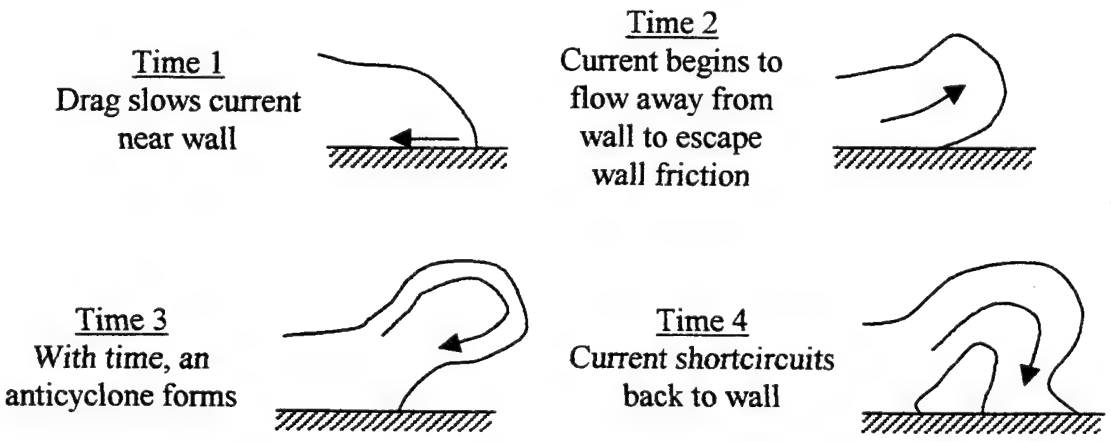

Figure 7 Schematic description and explanation of the nose meandering process

Rossby radius does give some indication of the lengths. In this case, noses typically require at least $100L$ to undergo meandering. In nature where L is O(10) km, this results in the coastline maintaining regular topography for at least 1000 km. Most coastlines possess many capes or peninsulas over this distance. At these changes in topography, separation will most likely occur. This problem was well treated by Stern and Whitehead (1990).

5. Conclusions

The presence of blocking instabilities was shown to drive a surface gravity current into a thin viscous boundary layer in a short amount of time. After this time, the gravity current propagated at rate consistent with the viscous-buoyancy balance. Due to the slow down from viscosity from the surface and sidewall, effects of the bottom Ekman layer were more pronounced. Ekman effects were observed for currents with predicted (from geostrophy) dimensionless depths as low as 0.2. These bottom-influenced currents then propagated at rate proportional to, but less than, their geostrophically-expected value.

In the far-field, the nose meandered to and from the sidewall. It was theorized that competition between the sidewall and surface boundary layer drove this phenomenon. The meandering was successfully scaled with a dimensionless quantity representing the balance between buoyancy and the effects of rotation and viscosity. The meandering process, in a few cases, ultimately caused the current to become separated from the wall and propagate slowly seaward.

Acknowledgements

I wish to thank the entire staff at the GFD summer program for providing many helpful ideas through the course of the summer. In particular, Melvin Stern, Jack Whitehead and Ross Griffiths aided in understanding many of the complexities involved with this new (for me, at least) type of research. John Salzig also deserves a special thanks for providing a quick hand running the experiments any time I needed it.

References

Griffiths, R. W. and Linden, P. F. 1981. The stability of buoyancy-driven coastal currents. *Dyn. Atmos. Oceans* **5**, 281-306.

Mooers, C. N. K. and Robinson, A. R. 1984. Turbulent jets and eddies in the California Current and inferred cross-shore transports. *Science* **223**, 51-53.

Stern, M. E. 1980. Geostrophic fronts, bores, breaking and blocking waves. *J. Fluid Mech.* **99(4)**, 687-703.

Stern, M. E. 1986. On the amplification of convergences in coastal currents and the formation of 'squirts'. *J. Mar. Res.* **44**, 403-421.

Stern, M. E., Chassignet, E. P. and Whitehead, J. A. 1997. The wall jet in a rotating fluid. *J. Fluid Mech.* **335**, 1-28.

Stern, M. E. and Whitehead, J. A. 1990. Separation of a boundary jet in a rotating fluid. *J. Fluid Mech.* **217**, 41-69.

Derivations of linear stability criteria for shear flow using Barston's method

Jürgen Theiss

1 Introduction

Some dynamical systems become unstable under certain conditions. Finding these conditions or criteria for instability to occur is of great interest in various areas of physics. Derivations of these stability criteria always take advantage of specific properties of these dynamical systems. Therefore most existing derivations are mostly not general enough to lead to further, stronger criteria or to be applied to other dynamical systems.

However, a very general method to derive stability criteria was developed by Barston (1977). This method allows the derivation of stability criteria for any linearised equations of motion of conservative systems if they can be cast into a specific but still very general form.

In this report I first outline in section 2 Barston's method in general terms. In section 3 I review Barston's derivation of the Fjørtoft theorem and Rayleigh's inflection point theorem for homogeneous parallel shear flow. Finally, in section 4, I apply Barston's method to derive the Richardson number criterion for stratified parallel shear flow and present an attempt to extend this criterion.

2 Barston's method

Barston's stability analysis can be applied to any dynamical system which can be expressed as an equation of the form

$$P\ddot{\xi} + A\dot{\xi} + H\xi = 0 \tag{1}$$

where P, A and H are time independent linear operators with P being hermitian and positive definite, A anti-hermitian and H hermitian. Their domain is an infinite-dimensional complex Hilbert space E with inner product $<,>$ and L_2-norm $||$. The function $\xi = \xi(t)$ is an element of E. Alternatively, equation (1) can be written as a first order system of the form

$$\dot{\zeta} = W\zeta \tag{2}$$

where

$$W = \begin{pmatrix} 0 & I \\ -P^{-1}H & -P^{-1}A \end{pmatrix}; \quad \zeta = \begin{pmatrix} \xi \\ \dot{\xi} \end{pmatrix} \tag{3}$$

Note that a unique solution ξ of equation (1) implies a unique solution $\zeta_1 = \xi$ and $\zeta_2 = \dot{\xi}$ of equation (2) and vice versa. Either equation can therefore be used to study stability properties of the dynamical system.

The stability properties of a dynamical system are closely related to the invariants of its equation of motion. These invariants or constants of motion are defined by

Definition *An operator G is a constant of motion if G is hermitian and*

$$\frac{\mathrm{d}}{\mathrm{d}t} < \zeta, G\zeta >= 0 \tag{4}$$

for every ζ being an element of the set of all solutions of equation (2).

Note that the operator G is said to be a constant of motion as opposed to the scalar $< \zeta, G\zeta >$ which is an actual constant of motion. Note also that there may be other constants of motion not of this form which are not considered in Barston's method.

Calculating expression (4) using (2) gives

$$\begin{aligned} \frac{\mathrm{d}}{\mathrm{d}t} < \zeta, G\zeta > &= < \dot{\zeta}, G\zeta > + < \zeta, G\dot{\zeta} > \\ &= < W\zeta, G\zeta > + < \zeta, GW\zeta > \\ &= < \zeta, [W^{\dagger}G + GW]\zeta > \end{aligned} \tag{5}$$

which leads to

Theorem 1 *If G is hermitian then*

$$\frac{\mathrm{d}}{\mathrm{d}t} < \zeta, G\zeta >= 0 \Longleftrightarrow W^{\dagger}G + GW = 0. \tag{6}$$

The condition on G on the right-hand-side of (6) is equivalent to the operator iGW being hermitian since

$$iGW = -iW^{\dagger}G = (iGW)^{\dagger}. \tag{7}$$

This condition facilitates deciding if a hermitian operator G is a constant of motion. It can thus easily be shown that, for instance, the operator

$$G = \begin{pmatrix} -iA & -iP \\ iP & 0 \end{pmatrix} \tag{8}$$

is a constant of motion. The more powerful property of theorem 1, however, is that it enables us to generate further constants of motion. If G is assumed to be a constant

of motion then the hermitian operator GiW, too, satisfies the condition on the right-hand-side of (6), since

$$W^{\dagger}(iGW) + (iGW)^{\dagger}W = (W^{\dagger}G + GW)iW = 0 \tag{9}$$

and thus GiW also qualifies as a constant of motion. This suggest an iterative procedure generating further constants of motion which have the form $G(iW)^n$ where $n = 2, 3, 4, \ldots$. For later reference the first three constants of motion in this series are given by

$$G = \begin{pmatrix} -iA & -iP \\ iP & 0 \end{pmatrix} \tag{10}$$

$$K_1 = GiW = \begin{pmatrix} H & 0 \\ 0 & P \end{pmatrix} \tag{11}$$

$$K_2 = G(iW)^2 = \begin{pmatrix} 0 & -iH \\ iH & iA \end{pmatrix}. \tag{12}$$

It might be noted also that theorem 1 and the fact that $G(iW)^n$ is a constant of motion whenever G is, are both true for any system of the form (2), whether or not W has the form (3). But it is when W has the form (3) that we can write down immediately the constant of motion of (8) or (10), and hence those of (11) and (12).

To establish the link between the constants of motion and the stability properties of the system we consider the trivial identity

$$\frac{<\zeta, G\zeta>}{<\zeta, \zeta>} <\zeta, \zeta> = <\zeta, G\zeta> \tag{13}$$

where G is a constant of motion and ζ an element of the set of all solutions of equation (2). Choose δ to be the smallest value the expression $\frac{<\zeta, G\zeta>}{<\zeta, \zeta>}$ takes on, with $<\zeta, G\zeta> > 0$ but finite, and introduce the norm defined by $|\zeta|^2 = <\zeta, \zeta>$. Equation (13) then gives the inequality

$$|\zeta|^2 \leq \frac{<\zeta, G\zeta>}{\delta} \tag{14}$$

If the constant of motion G is positive definite then the constant inner product $<\zeta, G\zeta>$ implies that ζ must be bounded. Thus, $\frac{<\zeta, G\zeta>}{\delta}$ in (14) represents an upper bound for $|\zeta|^2$. The term $<\zeta, G\zeta>$ is also often referred to as a Liapunov functional of the system. If, however, G is not positive definite then ζ can become infinitely large with $<\zeta, G\zeta>$ remaining a finite constant but δ tending to zero. The term $\frac{<\zeta, G\zeta>}{\delta}$ thus tends to infinity and no longer bounds $|\zeta|^2$.

In summary, the heart of Barston's method is

Barston's theorem *If the system has a constant of motion which is positive definite under certain conditions then the system is stable under these conditions.*

The reverse is true too which is shown by Barston (1971). However, this fact is not used below and the interested reader is referred to the reference.

3 Parallel shear flow in an inviscid homogeneous incompressible fluid

The equations governing the flow of an inviscid homogeneous incompressible fluid are given by the incompressibility condition

$$\nabla \cdot \mathbf{u} = 0 \tag{15}$$

the mass continuity equation

$$\frac{\partial \rho}{\partial t} + \mathbf{u} \cdot \nabla \rho = 0 \tag{16}$$

and the momentum equation

$$\frac{\partial \mathbf{u}}{\partial t} + \mathbf{u} \cdot \nabla \mathbf{u} = -\frac{1}{\rho} \nabla p. \tag{17}$$

The quantities $\rho(\mathbf{x}, t), \mathbf{u}(\mathbf{x}, t)$ and $p(\mathbf{x}, t)$ are the density, velocity and pressure of the fluid, respectively. The fluid is bounded only in the vertical direction by rigid boundaries at $z = 0$ and $z = a$. We assume the basic state to be a steady horizontal shear flow given by

$$\mathbf{u}_0 = U(z)\mathbf{e}_x \tag{18}$$

where$\mathbf{e}_x$ is the unit vector in the x-direction and with the density given by

$$\rho_0 = \rho_0(z). \tag{19}$$

We introduce small perturbations about that basic state. The fluid motion is thus described by

$$\mathbf{u} = \mathbf{u}_0 + \mathbf{u}_1(\mathbf{x}, t) \tag{20}$$

$$\rho = \rho_0 + \rho_1(\mathbf{x}, t) \tag{21}$$

$$p = p_0 + p_1(\mathbf{x}, t) \tag{22}$$

where the subscript 1 denotes the small perturbations. We insert (20)-(22) into the momentum equation (17) and linearise the resulting equations. Below we assume the density to be constant in the horizontal momentum equations (Boussinesq approximation) which simplifies the manipulations but does not alter the general properties of the results. The results below can be derived in complete analogy for variable density.

Multiplying the horizontal momentum equations by

$$\frac{\partial}{\partial z}\begin{pmatrix} \frac{\partial}{\partial x} \\ \frac{\partial}{\partial y} \end{pmatrix} \tag{23}$$

and the vertical momentum equation by

$$\frac{\partial^2}{\partial x^2} + \frac{\partial^2}{\partial y^2}, \tag{24}$$

respectively, from the left and subsequently subtracting both expressions eliminates the pressure. We thus have

$$-\frac{\partial^2}{\partial z^2}\dot{w}_1 - U\frac{\partial^3}{\partial x \partial z^2}w_1 + \frac{\partial}{\partial x}w_1\frac{\partial^2}{\partial z^2}U = \left(\frac{\partial^2}{\partial x^2} + \frac{\partial^2}{\partial y^2}\right)\dot{w}_1 + U\left(\frac{\partial^2}{\partial x^2} + \frac{\partial^2}{\partial y^2}\right)\frac{\partial}{\partial x}w_1. \tag{25}$$

Since the fluid is incompressible and the velocity component in the y-direction does not appear in (25) we can introduce a streamfunction given by

$$\mathbf{u} = \mathbf{e}_y \times \nabla\psi. \tag{26}$$

This streamfunction can be expressed in terms of its Fourier transform in the horizontal plane given by

$$\psi(\mathbf{x}, t) = \int_{-\infty}^{\infty} \phi(k_x, k_y, z, \omega) e^{i(k_x x + k_y y - \omega t)}\, \mathrm{d}k_x \mathrm{d}k_y \mathrm{d}\omega \tag{27}$$

where k_x and k_y are the wavenumbers in the horizontal plane and ω the wave frequency given by $\omega = \mathbf{k}c$ with $\mathbf{k} = \sqrt{k_x^2 + k_y^2}$ and c being the phase speed.

Without essential loss of generality we set $k_y = 0$ and $k_x = k$. Inserting (26) and (27) into (25) we arrive at the well known Rayleigh's equation,

$$(U - c)(D^2 - k^2)\phi - U''\phi = 0 \tag{28}$$

where $D = ' = \frac{\partial}{\partial x}$. Rayleigh's equation constitutes the starting point for classical stability analysis (Drazin 1981) which leads to Rayleigh's inflection point theorem, Fjørtofts theorem and Howard's semicircle theorem.

However, for Barston's method to be applied, Rayleigh's equation has to be expressed in the form given in (1). This is easily achieved by multiplying equation (28) by $(ik)^2$ reinstating the time derivative ($-ikc \rightarrow \frac{\partial}{\partial t}$) and expressing the streamfunction ϕ in terms of the displacement ξ of fluid particles given by

$$\phi = (U - c)\xi \tag{29}$$

which is obtained by Fourier transforming $w_1 = \frac{\mathrm{d}\xi}{\mathrm{d}t} = \frac{\partial\psi}{\partial x}$. Rayleigh's equation thus becomes

$$\left[\left(\frac{\partial}{\partial t} + ikU\right)(D^2 - k^2) - ikU''\right]\left(\frac{\partial}{\partial t} + ikU\right)\xi = 0 \tag{30}$$

which finally gives

$$P\ddot{\xi} + A\dot{\xi} + H\xi = 0 \tag{31}$$

where

$$P = -D^2 + k^2 \tag{32}$$
$$A = 2ik(-DUD + k^2U) \tag{33}$$
$$H = k^2(DU^2D - k^2U^2) \tag{34}$$

Alternatively, equation (31) can be written as the first order system (2)

$$\dot{\zeta} = W\zeta \tag{35}$$

where W is given in (3).

Rayleigh's equation in the form of equation (31) with (32)-(34) or in the form (35) fulfills the requirements for Barston's method to be applied. This means, if we found a positive definite constant of motion which becomes positive definite under certain conditions then the fluid flow would be stable. Unfortunately, for the case of Rayleigh's equation in (31), the constants of motion given in (10)-(12) cannot become positive definite. However, it could be the case that other constants of motion, obtained through the iterative method mentioned above or through linear combinations, turn out to be positive definite. Barston (1977) investigates the linear combination

$$k\nu G + K_1 \tag{36}$$

where ν is an arbitrary constant and G and K_1 are given by (10) and (11), respectively. To check if the constant of motion in (36) can become positive definite we need to calculate the inner product

$$< \zeta, [k\nu G + K_1]\zeta > \tag{37}$$

for every ζ being an element of the set of all solutions of (35). The inner product in (37) becomes

$$< \zeta_1, [H - ik\nu A]\zeta_1 > + < \zeta_1, -ik\nu P\zeta_2 > + < \zeta_2, ik\nu P\zeta_1 > + < \zeta_2, P\zeta_2 > . \tag{38}$$

Adding the identity $< ik\nu\zeta_1, Pik\nu\zeta_1 > - < ik\nu\zeta_1, Pik\nu\zeta_1 >= 0$ and using the fact that $-ik\nu$ is anti-hermitian, i.e. $< \zeta_1, -ik\nu P\zeta_2 >=< ik\nu\zeta_1, P\zeta_2 >$ expression (38) becomes

$$< \zeta_1, [H - ik\nu A - k^2\nu^2 P]\zeta_1 > + < \zeta_2 + ik\nu\zeta_1, P(\zeta_2 + ik\nu\zeta_1) > . \tag{39}$$

Since P in the second term is positive definite, we only need to consider the first term. Inserting the explicit expressions for P, A and H given in (32)-(34) into the first term of expression (39) gives

$$< \zeta_1, [H - ik\nu A - k^2\nu^2 P]\zeta_1 >= -k^2 \int_0^a (U - \nu)^2[|D\zeta_1|^2 + k^2|\zeta_1|^2] \, dx \tag{40}$$

This expression can never be made definite positive and thus according Barston's theorem no condition under which the fluid flow is stable can be found.

We could search for other constants of motion and investigate if they can become positive definite. Barston (1977) instead finds an ingenious way of confining his analysis on a subset of the whole solution space which contains all the unstable solutions in the case the fluid flow is assumed unstable. Restricted on this subspace some of the constants of motion above might become positive definite under certain conditions. To achieve that partitioning of the solution space, Barston first factorises the general equation given in (1)

$$P\ddot{\xi} + A\dot{\xi} + H\xi = 0. \tag{41}$$

Assuming some of the solutions of equation (41) to be of the form

$$\xi = e^{Qt} f \tag{42}$$

where Q is any linear operator and $f \in E$, the solution can be substituted into (41) to give the relation

$$PQ^2 + AQ + H = 0. \tag{43}$$

Using this relation we can express H in (41) in terms of P, A and Q which enables us to write equation (41) in the factorised form

$$\left(P\frac{\partial}{\partial t} + PQ + A\right)\left(\frac{\partial}{\partial t} - Q\right)\xi = 0 \tag{44}$$

Rayleigh's equation in (30) has that form already and thus Q can be readily identified to be

$$Q = -ikU. \tag{45}$$

One solution of Rayleigh's equation is thus, according to (42), given by

$$\xi = e^{-ikUt} f. \tag{46}$$

This is the continuous spectrum solution originally found by Case (1960a) as opposed to the discrete normal mode solutions. The fact that the solution in (46) is a continuous spectrum is due to the non-constant velocity profile $U = U(z)$ which can be easily seen if expressed in terms of discrete normal modes, i.e.

$$\xi = e^{-ikU(z)t} f = \int_{-\infty}^{\infty} e^{-ik\omega t} a(\omega)\delta(\omega - U(z))\, \mathrm{d}\omega f. \tag{47}$$

Changing back to the more general linear operator Q, the solution of the first order system (2), being equivalent to equation (41), is given by

$$\zeta = \begin{pmatrix} e^{Qt} f \\ e^{Qt} Q f \end{pmatrix} \tag{48}$$

Barston defines a set N of all points which are on the solution curves given in (48). We thus have

$$N = \begin{pmatrix} f \\ Qf \end{pmatrix}. \tag{49}$$

He then constructs a set M which is orthogonal to $G(N)$ where G is the constant of motion given in (10) acting on the set N, i.e.

$$M \perp G(N). \tag{50}$$

For an element $\begin{pmatrix} \zeta_1 \\ \zeta_2 \end{pmatrix}$ of M this orthogonality means that

$$< \begin{pmatrix} \zeta_1 \\ \zeta_2 \end{pmatrix}, G \begin{pmatrix} f \\ fQ \end{pmatrix} >= 0 \tag{51}$$

which, written out explicitly, implies

$$\zeta_2 = P^{-1}(Q^\dagger P - A)\zeta_1 \tag{52}$$

Barston then proves that in the case the fluid flow is unstable all unstable normal modes can be expressed as

$$\zeta = \zeta_M e^{i\omega t} \tag{53}$$

where $\zeta_M \in M$.

We are now in a position to check if the same linear combination of the constants of motion (36)

$$k\nu G + K_1 \tag{54}$$

can become positive definite if it's only acting on the subset M of all possible solutions. Again, we need to calculate

$$< \zeta, [k\nu G + K_1]\zeta > \tag{55}$$

but with $\zeta \in M$, which represents an additional constraint on the components of ζ given by (52). For the special case $Q = -ikU$ we have

$$P\zeta_2 = [ikUP - A]\zeta_1 \tag{56}$$

Using that additional constraint simplifies the calculation of expression (55) since 'mixed' terms are avoided. We straightforwardly obtain

$$< \zeta_1, [k^2(U - \nu)U'' + \tilde{L}P^{-1}\tilde{L}]\zeta_1 > \tag{57}$$

where $\tilde{L} = PkU + kUP + iA$. Since $\tilde{L}$ is hermitian the product $\tilde{L}P^{-1}\tilde{L}$ is positive definite. If in addition

$$k^2(U - \nu)U'' \geq 0 \tag{58}$$

then the whole operator in (57) is definite positive and according to Barston's theorem the fluid flow is stable. If we choose the arbitrary constant ν to be the velocity at the inflection point of the velocity profile, i.e. $\nu = U_s = U(z_0)$ where $U''(z_0) = 0$, then (58) becomes

$$k^2(U - U_s)U'' \geq 0 \tag{59}$$

This sufficient condition for stability is the well known Fjørtoft theorem. Condition (58) also implies Rayleigh's inflection point theorem. Whenever

$$U'' \neq 0 \tag{60}$$

everywhere, i.e. the velocity profile does not have an inflection, then ν can be chosen in such a way as to ensure condition (58) always to be true. Consequently, the fluid flow is stable. Clearly, the opposite of both conditions (59) and (60) are necessary conditions for instability.

4 Parallel shear flow in an inviscid stratified incompressible fluid

The equations governing the flow of an inviscid stratified incompressible fluid compared to its homogeneous counterpart differ only in the buoyancy term $-\mathbf{g}\frac{\rho}{\rho_0}$ in the momentum equation where $\mathbf{g}$ is the gravitational acceleration. Thus, as in the homogeneous fluid case, we have the incompressibility condition

$$\nabla \cdot \mathbf{u} = 0 \tag{61}$$

the mass continuity equation

$$\frac{\partial \rho}{\partial t} + \mathbf{u} \cdot \nabla \rho = 0 \tag{62}$$

but the momentum equation is given by

$$\frac{\partial \mathbf{u}}{\partial t} + \mathbf{u} \cdot \nabla \mathbf{u} = -\frac{1}{\rho}\nabla p - \mathbf{g}\frac{\rho}{\rho_0}. \tag{63}$$

Following exactly the homogeneous fluid case, we consider small perturbations about a basic state, linearise the equations, make the Bousinesq approximation and Fourier transform them in the horizontal plane. The result, equivalent to Rayleigh's equation, is the well known Taylor-Goldstein equation

$$(U - c)(D^2 - k^2)\phi - U''\phi + \frac{N^2}{(U - c)}\phi = 0 \tag{64}$$

with $N^2 = -g\frac{1}{\rho_0}\frac{\partial \rho}{\partial z}$ where N is the buoyany frequency. The Taylor-Goldstein equation is used as a starting point in classical stability analysis, especially it leads to the

central Richardson number criterion (Drazin & Reid 1981). In order to be able to apply Barston's method, equation (64) has to be written in the form given in (1). In complete analogy to the homogeneous fluid case we multiply equation (64) by $(ik)^2$, reinstate the time derivative $(-ikc \rightarrow \frac{\partial}{\partial t})$ and express the streamfunction in terms of the displacement ξ, i.e. $\phi = (U - c)\xi$. We thus have,

$$P\ddot{\xi} + A\dot{\xi} + H\xi = 0 \tag{65}$$

where

$$P = -D^2 + k^2 \tag{66}$$

$$A = 2ik(-DUD + k^2U) \tag{67}$$

$$H = k^2(DU^2D - k^2U^2 - N^2). \tag{68}$$

Equation (65) only differs, compared to the equivalent equation in the homogeneous fluid case (31), by the term $-k^2N^2$ in the operator H. This does not change the general properties of the first three constants of motion (10)-(12). Thus, we can draw the same conclusions as Barston for the homogeneous fluid case, that is that neither the constants of motion nor the linear combination (36) can ever become positive definite.

Instead of investigating other constants of motion and their linear combinations we follow Barston's idea of confining the stability analysis to a subset of the set of all solutions which contains all the unstable solutions in the case the fluid flow is unstable. This approach requires to factorise equation (65). Assuming, as in the homogeneous fluid case, one solution to be of the form

$$\xi = e^{Qt}f \tag{69}$$

where Q is any linear operator and $f \in E$, gives the relation (43)

$$PQ^2 + AQ + H = 0 \tag{70}$$

which determines Q. However, in the stratified fluid case the operator H, explicitly given in (68), contains the additional term $-k^2N^2$ whereas the operators P and A do not. Thus, equation (70) cannot be solved for Q. This is not surprising since the continuous spectrum for the stratified case which would be the result of this approach is not known explicitly. Case (1960b), however, found the asymptotic limit of the continuous spectrum of the form

$$\xi = te^{Qt}f. \tag{71}$$

Inserting this as a possible solution into equation (65) results in a more complicated, time dependent equation for Q which does not avoid the problem encountered assuming the simpler solution (69).

Another, alternative approach to find constants of motion which can become positive definite is to express the Taylor-Goldstein equation in terms of other variables than the streamfunction ϕ or the displacement ξ. An obvious choice is a substitution Howard (1961) used to prove, for the first time mathematically rigourously, the Richardson number criterion. Howard replaced the streamfunction ϕ by a function F given by

$$\phi = (U-c)^{\frac{1}{2}} F. \tag{72}$$

Due to the power of $\frac{1}{2}$ it proves difficult to understand the physical meaning of the function F. Nevertheless, we can substitute (72) into (64) and divide by $(U-c)^{\frac{1}{2}}$ to obtain

$$D[(U-c)DF] - k^2(U-c)F - \frac{1}{2}U''F + (N^2 - \frac{1}{2}U'^2)\frac{F}{(U-c)} = 0. \tag{73}$$

Note, this equation can be more easily derived by first dividing (64) by $(U-c)^{\frac{1}{2}}$, then calculating its adjoint (with $\phi^* = F$) and to multiply the result by $(U-c)^{\frac{1}{2}}$. Multiplying equation (73) by $(ik)^2(U-c)$ and reinstating the time derivative ($-ikc \rightarrow \frac{\partial}{\partial t}$) leads to

$$P\ddot{F} + A\dot{F} + HF = 0 \tag{74}$$

where

$$P = -D^2 + k^2 \tag{75}$$

$$A = 2ik(-DUD + k^2U) + 2ik(\frac{1}{2}U'D + \frac{1}{4}U'') \tag{76}$$

$$H = k^2(DU^2D - k^2U^2) - k^2(UU'D + \frac{1}{2}UU'' - (N^2 - \frac{1}{4}U'^2) \tag{77}$$

Unfortunately, the second terms of the operators A and H are not, as required by Barston's method, anti-hermitian and hermitian, respectively. In order to obtain a form of the Taylor-Goldstein equation (64) which does have the properties for Barston's method to be applied other substitutions have to be investigated.

It turns out to be very difficult to find appropriate substitutions to transform the Taylor-Goldstein equation (64) accordingly. However, what proves to be successful is a suggestion by Louis Howard to carry out two substitutions consecutively. The Taylor-Goldstein equation (64) is first transformed by the substitution (72) leading to equation (73) which is then further transformed by another substitution given by

$$F = (U-c)G. \tag{78}$$

After reinstating the time derivative in the usual way we finally obtain

$$(-D^2 + k^2)\left(\frac{\partial}{\partial t} + ikU\right)\left(\frac{\partial}{\partial t} + ikU\right)G + ik\left(\frac{3}{2}U'' + U'D\right)\left(\frac{\partial}{\partial t} + ikU\right)G + k^2\left(N^2 - \frac{1}{4}U'^2\right)G = 0 \tag{79}$$

which is more conveniently written as

$$P\overset{\circ\circ}{G}+A\overset{\circ}{G}+HG=0 \tag{80}$$

where

$$\begin{aligned} P &= -D^2+k^2 && (81)\\ A &= ik\left(\frac{3}{2}U''+U'D\right) && (82)\\ H &= k^2\left(N^2-\frac{1}{4}U'^2\right) && (83)\\ \circ &= \frac{\partial}{\partial t}+ikU && (84) \end{aligned}$$

Although A is not anti-hermitian and the operator $\circ = \left(\frac{\partial}{\partial t}+ikU\right)$ not the partial time derivative $\frac{\partial}{\partial t}$ as required, equation (80) can still be exploited. Just as equation (1) can be expressed as a first order system (2) so, in complete analogy, equation (80) can be expressed as

$$\overset{\circ}{\zeta}= W\zeta \tag{85}$$

where

$$W=\begin{pmatrix} 0 & I \\ -P^{-1}H & -P^{-1}A \end{pmatrix};\quad \zeta=\begin{pmatrix} G \\ \overset{\circ}{G} \end{pmatrix} \tag{86}$$

However, the operator $\circ = \left(\frac{\partial}{\partial t}+ikU\right)$ as opposed to the partial time derivative $\frac{\partial}{\partial t}$ does not commute with the operators P, A and H which alters the condition on the right-hand-side of (6) that defines constants of motion. The calculation in (5) therefore has to be expressed in terms of the operator $\circ$ in order to be able to substitute (85). Following (5) we thus have,

$$\begin{aligned} \frac{\mathrm{d}}{\mathrm{d}t}<\zeta,G\zeta> &= <\dot{\zeta},G\zeta>+<\zeta,G\dot{\zeta}>\\ &= <\overset{\circ}{\zeta},G\zeta>+<\zeta,G\overset{\circ}{\zeta}>+<\zeta,ik[UG-GU]\zeta>\\ &= <\zeta,W^{\dagger}G+GW+ik[UG-GU]\zeta> \end{aligned} \tag{87}$$

Thus, theorem 1 can not be used for systems of the form (80). Instead we have

Theorem 2 *If G is hermitian*

$$\frac{\mathrm{d}}{\mathrm{d}t}<\zeta,G\zeta>=0 \Longleftrightarrow W^{\dagger}G+GW+ik[UG-GU]=0 \tag{88}$$

Unfortunately, the condition on the right-hand-side of (88), due to the term $UG-GU$, makes it impossible to generate, knowing one constant of motion, further constants of motion as described below (9).

However, one constant of motion, satisfying the condition in (88) can be found to be

$$K_1 = \begin{pmatrix} H & 0 \\ 0 & P \end{pmatrix} = \begin{pmatrix} k^2(N^2 - \frac{1}{4}U'^2) & 0 \\ 0 & -D^2 + k^2 \end{pmatrix} \tag{89}$$

It can easily be seen that K_1 is positive definite if

$$N^2 - \frac{1}{4}U'^2 \geq 0. \tag{90}$$

We thus have derived the well known Richardson number criterion which states: If

$$\frac{N^2}{U'^2} \geq \frac{1}{4} \tag{91}$$

then the fluid flow is stable. Clearly, the opposite of condition (91) is a necessary condition for instability. Since no further constants of motion can be generated iteratively, additional, possibly stronger criteria cannot be found.

To avoid this restriction we can rewrite equation (85) in terms of the partial time derivative which gives

$$\dot{\zeta} = \bar{W}\zeta \tag{92}$$

where

$$\bar{W} = \begin{pmatrix} -ikU & I \\ -(-D^2 + k^2)^{-1}k^2\left(N^2 - \frac{1}{4}U'^2\right) & -(-D^2 + k^2)^{-1}ik\left(\frac{3}{2}U'' + U'D\right) - ikU \end{pmatrix} \tag{93}$$

and

$$\zeta = \begin{pmatrix} G \\ \dot{G} \end{pmatrix} \tag{94}$$

Note that equation (92) cannot be written in the equivalent form (1) since $\dot{\zeta} = \begin{pmatrix} \dot{G} \\ \ddot{G} \end{pmatrix}$ instead of $\dot{\zeta} = \begin{pmatrix} \dot{G} \\ \ddot{G} \end{pmatrix}$. However, Barston's method is entirely based on the first order system of the form (2) which implies that the second component of ζ does not necessarily have to be the partial time derivative of the first. Since we have merely rewritten equation (85) in the form (92) one constant of motion of the system is still K_1 given in (89). The alternative formulation (92) expressed in terms of the partial time derivative has the advantage that further constants of motion can be generated iteratively. Using K_1, we can determine

$$K_2 = K_1 i\bar{W} = \begin{pmatrix} k^2\left(N^2 - \frac{1}{4}U'^2\right)kU & ik^2\left(N^2 - \frac{1}{4}U'^2\right) \\ -ik^2\left(N^2 - \frac{1}{4}U'^2\right) & k\left(\frac{3}{2}U'' + U'D\right) + k(-D^2 + k^2)U \end{pmatrix}. \tag{95}$$

Further constants of motion, given by $K_1(iW)^n$ with $n = 2, 3, \ldots$ are not worth to be considered since they contain inverse powers of the operator $(-D^2 + k^2)$. Recalling

the constant of motion (10)-(12), K_1 in (89) is the second in this series of three. Thus the constant of motion G in (10) is given by $G = -iW^{-1}K_1$ which can be determined but the resulting expression proves to be too complicated.

The two available constants of motion (89) and (95) suggest themselves to be combined as

$$L = K_2 - k\nu K_1 = \begin{pmatrix} k^2\left(N^2 - \frac{1}{4}U'^2\right)k\tilde{U} & ik^2\left(N^2 - \frac{1}{4}U'^2\right) \\ -ik^2\left(N^2 - \frac{1}{4}U'^2\right) & k\left(\frac{3}{2}U'' + U'D\right) + k(-D^2 + k^2)\tilde{U} \end{pmatrix} \quad (96)$$

where ν is arbitrary and $\tilde{U} = U - \nu$. This combination gives us the advantage to choose the sign of $\tilde{U}$. Since under the condition (90) the constant of motion K_1 becomes positive definite there is no reason to find other constants of motion which become positive definite under the same condition. However, it is worth investigating under what conditions L in (96) becomes positive definite if we assume the opposite of condition (89),

$$N^2 - \frac{1}{4}U'^2 < 0 \quad (97)$$

i.e. K_1 is not positive definite any longer. Finding a constant of motion which can become positive definite under that condition would imply a stronger Richardson number criterion. As above, we calculate

$$< \zeta, [K_2 - k\nu K_1]\zeta > \quad (98)$$

where ζ are solutions of (92). Inserting the explicit expressions for K_1 and K_2 given in (89) and (95) and using similar manipulations as in calculating (37) we finally obtain

$$\int_0^a k\left[\frac{1}{2}U''|\overset{\circ}{G}|^2 + \tilde{U}|D\overset{\circ}{G}|^2 + k^2\tilde{U}|\overset{\circ}{G}|^2 - \left(N^2 - \frac{1}{4}U'^2\right)\frac{1}{\tilde{U}}|\overset{\circ}{G}|^2 + k^2\left(N^2 - \frac{1}{4}U'^2\right)\tilde{U}\left|G + \frac{i}{k\tilde{U}}\overset{\circ}{G}\right|^2\right] dx > 0 \quad (99)$$

If a condition were found for which the integrand is guaranteed always to be positive definite then a new stability criterion would be found. Choosing $\tilde{U}$ to be positive, the second, third and fourth terms are positive. The remaining terms can be simplified by using the Schwartz inequality and other techniques. Still, despite the help through the united efforts by Louis, Steve and Neil, no new stability criterion could be extracted from (99).

5 Conclusion

Barston's method appeals by its generality. Unfortunately, applying it to homogeneous and stratified parallel shear flow only produces already known stability criteria. Finding new, stronger criteria remains a challenge.

In Magnetohydrodynamics, however, Barston (1977) uses his method to derive a new stability criterion and there might be further physical systems for which that method will give new insight into their stability properties.

Acknowledgements

I would like to thank Norman Lebovitz for his inspiring lecture touching on Barston's work which prompted this project.

It was a great experience to be advised by Louis Howard and I wish I had any pre-knowledge on hydrodynamic stability that I could have even more benefitted from his vast knowledge and his clear explanations.

Also thanks to Neil Balmforth and Steve Meacham for their help and suggestions. Their enthusiasm in the subject area is striking and will keep me motivated beyond the GFD summer in Woods Hole.

References

BARSTON, E.M. **1971**, Eigenvalue problem for Lagrangian systems. IV. *J. Math. Phys.*, **12**, 1116-1892

BARSTON, E.M. **1977**, The systematic construction of Liapunov functionals in the linear stability of conservative steady flows. *Int. Engng. Sci.*, **15**, 71-93

CASE, K.M. **1960a**, Stability of inviscid plane Couette flow. *Phys. Fluids*, 3, 143-149

CASE, K.M. **1960b**, Stability of an idealized atmosphere. I. Discussions of results. *Phys. Fluids*, 3, 149-154

DRAZIN , P.G. & REID, W.H. **1981**, *Hydrodynamic stability.* Cambridge University Press.

HOWARD, L.N. **1961**, Note on a paper of John W. Miles. *J. Fluid Mech.*, 10, 509-512

Keir Colbo

W.H.O.I. GFD Summer Program 1997

Hydraulics of Branching Channels

Introduction

Many of the worlds' abyssal basins are connected by relatively narrow, constrictive sills such as the Vema Channel and the Romanche Fracture Zone. It has long been postulated that the flow through some of these regions is hydraulically controlled. By this we mean that there exists a critical control region, downstream of which the flow is supercritical and hence information only propagates in one direction. The flow through several of these sills has been modelled using basic hydraulic control theory (Gill 1977). Exclusively, these flows have been modelled using only a single channel, although often introducing complexities such as multiple layers, non-rectangular (ie. parabolic) geometries and frictional modification (Whitehead, Leetmaa and Knox 1974; Hogg 1983,1984; Whitehead 1988; Johnson and Ohlsen 1994). A casual examination of the topography in many of these sills is sufficient to reveal that they are far removed from the simple rectangular channels used in theory. One often notes the existence of multiple channels with different geometries. This work attempts to study the modification to single channel hydraulics that arises when multiple pathways exist for the flow. In a single channel, critical flow is a valid assumption for various physically plausible reasons. For instance, given the total flux, the energy is minimized when the flow is critical. However, with two channels the application of a froude number (Fr) criterion is not obvious. For this work I decided to consider a system in which the flow is critically controlled in each channel and hence $Fr = 1$ at the two sills. This also proves useful since it allows us to neglect the channel geometry below the sill. The validity of such an assumption will be discussed later. Furthermore, since I include arbitrary channel widths in my analysis, the critical control section is determined as a function of both bottom depth and channel width and so the control section does not need to be at a sill. Regardless of this point I will use the word sill to discuss the critical control region.

1 The Nonrotating Case

Consider a large basin which flows into a channel of width w_0, wherein the depth and unknown speed of the layer are d_0 and v_0 respectively (figure 1). At some later point this channel divides into two channels. Far downstream of the point of bisection, in each channel, there is a critical control region with bottom height h_{im} and critical width w_{ic} where $i = 1, 2$. In the region where the channel divides we might expect complex behaviour to occur, however if we assume that far upstream and downstream of this region the flow is

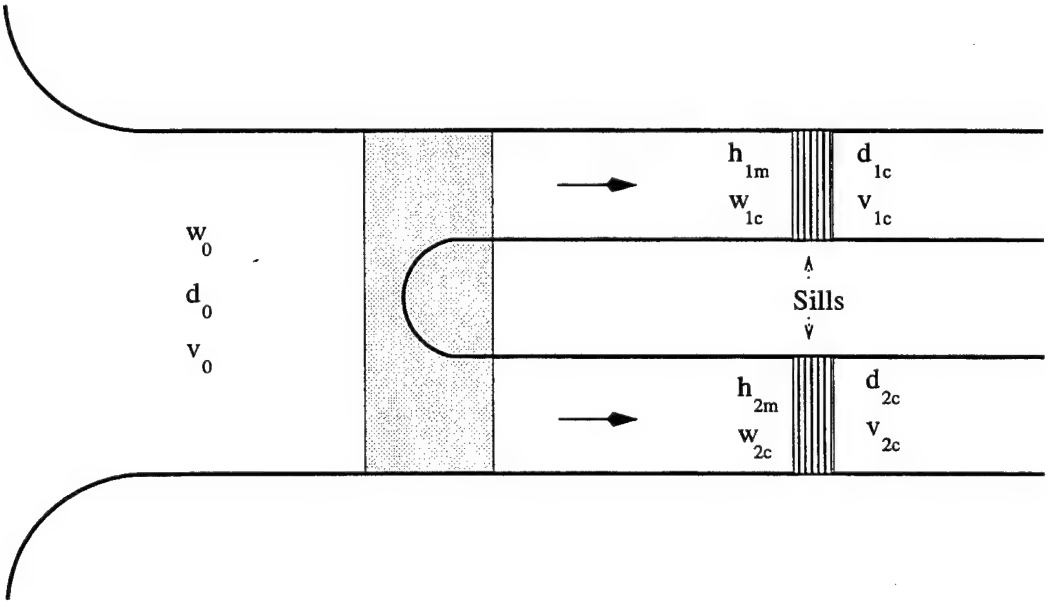

Figure 1: The geometry under consideration, where a single channel of width (w_0) and depth (d_0) branches into two channels each of which contain a sill, with depth above the bottom h_{im} and coincident width w_{ic}. The flow properties $(v_0, v_{1c}, v_{2c}, d_{1c}, d_{2c})$ are to be determined. The hatched region where the channel splits is ignored but assumed to be nondissipative.

constant across the channel than we can write a set of five equations for the unknowns.

$$v_0^{*2}/2 + g d_0^* = v_{ic}^{*\,2}/2 + g(d_{ic}^* + h_{im}^*) \quad (1)$$

$$v_{ic}^{*\,2} = g d_{ic}^* \quad (2)$$

$$Q^* = v_0^* w_0^* d_0^* = v_{1c}^* w_{1c}^* d_{1c}^* + v_{2c}^* w_{2c}^* d_{2c}^* = Q_1^* + Q_2^* \tag{3}$$

The first equation is just conservation of energy (Bernoulli function), applied along the left hand and right hand walls. The next represents the critical condition in each channel. That is we assume that long waves cannot propagate upstream against the current, so that their shallow water phase speed is equal to the water velocity at the sill. The final equation represents conservation of mass (volume) for the entire system[1]. Before preceding we first nondimensionalize in the following way.

$$d_{ic} = \frac{d_{ic}^*}{d_0^*} \quad ; \quad w_{ic} = \frac{w_{ic}^*}{w_0^*}$$
$$v_{1c} = \frac{v_{1c}^*}{(g d_0^*)^{1/2}} \quad ; \quad Q = \frac{Q^*}{d_0^* w_0^* (g d_0^*)^{1/2}}$$

This gives

$$v_0^2/2 + 1 = v_{ic}^2/2 + (d_{ic} + h_{im}) \tag{4}$$
$$v_{ic}^2 = d_{ic} \tag{5}$$
$$Q = Q_1 + Q_2 = v_{1c} w_{1c} d_{1c} + v_{2c} w_{2c} d_{2c} \tag{6}$$

These can be rearranged to form the equation

$$Q = \sum_{i=1}^{2} w_{ic} [\frac{Q^2}{3} + \frac{2}{3}(1 - h_{im})]^{3/2} \tag{7}$$

Also an equation for the critical depth can be formulated.

$$3d_{1c} = w_{1c}^2 d_{1c}^3 + w_{2c}^2 [d_{1c} + \frac{2}{3}(h_{1m} - h_{2m})]^3$$
$$+ 2w_{1c} w_{2c} [d_{1c}(d_{1c} + \frac{2}{3}(h_{1m} - h_{2m})]^{3/2} + 2(1 - h_{1m}) \tag{8}$$

Equation 8 is more complex than the one for the total flux, however it provides an easier starting point with which to determine the other fow parameters. Simply put it is easier to write down d_{2c}, v_{ic} and Q_i in terms of d_{1c} than in terms of Q. However before preceding with equation 8, we should

[1]Note that Eq. (1) assumes that whatever flow may occur near the region of bisection that there is no dissipation of energy.

first see what simple understanding we can derive from equation 7. Before preceding, we recall that for a single channel we have

$$\frac{1}{2}Fr_0^2 + 1 = \frac{3}{2}\frac{w_c^{2/3}}{Fr_0} + h_m/d_0 \tag{9}$$

For $h_m < d_0$ this cubic has either zero or two real roots. Furthermore, if roots exist one will be greater than one while the other will be less than one. Thus for single channel flow we remember that there is always a subcritical and a supercritical choice for the upstream flow, we shall see that this is not always true for the two channel case. In order to examine this four-dimensional phase space, we hold the geometry of one of the channels constant while varying that in the other. Equation 7 can be expanded into a sixth order polynomial in Q^2 for which we can easily find the roots. Similarly, equation 8 yields a sixth order polynomial in d_{1c}. However, we must then exclude those roots which represent physically unrealistic situations. We are therefore looking for states where Q_i and d_{ic} are positive for $i = 1, 2$. Furthermore, we wish the flow to be subcritical upstream of our two sills in the single channel, $v_0^2 < d_0$.

Before preceding to numerical solutions we might first see what we can learn analytically. As a first check, we note that for $h_{1m} = h_{2m} = h$ and $w_{1c} = w_{2c} = w_c/2$ we retrieve the single channel solution for width w_c and sill height h. Ensuring that the square root is well defined in equation 8 leads to the conditions

$$\frac{3}{2}d_{1c} + h_{1m} - h_{2m} \geq 0 \tag{10}$$

which eliminates the lower left section in figure 2. One other simple example to consider would be when there are no sills at all, so the control is entirely due to a change in width. In this case, we have the equation

$$v_0^6 + 6v_0^4 + (12 - \frac{27}{(w_{1c} + w_{2c})^2})v_0^2 + 8 = 0 \tag{11}$$

The solutions to this equation are the same as for a single channel in which there is no sill and the width at the critical control is $w_{1c} + w_{2c}$.

As an initial example we consider the case where we set $w_{2c} = 5$ and $h_{2m} = 0.5$. The figures 2 and 3 show the critical depth in channel 1 and the upstream Froude number in the single channel as a function of h_{1m} for

five different widths, $w_{1c} = [1, 3, 5, 9, 11]$. One of the first points to note is that there is not necessarily any flow for arbitrary geometric constraints. Note that the $w_{1c} = 5$ curve is not defined outside the approximate interval $0.17 < h_{1m} < 0.85$, while the $w_{1c} = 1$ or 3 curves have maximum sill heights for which there are physical solutions, and the $w_{1c} = 9$ and 11 curves have minimum h_{1m} values. Furthermore, the flow parameters are not necessarily single valued, as in the single channel case. However in contrast to a single channel the flow can have either zero, one or two physical flow states, and in the case of two states they can both be subcritical or both be supercritical. The most interesting point from an oceanographic point of view is when there are multiple subcritical states. For instance if we examine the $w_{1c} = 11$ curve in figure 3 for the region where h_{1m} is just bigger than 0.6, we note that there are two subcritical states, although one of these branches becomes supercritical at about $h_{1m} \approx 0.8$ while the other is subcritical until $h_{1m} \approx 1.05$. Similarly, the $w_{1c} = 3$ curve has multiple subcritical states for h_{1m} just smaller than a half.

2 Effects of Rotation

Rotation in single channel flows introduces the possibility of flow separation, where the free surface is no longer attached to one of the walls (Gill 1977, Pratt 1983,1984). Therefore, we must consider a set of four possible schemes where the flow in either channel can be separated or attached. In order to proceed we consider Gill's problem (1977) with an additional variable Ψ_s which denotes the streamline that separates the fluid in channel 1 from that in channel 2 (figure 4). We assign the left and right hand wall streamfunctions the values -1 and 1 respectively.

Given this setup we can write equations for the flux in each channel as well as ones for the average Bernoulli function in each channel. These are

$$2\overline{d_1}\hat{d}_1 = 1 - \Psi_s \tag{12}$$

$$2\overline{d_2}\hat{d}_2 = 1 + \Psi_s \tag{13}$$

$$\frac{q}{2}\left[\frac{\hat{d}_1^{\,2}}{T_1^2} + T_1^2(\overline{d_1} - 1/q)^2\right] + \overline{d_1} + h_1 = \overline{B_1} \tag{14}$$

$$\frac{q}{2}[\frac{\hat{d_2}^2}{T_2^2} + T_2^2(\overline{d_2} - 1/q)^2] \quad + \quad \overline{d_2} + h_2 = \overline{B_2} \tag{15}$$

Where $\overline{d_i}$ is the average and $\hat{d}_i$ is half the difference of the depths on the right and left hand walls. Also q is the potential vorticity far upstream in a quiescent reservoir and $T_i = \tanh(\sqrt{q}w_i/2)$. These apply equally well for separated flow, but in that case $\overline{d_1} = \hat{d}_1$ and the width of the channel w_1 is replaced with the width of the separated flow, w_{1e}.

We also need a critical condition to be applied at each sill. For attached flow this has the form

$$\frac{q\hat{d}_{ic}^2}{T_{ic}^2} \quad = \quad \overline{d_{ic}}[1 - T_{1c}^2(1 - q\overline{d_{ic}})] \tag{16}$$

while for separated flow we simply replace T_{ic} with T_{iec} and apply either equation 12 or 13. We note that for separated flow, where d_{ic} is strictly a function of Ψ_s that the critical condition at the sill is quadratic in T_{iec}^2 with coefficients that only depend on Ψ_s and q. Thus for separated flow we require the quadratic to have real roots which satisfy $0 < T_{iec}^2 < 1$. More precisely, we require that

$$0 < q < \frac{1}{2\overline{d_{1c}}}[1 - \sqrt{1 - \overline{d_{ic}^4}}] \tag{17}$$

This condition is represented in figure 5. From this we can see that there is a maximum, $q = 0.5$, above which we cannot have separated flow and that for separated flow in both channels, we in fact need $q \leq 1 - \frac{\sqrt{3}}{2} \approx 0.097$. This implies that for flow separation we need a deep upstream reservoir.

The six equations above are underdetermined since there are seven unknowns ($\overline{d_{ic}}, \hat{d}_{ic}, \overline{B_i}$ and Ψ_s). Furthermore there is no equation linking the two channels, such as equation 7 in the nonrotating case. We thus need to derive an additional equation. We know that

$$\frac{dB}{d\Psi} = q \tag{18}$$

which leads to

$$\begin{aligned} \int_{-1}^{1} \frac{dB}{d\Psi} d\Psi \quad &= \quad \int_{-1}^{1} q d\Psi \\ B|_{\Psi=1} - B|_{\Psi=-1} \quad &= \quad 2q \end{aligned} \tag{19}$$

Also we have

$$\overline{B_1} = (B|_{\Psi=1} + B|_{\Psi_s})/2 \tag{20}$$

$$\overline{B_2} = (B|_{\Psi=-1} + B|_{\Psi_s})/2 \tag{21}$$

Combining the above equations gives

$$\overline{B_2} = \overline{B_1} - q \tag{22}$$

3 Conclusions

We have seen that a multiple channel system exhibits distinct and somewhat unexpected differences from that of a simple channel. We see that if the assumption of critical flow at both sills is valid then this sets several possible relations between the pair of upstream variables (v_0, d_0). The difference between this and the single channel case is that there can be between zero and four physically possible states and that more than one of these can be subcritical. Rotation introduces a much more complexity into the problem primarily since we must generally solve multiple problems and then use some rational (such as minimum energy) to pick the appropriate flow state.

Bibliography

- Gill, A.E. (1977): The hydraulics of rotating-channel flow. *J. Fluid Mech.*,**80**, 641-671.

- Hogg, N.G. (1983): Hydraulic control and flow separation in a multi-layered fluid with applications to the Vema Channel. *J. Phys. Oceanogr.*, **13**, 695-708.

- Hogg, N.G. (1984): Multilayer hydraulic control with application to the Alboran Sea circulation. *J. Phys. Oceanogr.*, **14**, 454-466.

- Johnson, G.C., and D.R. Ohlsen (1994): Frictionally modified rotating hydraulic channel exchange and ocean outflows. *J. Phys. Oceanogr.*, **24**, 66-78.

- Pratt, L.J. (1983): On inertial flow over topography. Part 1. Semi-geostrophic adjustment to an obstacle. *J. Fluid Mech.*, **131**, 195-218.

- Pratt, L.J. (1984): On inertial flow over topography. Part 2. Rotating channel flow near the critical speed. *J. Fluid Mech.*, **145**, 95-110.

- Whitehead, J.A., A. Leetmaa and R.A. Knox (1974): Rotating hydraulics of strait and sill flows. *Geophys. Fluid Dyn.*, **6**, 101-125.

- Whitehead, J.A. (1989): Internal hydraulic control in rotating fluids - Applications to oceans. *Geophys. Astrophys. Fluid Dynamics*, **48**, 169-192.

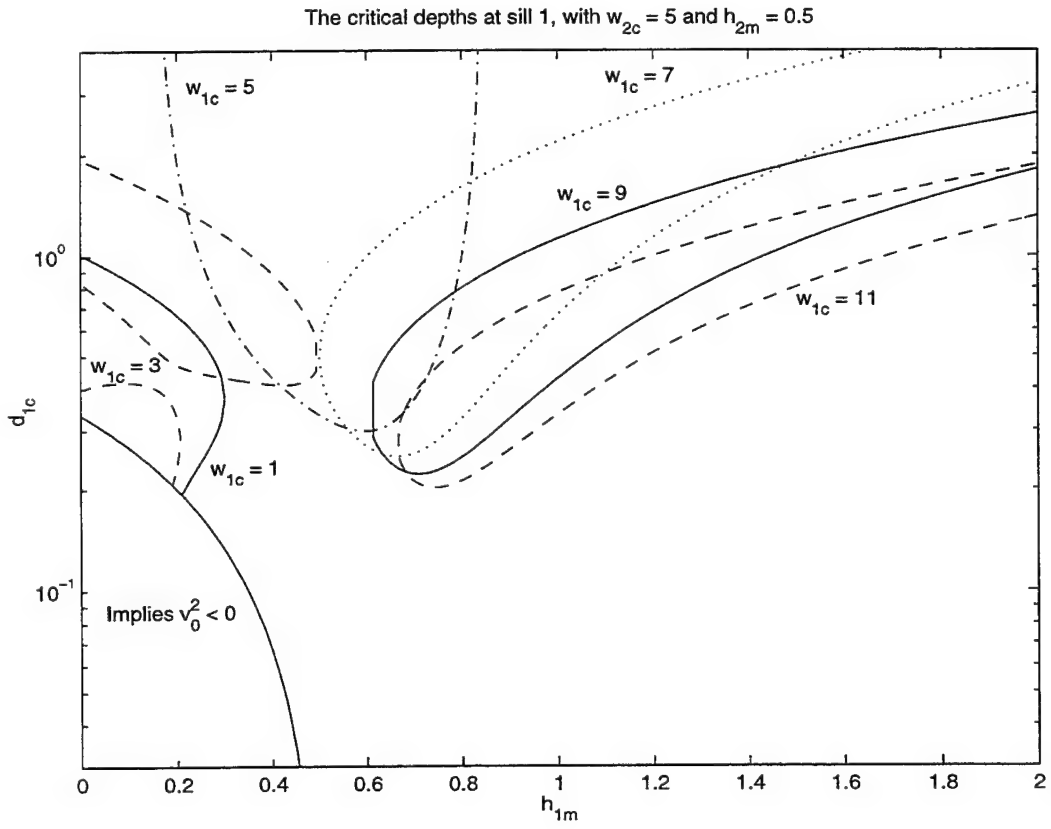

Figure 2: The depth of fluid at the control in sill 1 as a function of h_{1m} for five values of critical width, w_{1c} and for fixed geometry in the second channel, $(w_{2c} = 5, h_{2m} = 0.5)$. The region in the lower left corner is invalid since it implies $v_0^2 < 0$.

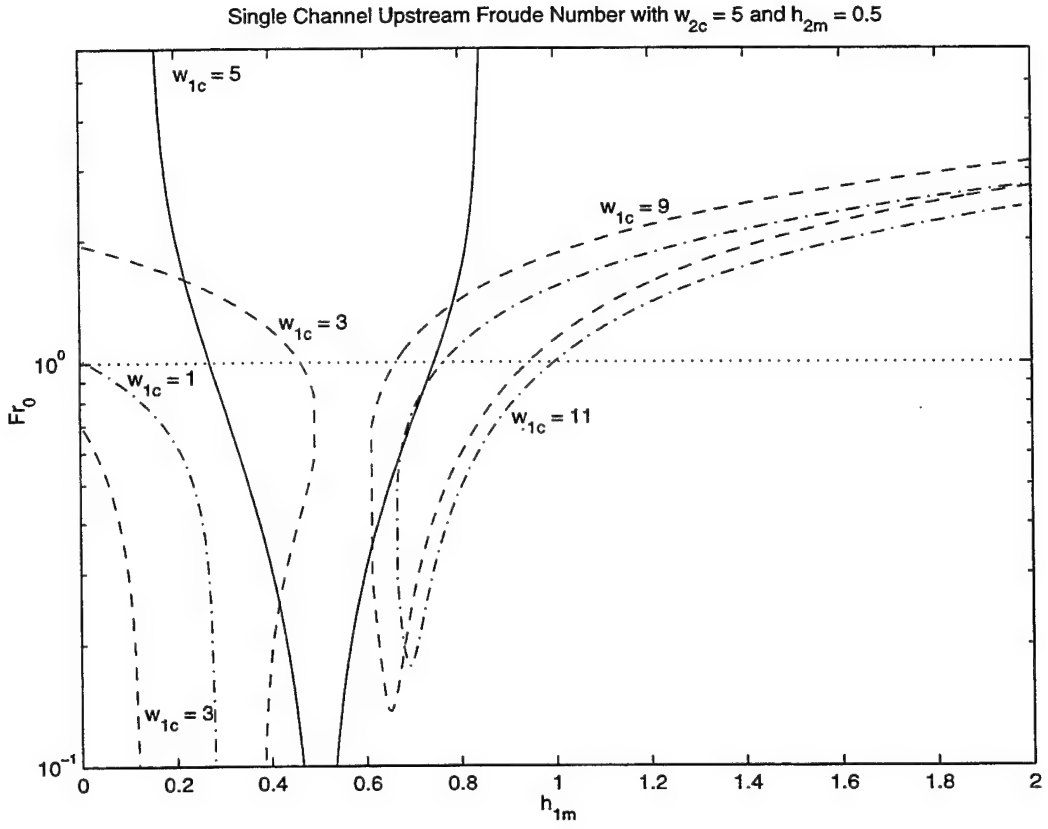

Figure 3: The upstream Froude number in the single channel as a function of h_{1m} for five values of critical width, w_{1c} and for fixed geometry in the second channel, $(w_{2c} = 5, h_{2m} = 0.5)$.

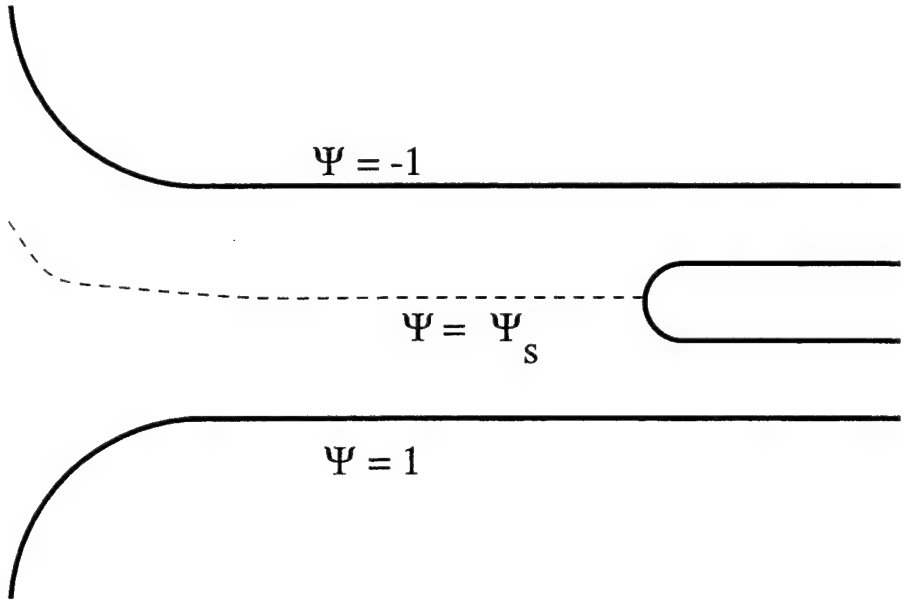

Figure 4: The geometry for rotating flow is similar to the nonrotating case in figure 1, with the addition of the streamline Ψ_s which must be determined. The total flux in the channel has also be scaled so that the streamlines on the right and left hand walls are 1 and -1 respectively.

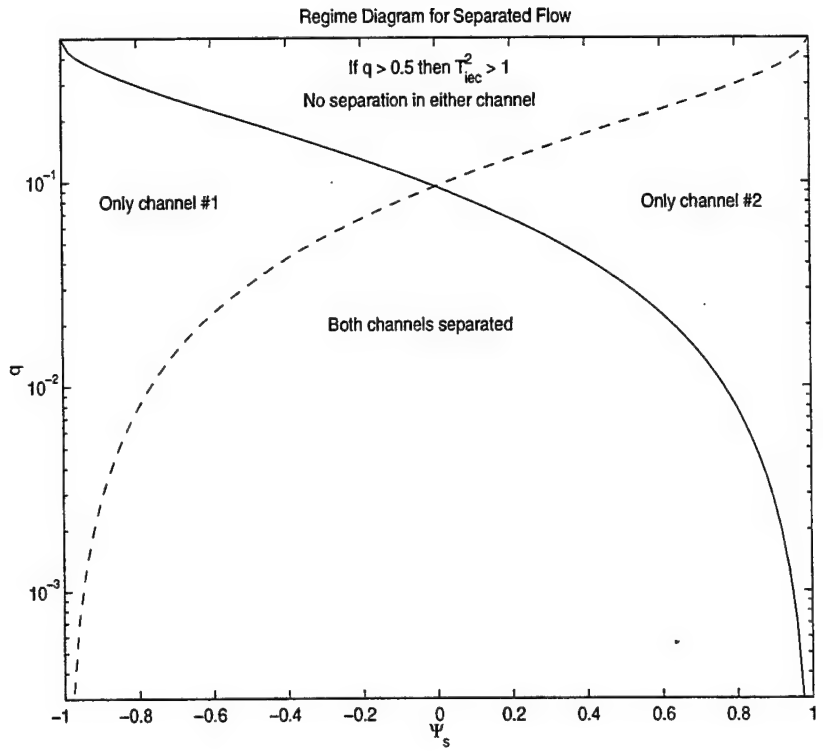

Figure 5: The regions of Ψ_s - q phasespace in which separated flow is possible. Note that attached flow is always a possibility.

Hydraulic Control with Entrainment

Katsurou Katsumata

1 Introduction

Hydraulic control theory has been widely used in physical oceanography to understand and predict the flows over sills or through contractions (e.g. Pratt, 1990). These flows are often subject to strong mixing, partly because the shallow complex geometry enhances the effect of tide, and partly because the flow accelerates as it approaches the channel (Lawrence, 1990). Helfrich (1995) points out the significance of the interfacial mixing in his laboratory experiments.

Although the effect of the friction has been taken into consideration in some hydraulic theories (Pratt, 1986; Johnson and Ohlsen, 1994), the effect of mass and momentum entrainment is uninvestigated. This work attempts to examine this effect. We start from a simple one-and-a-half layer model. Then, two layer exchange flow is considered with an intermediate layer due to the entrainment. The model has wide applications to the flow connecting a marginal or partially enclosed basin and ocean. The flow at the Strait of Bab al Mandab is studied as an example.

In this study, attention is restricted to the position of the critical control of a flow through a contraction without rotation. The incorporation of a sill is straightforward, though that of the rotation is not.

2 Theory

2.1 One and a half layer model

Pratt (1986) showed that for an abyssal flow under quiescent water of infinite thickness, a quadratic form of bottom drag shifts the position of the

critical control downstream, while the physical feature of the critical control that a long wave is stationary is unaffected. Here it will be shown that a simple parameterization of the entrainment between the inactive upper layer and the flowing layer causes opposite change.

The vertical velocity between the layers due to the entrainment is assumed to be always upward into the quiescent layer. The momentum and mass conservation are

$$\boldsymbol{C}\boldsymbol{v}_x = \boldsymbol{D}\boldsymbol{f}_x + \boldsymbol{A}w + \boldsymbol{a},$$

where

$$\boldsymbol{C} = \begin{pmatrix} u & g' \\ h & u \end{pmatrix} \quad \boldsymbol{v} = \begin{pmatrix} u \\ h \end{pmatrix} \quad \boldsymbol{D} = \begin{pmatrix} -g' & 0 \\ 0 & huY \end{pmatrix} \quad \boldsymbol{f} = \begin{pmatrix} b \\ Y^{-1} \end{pmatrix}$$

$$\boldsymbol{A} = \begin{pmatrix} 0 \\ -1 \end{pmatrix} \quad \boldsymbol{a} = \begin{pmatrix} -C_d u^2/h \\ 0 \end{pmatrix}$$

where $u(x)(>0), h(x)$ are respectively the velocity and thickness of the lower layer, g' is the reduced gravity, $b(x)$ is the bottom topography, $Y(x)$ is the width of the channel, and w is the vertical entrainment velocity, C_d is the bottom friction coefficient, and the quadratic form of the drag is used (Pratt, 1986).

Note that the effect of momentum entrainment does not appear in the momentum equation. In order to understand this, suppose a mass M_1 and M_2 representing water column of the upper layer and the lower layer respectively. They have velocity $u_1(t)$ and $u_2(t)$. In short time δt, suppose small amount of water $m \equiv \mu\delta t$ from M_2 is passed to M_1. The momentum change of the whole system is

$$\begin{aligned} &(M_1+m)u_1(t+\delta t) + M_2 u_2(t+\delta t) - M_1 u_1(t) - (M_2+m)u_2(t) \\ &= \left\{ M_1 \frac{\mathrm{d}u_1}{\mathrm{d}t} + M_2 \frac{\mathrm{d}u_2}{\mathrm{d}t} - \mu(u_2-u_1) \right\} \delta t + O(\delta t)^2. \end{aligned}$$

It is seen that to conserve the momentum of the system, the term $\mu(u_2-u_1)$ must be included in either the equation of motion of M_1 or that of M_2. It can be shown when $0 \le u_1 < u_2$ the term must be included in M_1, otherwise the kinetic energy of the system increases because it accelerates a faster mass.[1]

[1]Or. suitcase just dropped from a running car does not change the velocity of the

In another word, the effect of the momentum entrainment appears only in the layer that has lower speed.

The entrainment velocity w, due mainly to the instability of the interface, has been parameterized as a function of the layer Richardson number (Price, 1994), but in this study as the simplest model to start with, linear parameterization

$$w = \kappa u \tag{1}$$

is employed.

Eliminating u_x and introducing the Froude number $F \equiv \dfrac{u^2}{gh}$ yield

$$(F^2 - 1)h_x = b_x - F^2 \frac{h}{Y} Y_x + (C_d - \kappa)F^2.$$

This corresponds to equation (3.1) of Pratt (1986) and interpretation is similar; the critical control is given when $F^2 = 1$ where in order for h_x to remain finite, the right hand side must be zero. Namely, the critical point is where $b_x|_{x=x_c} - \dfrac{h}{Y} Y_x|_{x=x_c} = C_d - \kappa$ The stationarity of the long wave is present but the critical position is no longer at the point x_0 where $b_x|_{x=x_0} - \dfrac{h}{Y} Y_x|_{x=x_0} = 0$, but shifts downstream when $C_d > \kappa$ and upstream when $C_d < \kappa$.

2.2 Three layer model

The formulation of the previous section is now applied to an exchange flow, but in two layer flow it seems rather unnatural to have unidirectional entrainment. Accordingly we assume a thin middle layer between the top and the bottom layer to which the entrainment occurs.

The top layer has density ρ_1, thickness $h_1(x)$ and flowing along x at $u_1(x) > 0$, and the bottom layer has density ρ_2, thickness $h_2(x)$ and flowing at $u_2(x) < 0$. The density, velocity and thickness of the middle layer are $\rho_e, u_e(x)$ and $h_e(x)$ respectively. The middle layer can flow in either direction, but we assume $|u_e|$ is always less than $|u_1|$ and $|u_2|$.

car while it increases the velocity of the car when it is thrown backward, or decreases the velocity when it is thrown forward. Note that addition of energy to the system is necessary to throw the suitcase.

With $w_1 < 0$ and $w_2 > 0$ being the entrainment velocity from the top layer and from the bottom layer respectively, the mass conservation of each layer is

$$\begin{aligned} \rho_1(h_1u_1)_x &= \rho_1 w_1 \\ \rho_e(h_eu_e)_x &= -\rho_1 w_1 + \rho_2 w_2 \\ \rho_2(h_2u_2)_x &= -\rho_2 w_2. \end{aligned} \tag{2}$$

Similarly the momentum entrainment from the top layer to the middle and from the bottom to the middle is $\rho_1(u_e - u_1)w_1$ and $\rho_2(u_2 - u_e)w_2$, respectively. Note that this momentum entrainment only affects the middle layer.

The entrainment is parameterized, similarly to (1), as

$$\begin{aligned} w_1 &= \kappa(u_e - u_1) < 0 \\ w_2 &= \kappa(u_e - u_2) > 0 \end{aligned} \tag{3}$$

where κ is the entrainment constant and taken to be the same for both w_1 and w_2.

With the rigid lid approximation, hydrostatic, non-rotating gradual three-layer flow is described in a matrix form as

$$\boldsymbol{C}\boldsymbol{v}_x = \boldsymbol{D}\boldsymbol{f}_x + \boldsymbol{A}\boldsymbol{w} + \boldsymbol{a}, \tag{4}$$

with

$$\boldsymbol{C} = \begin{pmatrix} u_1 & 0 & 0 & g & g & g & 1 \\ 0 & u_e & 0 & r_1 g & g & g & r_1 \\ 0 & 0 & u_2 & r_1 r_2 g & r_2 g & g & r_1 r_2 \\ h_1 & 0 & 0 & u_1 & 0 & 0 & 0 \\ 0 & h_e & 0 & 0 & u_e & 0 & 0 \\ 0 & 0 & h_2 & 0 & 0 & u_2 & 0 \\ 0 & 0 & 0 & 1 & 1 & 1 & 0 \end{pmatrix} \quad \boldsymbol{v} = \begin{pmatrix} u_1 \\ u_e \\ u_2 \\ h_1 \\ h_e \\ h_2 \\ p/\rho_1 \end{pmatrix} \quad \boldsymbol{D} = \begin{pmatrix} -g & 0 \\ -g & 0 \\ -g & 0 \\ 0 & h_1u_1Y \\ 0 & h_eu_eY \\ 0 & h_2u_2Y \\ -1 & 0 \end{pmatrix}$$

where $r_1 \equiv \rho_1/\rho_e, r_2 \equiv \rho_e/\rho_2$, and $p(x)$ is the pressure at upper bounding surface. Note that the transport $u_ih_iY(i = 1, e, 2)$ is *not* constant due to the

mass entrainment.

$$\boldsymbol{A} = \begin{pmatrix} 0 & 0 \\ r_1(u_e - u_1)/h_e & r_2^{-1}(u_2 - u_e)/h_e \\ 0 & 0 \\ 1 & 0 \\ -r_1 & r_2^{-1} \\ 0 & -1 \\ 0 & 0 \end{pmatrix} \quad \boldsymbol{a} = \begin{pmatrix} 0 \\ 0 \\ C_d u_2^2/h_2 \\ 0 \\ 0 \\ 0 \\ 0 \end{pmatrix}$$

$$\boldsymbol{f} = \begin{pmatrix} b \\ Y^{-1} \end{pmatrix} \quad \boldsymbol{w} = \begin{pmatrix} w_1 \\ w_2 \end{pmatrix}.$$

Here we have seven unknowns $u_i(x), h_i(x), p(x)$ and seven first-order ODE's, so that the system is solved with seven constants. In most hydraulic problems, only four constants are given (usually the Bernoulli constants of each layer at the upstream and the total depth) then the three more constants (usually the transport of each layer) are determined by the critical or control condition. The three equations to determine the critical condition are obtained by eliminating the velocity $\mathrm{d}u_i/\mathrm{d}x$ between the mass conservation and momentum equation (see Appendix). The number of equations to determine the critical condition can be further reduced to two by eliminating p and the use of the rigid lid condition;

$$\boldsymbol{C'v'}_x = \boldsymbol{D'f}_x + \boldsymbol{A'w} + \boldsymbol{a'}, \tag{5}$$

where

$$\boldsymbol{C'} = \begin{pmatrix} F_1^2 - r & -F_e^2 \\ F_1^2 + F_2^2 - 1 & F_2^2 - (1-r) \end{pmatrix} \quad \boldsymbol{v'} = \begin{pmatrix} h_1 \\ h_e \end{pmatrix}$$

$$\boldsymbol{D'} = \begin{pmatrix} -r & F_e^2 h_e - F_1^2 h_1 \\ -1 & F_2^2 h_2 - F_1^2 h_1 \end{pmatrix}$$

$$\boldsymbol{A'} = \begin{pmatrix} \kappa\dfrac{r_1 u_1}{(1-r_1r_2)gh_1} + \kappa\dfrac{r_1(2u_e - u_1)}{(1-r_1r_2)gh_e} & -\kappa\dfrac{r_2^{-1}(2u_e - u_2)}{(1-r_1r_2)gh_e} \\ \kappa\dfrac{r_1 u_1}{(1-r_1r_2)gh_1} & \kappa\dfrac{r_2^{-1}u_2}{(1-r_1r_2)gh_2} \end{pmatrix} \quad \boldsymbol{a'} = \begin{pmatrix} 0 \\ C_d F_2^2 \end{pmatrix}$$

where

$$F_1^2 \equiv \frac{r_1 u_1^2}{(1-r_1r_2)gh_1}, F_2^2 \equiv \frac{r_2^{-1}u_2^2}{(1-r_1r_2)gh_2}, \text{ and } F_e^2 \equiv \frac{u_e^2}{(1-r_1r_2)gh_e}.$$

The correction terms $\boldsymbol{A'}$ due to the entrainment have very small (order of 10^{-3} or less) coefficients κ. Therefore if $|u_e|$ is small compared to $|u_1|$ or $|u_2|$, u_e in the term is neglected:

$$\boldsymbol{A'w} + \boldsymbol{a} = \begin{pmatrix} \kappa(-F_1^2 + F_1^2\frac{h_1}{h_e} - F_2^2\frac{h_2}{h_e}) \\ \kappa(-F_1^2 - F_2^2) - C_d F_2^2 \end{pmatrix}$$

Also used in (5) is

$$1-r_1 \sim 1-r_2 \sim 1-r_1r_2 \sim O(10^{-3}), \quad \text{so that} \quad r \equiv \frac{1-r_1}{1-r_1r_2} \approx 1 - \frac{1-r_2}{1-r_1r_2}.$$

Since we are considering an incompressible fluid, it is natural that the volume conservation also be satisfied, but at the cost of the simpleness of the layer model, the volume conservation holds only up to $O(1-r_1)$. The above approximations to neglect $1-r_1$ are essentially the Boussinesq approximation.

With Δ as the determinant of $\boldsymbol{C'}$ and $\widetilde{\boldsymbol{C'}}$ as the transposed cofactor matrix of $\boldsymbol{C'}$, (5) is written as

$$\Delta \boldsymbol{v'} = \widetilde{\boldsymbol{C'}}\{\boldsymbol{D'f}_x + \boldsymbol{A'w} + \boldsymbol{a}\}. \tag{6}$$

When the flow is critical, Δ is zero. Then

$$\Delta \equiv (1 - F_1^2 - F_2^2)F_e^2 - (r - F_1^2)(1 - r - F_2^2) = 0 \tag{7}$$

It is seen from (6) that the feature of the control that one of the characteristic velocities is stationary is present regardless of the correction due to entrainment and bottom drag for the characteristic velocities $\lambda_1, \lambda_2, \lambda_3, \lambda_4$, are eigenvalues of $\boldsymbol{C}$, and $\Delta = \lambda_1\lambda_2\lambda_3\lambda_4$.

At the control in order for the right side to be zero, the vector $\{\boldsymbol{D'f}_x + \boldsymbol{A'w} + \boldsymbol{a}\}$ must be an eigenvector for zero eigenvalue of $\widetilde{\boldsymbol{C'}}$. For the case of flat bottom (contraction only) the condition yields

$$g_1(F_1^2, F_e^2, F_2^2, h_1, h_2)\frac{h}{Y}Y_x = \kappa g_2(F_1^2, F_e^2, F_2^2, h_1, h_2), \tag{8}$$

where

$$g_1 = F_e^2(F_2^2\frac{h_2}{h} - F_1^2\frac{h_1}{h}) - (1 - r - F_2^2)(F_e^2\frac{h_e}{h} - F_1^2\frac{h_1}{h})$$

$$g_2 = (1 - r - F_2^2)(F_1^2\frac{h_1}{h_e} - F_2^2\frac{h_2}{h_e} - F_1^2) + F_e^2(F_1^2 + F_2^2) - \gamma F_2^2 F_e^2$$

where $\gamma \equiv C_d/\kappa$ and $h \equiv h_1 + h_e + h_2$ is the total depth.

In case of no entrainment and no bottom friction ($\kappa = 0, C_d = 0$) the critical condition is either $g_1 = 0$ or $Y_x = 0$. The former is the virtual control and the latter is the geometrical control.

At the control, we have six unknowns, that is, $F_1^2, F_e^2, F_2^2, h_1, h_2, Y_x/Y$. The equations that must hold at the control are (7) and (8). Therefore the system could be solved with four more constraints — two Bernoulli equations and two constraints on the transport. Due to the entrainment, those constraints have $O(\kappa)$ correction, then the unknowns are dependent on κ. Let the subscript 0 denote the value at the narrowest point, then equation (8) is expanded a

$$\begin{aligned}&\Big\{g_1(F_{10}^2, F_{e0}^2, F_{20}^2, h_{10}, h_{20}) + O(\kappa)\Big\}\left\{h\left(\frac{Y_x}{Y}\right)_0 + h\frac{\delta Y_x}{Y}\right\}\\ &= \kappa\Big\{g_2(F_{10}^2, F_{e0}^2, F_{20}^2, h_{10}, h_{20}) + O(\kappa)\Big\}.\end{aligned}$$

At the geometrical control, $\left(\frac{Y_x}{Y}\right)_0 = 0$, then the correction of the control point δY_x is evaluated as

$$\delta Y_x = \kappa\frac{Y}{h}\frac{g_2}{g_1}(F_{10}^2, F_{e0}^2, F_{20}^2, h_{10}, h_{20}). \tag{9}$$

2.3 Some special cases

The direction of the shift of the critical point due to entrainment and friction can be now calculated from (9). Before the application of the theory, two special cases are examined.

The entrainment layer is considered to be very thin. As $h_e \to 0$, the leading term in (9) is

$$\begin{aligned}\frac{g_2}{g_1} &\approx \frac{-(1-r-F_2^2)(F_2^2\frac{h_2}{h_e} - F_1^2\frac{h_1}{h_e})}{F_e^2(F_2^2\frac{h_2}{h} - F_1^2\frac{h_1}{h}) - (1-r-F_2^2)(-F_1^2\frac{h_1}{h})}\\ &= \frac{h}{h_e}\frac{-\dfrac{1-r-F_2^2}{F_e^2}}{\left(1 + \dfrac{1-r-F_2^2}{F_e^2}\dfrac{F_1^2h_1}{(F_2^2h_2 - F_1^2h_1)}\right)}\end{aligned}$$

In the applications, the velocity of the middle layer is so small that though h_e is a small number, F_e is small. Therefore

$$\frac{g_2}{g_1} \approx -\frac{h}{h_e}\frac{F_2^2 h_2 - F_1^2 h_1}{F_1^2 h_1}.$$

That unables us to decide the sign of the shift of the critical point more intuitively; negative x direction when $F_2^2 h_2 > F_1^2 h_1$ or bottom speed is more than the surface speed, and positive when $F_2^2 h_2 < F_1^2 h_1$.

Two layer limit is recovered from (5) just by $h_e \to 0$ and taking the lower component, which yields a two-layer rigid lid model with bottom drag, namely,

$$(F_1^2 + F_2^2 - 1)h_{1x} = (F_2^2 h_2 - F_1^2 h_1)\frac{Y_x}{Y} + C_d F_2^2.$$

It is seen that the critical points shifts in positive x direction when surface speed is more than the bottom speed and *vice versa*. The one and a half layer model of Pratt (1986) is recovered by $F_1^2 \to 0$.

3 Critical point of the Bab al Mandab Strait

The Strait of Bab al Mandab is a narrow and shallow channel that connects the Indian Ocean at southeast and the Red Sea at northwest. The Red Sea is about 1800 km long, 250 km wide in average, and 560m deep in average (Ross, 1983). The flow through the Strait of Bab al Mandab is influenced both by the monsoon wind and by the convection in the Red Sea, where the evaporation is roughly 2 m/year. In the winter (October – May) the northwestward wind and active sinking cause the surface waters flow from the Gulf of Aden into the Red Sea and the subsurface flow is to south. The reverse of the wind system in the summer leads to three layer structure of the flow; the surface and the bottom flowing out and the middle flowing into the Red Sea. Although the flow shows strong stratification ($2 - 4\ \sigma_\theta$), the Rossby deformation radius is $20 - 30$ km for the Strait is located at low latitude (13 degrees N), and the below discussion does not involve the effect of the rotation.

3.1 Hydraulic control

The geometry of the Bab al Mandab Strait provides two possible points for hydraulic control; the narrowest (19 km) point of the Strait by Perim Island, and the shallowest (160 m) point, 150 km inward to the Red Sea from the narrowest section.

Thanks to Drs.Murray and Johns, we are provided with the 10-month direct observation of the flow velocity at these two points and density at the shallowest point. The flow in each season is quite steady, and August is picked up for a typical summer flow while November data are used for a winter flow since no density data is available for February.

Table 1: Characteristic velocities in m/s calculated from the ordinary layer models.

month	shallowest	narrowest
Aug.	-1.6	-1.6
	-0.7	-0.8
	0.9	0.7
	1.4	1.5
Nov.	-0.8	-0.7
	0.7	0.9

First, the characteristic velocities of the system are calculated by adapting simple layered model to those observations. If the flow is hydraulically controlled, one of the velocities is zero. The velocities and densities are taken at the peak of the velocity, layer interface is set to the point of zero velocity, and the densities in each layer used at the narrowest point are the same as the value at the shallowest point. The formulae for the characteristics are found in Baines (1994) for three layer model and Armi (1986) for two layer model. The results are shown in table 1. The positive direction is into the Red Sea. It can be seen that such a simple model shows no flow is close to the control.

Furthermore for more realistic representation of the flow, the model in Baines (1994) is applied where the velocity in each layer can have linear

vertical shear with constant density in each layer. Number of layers is three and the results are shown in table 2. For the density, the values at the bottom of each layer are used in table 2, but similar results are obtained for the density at the middle of each layer.

Table 2: Characteristic velocities in m/s calculated from the shear layer models.

month	shallowest	narrowest
Aug.	-1.1	-1.0
	-0.6	-0.4
	0.7	0.8
	1.1	1.3
Nov.	-1.7	-1.7
	-0.3	-1.0
	0.4	0.1
	0.7	0.9

It is found that the winter flow at the narrow is almost controlled[2] but supercritical in the sense that the determinant, which is the product of all the characteristic velocities, is positive. Therefore it is expected the flow is critically controlled somewhere in negative x direction (towards the Gulf of Aden) of the narrowest position.

3.2 The effect of the entrainment and the bottom friction

Although the supercriticality found above might result from the crudeness of the model, the effect of the entrainment and the bottom friction is examined in this section.

A rough estimate of the gradient Richardson number

$$R_i \approx g\frac{\delta\rho\delta z}{\rho(\delta u)^2},$$

[2]This mode is the varicose mode where the displacement of each interface has different sign.

where δ means vertical difference, shows that the flow at the sill is stable due to the strong stratification ($\delta z \approx 40\text{m}, \delta u \approx 1\text{m/s}, \delta\rho/\rho \approx 3 \times 10^{-3}$ gives $R_i \approx 1.2$), but the estimate is based on the monthly mean flow velocity and Ross (1983) points out that the mixing occurring at the Strait can be traced by nutrient distribution.

The effect of the entrainment can be approximately estimated by the change of the density profile along the channel. From the density advection

$$\frac{\mathrm{d}\rho}{\mathrm{d}t} = \frac{w\delta\rho}{h}$$

the magnitude of the entrainment velocity is estimated as

$$w \approx \frac{h}{\Delta x}\frac{\Delta\rho}{\delta\rho}u,$$

where Δ, δ mean the horizontal and the vertical difference respectively. Figure 12 of Maillard (1986) shows that the heavy Red Sea water is mixed with the lighter ($\delta\rho = 0.5$ to $1.0\sigma_\theta$) water from the Gulf of Aden to change its density ($\Delta\rho = 0.5$ to $1.0\sigma_\theta$) in roughly $\Delta x = 100$km, and $h = 50$ to 100m. They give a number of the order 10^{-4}. Thus we choose $\kappa = 10^{-4}$.

Pratt (1986) and Price (1994) suggests a number of the order 10^{-3} for the drag coefficient, so we set $C_d = 10^{-3}$.

The Froude numbers and the layer thickness of the top and the bottom layer are estimated from the data. Two methods are used to estimated the middle layer Froude number F_e^2;

(I.) Assign arbitrary small speed, say, $u_e = 0.01$ m/s,

(II.) Require the critical control (7).

The width of the flow is assumed to be 10 km, and the depth is 200m.

Table 3: $\mathrm{d}Y/\mathrm{d}x$ estimation

Thickness of mid. layer	F_e^2 is given as	
	0.01	critical
2m	-0.2	-0.2
10m	-0.06	-0.01

The result of (9) is shown in table 3 for two different assumption of the thickness of the middle layer. The estimation is somewhat sensitive to the assumption of the thickness of the entrainment layer, but the estimation shows that the critical point shifts upstream — somewhere in Gulf of Aden.

The same prediction of upstream shift can be made by the discussion of the section 2.3 (i.e. the bottom speed is more than the surface).

4 Concluding remarks

The procedure to incorporate the correction term in the mass or momentum balance of the layer model can be extended to other form of the correction. One interesting application is the effect of the surface wind stress. Murray and Johns (private communication) suggest from the observation that the velocity of the flow in Bab al Mandab shows close correlation to the wind forcing in the synoptic and intraseasonal bands. The model that includes the effect of the surface wind stress is expected to clarify the mechanism that causes the close correlation. In this work, as a first attempt to incorporate the effect of the entrainment, approximated evaluation of the effect (9) has been used, but the system needs to be integrated from some upstream condition to evaluate the effect more quantitatively. With the integration, it is possible to parameterize the entrainment velocity (1, 3) as a function of the layer Richadson number.

This study is mainly concerned with the critical condition, but one significant effect of the entrainment is on the water property. Combination of the stream tube model of an outflow (Price, 1994) and hydraulic control theory has not yet been attempted.

In order to apply the theory to abyssal flows of the ocean or other wide straits, the effect of the rotation could no longer be neglected. It must be pointed out that even the qualitative estimation of the effect of bottom friction or entrainment in rotating hydraulics is still left to the future work.

Acknowledgements I would like to thank Drs. Larry Pratt, David Smeed, James Price, and Jack Whitehead for their patient help.

Appendix

The form of (4) found in the course of calculation to (5) is;

$$\begin{pmatrix} \hat{F}_1^2-1 & -1 & -1 & -1 \\ -r_1 & \hat{F}_e^2-1 & -1 & -r_1 \\ -r_1r_2 & -r_2 & \hat{F}_2^2-1 & -r_1r_2 \end{pmatrix} \begin{pmatrix} h_1 \\ h_e \\ h_2 \\ p_x/(\rho_1 g) \end{pmatrix}_x = \begin{pmatrix} 1 & \hat{F}_1^2 h_1 Y \\ 1 & \hat{F}_e^2 h_e Y \\ 1 & \hat{F}_2^2 h_2 Y \end{pmatrix} \begin{pmatrix} b \\ Y^{-1} \end{pmatrix}_x$$

$$+ \begin{pmatrix} u_1/(gh_1) & 0 \\ -r_1(2u_e-u_1)/(gh_e) & r_2^{-1}(2u_e-u_2)/(gh_e) \\ 0 & -u_2/(gh_2) \end{pmatrix} \begin{pmatrix} w_1 \\ w_2 \end{pmatrix} + \begin{pmatrix} 0 \\ 0 \\ -C_d\hat{F}_2^2 \end{pmatrix}$$

where $\hat{F}_i^2 \equiv u_i^2/(gh_i)$ $(i = 1, e, 2)$.

References

[1] Armi, L., 1986, "The hydraulics of two flowing layer with different densities", *J.Fluid Mech.*, **163**, 22–58

[2] Baines, P.G., 1994, *Topographic effects in stratified flows*, Cambridge University Press

[3] Helfrich, K.R., 1995, "Time-dependent two-layer hydraulic exchange flows", *J.Phys.Oceanogr.*, **25**, 360–373

[4] Johnson, G.C., and D.R. Ohlsen, 1994, "Frictionally modified rotating hydraulic channel exchange and ocean outflows", *J. Phys. Oceanogr.*, **24**, 66-78

[5] Lawrence, G.A., 1991, "Can mixing in exchange flows be predicted using internal hydraulics?" in [8].

[6] Maillard, C., and G.Soliman, 1986, "Hydrography of the Red Sea and exchanges with the Indian Ocean in summer", *Oceanol.Acta*, **9**, 249–269

[7] Pratt, L.J., 1986, "Hydraulic control of sill flow with bottom friction", *J.Phys.Oceanogr.*, **16**, 1970–1980

[8] Pratt, L.J. ed, 1990, *The Physical Oceanography of Sea Straits*, Kluwer Academic Publishers

[9] Price, J.F., and M.O.Baringer, 1994, "Outflows and deep water production by marginal seas", *Prog.Oceanog*, **33**, 161–200

[10] Ross, A.D., 1983, "The Red Sea", in *Estuaries and Enclosed Seas*, ed. B.H.Ketchum, Elsevier, 293–307

Flow in a Narrow Channel with Rotation and Friction

Jon Xinzhong Chen
Astronomy Department, Columbia University, New York, NY10027

September 29, 1997

In the ocean, due to different heating or cooling effects in different deep basins, there exist flows along the shallow area between the deep basins(Fig. 1), which can be modelled as a flow along a narrow channel(Fig. 2). In order to understand the variation of the elevation of the ocean, we have to know the transport along these "channels".

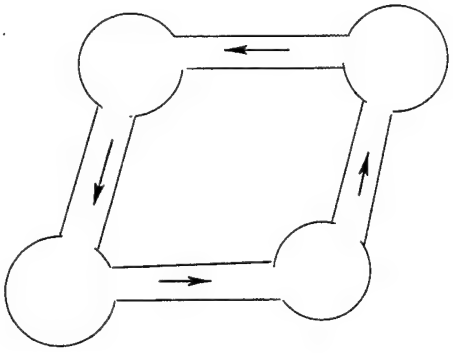

Figure 1: Flows between deep basins

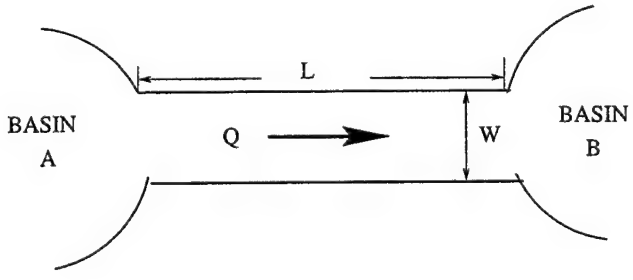

Figure 2: idealized model of narrow channel

Our original motivation is: when the flow is so fast that the inertial term is to be included, gravity wave will control the flow; when the flow is not so fast that the inertial term can be neglected, but friction and non-uniform rotation are to be considered, "Kelvin" wave (due to the friction) and Rossby wave may play the role in controlling the flow.

The results are: when inertial term is considered, there exists hydrolic control, we get the control condition with friction and rotation included; when inertial term is neglected, the friction term causes sort of "Kelvin" waves along the banks of the channel; they adjust the flow in the channel and control the transport in a subtle way; they also result in an anology of "shear diffusion", which greatly suppresses the nonlinear effect, making the linear description a good approximation.

In Part I, we sketch the case with inertial term. In Part II, we consider the case without inertial term.

1 With inertial term

In this part, we will derive the conditions for hydrolic control with rotation and friction. We don't use any assumption on the potential vorticity.

1.1 Coordinate System and Quantities

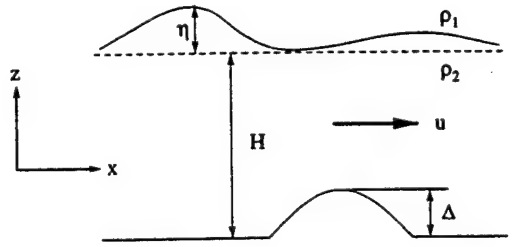

Figure 3: side view of the channel

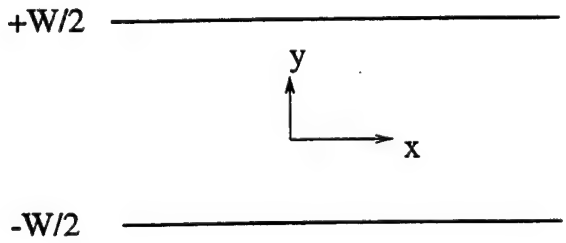

Figure 4: top view of the channel

As shown in Fig.3 and Fig.4, we take:
x, u : along channel
y, v : across channel
z : depth
$\eta(x, y, t)$: free surface
$H(x, y)$: depth from average surface
$\Delta(x)$: topography of bottom
ρ_1 : density of the upper layer (inactive layer with infinite depth)
ρ_2 : density of the lower layer (active layer)
$h(x, y, t)$: total depth
define $H_0 = H - \Delta$

1.2 Shallow Water Equations

When inertial term is considered, shallow water equations read:

$$\begin{cases} u_t + uu_x + vu_y - fv = -g'\eta_x - \epsilon u \\ v_t + uv_x + vv_y + fu = -g'\eta_y - \epsilon v \\ h_t + (hu)_x + (hv)_y = 0 \end{cases} \tag{1}$$

where

$$g' = \frac{\rho_2 - \rho_1}{\rho_2} g. \tag{2}$$

The first two are momentum balance equations and the last one is mass conservation law. Boundary condition is:

$$v|_{y=\pm\frac{W}{2}} = 0 \tag{3}$$

Scaling with: $\begin{cases} t \to Tt' \\ x \to Lx' \\ y \to Wy' \\ u \to Uu' \\ v \to Uv' \\ U = \frac{L}{T} \end{cases}$ and

$$\begin{cases} \epsilon_0 = \frac{\epsilon}{f_0} \\ R_0 = \frac{U}{f_0 L} = \frac{1}{f_0 T} \\ f \to f_0 f' = f_0(1 + \delta y) \\ \eta \to N_0 \eta' \\ a = \frac{N_0}{H_0} \\ h = H_0 h' = H_0(1 + a\eta' - \Delta') \\ A = \frac{gN_0}{f_0 UL} \end{cases} \tag{4}$$

We end up with the following equations (drop "prime"):

$$\begin{cases} R_0(u_t + uu_x + \frac{1}{\delta}vu_y) - vf = -A\eta_x - \epsilon_0 u \\ R_0(v_t + uv_x + \frac{1}{\delta}vv_y) + uf = -\frac{A}{\delta}\eta_y - \epsilon_0 v \\ \eta_t + (hu)_x + \frac{1}{\delta}(hv)_y = 0 \end{cases} \tag{5}$$

with boundary condition :

$$v|_{y=\pm\frac{1}{2}} = 0 \tag{6}$$

1.3 Asymptotic expansion

Now we expand the above equations with :

$$\begin{cases} \eta = \eta_0 + \delta\eta_1 + \cdots \\ u = u_0 + \delta u_1 + \cdots \\ v = v_0 + \delta v_1 + \cdot \end{cases} \tag{7}$$

where $\delta = W/L$ is the expanding parameter.
In the leading order, $O(\delta^{-1})$ we get:

$$\begin{cases} (h_0 v_0)_y = 0 \\ v_0 v_{0y} = -A\eta_{0y} \\ v_0 u_{0y} = 0 \end{cases} \tag{8}$$

then we have $v_0 = 0$, $\eta_0 = \eta_0(x,t)$, although u_{0y} is not necessarily zero from the above equations, we can take it as our assumption, which is consistent with the narrowness assumption. From the next order, $O(\delta^0)$, we get(after using the leading order equations):

$$\begin{cases} R_0(u_{0t} + u_0 u_{0x}) = -A\eta_{0x} - \epsilon_0 u_0 \\ \eta_{0t} + (h_0 u_0)_x = 0 \\ \eta_1 = -u_0 y/A + f_1(x,t) \end{cases} \tag{9}$$

From order $O(\delta^1)$, we get the linear equations for f_1,u_1,and η_2, which are:

$$\begin{cases} f_{1t} + ((f_1 + 1 - \Delta)u_0)_x + (h_0 u_1)_x + (h_0 v_2)_y - y(u_0^2)_x/A = 0 \\ R_0(u_{1t} + u_0 u_{1x} + u_1 u_{0x}) = -A\eta_{1x} - \epsilon_0 u_1 \\ u_1 + y u_0 = -A\eta_{2y} \end{cases} \tag{10}$$

average the equation by setting: $\overline{u_1} = \int_{-1/2}^{1/2} u_1 dy$, we have:

$$\begin{cases} f_{1t} + (f_1 + 1 - \Delta)u_0)_x + (h_0\overline{u_1})_x = 0 \\ R_0(u_{1t} + u_0 u_{1x} + \overline{u_1} u_{0x}) = -Af_{1x} - \epsilon_0\overline{u_1} \\ \overline{u_1} + y u_0 = -A\eta_{2y} \end{cases} \tag{11}$$

Solving this equation for $\overline{u_1}$,f_1,then putting f_1 back to equation(9), we readily get the along channel and cross channel strucure with rotation and friction correction included. To

see the consistence with the results already known(e.g. Larry 1986 without rotation), we solve the first two order steady equations to get:

$$(\frac{AC}{au_0^2} - R_0 u_0)u_{0x} = (\frac{A}{a}\Delta_x + \epsilon_0 u_0) \tag{12}$$

where $C = h_0 u_0$ is a constant.
The corresponding critical conditions are :

$$\begin{cases} \frac{AC}{au_0^2} - R_0 u_0 = 0 \\ A\Delta_x/a + \epsilon_0 u_0 = 0 \end{cases} \tag{13}$$

Condition $A\Delta_x/a + \epsilon_0 u_0 = 0$ will give us that Froude Number(F) is equal to 1, so for frictionless flow, the critical point is at the point where $F = 1$ and $\Delta_x = 0$, which is a well-known result.

The along-channel structure is determined by the following cubic equation:

$$R_0 u_0^2 + \frac{2AC}{au_0} + \frac{A}{a}\Delta = C_1 \tag{14}$$

where C_1 is a constant; when we use

$$Q_1 = \int_{-1/2}^{1/2} (u_0\eta_1 + u_1\eta_0)dy \tag{15}$$

to calculate the transport, we will get the correction of the transport caused by rotation and friction.

1.4 Enhanced diffusion

If we set $R_0 = 0$, we get:

$$\eta_{0t} = \frac{A}{\epsilon_0}(h_0\eta_{0x})_x \tag{16}$$

which is a difussive equation with a greatly enhanced diffusive coefficient, in a way it is similar to some kind of shear diffusion, resulted in by the "Kelvin" waves along the two banks of the channel.

2 Without inertial term

In this case, we start from the following equations:

$$\begin{cases} -fv = -g'\frac{\partial \eta}{\partial x} - \epsilon u \\ fu = -g'\eta_y - \epsilon v \\ h_t + (hu)_x + (hu)_y = 0 \end{cases} \tag{17}$$

The first two equations are geostrophic ballance equations with the simplist form of friction, the third one is mass conservation equation. From equation (17), we get:

$$\begin{cases} u = -\frac{fg'}{f^2+\epsilon^2}\eta_y - \frac{\epsilon g'}{f^2+\epsilon^2}\eta_x \\ v = \frac{fg'}{f^2+\epsilon^2}\eta_x - \frac{\epsilon g'}{f^2+\epsilon^2}\eta_y \end{cases} \tag{18}$$

Put (18) into (17), we have:

$$\eta_t + J[\eta, \frac{fg'}{f^2+\epsilon^2}(\eta + H)] = \nabla \cdot [\frac{\epsilon g'}{f^2+\epsilon^2}(\eta + H)\nabla\eta] \tag{19}$$

Equation (19) shows when β effect (rotation is nonuniform) is considered, there will be a nonlinear term in the equation which makes it similar to Burger's equation and may cause some interesting effects in controlling the flow. To apply equation (19) to a channel as shown in Fig.3, we have to include the boundary condition, which is simply that normal velocity vanishes along the two banks of the channel, i.e.

$$v = 0 \Longrightarrow f\eta_x = \epsilon\eta_y \tag{20}$$

at $y = \pm\frac{W}{2}$. The following simple considerations may give us the essential properties of the system.

(i) **Linear rotationless with $H = const$: friction dominates**

Symmetry consideration suggests that η is y-independent, so $\eta = \eta(x)$ for a steady flow. No rotation means $f = 0$. So from equations (19), we have

$$\eta_{xx} = 0(\text{small terms omitted}) \tag{21}$$

Boundary condition is automatically satisfied. The solution for (21) is $\eta = \frac{\Delta\eta}{L}x$, where L is the length of the channel. $\Delta\eta = \eta_u - \eta_d$ is the level difference between upstream and downstream. The corresponding transport is:

$$Q = U = -\frac{g'}{\epsilon}\frac{\Delta\eta}{L}. \tag{22}$$

Obviously Q is determined by friction. The isobath is shown in Fig.5.

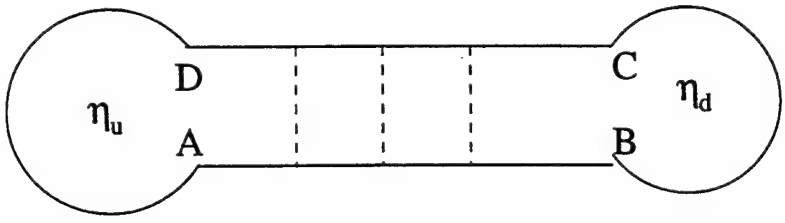

Figure 5: isobath for the case when friction dominates

(ii) $f = const, \epsilon/f$ **is small,** $H = const$**: rotation dominates**
Because $W/L \ll 1$, we have $\eta_{yy} \gg \eta_{xx}$, then equations (19) and (20) become:

$$\begin{cases} \eta_{yy} = 0 \\ f\eta_x = \epsilon\eta_y, y = \pm\frac{W}{2} \end{cases} \Longrightarrow \eta \propto (y + \frac{\epsilon}{f}x)$$

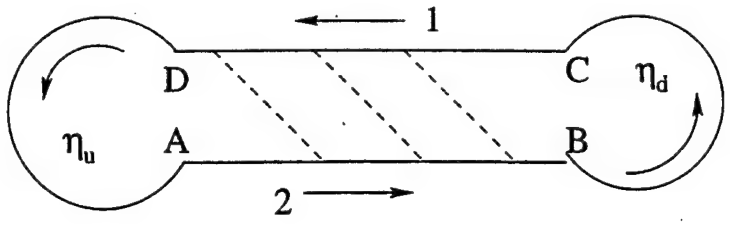

Figure 6: isobath for the case when rotation dominates, tilted by the "Kelvin"waves along the banks

We see that the isobath are tilted(see Fig. 6), we can think of this case as that two "Kelvin" waves propogate oppositely: "Kelvin" wave 1 along the north bank propogates from C to D, goes around the reservoir and diffuses away before reaching point A. It suggests us that the boundary condition for point A can be set as $\eta_A = \eta_u$; "Kelvin" wave 2 progates from A to B along south bank, similarly goes around the downstream reservoir and diffuses away before reaching C. So it is reasonable to take $\eta_C = \eta_d$ as boundary condition for point C. When $\epsilon/f \sim W/L$ i.e. $\epsilon_0 \sim \delta$, it follows that $\eta_D = \eta_B$, which is exactly the simulation result! (Later we will see.)

Similarly we can calculate the transport:

$$Q = \frac{g'}{f}\frac{(\eta_u - \eta_d)}{W} = \frac{g'}{f}\frac{\Delta\eta}{L} \cdot \delta \tag{23}$$

where $\delta = W/L$ is the aspect ratio. Now the transport is rotation-controlled.

(iii) H **is not constant**

When topography is considered to be like that in Fig.7, from last section, we can expect that "Kelvin" wave 1 is blocked, turns to EF then to B and brings a low value to there; "Kelvin" wave 2 turns to GH, then to D and brings a high value there. So there will be a high jump between HG and EF, the two sides of the bump. At the same time the flow will adjust. How is the transport changed? Does there exist Rossby wave? How does it behavior? How does the nonlinearity change the picture? In the following sections, we will investigate these questions.

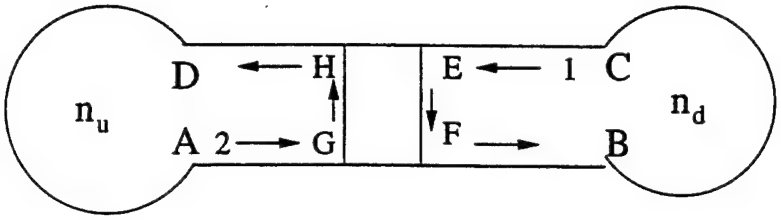

Figure 7: "Kelvin" waves are blocked by the bump

In section 2.1, we use variational principle to derive both "Kelvin" waves and Rossby wave in the linear approximation. We investigate how the topography and β effect change the normal modes, etc.

In section 2.2, three-level finite difference is used to describe the system. We will answer most of the above questions and confirm the conjecture by both calculation and simulation.

2.1 variational principle method

It is easy to show that equation $\eta_t + \vec{u} \cdot \nabla \eta = \nabla \cdot [\epsilon k \nabla \eta]$ with boundary condition $f\eta_s = -\epsilon \eta_n$ can be restated as equation $\eta_t + \vec{u_1} \cdot \nabla \eta = \nabla \cdot [\epsilon k \nabla \eta]$ with boundary condition $\eta_n = 0$, where $\eta_n = \frac{\partial \eta}{\partial x_n}$ is the normal derivative, and $\vec{u_1} = \vec{u} + fk\vec{s}\delta(\vec{r} - \vec{r_c})$, $\vec{s}$ is tangential unit vector, $\vec{r_c}$ is boundary.

The physical meaning is clear: if we are going to think the process as a diffusion process, then we have to satisfy boundary condition $\eta_n = 0$, which results in an extra convection term. This convection term is caused by friction and can be viewed as δ-function source, propogating along the boundary. That is why we can think of it as "Kelvin" wave.

In order to reduce this 2-D PDE to 1-D PDE, we use the following method, which incorporates the boundary condition into the equations resulted.

Set

$$\begin{cases} \alpha = \alpha_0 + \alpha_1 y + \alpha_2 y^2 \\ \eta = \eta_0 + \eta_1 y + \eta_2 y^2 \\ f = f_0 + y f_1 \\ or : \frac{1}{f} = \frac{1}{f_0}(1 - \beta y) \end{cases}, \tag{24}$$

where α_i, η_i are functions of x and t only, $i = 0, 1, 2$, then calculate integral

$$I = \int\int dxdy[\alpha\eta_t - h\vec{u} \cdot \nabla\alpha] = \int dx[A_0\alpha_0 + B_0\alpha_{0x} + A_1\alpha_1 + B_1\alpha_{1x} + A_2\alpha_2 + B_2\alpha_{2x}] \tag{25}$$

From $\frac{\delta I}{\delta \alpha_i} = 0$, we will get the equations: $A_i = B_{i,x}$, which are:

$$\begin{cases} \eta_{0t} + \eta_{2t} y_0^2 = \frac{g' H_0}{f_0}[\eta_{1x} - 2\beta y_0^2 \eta_{2x} \frac{\epsilon}{f_0} \eta_{0xx} + \frac{\epsilon}{f_0} \eta_{2xx}] + M_0 \\ \eta_{1t} y_0^2 = \frac{g' H_0}{f_0}[\eta_{0x} - 2\beta y_0^2 \eta_{1x} + 3 y_0^2 \eta_{2x} + \frac{2}{f_0} \eta_{1xx} - \frac{\epsilon}{f_0} \eta_1] + M_1 \\ \eta_{0t} y_0^2 + \eta_{2t} y_0^4 = \frac{g' H_0}{f_0}[-2 y_0^2 \beta \eta_{0x} + 3 y_0^2 \eta_{1x} - 4\beta y_0^4 \eta_{2x} \\ \qquad + \frac{\epsilon}{f_0}(y_0^2 \eta_{0xx} + y_0^4 \eta_{2xx} - 4 y_0^2 \eta_2)] + M_2 \end{cases} \tag{26}$$

where M_0, M_1, M_2 are nonlinear terms, and $\begin{cases} y_0^2 = \frac{1}{W} \int_{-W/2}^{+W/2} y^2 dy = \frac{W^2}{12} \\ y_0^4 = \frac{1}{W} \int_{-W/2}^{+W/2} y^4 dy = \frac{W^4}{80} \\ y_0^6 = \frac{1}{W} \int_{-W/2}^{+W/2} y^6 dy = \frac{W^6}{448} \end{cases}$

When setting $a = \frac{g H_0}{f_0}, b = \frac{g\beta}{f_0}, c = \frac{g}{f_0}$, we obtain:

$$\begin{cases} \eta_{0t} = a[(\frac{5}{2}\beta \eta_{0x} - \frac{3}{2}\eta_{1x} + \frac{3}{8}\beta W^2 \eta_{2x}) + \frac{\epsilon}{f_0}(\eta_{0xx} + 5\eta_2)] + N_0(\eta_i, \eta_j) \\ \eta_{1t} = a[(\frac{12}{W^2}\eta_{0x} - 2\beta \eta_{1x} + 3\eta_{2x}) + \frac{\epsilon}{f_0}(\eta_{1xx} - \frac{12}{W^2}\eta_1)] + N_1(\eta_i, \eta_j) \\ \eta_{2t} = a[(-\frac{30}{W^2}\beta \eta_{0x} + \frac{30}{W^2}\eta_{1x} - \frac{13}{2}\beta \eta_{2x}) + \frac{\epsilon}{f_0}(\eta_{2xx} - \frac{60}{W^2}\eta_2)] + N_2(\eta_i, \eta_j) \end{cases} \tag{27}$$

N_0, N_1, N_2 are all those nonlinear terms. For linear approximation, we can solve these diffusion equations. First we consider the case with a very small friction. The three characteristics are:

$$\begin{cases} \lambda_0 = -\beta a = -\frac{\beta g H_0}{f_0} \\ \lambda_{1,2} = \frac{a}{2W}[-7\beta W \pm 12\sqrt{2}] \end{cases} \tag{28}$$

The corresponding Rieman Invariances are:

$$\begin{cases} r_0 = \eta_2 - \frac{W^2}{4}\eta_0 \\ r_{1,2} = -\frac{W^2}{20}\eta_0 + \eta_2 - \frac{2W(3\beta W \pm 12\sqrt{2})}{5(8 \pm \beta W 12\sqrt{2})}\eta_1 \end{cases} \tag{29}$$

We see that $\lambda_0 = \frac{dx}{dt} = -\frac{\beta g H_0}{f_0}$ represents Rossby wave propogating from right to left, along these characteristics, $\eta_2 - \frac{W^2}{4}\eta_0$ is constant; $\lambda_{1,2}$ represent the two "Kelvin" waves with β-corrected velocity, their first order velocity is $\frac{6\sqrt{2}gH}{fW}$. Along these characteristics, r_1, r_2 will be constant. Of course, when diffusion is included, the values of r_0, r_1, r_2 are no longer constant along their characteristics. They will diffuse away. When the nonlinear terms are considered, it is a quasi-nonlinear system when friction terms are ignored. We have:

$$\begin{pmatrix} \eta_0 \\ \eta_1 \\ \eta_2 \end{pmatrix}_t = \begin{pmatrix} m_{11} & m_{12} & m_{13} \\ m_{21} & m_{22} & m_{23} \\ m_{31} & m_{32} & m_{33} \end{pmatrix} \begin{pmatrix} \eta_0 \\ \eta_1 \\ \eta_2 \end{pmatrix}_x,$$

where

$$
\begin{aligned}
m_{11} &= \tfrac{5}{2}a\beta + \tfrac{5}{2}b\eta_0 + \tfrac{9}{8}W^2\eta_2 - \tfrac{3}{2}c\eta_1 \\
m_{21} &= \tfrac{12}{W^2}a - 2b\eta_1 + \tfrac{12}{W^2}c\eta_0 + 3c\eta_2 \\
m_{31} &= -\tfrac{30}{W^2}a\beta - \tfrac{30}{W^2}\eta_0 - \tfrac{23}{2}b\eta_2 - \tfrac{30}{W^2}c\eta_1 \\
m_{12} &= -\tfrac{3}{2}a - \tfrac{3}{8}bW^2\eta_1 + \tfrac{9}{8}cW^2\eta_1 - \tfrac{3}{2}c\eta_0 - \tfrac{15}{16}cW^2\eta_2 \\
m_{22} &= -2a\beta - 2b\eta_0 - \tfrac{3}{5}bW^2\eta_2 + 3c\eta_1 \\
m_{32} &= \tfrac{30}{W^2}a - \tfrac{13}{2}b\eta_1 - \tfrac{15}{2}c\eta_1 - \tfrac{30}{W^2}c\eta_0 + \tfrac{45}{4}c\eta_2 \\
m_{13} &= \tfrac{3}{8}a\beta W^2 - \tfrac{702}{2240}bW^4\eta_2 + \tfrac{9}{8}bW^2\eta_0 - \tfrac{15}{16}cW^2\eta_1 \\
m_{23} &= 3a - \tfrac{3}{5}bW^2\eta_1 + 3c\eta_0 + \tfrac{3}{4}c\eta_2 \\
m_{33} &= -\tfrac{13}{2}a\beta - \tfrac{177}{56}bW^2\eta_2 - \tfrac{23}{2}b\eta_0 + \tfrac{45}{4}c\eta_1
\end{aligned}
$$

We can also solve for the three groups of characteristics and three Rieman Invariances. However, it is too long to be included here.

In order to get a sense on the steady state, we can start from a simpler system, namely, 2-level system, i.e. $\begin{cases} \alpha = \alpha_0 + y\alpha_1 \\ \eta = \eta_0 + y\eta_1 \end{cases}$. Using the same procedure, we derive the linear equations for the following cases:

(i) When $f \gg \epsilon, f = f_0(1+\beta y)$, take

$$
\begin{cases} u = -\frac{g\eta_y}{f} - \frac{\epsilon}{f^2}\eta_x \\ v = \frac{g}{f}\eta_x - \frac{\epsilon g}{f^2}\eta_y \end{cases} \tag{30}
$$

then

$$
\begin{cases} \eta_{0t} = H_x\frac{\eta_1 g}{f_0} + \frac{Hg\eta_{1x}}{f_0} + \frac{H\epsilon g}{f^2}\eta_{0xx} \\ \eta_{1t} = \frac{12gH\eta_{0x}}{W^2} - \frac{12H\epsilon g}{f^2W^2}\eta_1 - \frac{2g\beta H}{f_0}\eta_{1x} - \frac{gH\epsilon}{f^2}\eta_{1xx} - H_x\frac{g\beta}{f_0}\eta_1 \end{cases} \tag{31}
$$

When $H = const, f = const$ (so $\beta = 0$), the steady equation reduces to

$$
\begin{cases} 0 = \frac{Hg}{f_0}\eta_{1x} + \frac{H\epsilon g}{f^2}\eta_{0xx} \\ 0 = \frac{12gH}{W^2f_0^2}\eta_{0x} - \frac{12H\epsilon g}{W^2f^2}\eta_1 + \frac{H\epsilon g}{f^2}\eta_{1xx} \end{cases} \tag{32}
$$

Try $\begin{cases} \eta_0 = ax + b \\ \eta_1 = c \end{cases}$, we get

$$
\eta(x,y) = \frac{-\Delta\overline{\eta}f}{L\epsilon}y - \frac{\Delta}{L}x, \tag{33}
$$

where $\Delta\overline{\eta} = \eta_E - \eta_F = \frac{L\epsilon}{Wf}\Delta\eta, \Delta\eta = \eta_A - \eta_C = \eta_u - \eta_d$.

$$
u = -\frac{g\eta_y}{f} - \frac{\epsilon g}{f^2}\eta_x = \frac{g\Delta\overline{\eta}}{L\epsilon} + \frac{\epsilon g}{f^2L}\Delta\overline{\eta} \doteq \frac{g\Delta\overline{\eta}}{L\epsilon} = \frac{g\Delta\eta}{Wf} \tag{34}
$$

So we see that the expression depends on the definition of $\Delta\eta$. It also suggests that the orders of $\delta = \frac{W}{L}$ and $\epsilon_0 = \frac{\epsilon}{f}$ should be the same if $\Delta\overline{\eta}, \Delta\eta$ are to be the same order.

(ii) When $f \ll \epsilon$, take

$$
\begin{cases} u \doteq -\frac{fg}{\epsilon^2}\eta_y - \frac{g}{\epsilon}\eta_x \\ v \doteq \frac{fg}{\epsilon^2}\eta_x - \frac{g}{\epsilon}\eta_y \end{cases}, \tag{35}
$$

we have linear approximation:

$$\begin{cases} \eta_{0t} = H_x \frac{f_0 g}{\epsilon^2}\eta_1 + \frac{Hgf}{\epsilon^2}\eta_{1x} + \frac{Hg}{\epsilon}\eta_{0xx} \\ \eta_{1t} = \frac{12gHf}{W^2\epsilon^2}\eta_{0x} - \frac{12Hg}{\epsilon W^2}\eta_1 - \frac{f_0 g\beta H}{\epsilon^2}\eta_{1x} - \frac{gH}{\epsilon}\eta_{1xx} - H_x\frac{g\beta f_0}{\epsilon^2}\eta_1 \end{cases} \tag{36}$$

For steady state with $H = const, f = const$, it reduces to

$$\begin{cases} 0 = \frac{Hfg}{\epsilon^2}\eta_{1x} + \frac{Hg}{\epsilon}\eta_{0xx} \\ 0 = \frac{12gHf}{W^2\epsilon^2}\eta_{0x} - \frac{12Hg}{W^2\epsilon}\eta_1 + \frac{Hg}{\epsilon}\eta_{1xx} \end{cases} \tag{37}$$

And with $\frac{f}{\epsilon} \ll 1$, it turns out to be

$$\begin{cases} 0 = \frac{Hg}{\epsilon}\eta_{0xx} \\ 0 = -\frac{12Hg}{W^2\epsilon}\eta_1 + \frac{Hg}{\epsilon}\eta_{1xx} \end{cases} \tag{38}$$

Try $\begin{cases} \eta_1 \equiv 0 \\ \eta_0 = ax + b \end{cases}$
, we get

$$\eta = \frac{\Delta\eta}{L}\dot{x} \Longrightarrow u = -\frac{g}{\epsilon}\eta_x = -\frac{g\Delta\eta}{\epsilon L}, \tag{39}$$

which is what we got in the friction dominating limit.

2.2 Three-level Finite-different Method

Using the same scaling as in Section I, we will get the equation for depth η:

$$\eta_t - (a\eta + 1 - \Delta) + \delta^{-1}\Delta_x\eta_y = \epsilon_0[h(\eta_{xx} + \delta^{-2}\eta_{yy}) - 2\delta^{-1}h\eta_y + h_x\eta_x]_{(40)}$$

Corresponding dimensionless velocities are:

$$\begin{cases} u = -\frac{U_{//}}{a(1+\epsilon_0^2)}[\frac{\eta_y}{\delta} + \epsilon_0\eta_x] \\ v = \frac{U_{//}}{a(1+\epsilon_0^2)}[\eta_x - \frac{\epsilon_0}{\delta}\eta_y] \end{cases} \tag{41}$$

with $U_{//} = \frac{L}{T} = \frac{gH}{fL}$. Apply this equation to the three levels, namely, north bank η_1, central level η_0, and south bank η_2. Using the following replacements (see Fig.8):

$\frac{\partial\eta_0}{\partial y} = (\eta_1 - \eta_2), \frac{\partial^2\eta_0}{\partial y^2} = \frac{\eta_1+\eta_2-2\eta_0}{1/4}$

$\frac{\partial\eta_1}{\partial y} = \frac{\delta}{\epsilon_0}, \frac{\partial\eta_1}{\partial x} = \frac{\eta_+-\eta_0}{1}, \frac{\partial\eta_2}{\partial y} = \frac{\delta}{\epsilon_0}, \frac{\partial\eta_2}{\partial x} = \frac{\eta_0-\eta_-}{1}$

$\eta_+ = \eta_0 + \frac{\delta}{\epsilon_0}\eta_{1x}, \eta_- = \eta_0 - \frac{\delta}{\epsilon_0}\eta_{2x}$

$\frac{\partial^2\eta_1}{\partial y^2} = 4(2\eta_0 - 2\eta_1 + \frac{\delta}{\epsilon_0}\eta_{1x})$

$\frac{\partial^2\eta_2}{\partial y^2} = 4(2\eta_0 - 2\eta_2 - \frac{\delta}{\epsilon_0}\eta_{2x})$

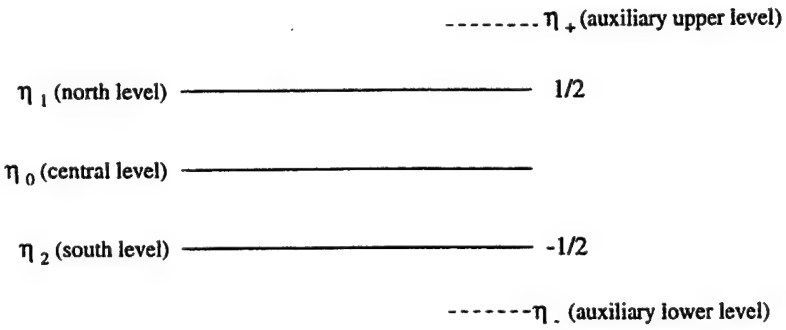

Figure 8: Orientation of levels

We readily get the following cases:

2.2.1 No topography, $\Delta = 0$, linear steady case:

The reduced equations can be written as:

$$\begin{cases} -\frac{4}{\delta}\eta_{1x} = \frac{8\epsilon_0}{\delta^2}(\eta_0 - \eta_1) \\ 0 = \eta_1 + \eta_2 - 2\eta_0 \\ \frac{4}{\delta}\eta_{2x} = \frac{8\epsilon_0}{\delta^2}(\eta_0 - \eta_2) \end{cases} \tag{42}$$

The solution is easy to get:

$$\begin{cases} \eta_1 = \frac{c_1+c_2}{2} + \frac{\epsilon_0}{\delta}c_1 x \\ \eta_2 = \frac{c_2-c_1}{2} + \frac{\epsilon_0}{\delta}c_1 x \\ \eta_3 = \frac{c_2}{2} + \frac{\epsilon_0}{\delta}c_1 x \end{cases} \tag{43}$$

where

$$\begin{cases} c_1 = \frac{(\eta_d-\eta_u)\delta}{\delta+\epsilon_0} \\ c_2 = \frac{(\eta_u+\eta_d)\delta+2\eta_u\epsilon_0}{\delta+\epsilon_0} \end{cases} \tag{44}$$

The boundary condition we used are:

$$\begin{cases} \eta_1(1) = \eta_C = \eta_d \\ \eta_2(0) = \eta_A = \eta_u \end{cases} \tag{45}$$

which is physicsally reasonable, as we have explained in the former sections. Equation (43) shows that the steady solution is three equally spaced parallel tilted lines, which is verified by simulation (see Fig. 9). We increase nonlinearity a from 0.01 to 0.134. It does not change the picture. We also see that when $\delta = \epsilon_0, \eta_2(1) = \eta_1(0)$, which is stated as $\eta_B = \eta_D$ in section 2.

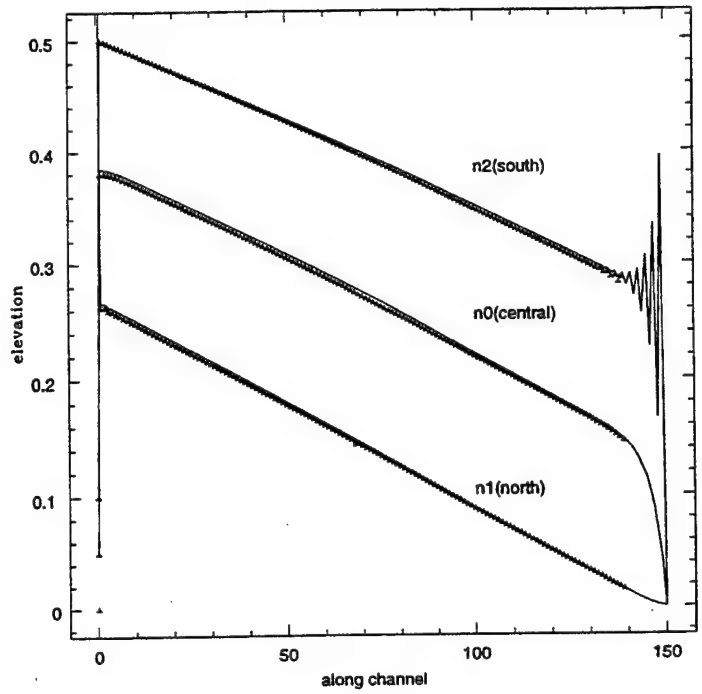

Figure 9: steady solution without bump (solid line: $a = 0$, dot line: $a = 0.13$)

2.2.2 Linear steady case with topography $\Delta(x)$:

We rewrite the equations as:

$$\begin{cases} \eta_{1x} = -b(\eta_0 - \eta_1) + \frac{\delta\nu}{4}\Delta_x \\ \eta_{2x} = b(\eta_0 - \eta_2) - \frac{\delta\nu}{4}\Delta_x \\ \eta_0 = \frac{1}{2}(\eta_1 + \eta_2) - \frac{1}{4}(\eta_1 - \eta_2)\Delta_x \end{cases} \tag{46}$$

where $b = \frac{2\epsilon_0}{\delta}, \nu = \epsilon_0 + \frac{1}{\epsilon_0}$ with boundary condition:

$$\begin{cases} \eta_1(1) = \eta_d \\ \eta_2(0) = \eta_u \end{cases} \tag{47}$$

In this case, the transport is calculated by:

$$Q = \frac{U_{//}}{a}\frac{(\Delta\eta + S - 1)}{\delta + \epsilon_0 S} \tag{48}$$

where

$$S = \int_0^1 e^{\Delta/2} dx \tag{49}$$

When we scale with $a = \frac{N_0}{H_0} = 1$, the transport becomes:

$$Q = \frac{gH}{fL} \frac{(\Delta\eta + S - 1)}{\delta + \epsilon_0 S} \tag{50}$$

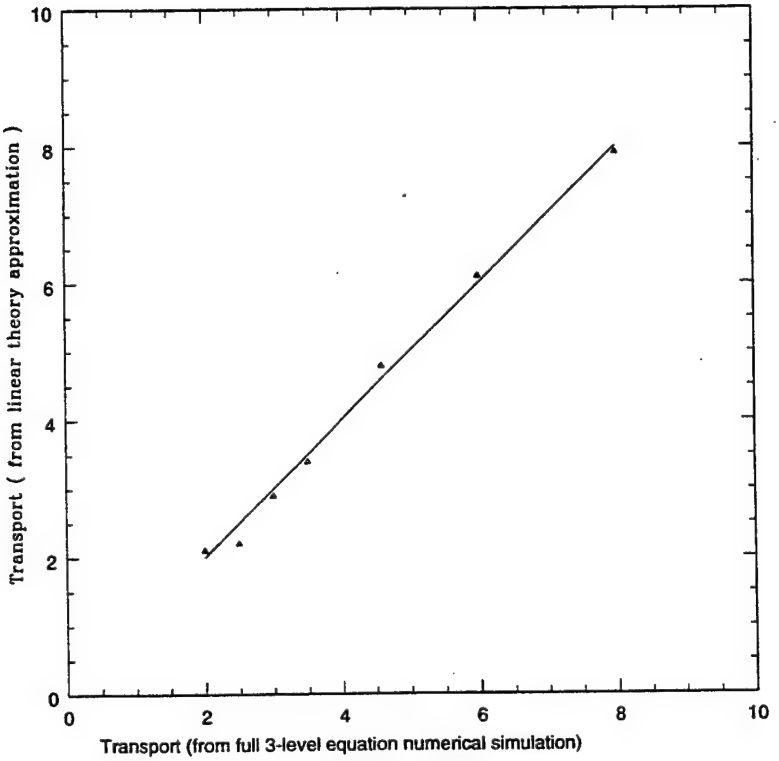

Figure 10: transports by linear theory and simulation

We notice the following:

(i) Usually S is about 1. For small bump, $S \doteq 1 + \frac{1}{2}S_1$, where S_1 is the side area of the bump.

(ii) When $\Delta\eta = \frac{\delta}{\epsilon_0} + 1$, transport is indenpendent of bump: $Q = \frac{gH}{fL\epsilon_0}$.

(iii) Q reduces to correct formula at two limits:

$$Q = \begin{cases} \frac{gH\Delta\eta}{fW}, & \delta \gg \epsilon_0 \\ \frac{gH_0\Delta\eta}{\epsilon L}, & \delta \ll \epsilon_0 \end{cases} \tag{51}$$

(iv) Simulation shows nonlinearity does not change Q more than 10%, as shown in Fig. 10.

2.2.3 Normal modes

Try

$$\eta_j \sim A_j e^{i(\omega t + kx)} \tag{52}$$

then we see 3 modes:

$$i\omega_0 = -\frac{8\epsilon_0}{\delta^2} + \lambda k i \rightarrow \text{Rossby wave} \tag{53}$$

$$i\omega_{1,2} = -\frac{8\epsilon_0}{\delta^2} \pm [(\frac{8\epsilon_0}{\delta^2})^2 - (\frac{4k}{\delta})^{x/2}] \rightarrow 2 \text{ Kelvin waves} \tag{54}$$

(i) ω_0 represents Rossby wave with phase speed $v_p = \lambda$, damping very fast (Fig.11)

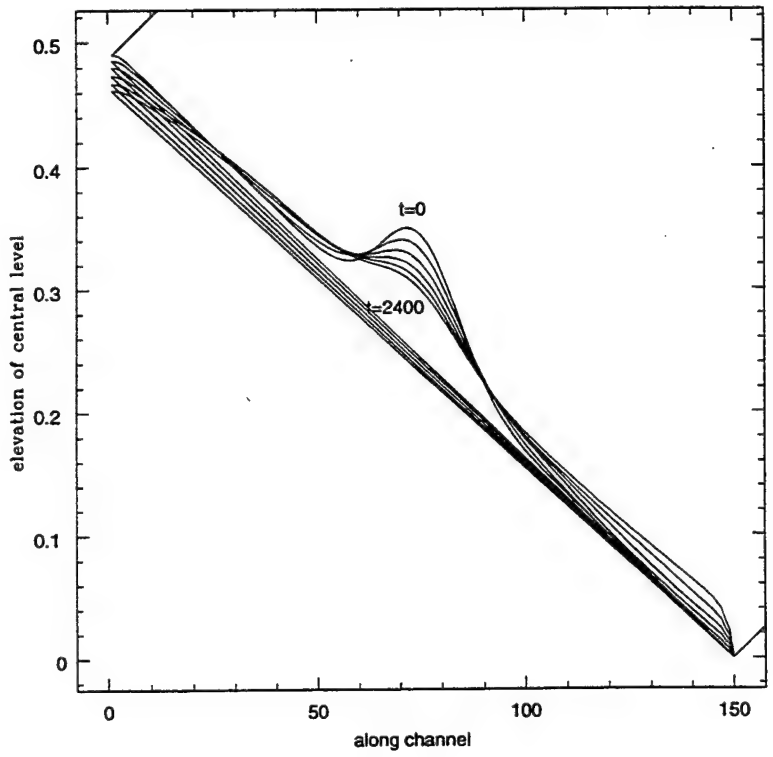

Figure 11: Evolution of central level

(ii) $\omega_{1,2}$ represent the two "Kelvin" waves propogating oppositely with the same speed $4/\delta$ (for short-wave limit), which is much faster than Rossby wave. (Fig. 12, Fig.13)

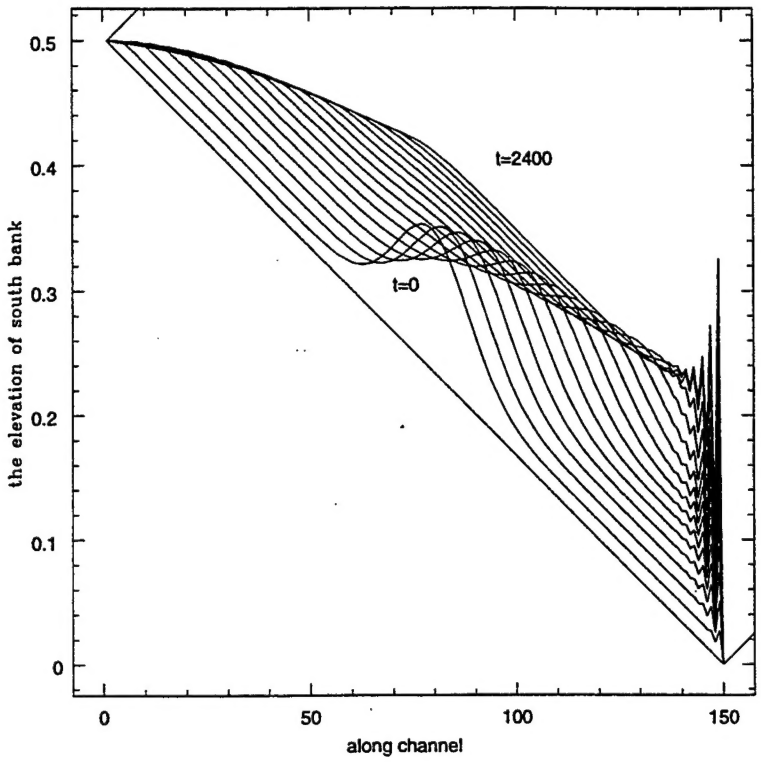

Figure 12: Evolution of south level

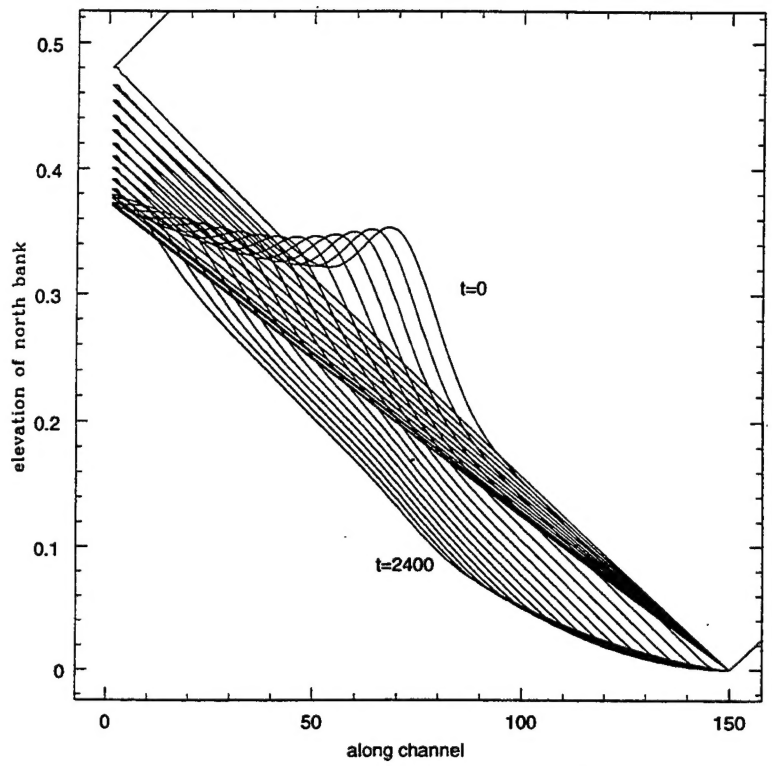

Figure 13: Evolution of north level

Acknowledgement

The author is deeply grateful to professor Rich Salmon for suggesting this project and for his patient guidance throughout the project. Thanks are also due to Professor Spiegel, my advisor, Neil, Steve and Larry Pratt, the principal lecturer, for their helps and encourages. The final tribute must go to Ms. Hongling Rao whose help, cooperation and understanding, at all stages of the project have been overwhelming.

References

[1] Gill, A. E., 1977,J. Fluid Mech, **80**, 641-671

[2] Pratt, L. J., 1986, J. Phys. Oceanogr., **16** 1970-1980

[3] Whitehead, J. A., 1989, Geophys. Astrophys. Fluid Dyn., **36**, 187-205

[4] Killworth, P. D., 1992, J. Phys. Oceanogr., **22**, 997-1017

DOCUMENT LIBRARY

Distribution List for Technical Report Exchange – July 1998

University of California, San Diego
SIO Library 0175C
9500 Gilman Drive
La Jolla, CA 92093-0175

Hancock Library of Biology & Oceanography
Alan Hancock Laboratory
University of Southern California
University Park
Los Angeles, CA 90089-0371

Gifts & Exchanges
Library
Bedford Institute of Oceanography
P.O. Box 1006
Dartmouth, NS, B2Y 4A2, CANADA

NOAA/EDIS Miami Library Center
4301 Rickenbacker Causeway
Miami, FL 33149

Research Library
U.S. Army Corps of Engineers
Waterways Experiment Station
3909 Halls Ferry Road
Vicksburg, MS 39180-6199

Marine Resources Information Center
Building E38-320
MIT
Cambridge, MA 02139

Library
Lamont-Doherty Geological Observatory
Columbia University
Palisades, NY 10964

Library
Serials Department
Oregon State University
Corvallis, OR 97331

Pell Marine Science Library
University of Rhode Island
Narragansett Bay Campus
Narragansett, RI 02882

Working Collection
Texas A&M University
Dept. of Oceanography
College Station, TX 77843

Fisheries-Oceanography Library
151 Oceanography Teaching Bldg.
University of Washington
Seattle, WA 98195

Library
R.S.M.A.S.
University of Miami
4600 Rickenbacker Causeway
Miami, FL 33149

Maury Oceanographic Library
Naval Oceanographic Office
Building 1003 South
1002 Balch Blvd.
Stennis Space Center, MS, 39522-5001

Library
Institute of Ocean Sciences
P.O. Box 6000
Sidney, B.C. V8L 4B2
CANADA

National Oceanographic Library
Southampton Oceanography Centre
European Way
Southampton SO14 3ZH
UK

The Librarian
CSIRO Marine Laboratories
G.P.O. Box 1538
Hobart, Tasmania
AUSTRALIA 7001

Library
Proudman Oceanographic Laboratory
Bidston Observatory
Birkenhead
Merseyside L43 7 RA
UNITED KINGDOM

IFREMER
Centre de Brest
Service Documentation - Publications
BP 70 29280 PLOUZANE
FRANCE

50272-101

REPORT DOCUMENTATION PAGE	1. REPORT NO. WHOI-98-09	2.	3. Recipient's Accession No.

4. Title and Subtitle
Rotating Hydraulic Control; 1997 Summer Study Program in Geophysical Fluid Dynamics

5. Report Date
July 1998

6.

7. Author(s) John A. Whitehead, Director

8. Performing Organization Rept. No.
WHOI-98-09

9. Performing Organization Name and Address
Woods Hole Oceanographic Institution
Woods Hole, Massachusetts 02543

10. Project/Task/Work Unit No.

11. Contract(C) or Grant(G) No.
(C) OCE-9314484
(G) N00014-97-1-0934

12. Sponsoring Organization Name and Address
National Science Foundation
Office of Naval Research

13. Type of Report & Period Covered
Technical Report

14.

15. Supplementary Notes
This report should be cited as: Woods Hole Oceanog. Inst. Tech. Rept., WHOI-98-09.

16. Abstract (Limit: 200 words)

Rotating Hydraulic Control was the topic of the thirty ninth year of the Geophysical Fluid Dynamics (GFD) program at the Woods Hole Oceanographic Institution. This theme was principally centered about those nonlinear problems in which either a free surface or internal stratification is so modified by flow that it acts to choke off increased flux as the forcing is increased. It is a peculiar form of convection, which shares many constraints with more general buoyancy driven motion but which has its own internal limits. Lectures and seminars were given by GFD staff and visitors, most of whom are founders of this young field of study. This volume contains notes from the talks given by the principal lecturers and written reports on the research projects carried out by the ten student fellows. The volume, therefore, summarizes a sizable percentage of the present understanding of the topic of Rotating Hydraulic Control.

17. Document Analysis **a. Descriptors**
convection
rotating hydraulic control
geophysical fluid dynamics

b. Identifiers/Open-Ended Terms

c. COSATI Field/Group

18. Availability Statement
Approved for public release; distribution unlimited.

19. Security Class (This Report)
UNCLASSIFIED

20. Security Class (This Page)

21. No. of Pages
274

22. Price

(See ANSI-Z39.18) *See Instructions on Reverse*

OPTIONAL FORM 272 (4-77)
(Formerly NTIS-35)
Department of Commerce